SEDIMENTOLOGICAL AND GEOCHEMICAL DYNAMICS OF EASTERN
EDREMIT BAY DURING HOLOCENE

A THESIS SUBMITTED TO
THE GRADUATE SCHOOL OF NATURAL AND APPLIED SCIENCES
OF
MIDDLE EAST TECHNICAL UNIVERSITY

BY

PİR ÇAĞATAY KARTAL

IN PARTIAL FULFILLMENT OF THE REQUIREMENTS
FOR
THE DEGREE OF DOCTOR OF PHILOSOPHY
IN
EARTH SYSTEM SCIENCE

JANUARY 2025

Approval of the thesis:

**SEDIMENTOLOGICAL AND GEOCHEMICAL DYNAMICS OF
EASTERN EDREMIT BAY DURING HOLOCENE**

submitted by **PİR ÇAĞATAY KARTAL** in partial fulfillment of the requirements
for the degree of **Doctor of Philosophy** in **Earth System Science, Middle East
Technical University** by,

Prof. Dr. Naci Emre Altun
Dean, **Graduate School of Natural and Applied Sciences**   _____

Prof. Dr. İsmail Ömer Yılmaz
Head of the Department, **Earth System Science**   _____

Prof. Dr. Mustafa Yücel
Supervisor, **Earth System Science, METU**   _____

Assist. Prof. Dr. Devrim Tezcan
Co-Supervisor, **Instute of Marine Science, METU**   _____

Examining Committee Members:

Prof. Dr. İsmail Yücel
Department of Civil Eng. and ESS, METU   _____

Prof. Dr. Mustafa Yücel
Institute of Marine Sciences, METU   _____

Prof. Dr. Sevinç Altıner
Department of Geological Eng., METU   _____

Assoc. Prof. Dr. Berna Yavuz Pehlivanlı
Department of Geological Eng., Yozgat Bozok University   _____

Assistant Prof. Dr. Gülsen Uçarkuş
Department of Geological Eng., İTÜ   _____

Date: 07.01.2025

I hereby declare that all information in this document has been obtained and presented in accordance with academic rules and ethical conduct. I also declare that, as required by these rules and conduct, I have fully cited and referenced all material and results that are not original to this work.

Name Last name : Pir Çağatay Kartal

Signature :

ABSTRACT

SEDIMENTOLOGICAL AND GEOCHEMICAL DYNAMICS OF EASTERN EDREMIT BAY DURING HOLOCENE

Kartal, Pir Çağatay
Doctor of Philosophy, Earth System Science
Supervisor: Prof. Dr. Mustafa Yücel
Co-Supervisor: Assist. Prof. Dr. Devrim Tezcan

January 2025, 199 pages

Comprehensive field and laboratory investigations were carried out to explain the relationships between sedimentation, tectonic activity, and climatic conditions in the Edremit Bay (Gulf of Edremit) during the Late Pleistocene to Holocene periods. For this purpose, a total of 60 marine core samples collected from the Edremit Bay (Gulf of Edremit) in 2019 using the MTA R/V Selen. The cores were subjected to analyses including ITRAX-XRF, magnetic susceptibility (MS), radiocarbon dating, grain size, $\delta^{18}O$ mass spectrometry, and total organic carbon analysis. These analyses have yielded significant insights into the region's paleoenvironmental and paleoceanographic history. The findings from the analyses align with global-scale Meltwater Pulses (MWPs), occurring between the Bølling–Allerød period (approximately 14,690 years ago) and the Holocene Warm Period (around 8,000 years ago). Additionally, the findings align with local-scale climatic results obtained from the Sofular Cave and cores from the northern Aegean Sea. It has been observed that the presence of terrestrial sedimentation in the basin, indicated by elements such as Fe, Ti, and K, is closely related to variations in magnetic susceptibility data and grain size changes. The Fe/Mn ratio has been used to make interpretations regarding changes in bottom water oxygen levels. Variations in grain size were strongly linked

to submarine morphology features (e.g., paleo-channels, faults) and sea-level fluctuations, offering valuable insights into the evolution of sedimentation dynamics within the basin. Based on these findings, a geological model was developed to explain the interplay of tectonic, climatic, and sedimentary processes that have shaped the Edremit Bay basin over time.

Keywords: Edremit Bay, Marine Core Sample, Paleoclimate, Paleoceanography, Sedimentation Dynamics

ÖZ

HOLOSEN DÖNEMİNDE EDREMİT KÖRFEZİ'NİN DOĞUSUNDAKİ SEDİMANTOLOJİK VE JEOKİMYASAL DİNAMİKLER

Kartal, Pir Çağatay
Doktora, Yer Sistem Bilimleri
Tez Yöneticisi: Prof. Dr. Mustafa Yücel
Ortak Tez Yöneticisi: Dr. Öğr. Üyesi Devrim Tezcan

Ocak 2025, 199 sayfa

Edremit Körfezi'nin, Geç Pleistosen-Holosen dönemleri arasındaki sedimantasyon, tektonik ve iklim koşulları arasındaki bağlantıları detaylandırmak için arazi ve laboratuvar çalışmaları yapılmıştır. Bu amaçla Edremit Körfezinden 2019 yılında MTA Selen R/V ile toplanan 60 adet denizel karot örneği, ITRAX-XRF, manyetik hassasiyet (MS), radyokarbon (C14) tarihlendirme, $\delta^{18}O$ kütle spektrometresi, total organik karbon ve tane boyu analizlerine tabii tutulmuştur. Bu analizlerin sonucunda bölgenin paleoiklim ve paleoşinografik bulguları ortaya konulmuştur. Analiz sonuçlarında elde edilen bulgular Bølling–Allerød (14,690 yıl) ile Holosen Sıcak Dönemi (8,000 yıl) yılları arasındaki global ölçekteki MWP (katastrofik su baskınları) ile uyumludur. Ayrıca elde edilen bulgular Sofular Mağarası ve Kuzey Ege Denizi'nden alınan karotların lokal ölçekteki iklimsel sonuçları ile de uygunluk göstermektedir. Havzadaki karasal malzeme varlığını gösteren elementler (Fe, Ti, K vb.) ile manyetik hassasiyet verileri, tane boyundaki değişim ile de yakından ilişkili olduğu gözlenmiştir. Fe/Mn oranı sayesinde dip suyu oksijen seviyesi değişimleri hakkında yorumlamalarda bulunulmuştur. Tane boyundaki değişiklikler, deniz altı morfolojisi (plaeokanal, fay vb.) ve deniz seviyesi değişimleri yakından ilişkili olup havzanın sedimantasyon dinamiklerinin nasıl gelişim gösterdiği konusunda

yorumlamalar ortaya konulmuştur. Tüm bu veriler ışığında bir model oluşturularak Edremit Körfezi havzasının tektonik-iklimsel- sedimantasyonu açıklamaya çalışan bir jeolojik model sunulmuştur.

Anahtar Kelimeler: Edremit Körfezi, Denizaltı Karot, Paleoiklim, Paleo-oşinografı, Sedimantasyon Dinamikleri

I dedicate this study to my wife and family, who have never lost faith in me, and

my soon-to -be-born daughter.

ACKNOWLEDGMENTS

TABLE OF CONTENTS

xii

LIST OF TABLES

LIST OF FIGURES

FIGURES

xvii

LIST OF ABBREVIATIONS

AES: Aegean Extensional System

BP: Before Present

cmbsf: Centimeters Before Surface

EKF: Edremit Körfezi Fayı

EMF: Edremit Midilli Fayı

GoE: Gulf of Edremit

GoS: Gulf of Saros

IC: Inorganic Compound

İASZ: İzmir-Ankara Suture Zone

İBTFZ: İzmir-Balıkesir Transform Fault Zone

ka: Thousand Ages

MS: Magnetic Susceptibility

MSCL: Multi-Sensor Core Logger

NAFZ: North Anatolian Fault Zone

TOC: Total Organic Compound

XRF: X-Ray Fluorescence

LIST OF SYMBOLS

Al: Aluminum

Ca: Calcium

Cl: Chlorine

Cr: Chromium

Cu: Cupper

Fe: Iron

K: Potassium

Ni: Nickel

Pb: Lead

Sr: Strontium

Ti: Titanium

Zn: Zinc

CHAPTER 1

INTRODUCTION

Marine geology focuses on understanding the environmental and process records from the core samples. This study builds on core analyses from the Eastern Edremit Bay (Gulf of Edremit) (GoE) coastal basin, via a suite of geochemical tools including ITRAX, μXRF scanners. Before presenting the approach and methodology, here main features driving the GoE geochemical dynamics are presented.

The geodynamic process for the neotectonic evolution of Turkey which is the Southern Aegean trench evolution, is directly affecting the Aegean coasts. The GoE is mainly affected by geological changes in the Kazdağ and Madra Mountains regions. The main tectonic elements are the western branches of the North Anatolian Fault Zone (NAFZ) and the İzmir-Ankara Suture Zone (İASZ) in the Northern part. The İzmir and Balıkesir Transform Fault Zone (İBTFZ) is another tectonic element that directly affected the southern part of the GoE. The GoE is mainly located between the intersection of the strike-slip regime of NAFZ and Aegean Extentional System (AES). The northern part of the basin displays a basin-wide step-like morphology due to a considerable amount of normal slip components. The northern margin of the Edremit basin is surrounded by thick and weakly consolidated delta fan deposits. GoE is bounded by Müsellim Strait at the west, which is located between Lesvos Island and the Biga Peninsula (e.g., McKenzie, 1972; Şengör,1979; Jackson and McKenzie,1988; Taymaz et al.,1991; Yılmaz et al., 2000; Gürer et al., 2001; Bozkurt, 2003; Gürer et al.,2003,2006; Gürer et al., 2009,2014; Yılmaz et al.,2010; Jolivet et al.,2013; Gürer et. al.,2016).
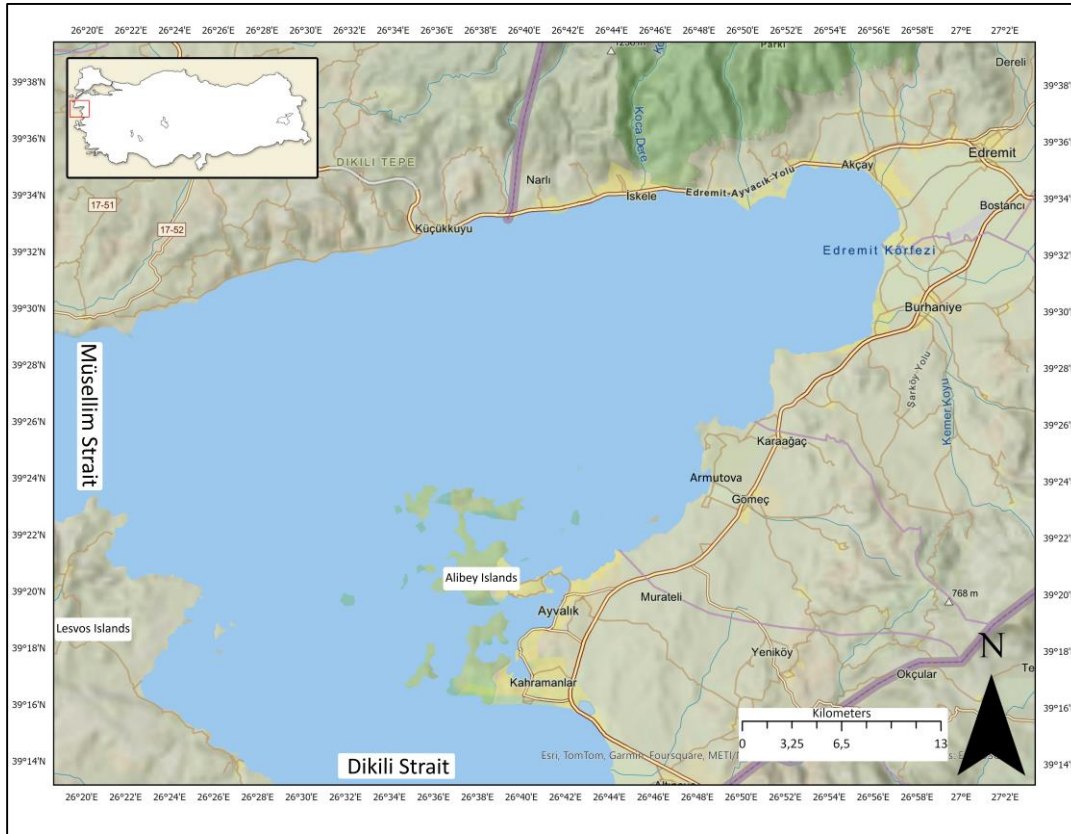
Figure 1.1 Geographic settings of study area

Northern and southern part of the gulf have different rotation direction. So, the strain extension axes are in the northern part NE-SW direction and the southern part has NW-SE strain axes. The interpretation of faults and associated mechanisms are varied in the north and southern parts. The geometry and type of the faults are unclear. For that reason, researchers' interpretations differ from each other's within the same study area. Beyhan (1999), Yaltırak (2003), Kurtuluş (2009) and Eytemiz (2020) interpretations are given in this study to compare their results (e.g., İşseven et al,1995; Schindler, 1997; Barka and 315 Reilinger, 1997; Kaymakçı et al.2007).

The Aegean Sea's circulation follows a basin-wide cyclonic pattern, with Eastern Mediterranean waters flowing north along the Turkish coast and a balancing southward current along the Greek coast. The sea's complex topography, along with numerous islands and varying weather conditions, generates smaller cyclonic and anticyclonic eddies throughout the region. In the GoE, currents flow from the north

and south, creating smaller eddies near the coast. Notably, an anticyclonic eddy has been observed east of the Alibey Islands (southern islands) within the gulf (Sayın et. al., 2011 and Duman et.al., 2018).

In the GoE, between 13,000 and 28,000 years ago, when sea levels were about 90 meters lower than today's sea level, the Würm Seismic Stratigraphic Unit was deposited, as observed by Yaltırak (2003). Based on the sea level curve and the maximum depth of the tectonically adjusted Müsellim Channel, Yaltırak (2003) concluded that around 10,000 years ago, sea levels were 60 to 90 meters below present levels. As sea levels rose during the Holocene, transgressive deposits likely accumulated over the delta regions along the basin's edge in the GoE. Studies specifically focused on sea level changes along Turkey's coastlines are limited; most data come from global research, which has mainly focused on changes since the Middle Holocene. These studies suggest that sea levels were about 120 meters lower during the last glacial maximum, reached approximately 3 meters above current levels in the Middle Holocene (around 5,000 years ago), and then gradually declined to present-day levels. Sea level rise has not been constant but marked by rapid melt events with stable periods in between. Global studies identify these rapid increases referred to as meltwater pulses (MWP-1a, b, and sometimes MWP-1a, b, c). Such abrupt shifts likely impacted marine environments, creating unique formations influenced by hydrodynamic conditions, seafloor topography, and sediment dynamics (e.g., Yaltırak, 2003; Stanford et al., 2011; Cooper et. al., 2018; Duman et.al., 2018). The effects of meltwater pulses (MWP-1a and MWP-1b) are evident in the GoE, where rising sea levels have altered sediment transport and deposition patterns. This study investigates these sediment dynamics using geochemical proxies and grain size analysis.

1.1   Purpose and Scope

The overarching aim of this thesis is to uncover of how relative shifts in climate and redox conditions have influenced sedimentation and geochemical dynamics

in the GoE. The thesis also seeks to identify major patterns of climate variability on centennial and longer time scales, including natural changes occurring from the late Pleistocene to the Holocene. In addition, this study utilizes geochemical proxies to conduct provenance analysis, tracing the origins of sediments in the region. For this purpose, a marine survey was conducted in the GoE by MTA's R/V Selen in 2019 to collect sediment cores from the different part of the gulf. The multi-proxy approach used in this thesis enabled the identification and characterization of shifts in climate and redox conditions in the GoE. By comparing these local changes with regional examples from the Aegean Sea, this study advances our understanding of how climate variability from the late Pleistocene to the Holocene influenced the depositional evolution of the gulf.

This thesis investigates the impact of sea level rise potentially driven by global catastrophic flooding events on sediment dynamics in the GoE. It addresses the complexities arising from tectonic activity in the study area. Additionally, this thesis emphasizes identifying the origin of transported sediments by analyzing specific elemental compositions. Multi-proxy analyses such as ITRAX-XRF, Multi-sensor Core Logger (MSCL), Total Organic Carbon (TOC), Radiocarbon dating, Oxygen Isotope and grain size from those cores allowed to investigate paleoclimate, paleoceonographic and deposition dynamics history of the gulf.

In summary, the specific aims of this thesis can be divided as followed below;

   I.   To reconstruct climate variability during the Late Pleistocene to Holocene in the gulf by using a multi-proxy approach in order to identify and characterize the relative climate and oceanographic oscillations.

  II.   To compile and integrate a geochemical and sedimentological record for the characterization of depositional evolution within the gulf.

 III.   To discuss main forcing factors related with depositional dynamics driving climate or tectonic variability in the gulf during this time interval.

 IV.   To understand sedimentation origins (provenance) and transport pathways.

1.2   Step-by-Step Analysis of Eastern Edremit Bay Sediments Through the Holocene

The step-by-step methodological workflow for analyzing Eastern Edremit Bay sediments during the Holocene interval is presented in Figure 1.2.
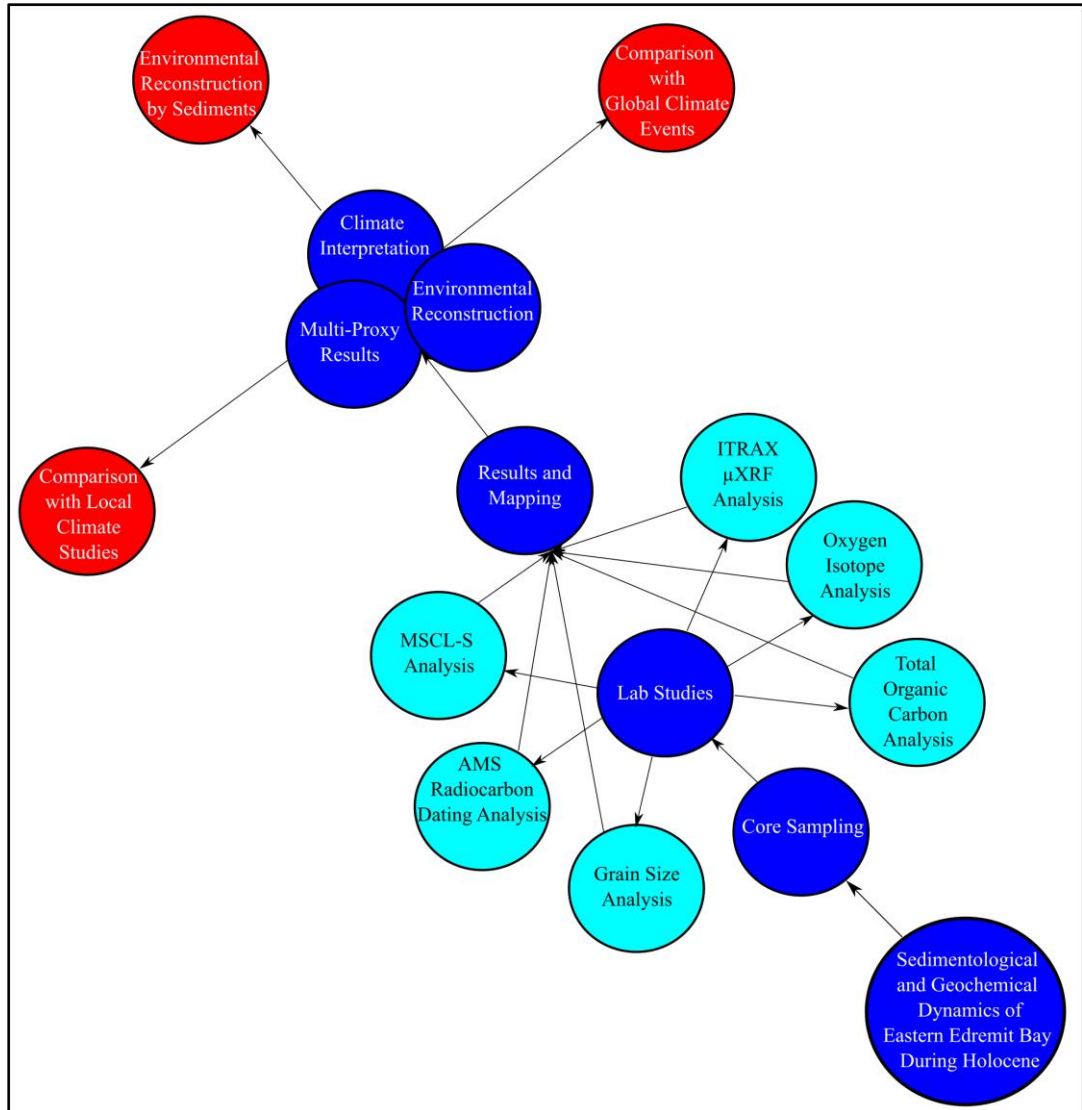
Figure 1.2 Methodological workflow of GoE study

CHAPTER 2

LITERATURE REVIEW

2.1   Geology of Biga Peninsula

The Biga Peninsula is a tectonic mosaic consisting of continental and oceanic fragments of different ages and origins, which has a complex geological history due to deformation and magmatism events under different conditions at different times. The majority rocks exposed in the Biga Peninsula is composed of volcanic, sub-volcanic, and plutonic rocks associated with core complexes and their exhumation (Figure 2.1). These core complexes are named Kazdağ, Çamlıca, Karabiga, and Karadağ Massifs (e.g., Okay and Satır, 2000; Beccaletto et al., 2007; Şengün et al., 2011; Tunç et al., 2012). The Kazdağ Massif (PMKk), which was metamorphosed during the Variscan period, is generally composed of gneisses, marbles, amphibolites, and metabasites. Due to the effect of the extensional regime that began after the collision (between the Arabian and Eurasian Plates along the Bitlis-Zagros Suture Zone), the Kazdağ Massif was exhumed by uplift along detachment faults during the Oligo-Miocene period. The region is characterized by a complex structural geology, with an active dextral strike-slip faulting and N–S extension. The basement rocks consist of Paleozoic metamorphic rocks and Mesozoic accretionary mélange, while intrusive rocks ranging from granite to quartz diorite cut these basement rocks. The area is also overlain by calc-alkaline and alkaline Oligocene-Miocene volcanic and related sedimentary rocks, which include andesite, latite, dacite, rhyodacite flow dome facies, and volcaniclastic sequences. These volcanic rocks are the primary host for epithermal gold and silver mineralization within the Biga Peninsula. Additionally, the region has experienced the formation of high-medium degree metamorphic, ophiolite, plutonic, volcanic, and sedimentary rocks (Okay et al.,1991).

LEGEND

Qal	Alluvium
Qysm	Slope Debris
Tplb	Bayramic Fm: Calcareous, Marly, Silty, Sandstone (Riverine and Lake)
Tmplg	Gulpinar Fm: Calcareous, Marly, Silty, Sandstone (Lake)
Tutt	Tastepe Bazalti: Olivine,Basalt, Pyroclastic Rocks
Tmat	Alcitepe Uyesi: Calcarenite Limestone, Sandstone, Marn and Claystone (Tide effect)
Tmi	Ilyasbasi Fm: Congolmerate, Sandstone, Claystone, Limestone, Mudstone, Marn
Tmbb	Babadere Dasiti: Dacite and Pyroclastic Rocks
Tmc	Camkabalak Ignimbiriti: Ignimbrite
Tmay	Ayvacik Volkaniti: Basalt, Basaltic Andesite, Andesite and Pyroclastic Rocks
Tmar	Arikli Ignimbiriti: Ignimbrite and Tuff
Tmbü	Huseyinfaki Volkaniti: Basaltic Andesite, Basalt, Andesite and Pyroclastic Rocks
Tmk	Kucukkuyu Fm: Conglomerate, Sandstone, Siltstone, Shale, Tuff, Marn
Tme	Ezine Volkaniti: Andesite, Pyroclastic Rocks
Tmbe	Behramkale Volkaniti: Andesite, Pyroclastic Rocks
Tmbi	Bademli Volkaniti: Andesite, Pyroclastic Rocks
Tmba	Babakale Volkaniti: Andesite, Basaltic Andesite, Pyroclastic Rocks
Tma	Araplar Volkaniti: Andesite, Pyroclastic Rocks
Tmyü	Yuntdag Volkaniti: Tuff, Coal-Bearing Formations, Andesite, Basaltic Andesite, Pyroclastic Andesite
Tmy	Yurekli Dasiti: Dacite, Pyroclastic Rocks
Tmh	Halazdag Volkaniti: Andesite, Pyroclastic Rocks
Toh	Hallaclar Volkaniti: Andesite, Dacite, Pyroclastic Rocks
Tompk	Granodiorite Porphyry
Og	Oligo-Miocene Granodiorite: Granit, Granodiorite, Monzonite
Kç	Cetmi Melanji: Ophiolitic Rocks, Calcareous, Radiolarite, Silt, Muscovite Schist, Blocks
s	Serpentinite
e	Eclogite
TR	Triassic Aged Crystalline Block
TRk	Karakaya Fm: Metasandstone, Metamudstone, Metavolcanic
Pb	Bozalan Fm: Recrystalized Limestone, Congolmerate, Metasandstone
TRkk	Karakaya Kompleksi: Metaconglomerate, Metasandstone, Sandstone, Sandy Limestone,Tuff, Metavolcanic, Permo-Carboniferous aged Limestone
TRkm	Mehmetalan Fm: Metatuff, Recrystalized Limestone
Pzs	Sazak Fm: Metatuff, Schist Marble
Pzsm	Marble
AMZ	Alakecili Miloniti: Cataclastic Rocks, Ultramylonite
Cs	Sutuven Fm: Schist, Sillymanite Schist, Granitic Schist, Marble, Migmatite (Metamorphic Age:Carboniferous)
Gg	Granitik Gnays: Metagranite
Msi	Sarikiz Mermeri: Marble, Schist
Mzt	Tozlu Fm: Metaperidotit, Serpentinite
TRf	Findikli Fm: Amphibolite Schist, Classiclastic Schist, Schist, Marble
TRfb	Babadag Mermeri: Marble
TRfa	Altinoluk Mermeri: Marble

Figure 2.1 GoE map of geology (Kartal et al., 2022)

The Kalabak Formation, presumably placed tectonically at the top of the Kazdağ Massif, is of Silurian age and comprises low-grade metamorphic units. Stratigraphically, it underlies the Torasan (Pzt), which is composed of phyllite and marble, and is overlain by the Sazak Formations (Pzs) consisting of marble-interbedded metavolcanites (Figure 2.1) (Okay et al., 1991; Aysal et al., 2012a). The

Kalabak Unit is locally unconformably and elsewhere tectonically overlain by the Triassic-aged Karakaya Complex (K-Trk) (Şengör et al., 1984; Okay et al., 1991). The Karakaya Complex, associated with the Paleotethys Ocean, comprises spilitic basalt (TRkç), metavolcanic (TRkm) arkosic sandstones (TRka), recrystallized limestones (TRkç) units, and Permian limestone blocks (Pk) juxtaposed along tectonic contacts (Figure 2.1) (e.g., Bingöl et al., 1975; Okay et al., 1996; Pickett and Robertson, 1996; Okay and Göncüoğlu, 2004). The Çamlıca Metamorphites, which underwent metamorphism during the Late Cretaceous, stratigraphically consist of metaserpentinite lenses and mica schists with marble interlayers at the bottom (Kças), and lower-grade metamorphites at the top (Kçap). The Karadağ Group is formed of Permian-Triassic recrystallized limestones (TRç) overlying Early Paleozoic-aged metamorphites (Eg). The Denizgören Ophiolite (Kd) of Cretaceous age tectonically overlays these two units (Figure 2.1) (Duru et al., 2012 and Okay et al., 1991). Pre-Tertiary units on the Biga Peninsula came together during the Late Cretaceous-Eocene period. The units, which underwent extensive deformation during the Alpine-Himalayan Orogeny and the neotectonic period, experienced compressional deformation during the Late Cretaceous-Eocene and Oligo-Miocene periods, extensional during the early-middle Miocene, and were deformed under a strike-slip fault dominated tectonic regime during the neotectonic period (Yılmaz et al., 2001). During the Late Cretaceous period, following the closure of the Neotethys Ocean and the subduction of the Anatolide-Tauride Block beneath the Sakarya Zone, a continent-continent collision occurred. Along the İzmir-Ankara-Erzincan Suture Zone, the Anatolide-Tauride Block and the Sakarya Zone converged, leading to various phases of magmatism related to subduction and continent-continent collision in the Northwestern Anatolia. The initial magmatic phase in the region is a product of post-collisional arc magmatism developed during the Eocene period. Magmatic rocks, ranging from basalt to dacite. The Eocene Volcanics are stratigraphically transitional with the upper zone's clastic Fıçıtepe Formation and Soğucak limestones, indicating that the Eocene volcanism developed underwater (Okay and Siyako, 1991; Genç et al., 2012). The Biga Peninsula experienced terrestrialization

and intense magmatic activity during the Oligocene period. This phase, which is widespread throughout the Biga Peninsula, displays characteristics of arc magmatism affected by crustal contamination (Yılmaz et al., 2001). The masses, which also have semi-depth and volcanic equivalents, were intruded into shear zones formed by detachment faults that caused the exposure of the Kazdağ Massif. These masses, which generally exhibit NW-SE orientations on the map, include the Evciler, Eybek, Kozak, Kestanbol, and Ilıca-Şamlı Plutons among others. These formations are calc-alkaline in character and high in K content, consisting of granodioritic, dioritic, and monzonitic bodies. The volcanics, which are exposed everywhere on the Biga Peninsula and are the surface equivalent of the plutons, have been divided into five formations based on lithological and geochronological characteristics: the Atikhisar Volcanite, Yeniköy Volcanite, Sarıçayır Volcanite, Bağburun Formation, and Hallaçlar Volcanite (Genç et al., 2012). In the Biga Peninsula, during the Early-Middle Miocene period, intense volcanic activity is observed simultaneously with lacustrine sediments. The volcanics, generally composed of lavas such as andesite, trachyandesite, trachyte, latite, and basaltic andesite and their pyroclastics, are named based on their geographic localities; Ezine Volcanite (Tme), Araplar Volcanite (Tma), Babakale Volcanite (Tmba), Bademli Volcanite (Tmb), Ortatepe Volcanite, Halazadağ Volcanite (Tmh), Şapçı Volcanite, and Yürekli Dacite (Tmy) (Figure 2.1) (Genç et al., 2012). The last magmatic phase in the Biga Peninsula corresponds to the late Miocene period. This period, characterized by the formation of rocks with a mafic character, is dominated by alkaline magmatic activity (Ercan et al., 1995). In the eastern part of the study area, on top of the Late Miocene terrestrial and lacustrine sediments of the İnönü Formation; the Pliocene-Quaternary-aged Hasanboğuldu Formation (PlQh), Travertines extending from the Pleistocene to the present (Qç), Slope debris (Qym), and Alluviums (Qa) have been deposited unconformably (Figure 2.1) (Okay and Siyako, 1991).

10

2.2   Tectonic Development of GoE

The geological evolution of Turkey and its vicinity is influenced by three main geodynamic activities. These are,

1. The ongoing collision between the Arabian and Eurasian Plates along the Bitlis-Zagros Suture Zone,
2. The Anatolian Block's westward progression via the North and East Anatolian Fault Systems, originating from the zone where the Arabian and Eurasian plates collide (as noted by McKenzie, 1972 and Şengör, 1979)
3. The African Plate being forced beneath the Eurasian Plate along the Southern Aegean Trench (highlighted in studies by McKenzie, 1972, Jackson and McKenzie, 1988, and Jolivet et al., 2013).

It is also believed that this subduction process contributes to the extensional geological setting in western Turkey (Gürer et. al., 2016).
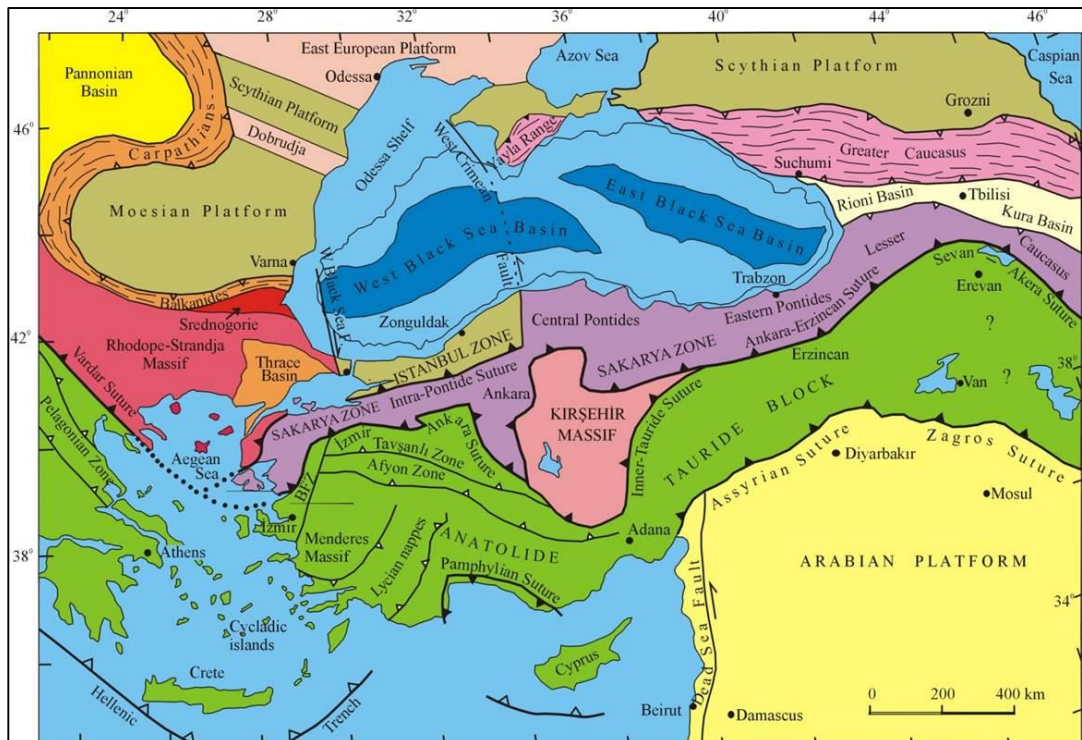
Figure 2.2 General tectonics of Turkey (Okay and Tüysüz, 1999)
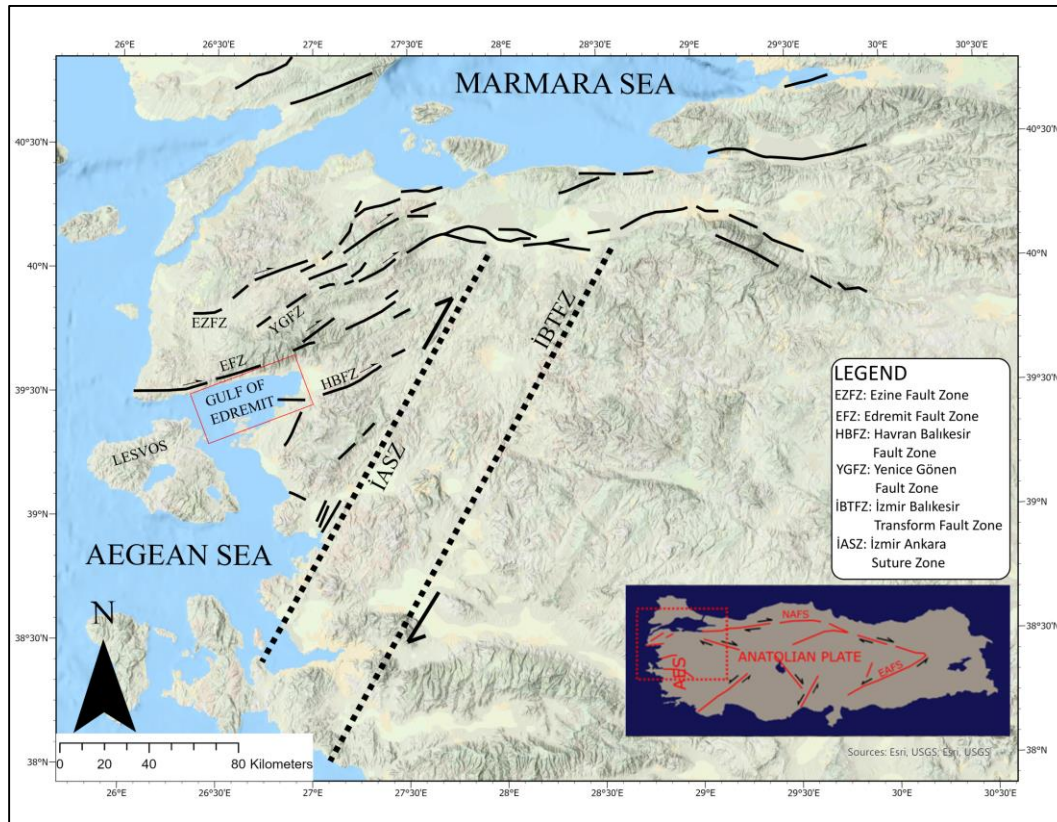
Figure 2.3 Major tectonic elements and fault zones around GoE

Structural data indicating deformation from both the Paleotectonic (before the Cretaceous) and Neotectonic (Miocene onwards) regimes are identified to the north of the GoE, as outlined by Yılmaz and Karacık (2001) and Yaltırak and Okay (2004). During the period spanning the Permian to the Early Triassic, thrust faults emerged as a result of the Tethys Ocean's subduction, which were subsequently elevated and folded throughout the Cretaceous tectonic activities, as noted by Yaltırak et al. (2000). The Neotectonic phase commenced with the development of N-NE to S-SW oriented extensional faults, driven by a N-S compressional regime present in the Early to Middle Miocene. Furthermore, this period witnessed the continuation of the compressive forces, leading to the creation of a fold axis with an E-W orientation (Kurtuluş et. al., 2009).

The N-S compressive forces that initiated in the Late Miocene led to the formation of obliquely oriented normal faults with a predominant NE-SW and N-NE to S-SW

direction, featuring a primary dip-slip movement along with a minor strike-slip component, as identified by Yılmaz and Karacık (2001). These NE-SW trending faults, located to the North of the Edremit Gulf and influential in shaping the Ezine Grabens, further contributed to the formation of the Etili and Gülpinar Grabens. The ongoing N-S compression in the area prompted the emergence of an erosional planar landscape. The Kazdağ Horst, positioned to the north of the GoE, reached its current height due to E-W oriented faults. Situated to the north of the GoE, the Bayramiç Graben is a secondary half-graben linked with the uplift of the Kazdağ Horst. The formation period of the Edremit Graben remains uncertain, but it is presumed to be from the Pleistocene-Quaternary era, influenced by structural formations dating back to the Late Miocene to Early Pliocene, according to Yılmaz and Karacık (2001).

The study area for this thesis work is the Gulf of Edremit, located in the Northwestern Turkey. In the northern part Kazdağ and southern part Madra Mountains are located. The main structural elements are western branch of NAFZ and İBTFZ. The İBTFZ is located at the southeast of the region. The importance of the İBTFZ noticed as intersection of AES and Anatolian Domain (e.g., Kaya, 1979; Uzel et al., 2013; Özkaymak et al., 2013; Gessner et al., 2013). Our research area is located where the right-lateral strike-slip dynamics of the ENE to WSW oriented NAFZ intersect with the N-S extension caused by the AES. Consequently, it's acknowledged that the region's neotectonic deformation has been concurrently influenced by these two elements. (Gürer et. al., 2016)
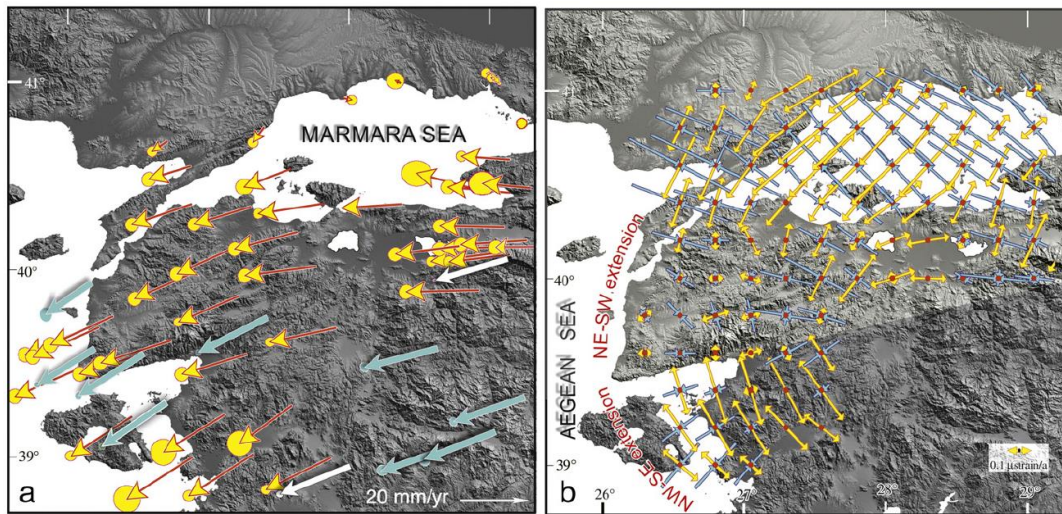
Figure 2.4 a. The combined velocity field of western Anatolia relative to stable Eurasia is shown. Thick blue arrows represent the velocities of survey-mode sites as determined by Aktuğ et al. (2009), while thick white arrows indicate the velocities at CGPS stations, also determined by Aktuğ et al. (2009). Thin red-yellow arrows represent velocities obtained from Reilinger et al. (2006), combined with the velocity field from Aktuğ et al. (2009). Error ellipses indicate 95% confidence intervals. b. Normal strain rates derived from GPS data are shown. Yellow arrows represent extensional strain, while blue arrows indicate compressional strain. The average strain rate is 0.11 µstrain/year, with a maximum extensional strain rate of 0.31 µstrain/year. The average compression rate is −0.12 µstrain/year, with a maximum compression rate of −0.47 µstrain/year (Straub and Kahle, 1997). (Gürer et al., 2016)

The northern edge of the basin is characterized by, basinwide-facing, step-like topography, a result of significant normal fault slip along the margin's boundary faults. However, the high gradient transverse drainage system that traverses the northern margin has extensively fragmented this morphotectonic feature. Notably, the northern edge of the Edremit Basin is framed by large, loosely consolidated deposits of fan aprons. In contrast, the southern boundary features gently sloping hillsides. The region's tallest mountain, Kazdağ, reaches an elevation of 1774 meters. The gulf stretches over 80 kilometers in length, with its width expanding from 1 to 5 kilometers on the eastern end to 30 kilometers towards the west. The northern shelf of the gulf is notably steep and confined. Conversely, the shelf regions on the east and south sides are broader and have a gentler slope. The average depth of the gulf's sea level stands at 100 meters, plunging to its deepest at 139 meters in a NE-SW

14

orientation. The gulf is delimited by the Müsellim Strait, marking the narrowest distance between Lesvos Island and the Biga Peninsula on the west. (Figure 2.5) (Gürer et. al., 2016).
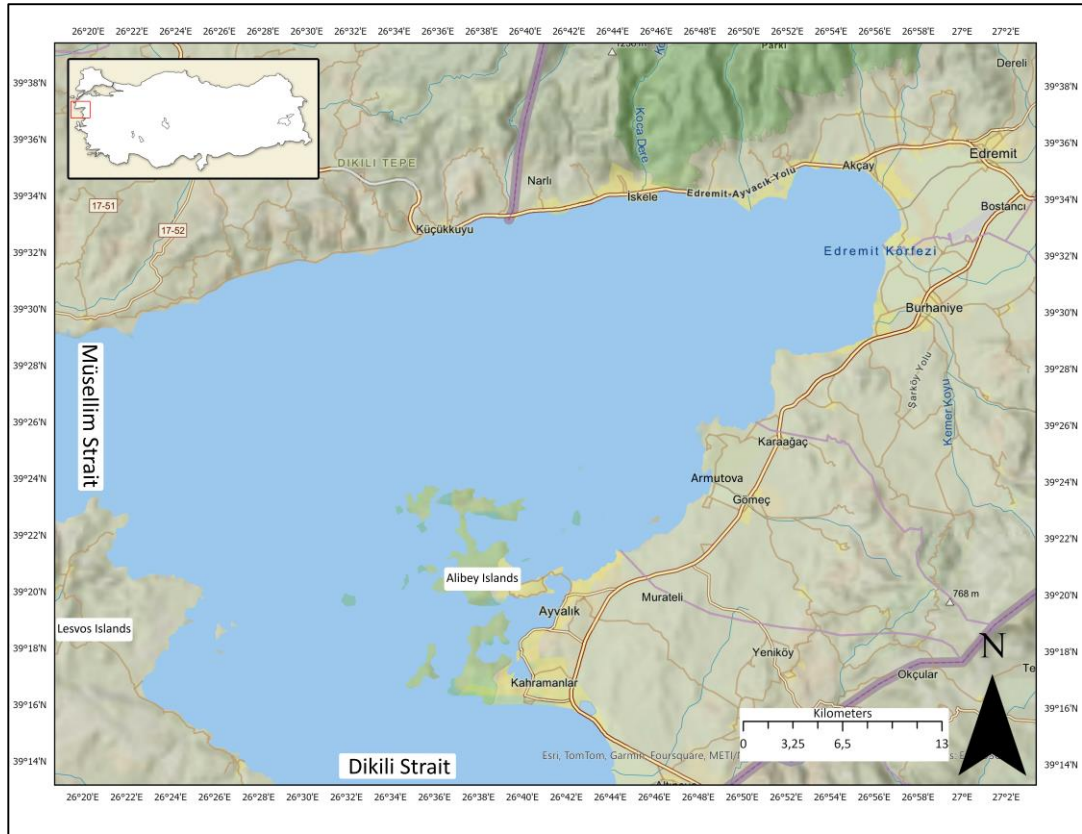
Figure 2.5 Geographic settings around GoE

Numerous paleomagnetic (İşseven et al., 1995; Schindler, 1997; Kaymakçı et al., 2007) and GPS studies (Straub and Kahle, 1997; Straub, 1997; Aktuğ et al., 2009) have been conducted in the area to realize the formation process of the Edremit Basin. These paleomagnetic investigations consistently indicate a counterclockwise rotation of 7 to 40 degrees around the basin. The study by İşseven et al. (1995) highlights that the northern and southern segments surrounding the GoE exhibit divergent rotation directions, a contrast that has contributed to the basin's evolution (Gürer et. al., 2016).

GPS observations reveal that the Biga Peninsula and its vicinity are moving W-SW at a rate of 2 to 3 centimeters per year according to McClusky et al. (2000), Straub and Kahle (1997) and Aktuğ et al. (2009). Furthermore, GPS vectors and the derived strain directions suggest that there are strain extension axes oriented in a NE-SW direction in the northern part of the GoE. In contrast, a NW-SE strain axis is prevalent in the southern part, as indicated by Barka and Reilinger (1997).

Investigations using multi-channel seismic reflection and seismicity data, alongside geological and morphological insights Boztepe-Güney et al. (2001), have shed light on the tectonic characteristics of the continental shelf near the Bababurnu promontory. These studies have led to several key findings. Firstly, the GoE is delineated as a basin primarily shaped by E-W trending faults, originating in the Late Pliocene to Pleistocene era. Secondly, The N-S extensional dynamics responsible for the gulf's westward expansion are still active. Finally, a significant fault zone, aligned with the GoE's coastline, plays a crucial role in shaping its coastal topography.

Further analysis by Kurtuluş et al. (2009) proposed a structural map and tectonic framework for the Edremit Gulf, based on the interpretation of 21 seismic profiles arranged in NE-SW and NW-SE orientations within the gulf. Their findings suggest the absence of strike-slip faulting, with the gulf's form being dictated by East-West trending normal faults. Yaltırak et al. (2012) categorized the Bababurnu Basin as a pull-apart structure in the northeastern Aegean Sea, informed by offshore seismic observations. Yılmaz and Karacık (2001) examined the area's geological structures, characterizing the Kazdağ Mountain and Edremit Basin as being defined by normal faults, forming horst and graben structures respectively.

Some researchers consider the Kazdağ uplift to be a metamorphic core complex that developed during the Oligo-Miocene period (e.g., Okay and Satır, 2000; Beccaletto and Steiner, 2005; Bonev et al., 2009; Cavazza et al., 2009). Bonev et al. (2009) analyzed extensional structures at the southern flank of Kazdağ Massif, concluding that its elevation was caused by Aegean post-orogenic back-arc extension. These

structures, located to the north and south of Kazdağ Massif, exhibit contrasting dips and kinematic behaviors, suggesting a divergent extension mode-oriented NE-SW during the late Oligocene for the massif's western segment.

On the other hand, Erdoğan et al. (2013) argued that the interaction between foliation planes and tectonic boundaries within the metamorphic formations of the Kazdağ Massif challenges the concept of a core complex. They proposed that the recent elevation of the Kazdağ Massif occurred through processes associated with the NAFZ during the Plio-Quaternary Period.

The region encompasses numerous faults that emerged with distinct kinematic characteristics throughout the Neogene-Quaternary Period. To date, the structural and kinematic connections between these faults and the surrounding rocks have yet to be thoroughly investigated.

There is a debate center around the fault geometries and types responsible for the basin's creation and maintenance, their structural interrelations, and their connections to the Upper Cenozoic sedimentary and volcanic rocks within the area. The theories proposed by various researchers on the basin's origin include:

1. The involvement of strike-slip faults linked with the NAFZ, as suggested by Okay and Satır (2000).
2. The combined influences of NAFZ and AES, as pointed out by Yılmaz and Karacık (2001) and Boztepe-Güney et al. (2001).
3. The role of normal faults associated with the AES, as proposed by Kurtuluş et al. (2009).

However, none of these propositions have been backed by comprehensive kinematic studies, especially concerning the Late Miocene to Quaternary faults in and around the Edremit Basin.

2.3   Coastal Plains, Deltas and River Basins Around GoE

Deltas are formed by sediment charged streams enter the still waters (lake, inland sea or ocean). The stream's flow slows, sediments are deposited by the weakening current, forming three distinct types of beds. Foreset beds consist of coarse particles that settle quickly as they enter the water, creating sloping layers extending from the delta front. These beds are typically overlaid by thin, horizontal topset beds formed during flood events. Meanwhile, finer silts and clays settle farther from the stream's mouth in nearly horizontal layers known as bottomset beds (Tarbuck et al., 2017).
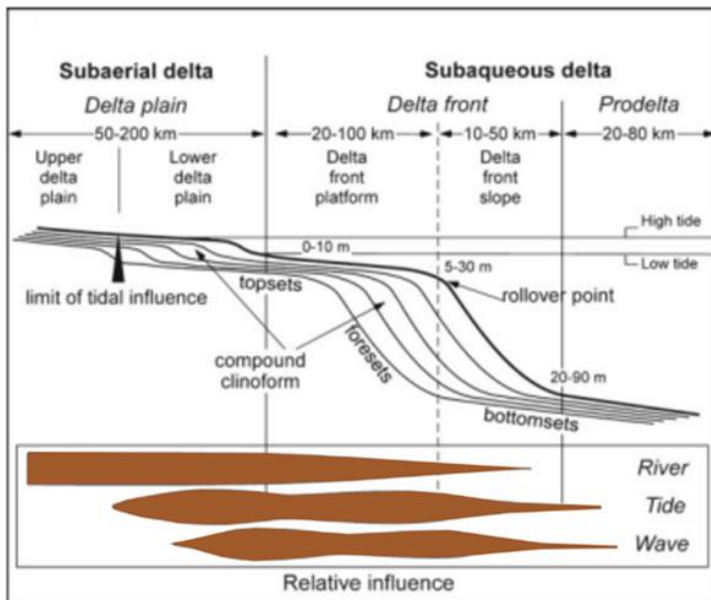
Figure 2.6 Morphologic feature of delta System (Redrawn by Hori and Saito, 2007)

In this study, it is considered that the river's relative influence has a greater impact on the GoE. There are 3 main parts of the deltas. These are delta plain, delta front and prodelta. The schematical view of these parts are seen in the Figure 2.7.
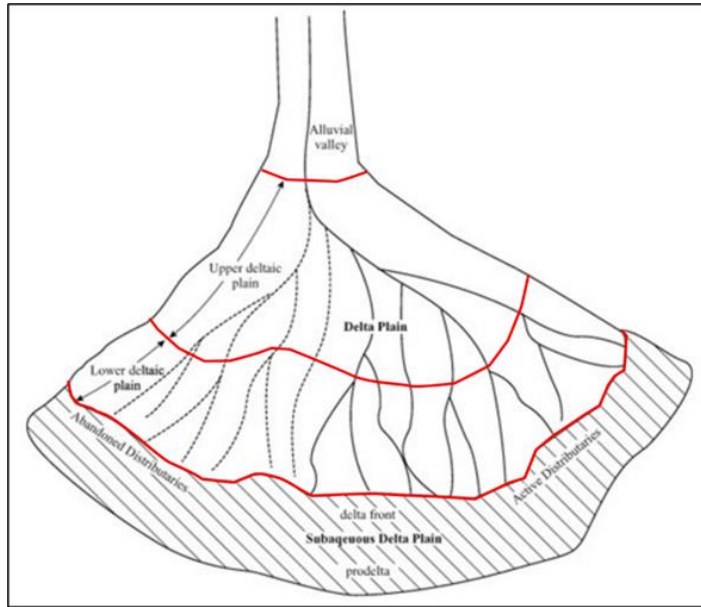
Figure 2.7 Schematic diagram depositional environment of a delta (Modified from Coleman and Prior,1980)

The primary driver of sediment accumulation in marine environments is the erosion and transport of material from terrestrial sources. The GoE is notably influenced by freshwater inputs from both its northern and southern regions. For this reason, understanding the characteristics of the coastal plain and deltas in the region is of great importance.

On the southern face of Mount Kazdağ, coastal plains lie in a narrow strip in front of the lowlands. The valleys extending from these coastal plains towards the Kazdağ face continue northward. These valleys lead to deltas that extend into the Gulf of Edremit. These deltas are the Ahmetli, Küçükkuyu, Mıhlı, and Altınoluk deltas. As you move from west to east, the deltas cover increasingly larger areas. Among the plains in the study area, the Edremit Plain covers the largest area. Although the Edremit Plain is considered a graben plain, there is no fault control between Akçay and İnönü along the northern edges of the plain (Yılmaz and Karacık, 2001).

The coastal area between Akçay and Edremit streams consists of wetlands that can be considered marshes. The broad alluvial cones that fill the wide valley beds at the river mouths along the northern face of the Edremit Plain are not found in the

19

southern part. The northern part of the gulf, apart from the deltas extending from Mount Kazdağ into the gulf, shows a linear coastline. This linearity is caused by the displacement of sediments within the deltas and the erosion of the deltas by waves driven by the consistently east-west blowing winds (Yaltırak, 2003).

The alluvial thickness of the Edremit Plain ranges between 1 and 150 meters. According to DSİ (State Hydraulic Works) drillings, it starts with gravel and blocky river deposits at the base (Özhan et al., 1977) and turn into clay and silt dominant deposition at the top. The coastal area between Akçay and Burhaniye, where lagoons and marshes are found, consists entirely of sandy beaches. The coastal plain between Akçay and Güre, which is an extension of the Edremit Plain, is composed of coarse grained materials (Yaltırak, 2003).

The river basins in the region are listed from west to east, these are the Pınarbaşı, Kuruçay, Akçay, Zeytinli, and Edremit Basins. South of the Edremit Basin, as you move further south, there are the Havran River and Karınca River Basins (Ak, 2019).

Table 2.1 Drainage density of the river basins around GoE (Ak, 2019)

River Name	Basin Area (A)	Total River Lengths (L)²	Drainage Density (Dd)
Zeytinli River	166.99	169.92	1.0175
Havran River	526.58	568.39	1.0779
Edremit River	107.22	130.91	1.2209
Karınca River	332.36	430.07	1.2939
Akçay Stream	36.8	53.01	1.4404
Pınarbaşı Stream	20.77	47.54	2.2888
Kuruçay Stream	10.03	23.87	2.3798

So, the basin area and drainage density are plotted in the Figure 2.8.
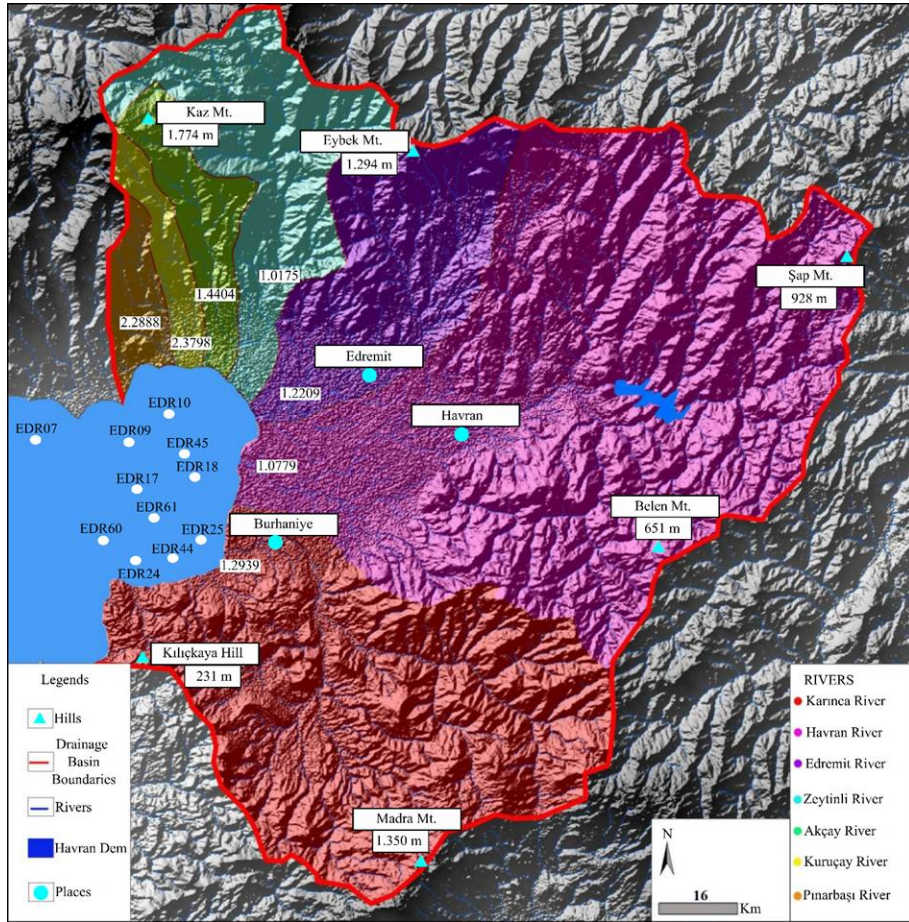
Figure 2.8 The Location of the River Basins (Redrawn by Ak, 2019)

Finally, Kuruçay and Pınarbaşı Rivers which have the highest drainage densities with respect to other rivers. These two rivers are located at the northern part of the study area. So, it is observed that the drainage densities in the northern part of the study area are higher compared to the drainages in the southern part.

Titanium is a key indicator of detrital input towards to marine environment in element proxy analysis. For this reason, the findings on Ti concentrations from research conducted by Ak (2019) have been incorporated into this study. Titanium element has low solubility in water, so it can remain suspended in the water mass for extended periods. Because it is a more resistant and heavier element compared to others, titanium is frequently used in sediment provenance analysis. Additionally, as an inert element, titanium is non-reactive in aquatic environments, limiting its

participation in oxidation or reduction reactions, which makes it play a crucial role in sediment transport (Du et al.,2012). In the study of Ak (2019), we see that XRF analysis was conducted on samples taken from the rivers, which are feeding the GoE. When compared with Ti concentrations from Ak (2019) study, where samples were taken from the rivers, it was found that the Edremit and Zeytinli River basins in the northern part of the gulf showed Ti concentrations of 21% and 24%, respectively. These areas also exhibit high concentrations of titanium in the marine environment. On the other hand, the Ti concentrations in the samples taken from the Karınca and Havran River basins in the southern part of the gulf are around 18% and 19%, respectively.

Table 2.2 Titanium concentration of rivers around GoE (Ak, 2019)
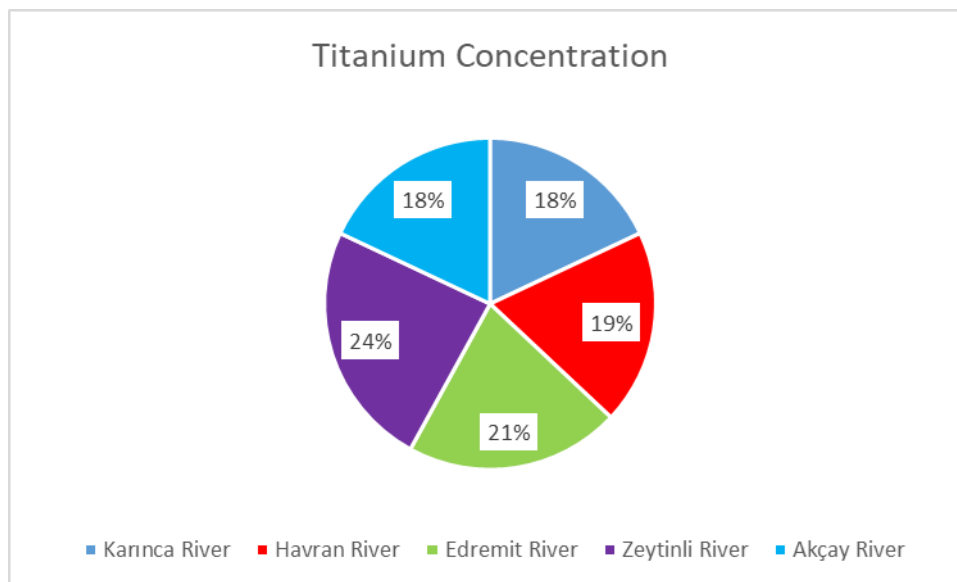
2.4 Oceanography of GoE

The general current system of the Aegean Sea can be described as a cyclonic circulation on a basin scale (Figure 2.9). The waters of the Eastern Mediterranean enter from the southeastern end of the basin and move northward along the Turkish coast. This current is balanced by a southward current along the Greek coast. The

presence of islands, along with the complex topography and meteorological conditions, creates mesoscale cyclonic and anticyclonic eddies throughout the basin.
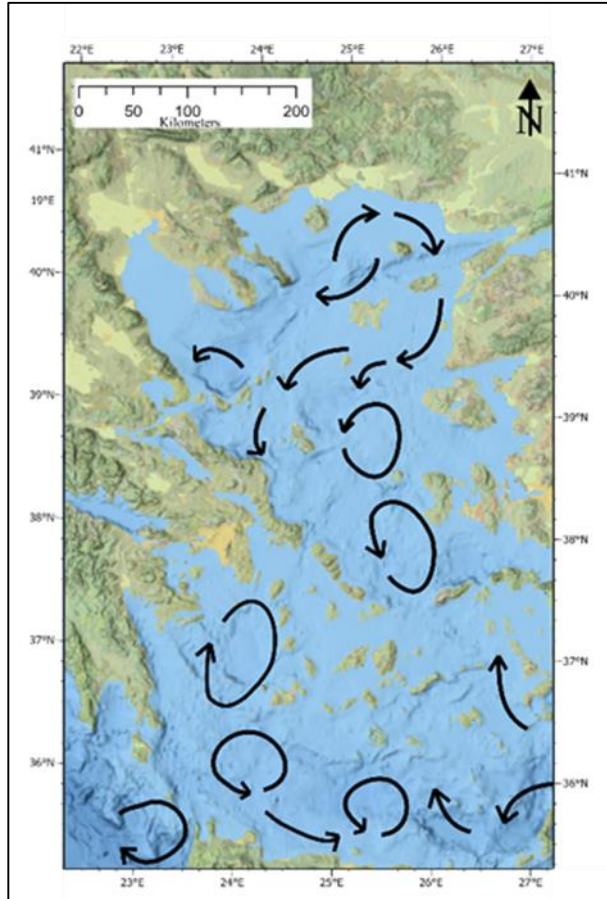
Figure 2.9 General circulation system in Aegean Sea (Redrawn by Sayın et al., 2011)

For the work reported in this thesis, the measurements in the Gulf of Edremit were conducted during two separate periods: October 19-25, 2017 and December 5-17, 2017. The current map is presented in Figure 2.10. In both measurement periods, a weak wind was blowing from the north. Water enters the gulf from both the south and the north. In the inner areas, due to the coastal structure, the currents become complex, forming small eddies. An anticyclonic eddy was observed in the gulf, east of the Alibey Islands (southern islands).
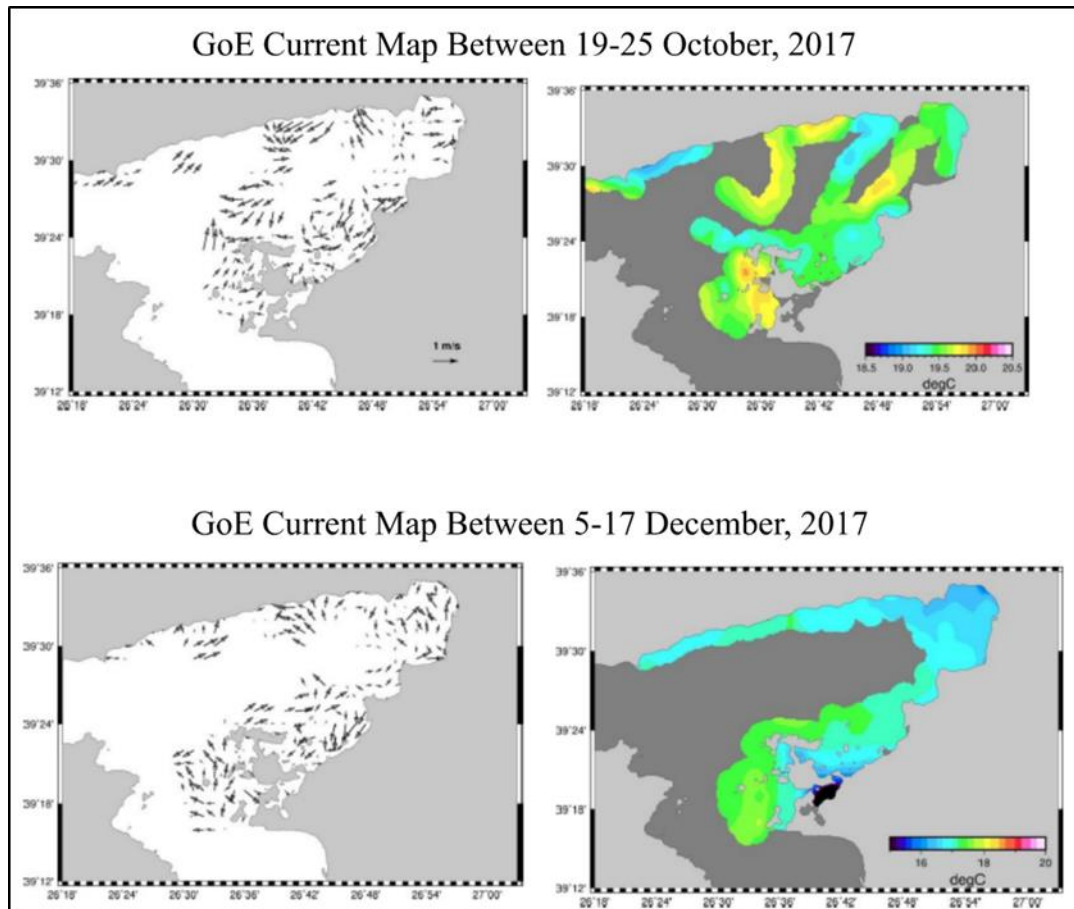
Figure 2.10 Current system in GoE (Duman et.al, 2018)

2.4.1 Sea Level Change within GoE

According to Yaltırak (2003) during the period between 13,000 and 28,000 years ago, when sea level was approximately 90 meters below today's level, the Würm Seismic Stratigraphic Unit was deposited, based on the comparison of the tectonically adjusted maximum depth of the Müsellim Channel and the sea level curve (Figure 2.11). According to this, it is concluded that around 10,000 years ago, the sea level was approximately 60 to 90 meters below its current level. Considering this, it is likely that during the Holocene, with the continuous rise in sea level, a transgressive deposition covered the deltas along the edge of the basin in the GoE. In fact, Yaltırak (2003) described the Holocene Seismic Stratigraphic Unit as a unit that covers the deltaic units located on the edge of the transgressive basin.

24
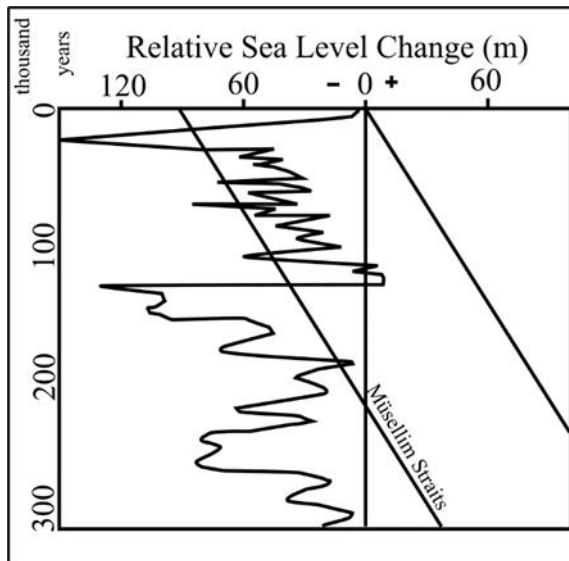
Figure 2.11 Relative sea level change (Yaltırak, 2003)

Direct studies on sea level changes along the coasts of Turkey are extremely limited, and most of the existing data have been linked to findings presented in other global studies. Most of these investigations focus primarily on the period after the Middle Holocene. According to global studies, sea levels were approximately -120 meters during the last glacial period, peaked at +3 meters during the Middle Holocene (around 5,000 years ago), and then gradually receded to present-day levels (e.g., Fairbanks, 1989; Bard et al., 1990, 1996; Lambeck et al., 2002; Siddall et al., 2003; Peltier and Fairbanks, 2006; Stanford et al., 2011).

According to Duman et al. (2018), recent studies have revealed that sea level rise has not occurred at a relatively constant rate; instead, there have been periods dominated by rapid melt events and stable intervals in between (Stanford et al., 2011 and Cooper et al., 2018). These global studies highlight varying findings on the timing and effects of rapid glacial melt events (Table 2.3 and Figure 2.12). The process, often referred to as a "Flood," resulted from rapid melt triggers and subsequent sea level rises, identified as MWP-1a, b, and in some cases, MWP-1a, b, c. The timelines, impact durations, and associated sea level changes are outlined in Table 2.3. Such abrupt shifts could have significant effects on the marine environment, potentially leading

to unusual formations depending on hydrodynamic conditions, seafloor topography, and sedimentary deposits.

Table 2.3 MWP's periods and sea level change max, min and avg. meters (Stanford, et al., 2011)

Period (Stanford et al., 2011)	Date (years before present)	Sea Level (m)
MWP-1b (upper)	8600	(min) -24 m
		(max) -20 m
		(avg) -22 m
MWP-1b (lower)	11600	(min) -62
		(max) -57
		(avg) -60
Younger Dryas		
MWP-1a (upper)	12800	(min) -76 m
		(max) -70 m
		(avg) -73 m
MWP-1a (lower)	14500	(min) -95 m
		(max) -91 m
		(avg) -93 m
Bolling warming		
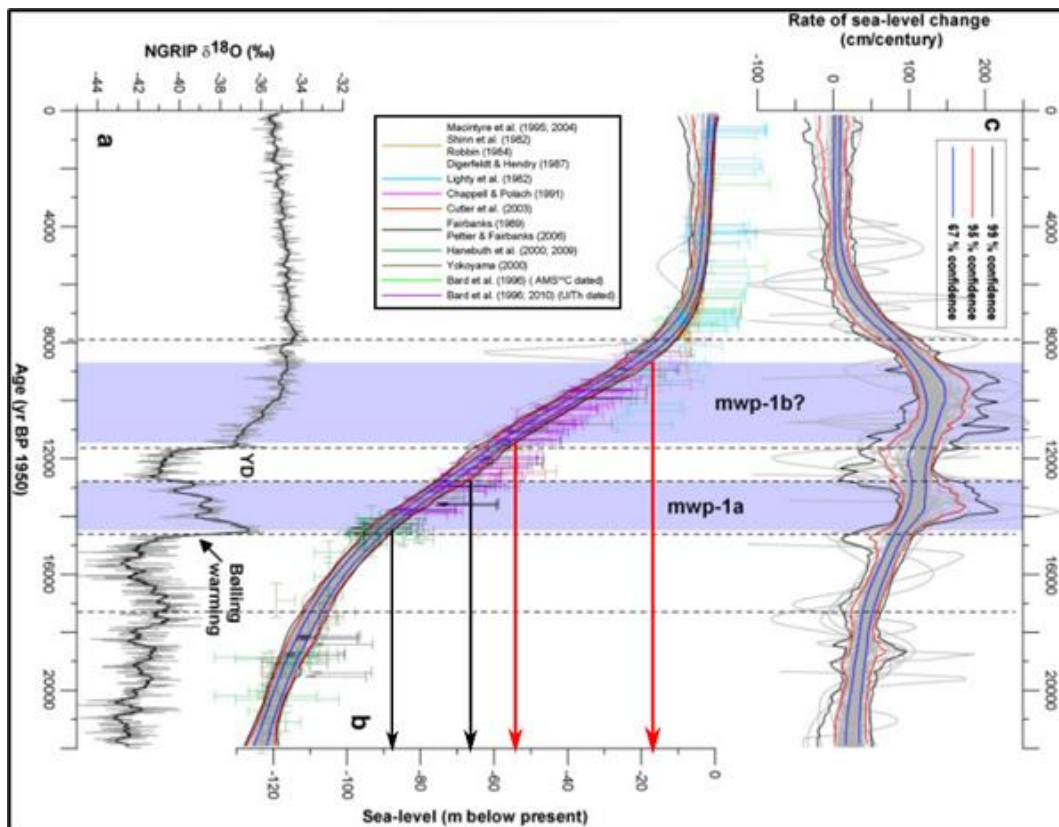
Figure 2.12 NGRIP δ18O, global sea level change results (Stanford et al., 2011)

Based on the data presented in Table 2.3 and Figure 2.12, the possible flood period data for the Aegean Sea and the surrounding area appear to be consistent with global sea level change data.

2.5   Global Climate Periods
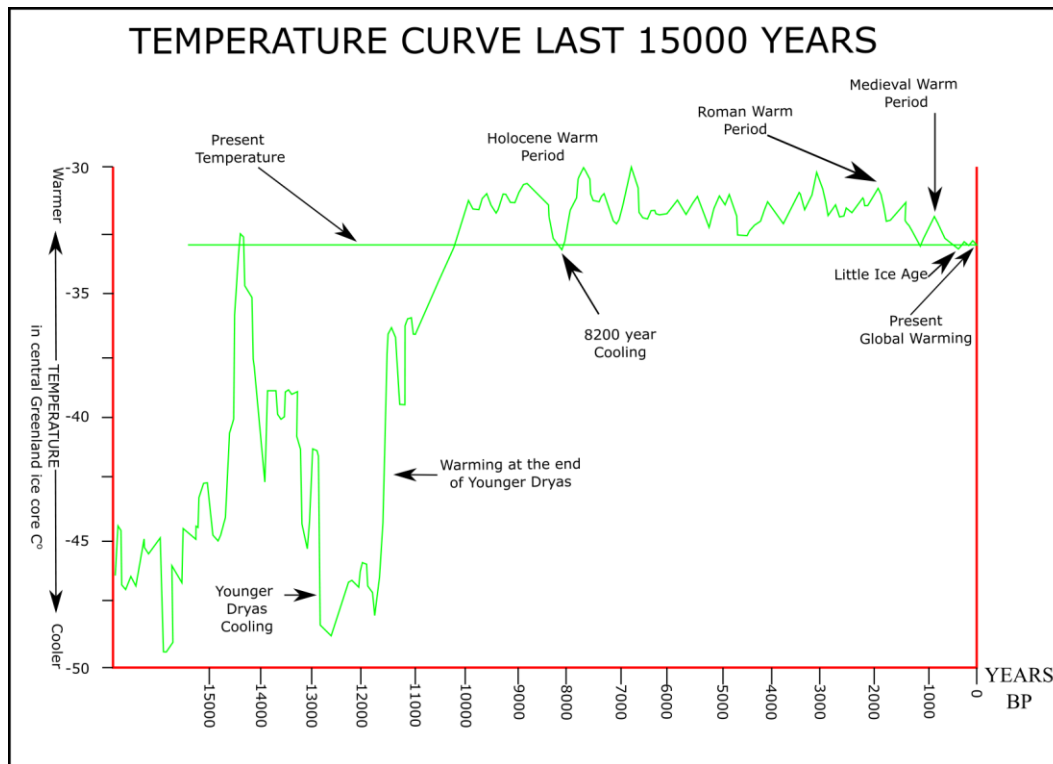
Figure 2.13 Global temperature curve last 15 ka BP (Redrawn by, Thomasson and Gerhard, 2019)

Global temperature curve showing that in the past 15000 years' changes. At this time interval there are specific events like Younger Dryas Cooling and Warming Events, 8.2 ka Cooling Event, Roman Warm Period, Medieval Warm Period, Little Ice Age and Present Global Warming.

Younger Dryas Cooling and Warming Events: The Younger Dryas (12,900–11,700 years ago) was a brief but significant cooling event following a period of warming at the end of the last Ice Age, preceding the onset of the Holocene. Marked by abrupt temperature shifts, it had profound impacts on global climates and ecosystems. This cooling is attributed to disruptions in thermohaline circulation, likely caused by freshwater influx from melting ice sheets into the North Atlantic (Alley, 2000).

8.2 ka Cooling Event: The 8.2 ka event, occurring approximately 8,200 years ago, was a sudden cooling episode lasting around 150 years. Likely triggered by the rapid release of meltwater from the Laurentide Ice Sheet, which disrupted the Atlantic Meridional Overturning Circulation (AMOC), this event caused significant climate shifts. Paleoclimatic evidence from ice cores, marine sediments, and terrestrial records highlights its impact on early Holocene weather patterns, ecosystems, and human societies (Alley et al., 1997).

The Holocene Warm Period: The Holocene Climatic Optimum, occurring between 9,000 and 5,000 years ago, was a period of elevated global temperatures, particularly in the Northern Hemisphere. This warming, driven by increased solar radiation due to orbital changes, led to ecological shifts such as forest expansion and changes in species distributions. Human civilizations flourished during this time, with advancements in agriculture and population growth. Paleoclimatic evidence from ice cores, pollen records, and marine sediments provides detailed insights into the climatic conditions of this era (Mayewski et al., 2004).

Roman Warm Period: The Roman Warm Period (250 BCE–400 CE) was a phase of relatively warm climate in the Northern Hemisphere, which supported the expansion and prosperity of the Roman Empire. Warmer temperatures and increased rainfall likely boosted agricultural productivity, fostering population growth and economic development. Paleoclimatic evidence from tree rings, ice cores, and sediment records confirms the favorable climatic conditions that contributed to the flourishing of Roman civilization (Lamb, 1995).

The Medieval Warm Period: The Medieval Warm Period (950–1250 CE) was marked by unusually warm climate conditions, particularly in the North Atlantic region. Mild temperatures supported agricultural expansion to higher altitudes and northern regions, boosting food production and population growth. This period also saw the flourishing of medieval societies and human settlements. Paleoclimatic evidence from tree rings, ice cores and sediment records highlights higher temperatures and altered precipitation patterns during this time (Lamb, 1965).

The Little Ice Age Period: The Little Ice Age (1300–1850 CE) was a period of significant climate cooling, particularly in the Northern Hemisphere, marked by shorter growing seasons, crop failures, and glacial expansion. Harsh winters and cooler summers led to food shortages and population declines in some regions. Likely causes include volcanic eruptions, reduced solar activity, and changes in oceanic circulation. Evidence from historical records, tree rings, ice cores, and glacial deposits highlights this extended phase of colder temperatures and climatic instability (Grove, 2004).

Present Global Warming: Current global warming refers to the ongoing rise in global temperatures, primarily driven by human activities such as fossil fuel combustion, deforestation, and industrial emissions. These activities increase greenhouse gas concentrations, intensifying the greenhouse effect and trapping more heat in the atmosphere. The consequences include more extreme weather events, rising sea levels, and disruptions to ecosystems and biodiversity. Temperature records, satellite data, and climate models consistently document a significant increase in global temperatures over the past century (Intergovernmental Panel on Climate Change [IPCC], 2021).

CHAPTER 3

METHODS

In 2018, Edremit project was assigned by the General Directorate of Mineral Research and Exploration's Department of Marine Research to determine the sedimentological and geochemical characteristics of the Gulf of Edremit.

3.1 Core Sampling

In 2019, the sediment core sampling studies of the Gulf of Edremit were completed by the R/V MTA SELEN Research Vessel.

Figure 3.1 MTA SELEN Research Vessel

60 core samples were collected using the gravity corer device. These core locations were homogeneously determined within the gulf. The map of core locations is seen in Figure 3.2.
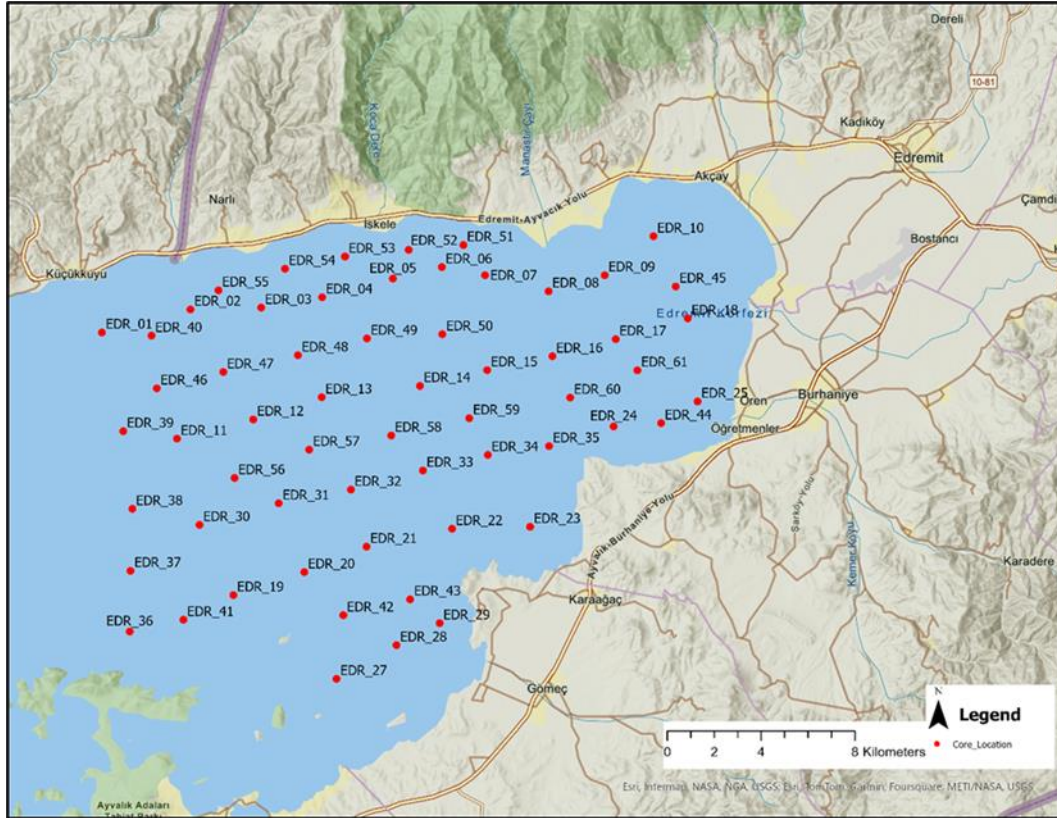
Figure 3.2 Core locations in study area

The samples were collected with the help of RV/MTA Selen in 2019 from 60 different locations. Between the two location sites, the length did not exceed 3 kilometers. The gravity corer is widely used for sediment sampling at the bottom of the lake or sea. Gravity carries the core to the bottom of the water body. The gravity corer operator needs a winch to lower, raise, and free-fall the corer. The advantages of the gravity corer are simple and relatively reliable. The disadvantages of the gravity corer are the length and weight, and these can cause hard to control the corer. The schematic illustration of a piston corer working principle is seen in Figure 3.3.
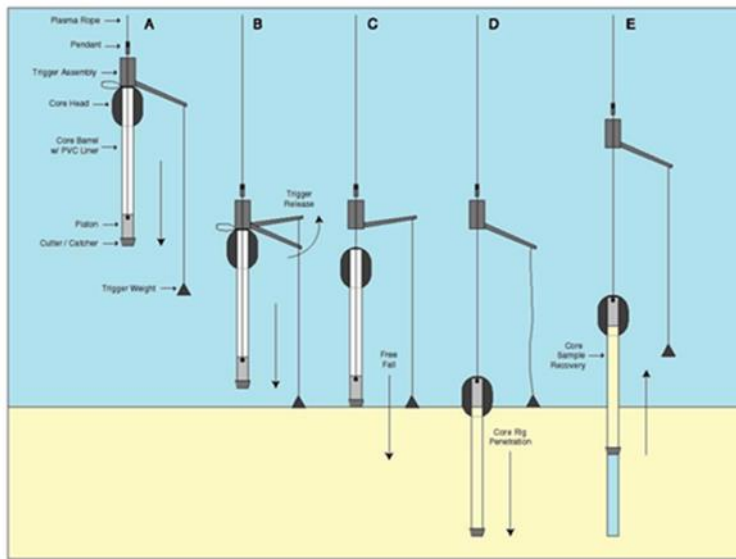
Figure 3.3 Schematic view of gravity piston corer working principle (from TDI-Brooks Handbook, 2022)

The trigger release part is the only difference between the piston corer and the gravity corer. Gravity corer does not have any trigger release part. At sampling operation before 5 meters depth to the bottom of the seabed, the free-fall mechanism of the winch is activated. Gravity corer freely falls to the seabed and penetrates through the sediment. (TDI Brooks Handbook, 2022) Then, the corer slowly rises with the winch to the vessel. After accomplishing the sampling process, the sample should be covered carefully because chemical contamination is a considerable risk for the research. (Figure 3.4) Also, samples should be stored in exceptional conditions like +4, -4 ºC.
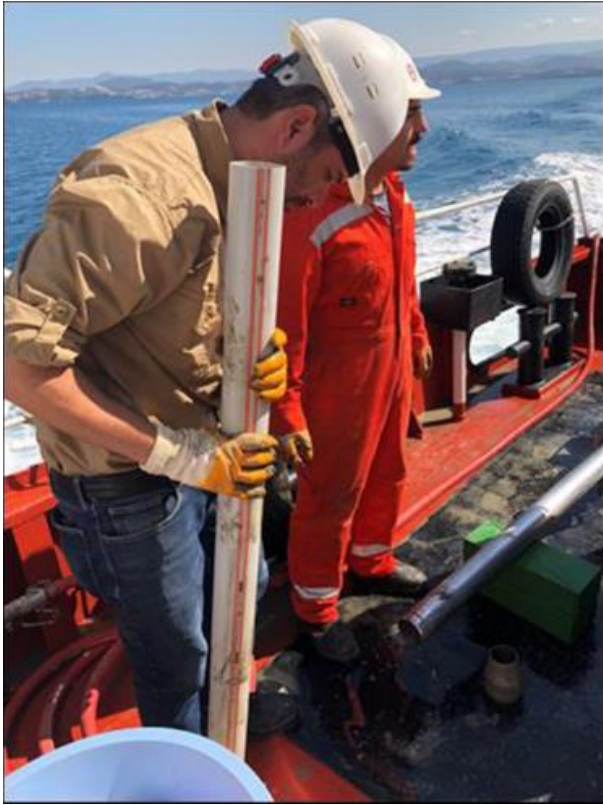
Figure 3.4 Gravity corer operation in GoE

3.2   Lab Studies

Within the scope of the project, the transportation and storage of the collected cores under appropriate environmental conditions were of significant importance. These cores were placed in the cold storage facility at the General Directorate of Mineral Research and Exploration (Ankara) headquarters. The initial stage of core analysis involves longitudinally splitting the PVC tubes. (Figure 3.5) With the help of a core cutting device found in the Marine Research Laboratory, the PVC tubes were cut and divided into two equal halves.

Figure 3.5 Sample dividing into equal half

One half of the core sample was prepared for analysis, while the other was packaged and labeled to be kept as a reference sample. (Figure 3.6)

Figure 3.6 Preparing core samples for XRF measurement

3.2.1   MSCL-S Analysis

Physical properties, including magnetic susceptibility (MS), were measured at 1 cm resolution using a Geotek Multi-Sensor Core Logger Analyzer in the MTA Marine Research Department Lab, following standard procedures (Weaver and Schultheis, 1990). This data was used to assess variations in the relative amount of terrigenous (land-derived) input.

3.2.2   ITRAX µXRF Analysis

The development of X-ray fluorescence (XRF) core scanning technology has revolutionized marine geology and paleoenvironmental research by enabling high-resolution, non-destructive chemical analysis of sediment cores. Introduced in the late 1980s with the CORTEX scanner and later advanced by instruments like the AVAATECH and Eagle II and III BKA scanners, XRF technology has facilitated precise, sub-millimetric elemental analysis of marine, lacustrine, and terrestrial sediments. This innovation, rooted in early geochemical and sedimentological studies from the mid-20th century, has allowed researchers to reconstruct past environmental and climatic conditions with unprecedented accuracy, leveraging proxies such as elemental composition, magnetic susceptibility, and organic content. Modern XRF scanners provide detailed insights into climate variability across decadal to millennial scales, with applications expanding beyond marine science to lake and terrestrial records, as well as environmental forensics. By bridging qualitative and quantitative approaches, XRF scanning has become a cornerstone of paleoceanography, documenting key events like Holocene climatic shifts and enabling a deeper understanding of sedimentary archives, from the early geochemical studies of the 1930s to the rapid advancements in high-resolution research in the 2000s (Rothwell and Croudace, 2015).

Typical applications and impact of XRF core scanning technology in marine sediment analysis are listed below,

Core Characterization: XRF core scanners allow for the detailed characterization of marine sediments by providing elemental compositions across different layers. This information is crucial for understanding the sediment's origin, depositional environment, and changes over time.

Climate Change Studies: One of the primary applications of XRF scanning in marine sediments is the reconstruction of past climate conditions. By analyzing element proxies such as calcium (Ca), iron (Fe), and others, scientists can infer changes in climatic conditions, oceanography, and terrestrial inputs over geological timescales.

Event Detection: Marine sediments are repositories of information on past events like volcanic eruptions, floods, tsunamis, earthquakes, and landslides. XRF core scanners can identify specific layers enriched in elements associated with these events, such as ash layers (tephra) from volcanic eruptions, characterized by sudden increases in elements like silicon (Si), potassium (K), and others.

Anthropogenic Impacts: The technology is also applied to assess human impacts on marine environments, such as pollution. Heavy metal concentrations, for example, can be traced to identify periods of increased industrial activity or environmental regulations.

Sedimentological Events: XRF scanning has been pivotal in recognizing and analyzing sedimentological features within cores, including turbidites, which are sediment layers deposited by underwater landslides or turbidity currents.

Provenance Studies: The elemental makeup of marine sediments can provide insights into their provenance, or origin, helping to trace the pathways of sediment transport and deposition. This is especially useful in studies of continental margin erosion and sediment delivery to the deep sea.

Facies Interpretation and Core Correlation: XRF core scanning data aid in the interpretation of sedimentary facies, or distinct types of sediment layers that represent different depositional environments.

Diagenetic Studies: Diagenesis refers to the physical, chemical, and biological changes that occur to sediment after its initial deposition. XRF scanning can detect diagenetic alterations in marine sediments by identifying changes in element concentrations that indicate processes like mineral transformation and authigenesis (Rothwell and Croudace, 2015).

3.2.2.1 Sample Preperation

Accurate sample preparation is crucial for reliable geochemical data in environmental and paleoclimatic studies. To prevent core drying and shrinkage, sediment cores are covered with a high-purity polypropylene film, which minimizes water loss but may cause a thin water layer to form, affecting XRF measurements, particularly for lighter elements due to increased absorption and scattering (Rothwell and Croudace, 2015). The air gap between the detector and the sample further influences the detection of lighter elements, an issue mitigated by technologies like the ITRAX scanner, which uses a vacuum-pumped nozzle to reduce this gap. Response depth, or the maximum depth at which X-rays contribute to the detected signal, varies by element; heavier elements, with higher-energy emissions, have greater response depths compared to lighter elements, as dictated by Moseley's law (Potts P. J. and Webb P. C., 1992). Factors such as sediment composition, matrix density, and X-ray energy impact response depth, emphasizing the need for careful interpretation of XRF data when comparing elemental concentrations or analyzing fine sediment layers. The mass attenuation coefficient, determined by the sediment's composition, also plays a key role in radiation interaction and signal detection (Jenkins and De Vries, 1970).

These core samples were analyzed for multi element composition at 1 mm- 5 sec. resolution using an ITRAX µXRF core scanner, equipped with X-Ray radiography and RGB high resolution camera at the MTA Marine Research Laboratory. A fine-focus Mo X-ray tube is used as a source of the device. The relative elemental

abundances were recorded as counts per second (cps) and the element ratio profiles were applied to reconstruct the paleoenvironmental change within the gulf.

Figure 3.7 (a) Core sample and (b) ITRAX µXRF core scanner

3.2.2.2   Interpretation of µXRF Data Set and Geochemical Proxies

µXRF data set is mainly composed of relative abundance of major elements and oxides. So, geochemical proxies are employed to interpret the data set. The geochemical composition of sediments is shaped by factors such as source rock type, weathering, transport mechanisms, depositional conditions, and diagenesis. Major elements like Al, Si, K, Ca, Fe, and Ti are primarily terrigenous, derived from the erosion of continental rocks, while Si and Ca can also originate from marine biogenic sources. Elements like Fe and Mn may undergo diagenetic alterations, while Ti remains redox-insensitive and is a reliable marker of the detrital component (Rothwell & Croudace, 2015). Element pathways are seen in the Figure 1.19. Statistical analysis of geochemical data aids in identifying sediment sources, with minor elements, particularly d-block transition metals, serving as proxies for

productivity and detrital metal flux. The accumulation of metals in sediments is influenced by both detrital input and redox conditions, which regulate their cycling and preservation (Finney et al., 1988; Shaw et al., 1990). Advanced techniques, such as using Cr X-ray tubes, improve the accuracy of lighter element analyses by mitigating matrix effects (Rothwell & Croudace, 2015).

1-Aeolian Dust Input: Hinterland aridity/wind strength High Fe, Ti, Si and K

2-Fluvial Input: Hinterland climate/precipitation and runoff High Fe, Ti, K, Al, Zr/Rb

3-Coastal Erosion: Environmental energy/water depth High Fe, Ti, K, Al

4-Volcanic Eruptions: Ash layer/cryptotephras High Fe, Ti, and Zr

5-Export Productivity: High Ca, Ba, Br, Si/Ti, Si/Al

6-Diagenesis and Authigensis: Redox conditions, elemental mobilisation High Mn, Cu, As changes in S, Fe/Ti

7-Ice Rafting: Heinrich layers, climate change High Ca/Sr (if rich in detrial Ca), Si/Sr(if rich in silicates), high Ti, Fe, Al

8-Deep Sea Sediment: Debris flows/turbidity flow High Fe, Si, Ti

9-Hydrothermal Activity: Proximity to vent fields High Fe, Mn, trace elements

10-Submarine Volcanism:High Fe, Mn, trace elements

11-Fall-out from High Altitude jet-streams: Supply of Fe, Ti, Si

Modified from Rothwell,1989.

Figure 3.8 Element pathways to and within the marine environment, with environmental indicators (modified from Rothwell, 1989)

Calcium (Ca)

Ca in marine sediments can be derived from biogenic or detrital sources, with biogenic sources generally being more significant in volume. Ca is predominantly present as calcium carbonate (CaCO3), which is used by marine plankton, such as foraminifers and coccolithophorids, to form their tests. Integral Ca is recognized as a proxy for oceanic productivity, with variations typically reflecting CaCO3 stratigraphy in pelagic cores. In near-shore and estuarine environments, detrital sources may play a more substantial role. For instance, in some Chilean Fjord sediments, about half of the Ca content was attributed to carbonates, with the remainder from weathering of plagioclases in the fjord watershed (Rebolledo et al., 2008).

Use: Ca typically shows an inverse correlation with iron (Fe) and other terrigenous elements. Climatic variations modulate productivity, resulting in lower Ca levels during glacial periods and higher levels during interglacials (Arz et al., 2001; Gebhardt et al., 2008; Rooij D. van et al., 2007). Thus, Ca is an effective climatic indicator and useful for establishing stratigraphic frameworks (Jorry et al., 2011; Kwiecien et al., 2008). Lower Ca levels may indicate carbonate dissolution or dilution by terrigenous material. Ca dissolution can act as a proxy for bottom-water corrosiveness and alkalinity, relating to oceanic water mass changes (Arz et al., 2001; Gebhardt et al., 2008). The detrital origin of Ca can be inferred if it correlates with Fe, mirroring terrigenous supply (Röhl et al., 2004). Distinguishing between biogenic and detrital carbonate can be achieved using the Ca/Sr ratio, as strontium (Sr) is fixed by calcifying organisms along with Ca. Co-variation of Ca and Sr indicates a biogenic source of CaCO3 (Carlson et al., 2008).

Limitations: In marginal environments, variations in Ca may reflect dilution by terrigenous material rather than productivity changes. For example, in a core from the Nile margin, low Ca levels during pluvial periods were primarily due to terrigenous dilution. Carbonate-rich facies, which occurred systematically during glacial/arid periods, showed a significant decrease in accumulation rate, interpreted as a reduction in Nile flood intensity (Revel et al., 2010).

Ca/Ti

The ratio of calcium to titanium (Ca/Ti) serves as a useful proxy for assessing relative changes in biogenic versus lithogenic sedimentation and for recording carbonate content (Piva et al., 2008). This ratio has an advantage over the calcium to iron (Ca/Fe) ratio because titanium (Ti) is inert, meaning it does not undergo diagenetic changes. Thus, Ca/Ti provides a more stable and reliable measure for distinguishing between biogenic calcium carbonate and lithogenic sediment contributions.

Ca/Sr

Biogenic calcium carbonate ($CaCO_3$) precipitated by coccoliths and foraminifers contains higher strontium (Sr) levels than inorganic $CaCO3$ or dolomite. Consequently, the Ca/Sr ratio can be employed to rapidly detect ice-rafted debris (IRD) layers rich in detrital carbonate. For example, certain Heinrich layers exhibit larger Ca/Sr ratios when detrital carbonate content is high and biogenic $CaCO_3$ is low (Hodell et al., 2008). This makes the Ca/Sr ratio an effective tool for identifying changes in sediment composition related to detrital versus biogenic carbonate sources.

Strontium (Sr)

Use: Sr is an alkaline earth metal that is fixed by calcifying organisms simultaneously with Ca, making it a reliable marker for biogenic origin. Since Ca can also come from terrigenous sources such as feldspars and clays, the co-variation of Ca and Sr indicates that Ca is mainly sourced from biogenic $CaCO3$. Sr is preferentially incorporated into aragonite, making it useful for distinguishing between foraminiferal calcite and coralline or pteropod aragonite. This distinction is particularly relevant in studies of cold-water carbonate mounds (Richter et al., 2006). Despite often being a trace element, Sr produces a strong response when excited using rhodium (Rh) and molybdenum (Mo) target tubes, enhancing its detectability.

Iron (Fe)

Fe is one of the most abundant elements on Earth, composing a significant portion of the outer and inner core and ranking as the fourth most prevalent element in the crust after oxygen (O), silicon (Si), and aluminum (Al). In the Earth's crust, Fe predominantly exists in the form of Fe oxide minerals such as hematite and magnetite. In marine sediments, Fe typically reflects changes in the carbonate/clay ratio. Its high abundance, strong signal relative to other elements, and excellent signal-to-noise ratio make it a preferred proxy in environmental and process studies. Generally, variations in Fe content relate to the terrigenous fraction of the sediment

and/or dilution of CaCO3. Fe often correlates with other terrigenous markers like titanium (Ti) but may be less reliable due to its sensitivity to redox conditions. High Fe levels in intervals with low sediment redness usually indicate the concentration of Fe oxide-bearing minerals (Westerhold et al., 2007).

Use: Iron is widely used to document variations in terrigenous sediment delivery, which provides insights into continental humidity/aridity, precipitation, river runoff, aeolian dust flux, and wind strength-conditions and processes commonly associated with climatic forcing (Vidal et al., 2002 and Grützner et al., 2003). Due to its redox sensitivity, Fe can also identify secondary diagenetic features or new mineral formation through authigenesis, such as framboid layers (Seeberg-Elverfeldt et al., 2005). High levels of Fe and sulfur (S) may indicate reducing conditions (Sluijs et al., 2009). An environment with Fe levels slightly below the average shale level suggests a generally reducing suboxic setting, especially if accompanied by high S and Mn values significantly below the average shale level and high trace element/Al ratios (Sluijs et al., 2008). Although Fe and Ti are closely related in terrigenous fractions, Fe can be remobilized diagenetically in pore waters, whereas Ti is inert. Therefore, a strong correlation between Fe and Ti suggests minimal diagenetic influence. Positive correlation of Fe towards core tops may result from dilution due to increasing water content (Mohtadi et al., 2007). Fe and Ti, being denser lithogenic elements, may covary with density and can thus be used as negative indices of surface productivity (Agnihotri et al., 2008).

Mn/Fe

The Mn/Fe ratio is utilized to assess redox conditions in marine sediments. Manganese (Mn) is mobile under sub-oxic conditions and separates from iron (Fe) during diagenesis (Marsh et al., 2007). Constant Mn/Fe ratios indicate oxic conditions without element fractionation. Peaks in the Mn/Fe ratio occur during sub-oxic diagenesis when Mn is mobilized and diffuses along concentration gradients to precipitate at new oxic/post-oxic boundaries. Non-steady state diagenesis, such as

oxic burn-down through turbidites, can also lead to the formation of Mn/Fe peaks (Thomson et al., 1993).

Potassium (K)

K is generally associated with terrestrial siliciclastics, such as illite clays (potassium mica) and potassium feldspar (microcline, orthoclase, sanidine). Illite is the primary mineralogical carrier of K, and in fine-grained sediments, high K content indicates a high illitic component.

Limitations: The K peak in the XRF intensity spectrum is adjacent to the Ca peak, making it susceptible to interference from varying Ca signals. Normalizing K counts per second to total counts can improve the accuracy of the K signal (Kujau et al., 2010).

Use: As an important terrigenous indicator, K is used as a proxy for fluvial input, allowing inferences about hinterland humidity/aridity and climatic modulation (Holzwarth et al., 2010; Kuhlmann et al., 2004; Romero et al., 2008).

3.3   Grain Size Analysis

Grain size analysis is a fundamental aspect of sedimentology that provides significant insights into sediment transport, depositional environments, and post-depositional processes. This chapter focuses on the methods of grain size analysis in marine sediments, emphasizing its importance in understanding sediment dynamics and environmental conditions.

Grain size distribution in marine sediments was analyzed using a combination of sieve analysis and laser diffraction techniques. Sieve analysis is employed for coarse fractions (>63 µm), whereas laser diffraction is used for finer fractions. The integration of these methods ensures a comprehensive analysis across a broad range of particle sizes (Folk and Ward, 1957; Blott and Pye, 2001). In this study laser diffraction method was used for grain size analysis. Malvern Panalytical

HYDRO3000 Master seizer device was used for analysis of grain size. The main idea of grain size distribution data revealed a predominance of fine to very fine sand, with significant variations across different sampling sites. Grain size analysis provides valuable information on sediment transport mechanisms and depositional environments. For instance, in fine grained sediments typically indicate low-energy environments where fine particles can settle and accumulate. The sorting and skewness parameters further support the interpretation of a relatively calm depositional setting with minimal reworking of sediments (Folk and Ward, 1957; Blott and Pye, 2001).

The Wentworth grain size classification is a widely used system for categorizing sediment particles based on their size. Developed by Chester K. Wentworth in 1922, this classification provides a standardized framework for describing the size distribution of sediments, which is crucial for sedimentological studies, sediment transport analysis, and environmental reconstruction. It provides a standardized method for describing sediment grain sizes, facilitating communication and comparison among researchers

The Wentworth scale divides sediment particles into various size categories, ranging from clay to boulders. Each size class has specific boundaries defined in millimeters (mm). (Figure 3.9)

Millimeters (mm)	Micrometers (µm)	Phi (φ)	Wentworth size class		Rock type
4096		-12.0	Boulder		
256		-8.0	Cobble	Gravel	Conglomerate/ Breccia
64		-6.0	Pebble		
4		-2.0	Granule		
2.00		-1.0	Very coarse sand		
1.00		0.0	Coarse sand		
1/2 0.50	500	1.0	Medium sand	Sand	Sandstone
1/4 0.25	250	2.0	Fine sand		
1/8 0.125	125	3.0	Very fine sand		
1/16 0.0625	63	4.0	Coarse silt		
1/32 0.0310	31	5.0	Medium silt	Silt	Siltstone
1/64 0.0156	15.6	6.0	Fine silt		
1/128 0.0078	7.8	7.0	Very fine silt		
1/256 0.0039	3.9	8.0	Clay	Mud	Claystone
0.00006	0.06	14.0			

Figure 3.9 Grain-size classification diagram for siliciclastic sediments (modified after Wentworth, 1922)

3.3.1 Laser Diffraction Method and Sample Preparation

Laser diffraction is a widely used technique for particle size analysis, particularly effective for measuring the size distribution of fine and ultrafine particles in a variety of materials, including marine sediments. This method offers several advantages, such as high resolution, rapid analysis, and the ability to measure a wide range of particle sizes. The laser diffraction method is based on the principle of light scattering. When a laser beam passes through a dispersed particulate sample, the particles scatter the light at angles that are inversely proportional to their size. Larger particles scatter light at small angles, while smaller particles scatter light at larger angles. By measuring the intensity and angle of the scattered light, the particle size distribution can be determined.

In this study, samples were taken every cm from top of the 3 cm of core samples. The idea is identifying the whole basin hydrodynamic changes. Finally, grain size distribution change maps were generated by using the data set at ArcGIS. According to that whole basin grain size distribution maps, some of the core locations were picked. Then, these cores were sampled every 5 cm intervals until the end of the cores. According to that, the regional reconstruction of the paleoenvironment was interpreted at the end of this study.

I. Homogenization: Homogenize the sediment sample to ensure consistency. This can be done by mixing the sample thoroughly with a spatula.
II. Dispersant Addition: Add a dispersant to the subsample to prevent particle agglomeration. Common dispersants include sodium hexametaphosphate or Calgon. The concentration and type of dispersant depend on the sediment's mineralogical composition (Beuselinck et al., 1998).
III. Ultrasonic Treatment: Apply ultrasonic treatment to the sample to further disperse the particles. Ultrasonication helps break up aggregates and ensures that individual particles are measured (Blott and Pye, 2001).

There are 2 types of dispersion of measurement, these are wet dispersion and dry dispersion. In this study wet dispersion was used. For wet dispersion, suspend the sample in a suitable liquid medium, usually water, in a sample cell. Ensure that the sample is adequately mixed to maintain a uniform suspension during the measurement. At final stage, the prepared sample introduced into the laser diffraction instrument. Record the scattering data, ensuring that the sample concentration is within the optimal range for the instrument to avoid multiple scattering effects (Beuselinck et al., 1998).

3.4 AMS Radiocarbon Dating ^{14}C

Radiocarbon dating is a fundamental method for determining the age of organic materials by measuring the decay of carbon-14 (^{14}C), a radioactive isotope formed in the atmosphere and incorporated into living organisms. Upon an organism's death, the uptake of ^{14}C ceases, and the isotope decays at a known half-life of approximately 5,730 years, enabling scientists to calculate the time since death. This technique has

revolutionized fields such as archaeology and sedimentology by providing precise chronological frameworks for ancient organic materials (Reimer et al., 2020). In sedimentology, radiocarbon dating is crucial for reconstructing the timing of sediment deposition, offering insights into past environmental conditions, sediment flux changes, and sea-level variations. By analyzing organic matter within sediment cores, such as plant remains and shells, researchers can build detailed chronologies of climatic and ecological changes over geological timescales. Recent advancements, such as the IntCal20 Northern Hemisphere calibration curve, have significantly improved the accuracy and range of radiocarbon dating, highlighting its ongoing importance in refining historical and paleoenvironmental timelines.

The calibration of radiocarbon dates to calendar years is critical due to variations in atmospheric ^{14}C concentrations over time. The latest calibration curve, IntCal20, developed by the IntCal Working Group (IWG), incorporates a wealth of new data, including annually resolved ^{14}C measurements from tree rings, lake sediments, foraminifera, speleothems, and corals. Extending to approximately 13,910 cal BP as a fully atmospheric record, IntCal20 improves accuracy through rigorous data screening, increased geographic and temporal coverage, and corrections for marine reservoir ages (MRA), which account for spatial and temporal variations in ocean circulation. These advancements significantly enhance the precision of radiocarbon dating, enabling more accurate reconstructions of historical timelines, environmental changes, and human history over the past 55,000 years. By integrating advanced statistical methods and diverse datasets, IntCal20 marks a major advancement in radiocarbon calibration, reinforcing its central role in archaeology, paleoclimatology, and earth science research (Reimer et al., 2020).

3.4.1 Sample Preparation

The age information of the core sample is crucial for the correlation of the cores, like changes in the chemical content and physical properties. The length, location and water depth properties determine samples.

To prepare the sample for analysis, a pre-treatment process is required to remove clay- and silt-sized particles. This involves the use of an ultrasonic bath to separate particles of different sizes. The sample solutions are placed in the ultrasonic bath and subjected to vibrations at a frequency of 37 kHz for 10 minutes. Following this, the solution is passed through a 0.062 mm sieve to separate finer particles. This process of ultrasonic vibration and sieving is repeated multiple times until the water within the sample solution becomes clear, ensuring thorough particle separation. Once this step is complete, the sample is dried to prepare it for further examination.

The dried samples are then analysed using a stereomicroscope, which facilitates the identification and selection of specific materials used for radiocarbon dating (^{14}C analysis). These materials include planktonic foraminifera, bivalves, charcoal, wood, and seeds. Using the stereomicroscope, these components are meticulously collected from the dried samples for radiocarbon dating purposes. This detailed sample preparation ensures accuracy and precision in the selection of suitable materials for radiocarbon age determination. The selected materials from the stereomicroscope view are seen in Figures between 3.10-3.13.
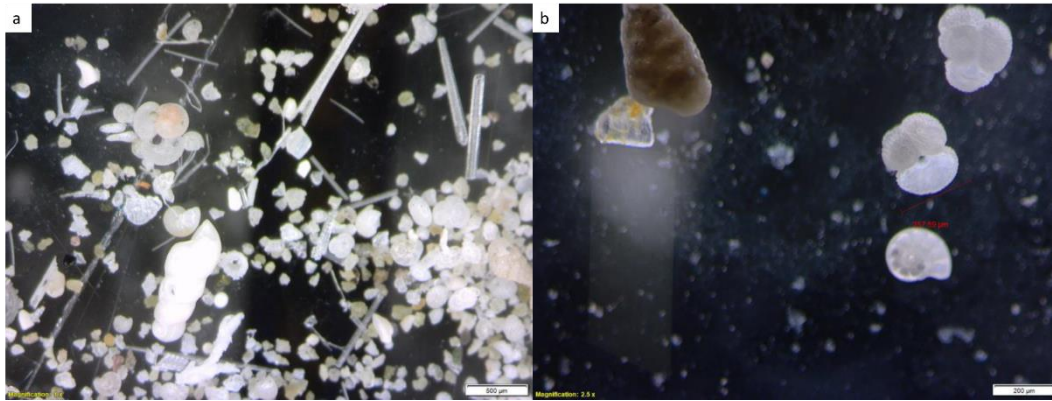
Figure 3.10 (a) EDR37/137-138 cmbsf- planktonic foraminifera (b) EDR37/139-140 cmbsf- planktonic foraminifera
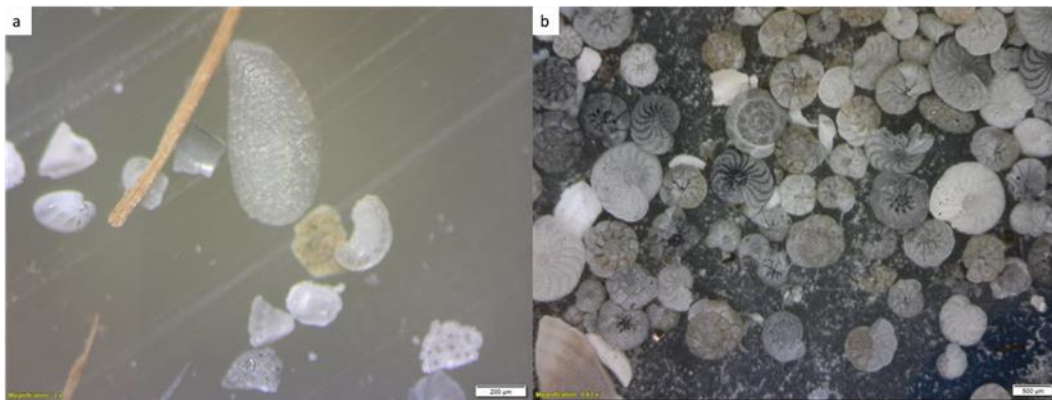
Figure 3.11 (a) EDR23/141-142 cmbsf- transparent bivalve (b) EDR10/136-137 cmbsf- benthic foraminifera
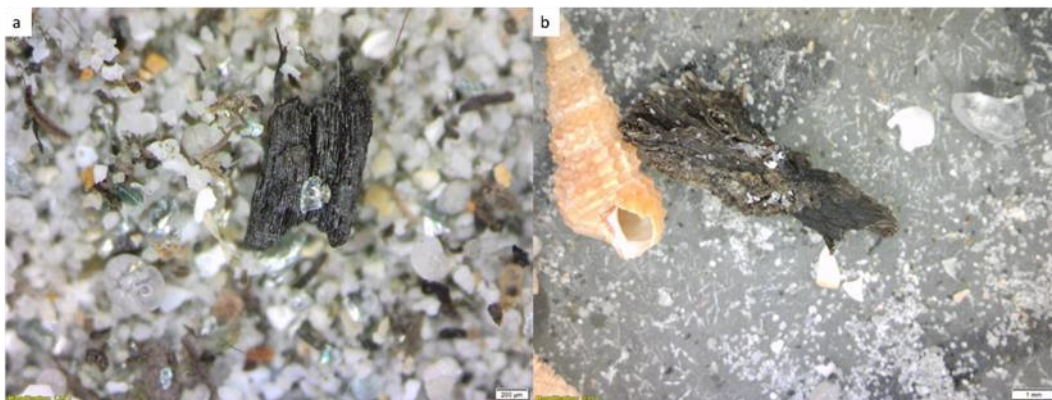
Figure 3.12 (a) EDR51/139-140 cmbsf- charcoal (b) EDR47/139-140 cmbsf- wood
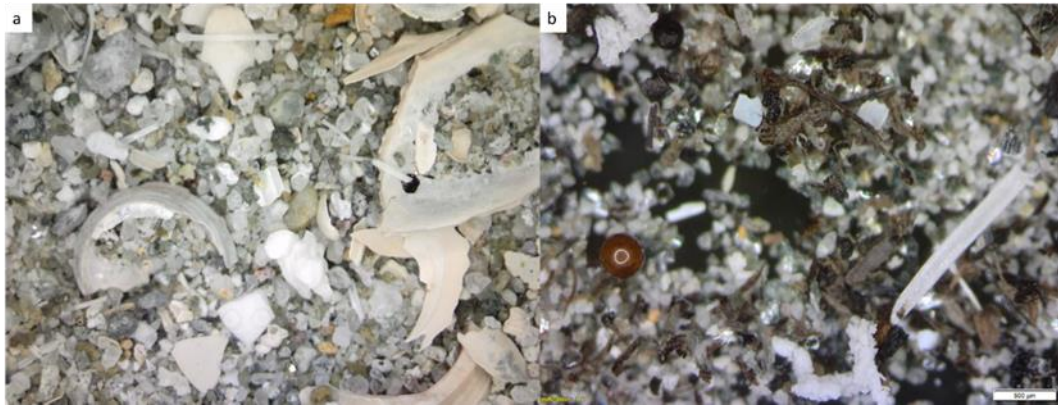
Figure 3.13 (a) EDR12/86-87 cmbsf- shell and bivalve fragments (b) EDR51/139-140 cmbsf- seed

3.4.2   Radiocarbon Age Calibration and Average Sedimentation Rate Calculation

Calibration is essential to convert radiocarbon ages into calendar ages, enabling more accurate chronological reconstructions. Radiocarbon calibration was using the Calib tool in conjunction with the Marine20 calibration curve in this study. Furthermore, it details the calculation of sedimentation rates based on calibrated ages, an approach critical to understanding depositional processes within sedimentary environments.

Radiocarbon calibration was performed using the Calib 8.2 tool (Stuiver et al., 2021). The Marine20 calibration curve, specifically designed for marine samples, was employed to account for fluctuations in global marine reservoir effects (Heaton et al., 2020). This calibration curve integrates updated data from marine environments, improving precision and reliability in marine radiocarbon dating.

Radiocarbon ages, expressed in years BP (Before Present, 1950), are inputted alongside their corresponding standard deviations (e.g., $\pm 1\sigma$ or 2σ). Marine reservoir corrections (ΔR) are applied using region-specific values to account for deviations in radiocarbon levels between the global ocean and the local study area.

I. Radiocarbon dates were compiled into a spreadsheet, documenting sample IDs, lab codes, radiocarbon ages, and errors. Local ΔR values and uncertainties were retrieved from published databases.

II. The Calib 8.2 tool was initialized, and the Marine20 curve was selected as the calibration curve.

III. Radiocarbon ages, along with local ΔR, were inputted into the software. The calibrated calendar ages and corresponding 1σ and 2σ confidence intervals were generated.

Age-depth models are essential for interpolating ages between radiocarbon-dated horizons, providing a continuous chronological framework for sedimentary sequences. Sedimentation rates provide insights into depositional processes and environmental changes over time. These rates are calculated by relating sediment core depth intervals to the calibrated radiocarbon ages of sampled horizons. Able to construct a reliable age-depth model, it is essential to have more than one age data point from the same core sample. However, in this study, each core sample contains only a single age data point from a specific depth. As a result, it is not possible to create an accurate age-depth model with the available dataset. Therefore, the top of each core sample is assumed to represent the present day, and this assumption is used to calculate an average sedimentation rate for the respective sampling locations.

3.5 Total Organic and Inorganic Carbon Analysis

Total Organic Carbon (TOC) and Inorganic Carbon (IC) analyses are fundamental tools for studying carbon cycles across various ecosystems, including the marine environment. TOC measures carbon bound in organic compounds, while IC quantifies carbon found in inorganic forms, such as carbonates and bicarbonates. These analyses have evolved significantly since their origins in the early 20th century, with advancements like high-temperature combustion and coulometric detection enabling precise measurements. TOC and IC are widely used in fields such as environmental monitoring, water quality assessment, and industrial process

management. In environmental applications, TOC and IC analyses provide insights into pollution levels, ecosystem health, and carbon fluxes, particularly in marine ecosystems where carbon cycling is vital for understanding global carbon dynamics.

In marine applications, TOC and IC analyses are critical for understanding the ocean's role in the global carbon cycle and its impact on climate change. Oceans act as both a carbon source and sink, absorbing about one-third of anthropogenic CO_2 emissions. TOC and IC measurements help scientists study carbon sequestration processes, where marine organisms convert dissolved inorganic carbon into organic matter that sinks to the ocean floor. These analyses also enable the monitoring of marine ecosystem health; as elevated TOC levels may indicate organic pollution affecting biodiversity. Furthermore, by tracking the movement of carbon between the atmosphere, ocean surface, and deep ocean, researchers gain insights into the ocean's capacity to mitigate climate change and predict future CO_2 trends, contributing to a deeper understanding of global climate scenarios (e.g., Hedges and Oades, 1997; Druffel et al., 1992; Sabine et al., 2004).

Sapropel layers are dark, organic-rich sedimentary deposits formed under conditions of enhanced primary productivity and anoxia in marine environments. These layers result from increased nutrient input, often driven by climatic changes such as monsoon intensification, which stimulates phytoplankton blooms and organic carbon deposition (Emeis et al., 2000). Water column stratification further creates anoxic bottom waters, preserving organic matter by inhibiting decomposition (Rossignol-Strick et al., 1982). Climatic factors, such as warmer temperatures and increased rainfall during interglacial periods, enhance nutrient runoff and sapropel formation (Rohling, 1994). The study of TOC-rich sapropels provides critical insights into past oceanographic and climatic conditions, contributing to our understanding of the global carbon cycle and environmental change.

3.5.1 Sample Preparation

In this study the prepared samples which are EDR-23 and EDR-47 were sent to METU-IMS laboratories to analyze the TC and IC amounts. The reason for the selection of these two cores is they have a radiocarbon age data and their elemental changes were different. Every 5 cm intervals from top of the core were sampled. Then there are some procedures that follow for total carbon measurements from EPA method 415.1 (EPA,1999). These are;

I. For sediment samples using appropriate methods to avoid contamination
II. For solid samples, dry and grind to a fine powder to ensure homogeneity.
III. Acidify the sample to remove inorganic carbon. This is typically done by adding a strong acid, such as hydrochloric acid (HCl), which converts inorganic carbonates to CO_2 gas.
IV. The CO_2 gas is then purged from the sample using an inert gas such as nitrogen (N_2).
V. Transfer the acidified sample to a high-temperature furnace, typically set between 680°C to 1,000°C.
VI. During combustion, organic carbon is oxidized to CO_2.
VII. The CO_2 produced during combustion is transported by a carrier gas to a CO_2 detector, such as a non-dispersive infrared (NDIR) detector.
VIII. The detector quantifies the CO_2 concentration, which correlates to the amount of organic carbon in the sample.
IX. The TOC is calculated by comparing the CO_2 signal to a calibration curve obtained from known standards.

Afterwards to identify the Inorganic carbon testing there are some procedures to be followed by EPA method 415.1 (EPA, 1999). These are;

I. For solid samples, ensure they are dry and finely powdered.
II. Place the sample in an acidification chamber.
III. Add a strong acid, such as HCl, to the sample to release CO_2 from inorganic carbonates.
IV. Capture the CO_2 gas released during acidification using a gas-tight syringe or other appropriate method.
V. Ensure that all CO_2 generated from the inorganic carbonates is collected.
VI. The captured CO_2 is then directed to a CO_2 detector, such as an NDIR detector.
VII. The detector quantifies the CO_2 concentration.

VIII.   The IC is calculated by comparing the CO_2 signal to a calibration curve obtained from known standards.

Finally, for the TC calculation (U.S. EPA Method 415.1) t the IC value is subtracted from the TC value to obtain the TOC.

3.6   δ18O/ δ16O Isotope Ratio Mass Spectrometer Analysis

The analysis of oxygen isotopes, specifically Oxygen-18 ($\delta^{18}O$) and Oxygen-16 ($\delta^{16}O$), has been instrumental in reconstructing climatic and environmental changes over geological timescales. Advances in mass spectrometry in the mid-20th century enabled precise measurements of isotope ratios, leading to the pioneering work of Harold Urey (1948) and Cesare Emiliani (1955). Urey (1948) research on isotope fractionation principles and Emiliani (1955), studies on foraminifera shells demonstrated that variations in $\delta^{18}O/\delta^{16}O$ ratios are influenced by temperature and ice volume, establishing these isotopes as key proxies for paleoclimatic reconstruction (Urey,1948; Epstein et al., 1953; Emiliani, 1955).

Oxygen isotope analysis, conducted using an Isotope Ratio Mass Spectrometer (IRMS), measures the ratio of $\delta^{18}O$ to $\delta^{16}O$ in samples such as marine sediments, ice cores, and carbonate shells of marine organisms. The $\delta^{18}O/\delta^{16}O$ ratio is influenced by temperature and global ice volume, providing a valuable proxy for reconstructing past climates. During colder periods, ice sheets preferentially trap the lighter $\delta^{16}O$, leaving the ocean enriched in $\delta^{18}O$, while warmer periods see melting ice release $\delta^{16}O$ back into the ocean, reducing the $\delta^{18}O/\delta^{16}O$ ratio (Shackleton, 1982). This method has become a cornerstone of paleoclimatology, enabling scientists to infer sea surface temperatures, ice volumes, and climatic shifts over hundreds of thousands of years.

In marine climate studies, foraminifera shells are particularly valuable for $\delta^{18}O$ analysis. These microscopic marine organisms incorporate oxygen isotopes from seawater into their calcium carbonate ($CaCO_3$) shells, reflecting the isotopic

composition of the ocean during their lifetimes. When foraminifera die, their shells settle into marine sediments, preserving a continuous record of past climate conditions. Higher $\delta^{18}O/\delta^{16}O$ ratios in these shells typically correspond to glacial periods with extensive ice sheets, while lower ratios indicate interglacial periods with reduced ice volume. By analysing these isotopic variations, scientists can reconstruct detailed records of climatic events such as glacial-interglacial transitions, abrupt climate changes, and long-term temperature trends.

Additionally, oxygen isotope analysis aids in understanding the mechanisms driving climate change. By comparing isotopic records from different regions and depths, researchers can infer shifts in ocean circulation patterns, ice sheet dynamics, and the influence of greenhouse gases on global temperatures. These insights are crucial for interpreting past climate variability and predicting future changes in response to anthropogenic activities (Zachos et al., 2001). The integration of oxygen isotope data with other paleo-climatic proxies allows for a comprehensive reconstruction of Earth's climate history and its underlying drivers.

3.6.1   Sample Preparation

In this study the TOC analyzed samples EDR-23 and EDR-47 were selected. According to TOC levels several depths were picked for sampling. 30 different sampling levels are selected and samples were prepared from these levels. The samples were sent to METU Central Lab/ Isotope Ratio Mass Spectrometer Lab for test. In METU Central Lab / Isotope Ratio Mass Spectrometer Lab DeltaPlus XP Isotope Ratio Mass Spectrometer was used. They follow ThermoFinnigan test procedure in their lab.

The procedures of the test are followed,

I.   Sample Preparation: Dry them at 60°C to remove moisture. Grind the dried sediment into a fine powder using a mortar and pestle or mechanical grinder.

II. Weighing and Encapsulation: Weigh approximately 1-2 mg of the homogenized sediment powder. Encapsulate the weighed sample in a tin capsule.

III. Carbonate Removal (Optional): If carbonates are present, treat the sample with 10% HCl until effervescence stops. Rinse with distilled water and dry the sample again. Re-homogenize the sample post-acid treatment.

IV. Load the tin capsules into the autosampler of the DeltaPlus XP IRMS.

V. The autosampler introduces the samples into the combustion furnace where they are combusted at around 1000°C. The combustion produces CO_2, N_2, and H_2O.

VI. The gases pass through a gas chromatograph to separate CO_2 from other gases.

VII. The purified CO_2 is introduced into the ion source of the DeltaPlus XP IRMS. Ionization occurs, and ions are accelerated through a magnetic field.

VIII. The magnetic field separates ions based on their mass-to-charge ratio. Detectors measure the intensities of ^{18}O and ^{16}O ions. The instrument calculates the $^{18}O/^{16}O$ ratio from the detected intensities (Sharp, 2017).

3.7   Map Studies

3.7.1   Bathymetry Map

In this study, ArcGIS software was utilized to create a detailed bathymetric map, which is essential for analyzing underwater depths and supports applications such as navigation, environmental monitoring, and marine research. The process began with acquiring high-resolution bathymetric data from marine chartplotters, which were digitized using ArcGIS. The data was then converted into a compatible format, such as raster or shapefile, and projected using the WGS_1984_UTM_Zone_35N coordinate system to ensure spatial accuracy.

The core steps in bathymetric mapping included interpolation, contour generation, and symbolization. Interpolation, specifically the Inverse Distance Weighting (IDW) method, was applied to create a continuous surface from discrete data points. IDW estimates unknown values based on proximity, with closer points having greater influence, offering simplicity and efficiency but with limitations such as edge effects

and isotropy assumptions. Contour lines were generated at 2-meter intervals from the interpolated raster, improving the map's vertical resolution and readability. Effective visualization was achieved through symbolization, with customized color ramps and labels to distinguish depth ranges, and deeper areas represented in darker blue shades.

The final step involved designing a comprehensive map layout, including essential elements such as a title, legend, scale bar, and north arrow, ensuring both clarity and visual appeal. This systematic process demonstrated the powerful capabilities of ArcGIS in producing high-resolution bathymetric maps, which are invaluable for marine science and environmental studies.
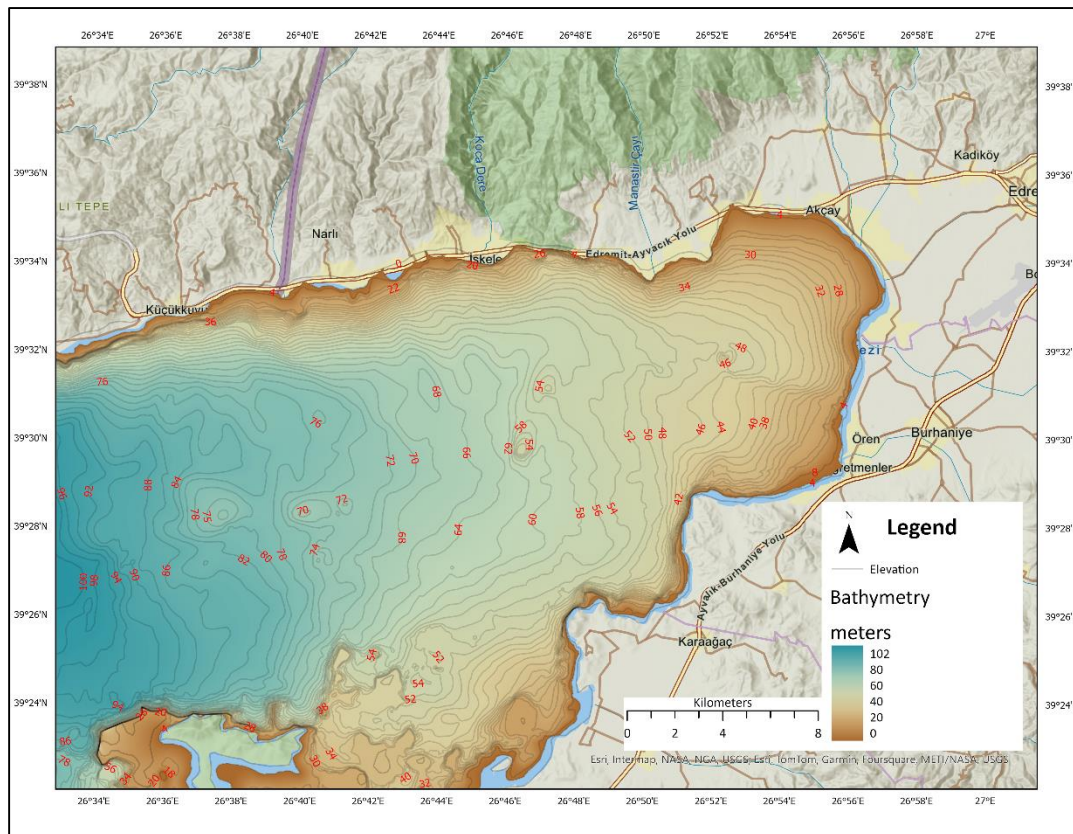
Figure 3.14 Bathymetry map of study area

3.7.2   Grain Size Distribution Map

Grain size distribution map provide crucial information about the texture and composition of sedimentary deposits, which can be used to interpret depositional environments and sediment transport mechanisms. This section outlines the step-by-step process of creating a grain size distribution map using ArcGIS, a powerful geographic information system software. In this study, to enhance grain size distribution map 60 different core samples' first 3 centimeters average grain size data were used in ArcGIS software. The following steps are given in below to generate grain size distribution map,

Field Sampling: Collect sediment samples from the study area. Ensure that the sampling locations are accurately recorded using GPS for precise spatial reference.

Lab Analysis: In this study the grain size analysis was accomplished with the Laser Diffraction Method. Record the results in a spreadsheet, noting the percentages of different grain size fractions (e.g., sand, silt, clay).

Spreadsheet Organization: Organize the grain size data in a spreadsheet with columns for location coordinates (latitude and longitude), grain size fractions, and other relevant attributes.

Import Data to ArcGIS: Import the spreadsheet data as a point layer. Ensure that the coordinate system of the data matches the coordinate system of the map.

Interpolation Method Selection: Choose an appropriate interpolation method to create a continuous surface representing grain size distribution. Common methods include Inverse Distance Weighting (IDW), Kriging, and Spline. In this study IDW was used as a method of interpolation.

Perform Interpolation: Use the selected interpolation method to create raster layers for each grain size fraction. This involves creating a surface that predicts grain size distribution between sampled points.

Raster Layer Visualization: Visualize the raster layers to inspect the spatial distribution of grain sizes. Adjust the symbology to represent different grain size classes with distinct colors.

Combine Layers: If necessary, combine the raster layers to produce a composite grain size distribution map. This can be done using map algebra or raster calculation tools in ArcGIS.

Create Layout: Design the map layout by adding essential map elements such as a title, legend, scale bar, north arrow, and annotations. Ensure that the map is clear and easy to interpret.

Finally, grain size distribution maps are very informative maps that enhance the understanding of sediment characteristics and their spatial variability. These maps serve as valuable tools in various scientific and environmental applications, providing insights into the geological history and sediment dynamics of the study area.

3.7.3   Elemental Concentration Change Map

This section outlines the procedure to create such a map, ensuring accuracy and clarity in representing the spatial distribution and changes in elemental concentrations across different samples. In this study 60 different core samples locations µXRF analyses were performed. µXRF results are composed mainly of major oxides and trace elements. The list of the major oxides and trace elements is given in the below. So, the elements listed below can be drawn as an elemental concentration change map. However, drawing all these elements and oxides changes depending on the data quality. For that reason, some elements and oxides were picked with respect to its data quality. To identify an elemental concentration, the first several centimeters' data were analyzed. The major oxides and trace elements that the ITRAX device can measure are given below.

Major Oxides: **Al_2O_3, SiO_2, K_2O, CaO, TiO_2, MnO, Fe_2O_3**

Trace Elements: **Al, Si, Cl, Ar, K, Ca, Ti, V, Cr, Mn, Fe, Ni, Cu, Zn, Sr, Zr, Ag, Ba, Au, Pb**

The steps that can be followed to create an elemental concentration change map are the same as those used generate grain size distribution change maps. The only difference is that, instead of grain size fraction data, the average concentration of an element for several centimeters of data is imported to ArcGIS software.

Field Sampling: Collect sediment samples from the study area. Ensure the sampling locations are accurately recorded using GPS for precise spatial reference.

Lab Analysis: Record the μXRF results in a spreadsheet, noting the average concentration of an element within several centimeters' data.

Spreadsheet Organization: Organize the element concentration of an element data in a spreadsheet with columns for location coordinates (latitude and longitude).

Import Data to ArcGIS: Import the spreadsheet data as a point layer. Ensure that the coordinate system of the data matches the map's coordinate system.

Interpolation Method Selection: In this study IDW was used as a method of interpolation.

Perform Interpolation: Use the selected interpolation method to create raster layers for each grain size fraction. This involves creating a surface that predicts the concentration of elements between sampled points.

Raster Layer Visualization: Visualize the raster layers to inspect the spatial distribution of grain sizes. Adjust the symbology to represent different grain size classes with distinct colors.

Combine Layers: If necessary, combine the raster layers to produce a composite grain size distribution map. This can be done using map algebra or raster calculation tools in ArcGIS.

Create Layout: Design the map layout by adding essential map elements such as a title, legends scale bar, north arrow, and annotations. Ensure that the map is clear and easy to interpret.

CHAPTER 4

RESULTS

4.1 Unlocking Time: Age Constraints from Sedimentary Cores in GoE

The radiocarbon age results will be presented in this section. The selected cores were determined after a long period of examining the samples under a microscope. First, samples which are located deeper part of the basin and long lengths specifically chosen. However, when the sampling process did not yield sufficient material suitable for carbon-14 measurement under the microscope, other core samples also are considered. As a result, seven cores, which are believed to best represent the region, are selected. One age data point is obtained from each core sample. Unfortunately, in some cases, due to insufficient material from the end of the core, samples are also taken from the middle levels or areas near the top of the core. Briefly the selected cores are listed below in order;

    I.   EDR10
   II.   EDR23
  III.   EDR25
  IV.   EDR28
   V.   EDR30
  VI.   EDR47
 VII.   EDR51

Samples were taken from the deepest parts of the cores mentioned above. As described in the methodology section, these samples are first examined under a microscope in the laboratory to check and collected for a sufficient amount of bivalves, woods, charcoal, and planktonic foraminifera. After that, the AMS Laboratory at the TÜBİTAK MAM campus is found. The materials that could provide a sufficient amount of radiocarbon age are weighed using a precision scale and then sent to the TUBİTAK AMS Laboratory. The results are given in Table 4.1

Table 4.1 Radiocarbon official results from TÜBİTAK AMS Lab

Lab No	Core Sample and Depth (cmbsf)	Radiocarbon Age	Sample Type
TÜBİTAK-2991	EDR10-140cmbsf	8491±38	Shell, Bivalve
TÜBİTAK-2992	EDR51-139cmbsf	1679±34	Wood, Charcoal and Seed
TÜBİTAK-2993	EDR47-139cmbsf	12138±49	Wood, Charcoal and Seed
TÜBİTAK-2994	EDR30-143cmbsf	12428±45	Wood, Charcoal and Seed
TÜBİTAK-2995	EDR25-15cmbsf	2812±30	Shell, Bivalve
TÜBİTAK-2996	EDR23-96cmbsf	3420±30	Shell, Bivalve
TÜBİTAK-2997	EDR28-42cmbsf	7921±38	Shell, Bivalve

These results indicate the radiocarbon age. A series of applications were used to convert the radiocarbon age into calendar age.

The radiocarbon age and calendar age are not identical. The radiocarbon age needs to be converted calendar age. The reason is 14C concentration in atmosphere changing with radiocarbon production in atmosphere. This radiocarbon production changing is caused from variation of Earth's magnetic field, solar activity and carbon cycle. For this conversion a calibration curve was generated by researchers. There is several software which includes calibration curves in it. The software is available online. These are CALIB and CaliBomb, CalPal and Oxcal. In this study, Calib Rev 8.2 was used. In Calib Rev 8.2, Marine20- the marine radiocarbon age calibration curve helped me to find calibrated ages before present. In marine sediments radiocarbon calibration, a term which is called as reservoir correction factor, ΔR is needed. ΔR a regional offset from the global marine age for the sample. Our samples are located at the North Aegean Sea, the ΔR value for one of the North Aegean Sea study are calculated as -8 and ΔRErr value is 40. So, for calibration of the

radiocarbon ages, the same values of ΔR and ΔRErr is assumed for this study. (Siani et al., 2000)

4.1.1 Tracing Time: Calibrating Time and Sedimentation Rates in Holocene

When evaluating radiocarbon age dating results, two distinct age ranges are derived, corresponding to 1-sigma and 2-sigma probability intervals. These ranges represent the statistical uncertainty associated with the measured radiocarbon ages. The 1-sigma range typically provides a narrower interval, reflecting a 68.3% confidence level, while the 2-sigma range offers a broader interval with a higher confidence level of 95.4%, making it more reliable for accurate age estimations (Reimer et al., 2020). For this study, the 2-sigma range was prioritized due to its higher probability of encompassing the true age. Within this range, the median probability values were selected as representative age estimates, as they provide a balanced central value that minimizes the influence of skewed distributions or outliers.

The selection of median probability values ensures consistency and enhances the reliability of chronological interpretations. These values were then used to correlate the radiocarbon-dated samples with their respective depths, providing a robust framework for constructing the age-depth relationship of the sediment cores. The visual representation below illustrates the correlation between the lengths of the core samples and the corresponding radiocarbon ages, highlighting the temporal resolution achieved through this approach. This method is integral for developing precise age models, which are crucial for understanding sedimentary processes, environmental changes, and paleo-environmental reconstructions.

Table 4.2 Calibrated radiocarbon age results and before present

	EDR_10
	Radiocarbon Age BP 8491 +/- 38
	Delta R = -8.0 +/- 40.0
	68.3 (1 sigma) cal BP 8789 - 9010
	95.4 (2 sigma) cal BP 8664 - 9120
	Median Probability: 8908
	EDR_23
	Radiocarbon Age BP 3420 +/- 30
	Delta R = -8.0 +/- 40.0
	68.3 (1 sigma) cal BP 3023 - 3223
	95.4 (2 sigma) cal BP 2933 - 3323
	Median Probability: 3124
	EDR_25
	Radiocarbon Age BP 2812 +/- 30
	Delta R = -8.0 +/- 40.0
	68.3 (1 sigma) cal BP 2296 - 2488
	95.4 (2 sigma) cal BP 2183 - 2614
	Median Probability: 2392

Table 4.2 (continued)

	EDR_28 Radiocarbon Age BP 7921 +/- 38 Delta R = -8.0 +/- 40.0 68.3 (1 sigma) cal BP 8147 - 8321 95.4 (2 sigma) cal BP 8034 - 8374 **Median Probability: 8222**
	EDR_30 Radiocarbon Age BP 12428 +/- 45 Delta R = -8.0 +/- 40.0 68.3 (1 sigma) cal BP 13730 - 13961 95.4 (2 sigma) cal BP 13602 - 14032 **Median Probability: 13827**
	EDR_47 Radiocarbon Age BP 12138 +/- 49 Delta R = -8.0 +/- 40.0 68.3 (1 sigma) cal BP 13378 - 13578 95.4 (2 sigma) cal BP 13284 - 13697 **Median Probability: 13477**

Table 4.2 (continued)

	EDR_51
	Radiocarbon Age BP 1679 +/- 34 Delta R = -8.0 +/- 40.0 68.3 (1 sigma) cal BP 992 - 1167 95.4 (2 sigma) cal BP 923 - 1248 **Median Probability: 1082**
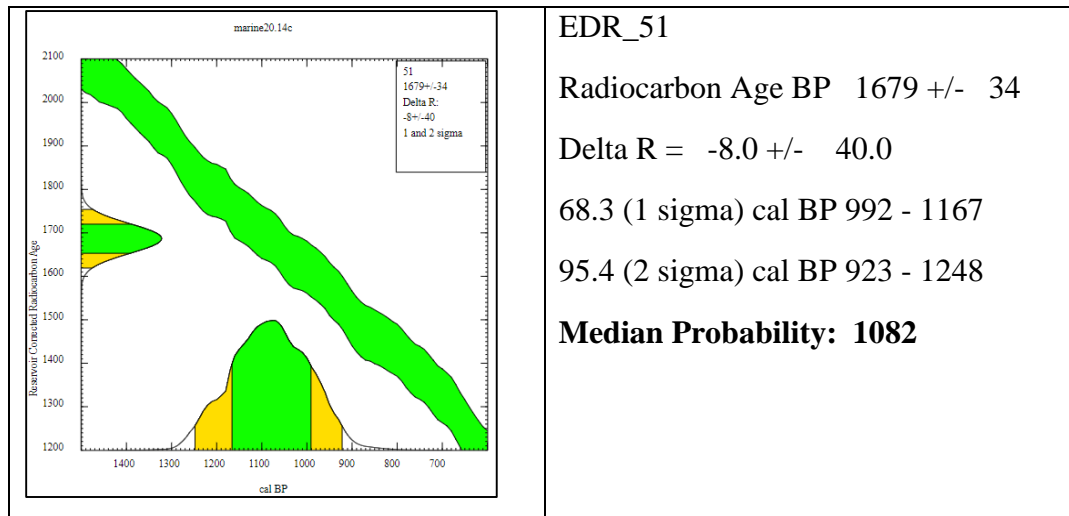
As seen in the Table 4.2 and 4.3, the oldest core is identified as EDR30. This core is located at the deepest part of the study area. When compared to the EDR47, the proximity of the ages serves as a validation of the age estimates. Subsequently, despite the lengths of cores EDR28 and EDR25, their bottom ages are resulted as 10,000 years. The youngest age resulted from core EDR51, it is located northbound of the study area. In conclusion, the average sedimentation rate varies across different parts of the basin.

Table 4.3 Sedimentation rate of radiocarbon aged core samples

Core ID	Radiocarbon Age Sampling (mm)	Age	Sedimentation Rate (mm/year)
EDR10	1400	8908	0,1572
EDR23	980	3124	0,3137
EDR25	160	2392	0,0669
EDR28	420	8222	0,0511
EDR30	1400	13827	0,1013
EDR47	1390	13477	0,1031
EDR51	1400	1080	1,2963

Sedimentation rates exhibit spatial variability across the study area, influenced by several factors. These include the density of drainage networks supplying sediment to the basin and the distance of core sampling locations from these networks. Additionally, structural features such as fault zones, fault concentrations, and the proximity of cores to fault-dense areas significantly impact sedimentation patterns. Radiocarbon dating results reveal that the highest sedimentation rate is observed in core EDR51. This aligns with findings by Ak (2019), which highlight a higher drainage density in the northern part of the study area, where core EDR51 is located. The elevated sedimentation rate in this core reflects the increased sediment supply associated with the region's dense drainage network and seafloor structural dynamics.
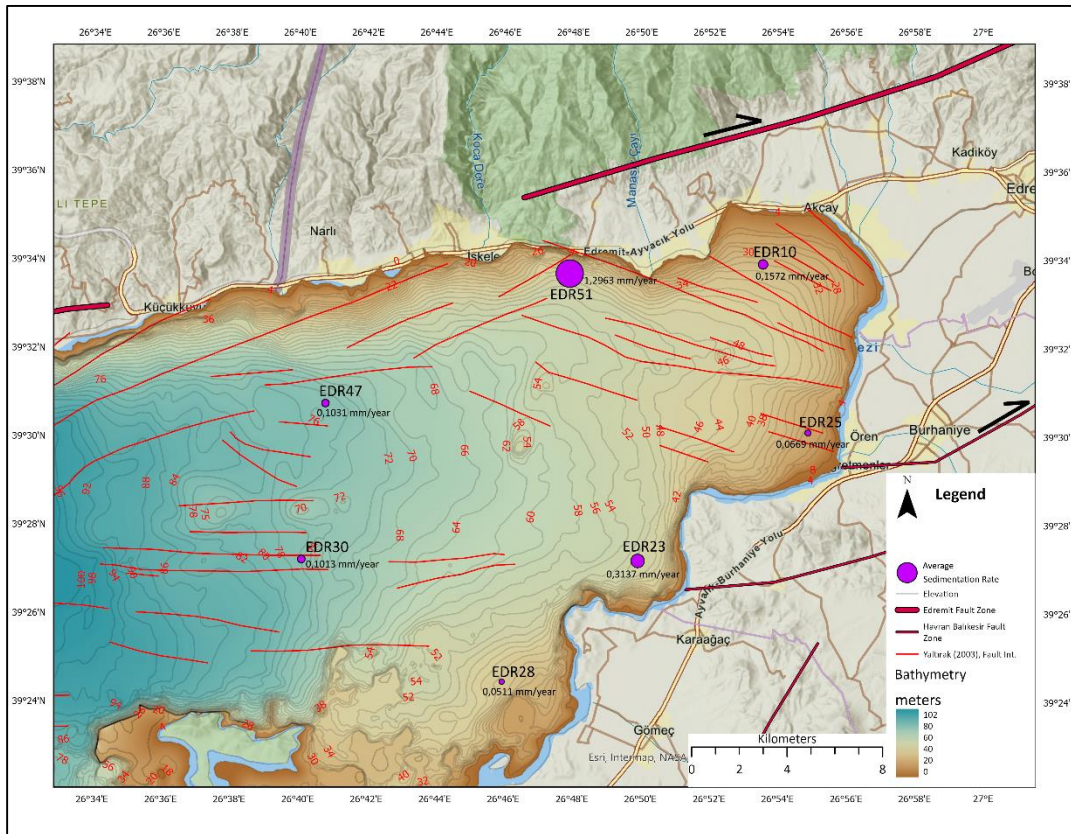
Figure 4.1 Sedimentation rate change map with Yaltırak (2003) fault interpretations

The highest sedimentation rate is observed in core EDR51 which is located at the northbound. According to seafloor morphology, the northern part of the study area displays relatively steeper slope. Yaltırak (2003) fault interpretations indicate a concentration of faulting in the northern section, directly influencing the seafloor morphology and, consequently, the deposition characteristics of cores in this region.

Faults are also observed in the middle and southern parts of the study area with respect to Yaltırak (2003), but these faults appear to have a less impact on seafloor morphology. In nature there are 3 processes for the sediments, these are erosion, transportation and deposition. Sediments transported by northern streams continue their transportation process within downslope in the marine environment. This can cause for the high sedimentation rate in the northbound.

70

However, in the southbound, core EDR23 is located in an area with high gradient slope, which explains why this core has the second-highest sedimentation rate. Seafloor morphology plays a critical role in shaping depocenters. However, factors such as the discharge characteristics of catchments, the amount of transported material, and sea level changes also influence the location of depocenters. The resulting slope change map, which overlays sedimentation rates and Yaltırak (2003) fault interpretations onto the slope change map, which is shown in the Figure 4.2.
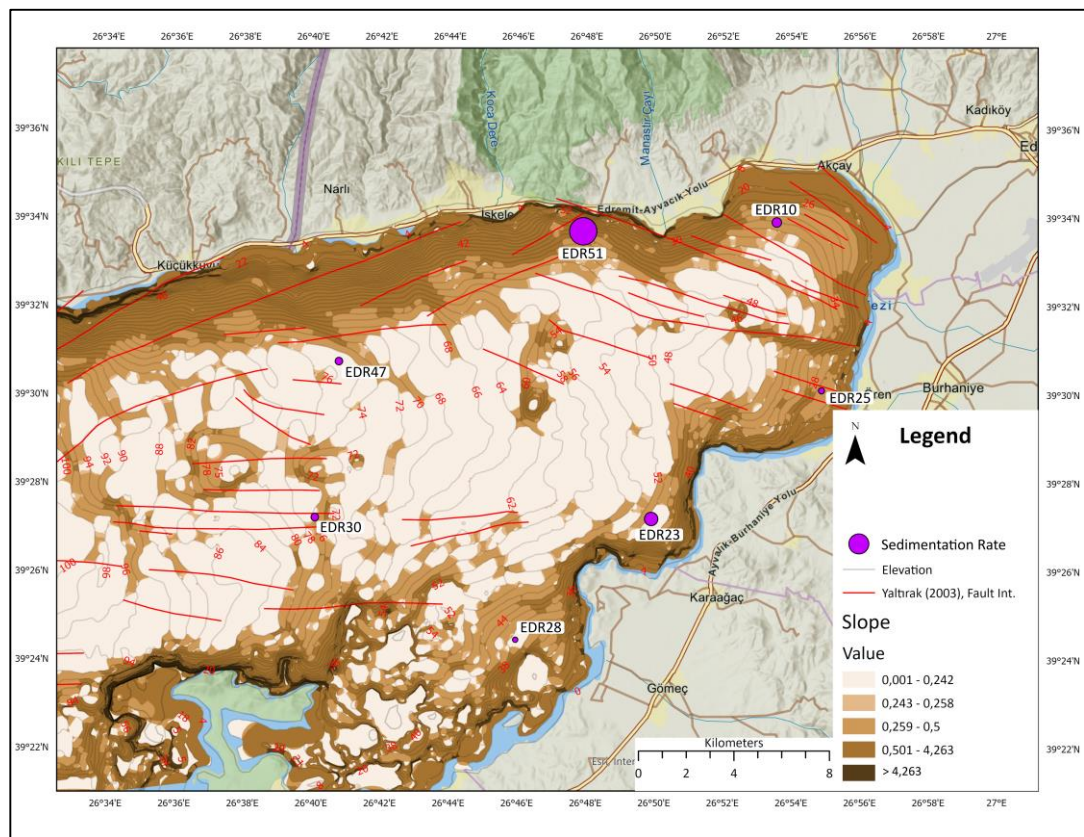

Figure 4.2 Slope change map with Yaltırak (2003) fault interpretations

In Figure 4.3, the correlation of core samples based on their ages is clearly illustrated.
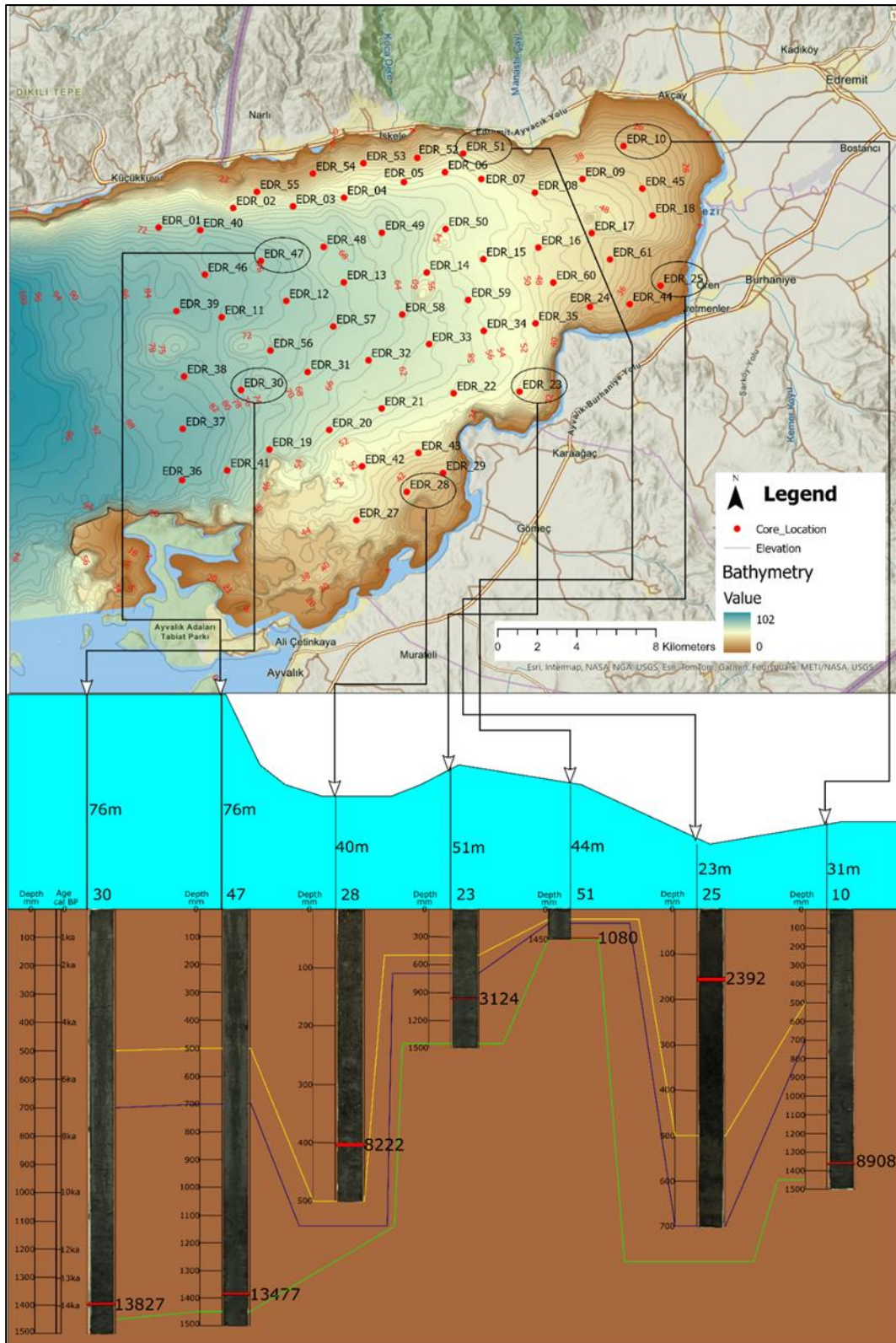
Figure 4.3 Correlation of radiocarbon aged core samples and locations

4.2   Revealing Paleoenvironmental Dynamics Through Multiproxy Synergy

The results of the ITRAX, total organic carbon, and oxygen isotope analysis mentioned in the materials and methods section are presented here. All of these analyses included interpretation is called as multi-proxy analysis. In this study, ITRAX stands out as the most intensively used analysis. From previously collected core samples, 60 cores were systematically obtained to best summarize the eastern part of the Edremit Bay. It is a well-known fact that ITRAX results alone are insufficient for marine climate or tectonic studies. Therefore, analysis such as organic carbon and oxygen isotopes were conducted to support the elemental data. Unfortunately, due to the high cost of total organic carbon and oxygen isotope analysis, the total organic carbon analysis was conducted on the entire sample (every 5 cm interval) for only two cores. Meanwhile, the oxygen isotope analysis was partially conducted at specific intervals in these two cores based on elemental and total organic carbon results. Total organic carbon analyses were performed at the METU IMS Laboratory, while oxygen isotope analysis was conducted at the METU Central Laboratory. The radiocarbon aged 7 core samples which are representing the geochemical characteristics of the study area interpreted comprehensively. These core sample's locations are illustrated in the Figure 4.4.
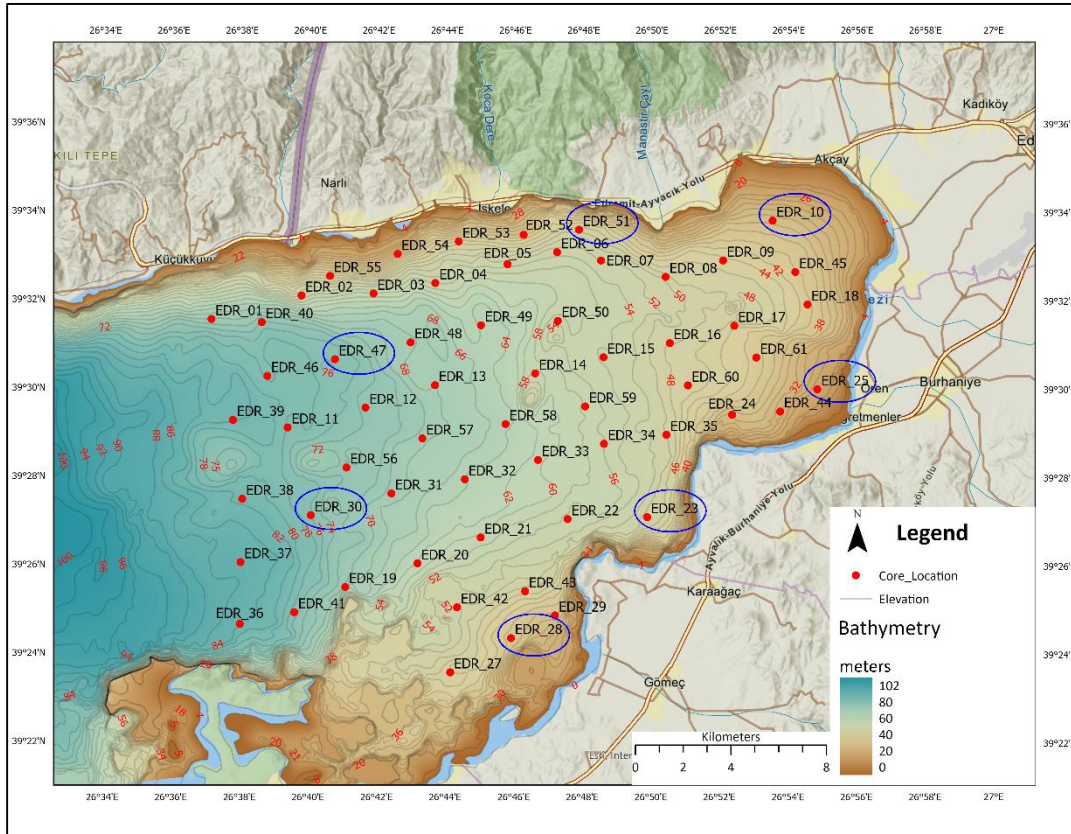
Figure 4.4 Radiocarbon aged core sample's locations

Table 4.4 indicates which analyses were performed on which core samples.

Table 4.4 List of the analysis performed core samples

Core ID	Water Column Depth (m)	ITRAX	Radiocarbon Sampling Interval cmbsf	Radiocarbon Sample Type	TOC	δ18O/ δ16O Isotope
10	31	Whole Core (1mm/5sn Resolution)	136 cmbsf	Bivalve		
23	51	Whole Core (1mm/5sn Resolution)	96 cmbsf	Bivalve		
25	23	Whole Core (1mm/5sn Resolution)	15 cmbsf	Bivalve		
28	40	Whole Core (1mm/5sn Resolution)	42 cmbsf	Bivalve		
30	76	Whole Core (1mm/5sn Resolution)	139 cmbsf	Organic Matter (charcoal, wood)		
47	76	Whole Core (1mm/5sn Resolution)	138 cmbsf	Organic Matter (charcoal, wood)		
51	44	Whole Core (1mm/5sn Resolution)	136 cmbsf	Organic Matter (charcoal, wood)		

The official δ13C and δ18O results for cores EDR23 and EDR47 are shown in the Figure 4.5. The TOC and C/N ratios, along with δ13C and δ18O, are given in the results of cores EDR23 and EDR47, alongside the elemental results.

ORTA DOĞU TEKNİK ÜNİVERSİTESİ
MERKEZ LABORATUVARI
AR-GE EĞİTİM VE ÖLÇME MERKEZİ
Üniversiteler Mah. Dumlupınar Blv. No:1, 06800 Çankaya Ankara/TÜRKİYE
Tel: +90 312 210 64 21 Fax: +90 312 210 64 25 e-posta: merlab@metu.edu.tr http://www.merlab.odtu.edu.tr

DENEY RAPORU
ANALYSIS REPORT

DENEY SONUÇLARI – ANALYSIS RESULTS

Etiket No	SET	Numune Adı	δ13C(‰) vs VPDB	δ18O(‰) vs VPDB
1		EDR23 10_11	-0,90	-3,88
2		25_26	-1,27	-4,10
3		30_31	-1,25	-3,81
4		5_6	-1,15	-3,14
5		15_16	-1,08	-3,62
6		20_21	-1,30	-3,99
7	EDR23	50_51	-0,81	-3,28
8		55_56	-0,73	-3,21
9		60_61	-1,31	-3,69
10		85_86	-1,37	-3,14
11		90_91	-1,15	-2,56
12		95_96	-2,28	-3,00
13		100_101	-0,86	-2,11
14		EDR47 5_6	-0,72	-1,98
15		10_11	-0,49	-1,75
16		15_16	-1,72	-2,98
17		20_21	-1,68	-3,42
18		25_26	-1,83	-3,37
19		30_31	-0,77	-2,37
20		55_56	-0,02	-1,39
21		60_61	-0,25	-1,92
22	EDR47	65_66	-1,34	-2,81
23		100_101	0,63	-2,37
24		105_106	0,91	-2,30
25		110_111	0,60	-2,07
26		115_116	0,37	-3,78
27		120_121	0,36	-5,63
28		125_125	0,37	-6,59
29		130_131	-0,63	-8,02
30		135_136	-0,60	-8,12

Figure 4.5 Oxygen and Carbon Isotopes Official Results from the METU Central Lab

ITRAX and other analysis results of radiocarbon aged core samples are given in order.

4.2.1   EDR10 Core Insight: A Proxy-Driven Element Perspective

First, when interpreting the elemental changes in the cores, it is more logical to divide them into sections that refer to as "events('EV')" in this study. Later, based on the elemental changes within these events, interpretations are made regarding environmental changes during sediment deposition. In the Figure 4.6, starting from the left, a lithostratigraphic column section is provided to observe the types of color changes along the core according to the Munsell Color Chart. The age data with radiographic photo is also presented immediately to the right of this lithostratigraphic column. Then, the grain size variation chart is given.

In the first approximately 75 cmbsf from the top of the core, deposition type is mixture of clay and silt. Following this, between 75 cmbsf and 105 cmbsf shows a deposition of medium to coarse-grained sand, suggesting a larger grain size in this interval. Additionally, the circular symbols represent the remnants of certain living organisms, such as bivalves and shell found in the environment. From 105 cmbsf to the end of the core, another deposition with a high concentration of clay and silt is observed.

Immediately next to the lithostratigraphic section, there is a radiographic photo of the core section and next to the radiographic photo of core sample a graph showing the grain size change within every 5 cm from the top of the core. The increase in medium to coarse-grained sand where the grain size increases, as seen in the paleo-stratigraphic section, serves as a validation. Generally, between the 50 cmbsf and 70bsf cm range, there is a gradual increase in grain size. Subsequently, a significant increase in grain size is observed around 70 cmbsf to 100 cmbsf, where bands of coarse and very coarse sand are evident. Based on the grain size change, separate between 50-70 cmbsf and 70-100 cmbsf intervals and specify as events. So, these intervals are referred to as event1 (EV1) and event2 (EV2), respectively. The depositional environment should be changed within these intervals. Immediately after 100 cm, the grain size gradually decreases up to 120 cmbsf. A fine-grained layer

is seen between the coarse-grained layers, which is indicating the presence of another event, which can be determined as event 3 (EV3).

The interpretations of such marine core samples study typically starts from the older ages to the younger ages.

EV3: In Figure 4.7 between 8 ka and 6.65 ka, there is an increase in the K and Fe elements, while magnetic susceptibility (MS) shows minor fluctuations. These changes suggest an increase in grain size and the possible transport of materials from the land. Although the Fe/Mn ratio is below the average value (average value of the whole Fe/Mn data set of EDR10), it shows an increasing trend, which can be linked to an increase in the oxygen content in the environment, likely due to the influx of terrestrial material. The average value of whole data set is given in the graph for Ca/Ti and Ca/Sr ratios. The ratios are showing more than average, which suggests that the environment may have been relatively humid and warm. A humid and warm climate would enhance surface runoff, facilitating the transport of material from land to sea.

EV2: In Figure 4.7 above the EV3, between 6.65 ka and 4.5 ka, there is an increasing trend in the K, Fe, and MS values. This trend indicates high detrial input. Around 4.5 ka, coarse-grained materials were deposited in the environment. The Fe/Mn ratio increases significantly, raising above the core average, which may suggest an increase in the oxidation state of the environment during that period. On the other hand, Ca and Sr levels are rising, when Fe/Mn ratio is low due to the lower oxygen content in the environment, leading to the preservation of bivalves and shells, whose remnants accumulated in the sediment. The Ca/Sr and Ca/Ti ratios have positive trend, indicating that the environment may have relatively wet and warm period.

EV1: In Figure 4.7 above the EV2, between 4.5 and 3.3 ka, a decrease in K and Fe elements is observed. This suggests that there was no significant input of terrestrial material during this period. The Fe/Mn ratio generally shows a positive trend, indicating a further increase in bottom water oxygen levels. The decrease in the Ca/Ti and Ca/Sr indicates that the climate getting relatively colder and drier.
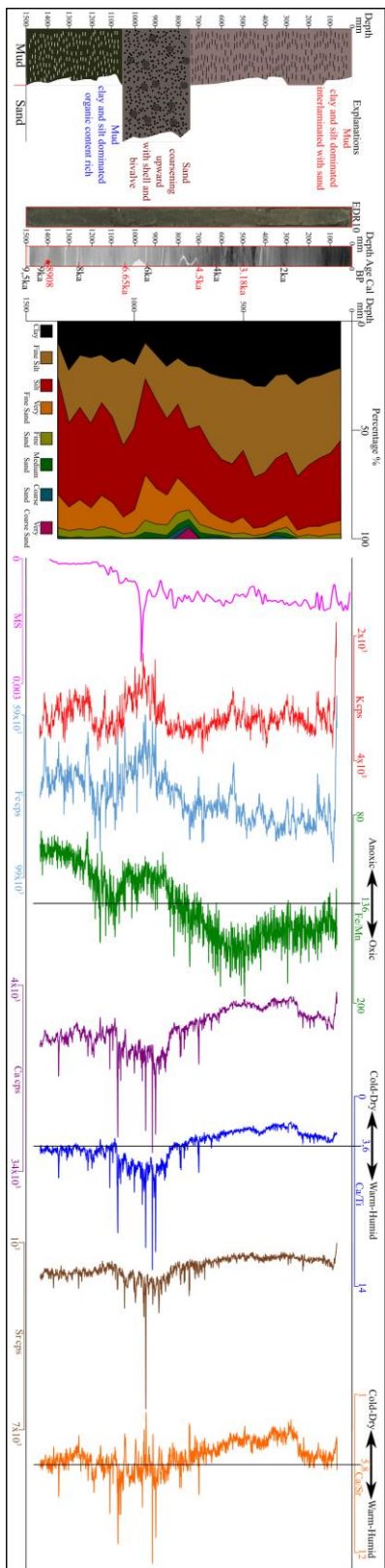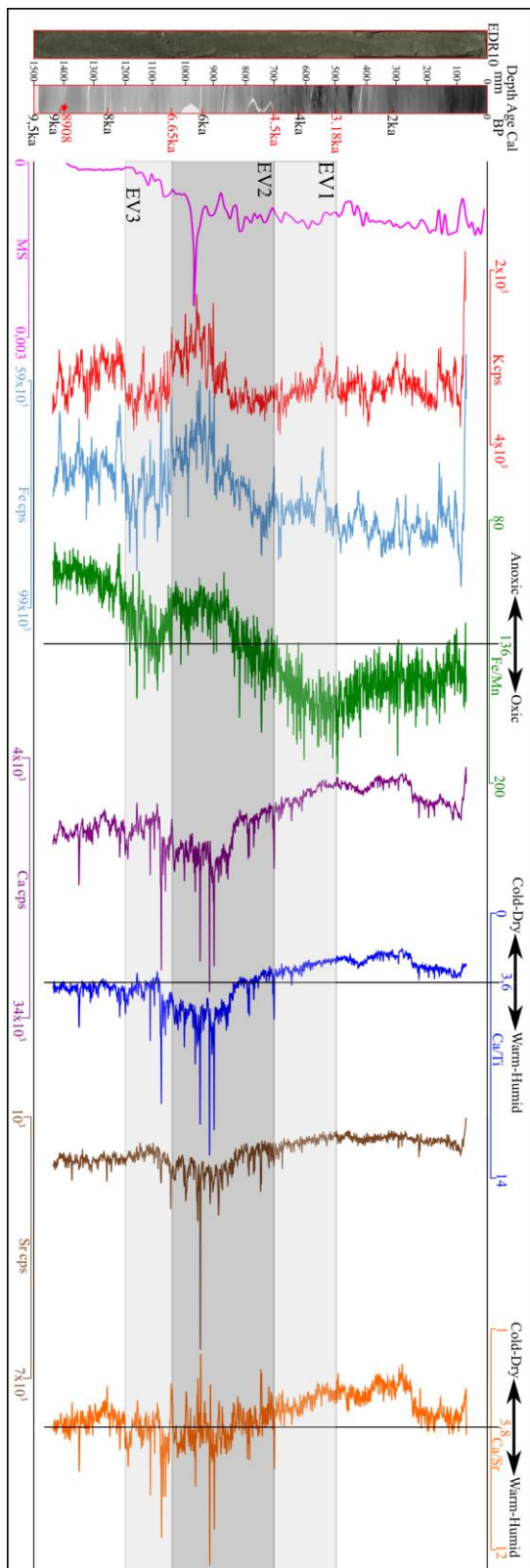
Figure 4.6 EDR10 results without events

78

Figure 4.7 EDR10 results with events

4.2.2 EDR25 Core Insight: A Proxy-Driven Element Perspective

In the Figure 4.8, from left to right, we observe the color changes along the core according to the Munsell Color Chart in a lithostratigraphic column section. The first 10 cmbsf consists of a mixture of clay and silt, while after 10 cmbsf, the sediment distribution includes sand-sized grains. Additionally, after the first 10 cmbsf, shell and bivalve fragments are seen. A sudden and noticeable color change between approximately 38 cmbsf and 42 cmbsf has also been examined. Starting from 55 cmbsf, dark-colored sapropelic layers with a high concentration of organic matter have been examined. The age data with radiographic photo is also presented immediately to the right of this lithostratigraphic column. Next to the radiographic photo of core sample, the grain size variation along the core is seen. After the first 10 cmbsf, the increase in grain size, which is also visible in the stratigraphic section, is reflected in the grain size variation graph. The color change between 38 cmbsf and 42 cmbsf corresponds to a decrease in clay and silt-sized sediments, with a relative increase in grain size. Overall, fine and medium sand sized sediments are predominant. When separating the events based on both the grain size variation and changes in the stratigraphic section, as seen in Figure 4.8, there are four events are interpreted, event1 (EV1) from 4.7 ka to 6 ka, event2 (EV2) from 6 ka to 7.1 ka, event3 (EV3) from 8 ka to the base of the core.

EV3: In Figure 4.9, around 9.5 ka, there is a significant increase in the Fe/Mn ratio, this suggests that, during this brief period a sudden decrease in oxygen state is seen. The presence of the dark, banded layers with high clay content mentioned in the lithostratigraphic section can be presented as evidence that, an organic-rich material was deposited and preserved perhaps due to lower oxygen levels. In low-oxygen (anoxic) environments, organic matter is better preserved because oxygen-rich conditions accelerate the decomposition of organic matter by microorganisms. In regions with high sedimentation rates, organic matter can be buried and preserved more rapidly. Fast accumulation prevents organic matter from remaining exposed in oxygenated surface environments for extended periods, thus slowing down

decomposition. This is evidence for increased MS values in this period, which is indicating a higher sedimentation rate and terrestrial input. This is further supported by the increase in K element concentrations. Peaks above the average value in the Ca/Sr ratio suggest that the period may have been relatively warm and humid.

EV2: In Figure 4.9, above the EV3, between 7 ka and 6 ka, the levels of Fe and K, both terrestrial elements, are very high. This can be associated with the increase in grain size. A noticeable decline in elements like Ca and Sr is also observed. The Fe/Mn ratio remains at core average, indicating that increasing in oxygen state is relatively high during this interval. The Ca/Ti and Ca/Sr ratios are more than core average, so suggesting relatively warm and humid period. This warm and humid condition likely facilitated the transport of terrestrial elements like Fe and K.

EV1: In Figure 4.9, above EV2, between 6 ka and 4.7 ka, the level of Fe and K elements are increased. The MS values are variable. It is indicating for detrial input is getting higher. The Fe/Mn ratio is more than core average, pointing to higher dissolved oxygen levels. The Ca/Ti and Ca/Sr ratios decrease in this period, suggesting that the climate condition changes into relatively cold and dry conditions.
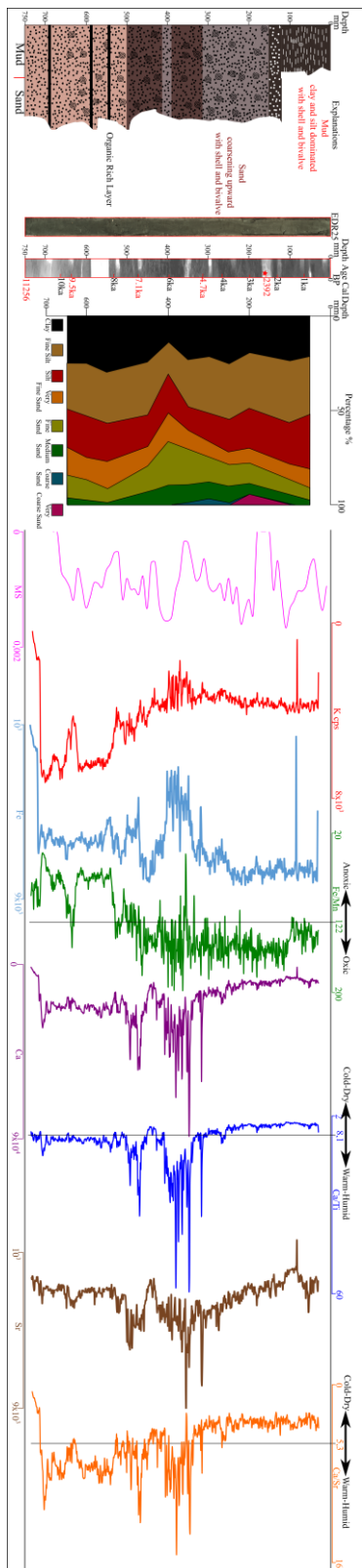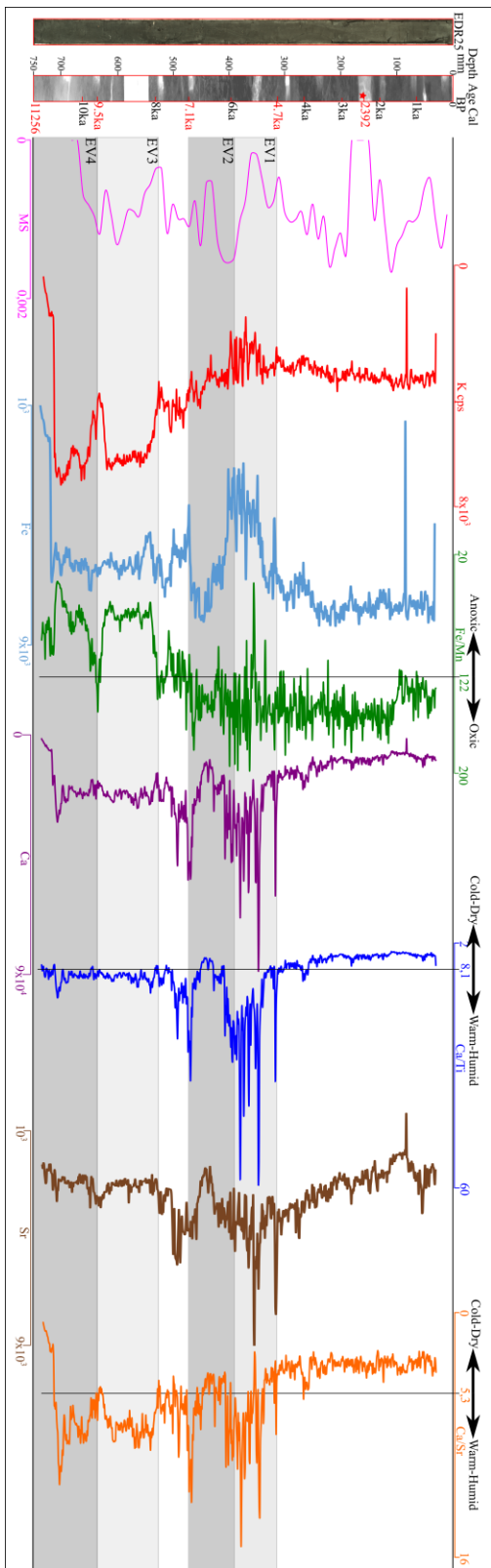
Figure 4.8 EDR25 results without events

Figure 4.9 EDR25 results with events

83

4.2.3 EDR28 Core Insight: A Proxy-Driven Element Perspective

In the Figure 4.10, from left to right, a lithostratigraphic column section with the color changes along the core according to the Munsell Color Chart is seen. Then, a radiographic photo of the core sample with radiocarbon age and grain size variation graph are observed. Overall, at the grain size change table, the core shows a predominantly homogeneous distribution. Along with the clay and silt mixture, sand-sized sediments interlaminated within the core. A noticeable color change has been examined from 20 cmbsf. According to the grain size change graph, coarse-grained materials are deposited at the level of the color change at 20 cmbsf. The boundaries of the events have been determined based on the changes in elements in this sample. Accordingly, event1 (EV1) has been identified between 1.5 ka and 5 ka, and event2 (EV2) between 5.7 ka and 7.7 ka.

EV2: In Figure 4.11, between 7.7 ka to 5.7 ka, the K and Fe element values show a negative trend. A negative peak in MS is observed, which could be attributed to low terrestrial influx. Additionally, the Fe/Mn values tracing below core average level, indicating a further decrease in bottom water oxygen levels. The Ca/Sr and Ca/Ti values also show a trend below core average level, suggesting that this period was likely cold and dry. The negative peak in MS and the Fe and K elements negative trends further supports the notion that terrestrial input is very limited during this time.

EV1: In Figure 4.11, above the EV2, between 5 ka to 1.5 ka the values of K and Fe elements show fluctuations around their average levels, which is indicating very localized changes. The Fe/Mn ratio generally remains above the core average, which is indicating the presence of a further higher bottom water oxygen level. Similarly, the Ca/Sr and Ca/Ti values also show peaks above the core average levels, which could suggest a warm and humid climate conditions.
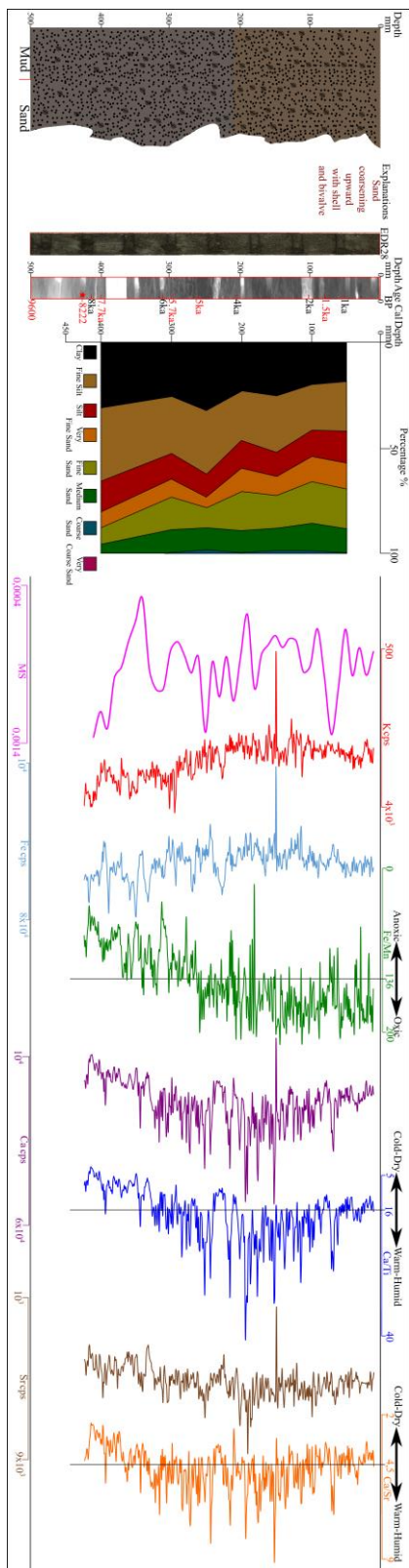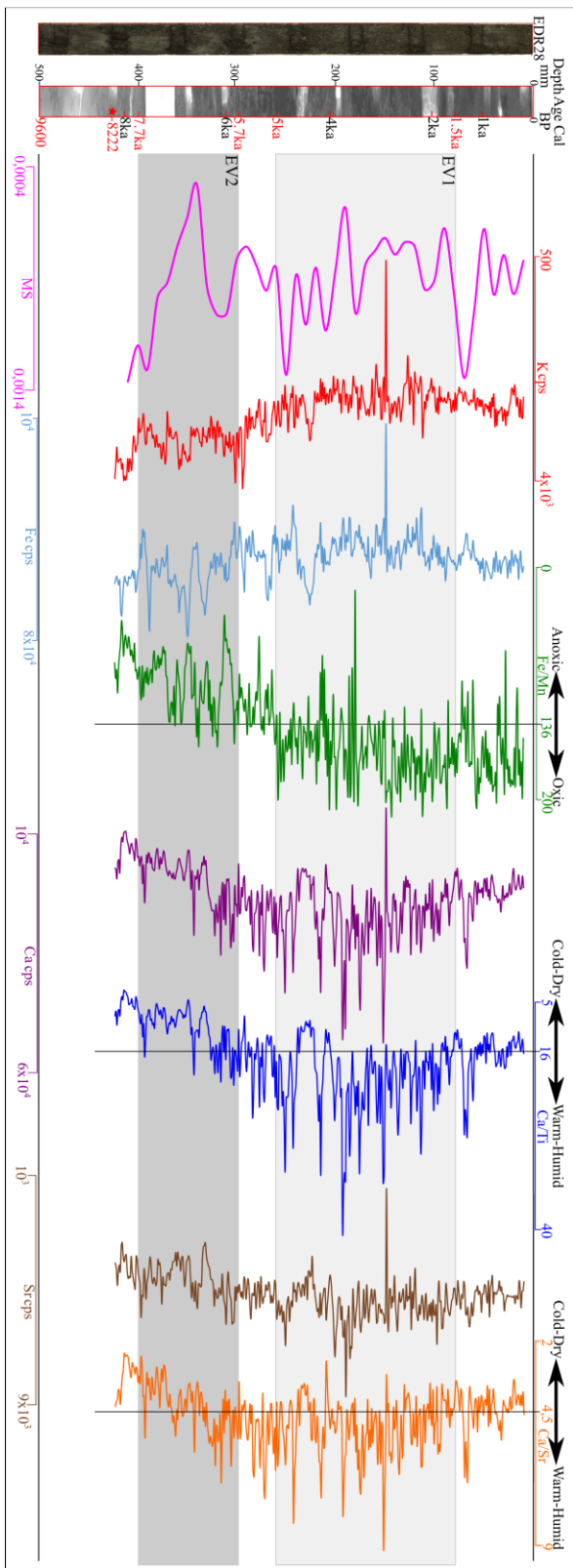
Figure 4.10 EDR28 results without events

Figure 4.11 EDR28 results with events

4.2.4 EDR30 Core Insight: A Proxy-Driven Element Perspective

In the Figure 4.12, from left to right, the color changes along the core according to the Munsell Color Chart in a lithostratigraphic column section is seen. EDR30 is one of the deepest cores in the study area and has the oldest age, approximately 15 ka BP. Color changes according to the Munsell Color Chart are observed at 35 cmbsf and 100 cmbsf from the top of the core. At the 100 cmbsf, there is a deposition of clay and silt mixture. Following this, deposits of coarser-grained materials, including sand-sized sediments, have been observed. Additionally, shell and bivalve fragments were examined after the 100 cmbsf. At the grain size change graph, from 15 cmbsf to 35 cmbsf, clay and silt-sized materials are dominant. A noticeable color change in the stratigraphic column section corresponds to this interval. Between 35 cmbsf and 50 cmbsf, silt-sized grains become slightly more dominant, as reflected in the grain size change graph. After 100 cmbsf, the grain size shifts to silt and sand, indicating a coarsening upward trend. This change is also mentioned in the lithostratigraphic section. Events in this core have been identified by examining changes in grain size and elemental composition. Event1 (EV1) is defined between 3.2 ka and 6 ka, event2 (EV2) is limited to the period between 6 ka and 10 ka, and the section from 10 ka to the bottom of the core is determined as event3 (EV3).

EV3: In Figure 4.13, the grain size shows a noticeable increase in coarse grains due to the presence of sand-sized particles. From bottom age to 12 ka, the K and Fe elements display a negative trend, followed by increasing oscillations towards the 10 ka. The Fe/Mn ratio indicates the lowest oxygen content in the environment during this period. Similarly, the Ca element increases until around 12 ka, then decreases towards 10 ka. The MS values show positive fluctuations from bottom age of the core to the 10ka, which is indicating a significant increase in detrital input. So, the Ca is probably originated from the land. The Sr element shows a rise until 13 ka. Then from 13 ka towards to 10 ka it is decreasing. Based on the Ca/Sr and Ca/Ti ratios are lower than core average values, so this period suggests sediment deposition occurred in a colder and drier environment.

EV2: In Figure 4.13, above the EV3, the grain size distribution is similar with the EV1. The trends of K and Fe elements remain around the average. In this event, there is a noticeable decrease in the amounts of Ca and Sr. The decrease in MS values suggests a reduction in terrestrial input. The Fe/Mn ratio shows a positive trend above the core average, implying that the further oxygen content is higher in this period. Although the Ca/Ti and Ca/Sr ratios have also decreased, their values remain close to the average, leading to the conclusion that the environment during this period was likely colder and drier compared to EV1.

EV1: In Figure 4.13, above the EV2, the grain size is mixture of clay and silt; the K and Fe elements show fluctuations. The Fe/Mn ratio displays average values, with a slight upward trend around 6 ka, indicating a relative increase in bottom water oxygen levels. The Ca and Sr elements exhibit peaks and a positive trend, suggesting that the environment might have been warm and humid, as indicated by the positive trends in the Ca/Ti and Ca/Sr ratios. The MS values show a negative trend from top to the bottom of the core, indicating that detrital input was higher at the top and decreased towards the bottom. The Ca and Sr elements may have a terrestrial origin.
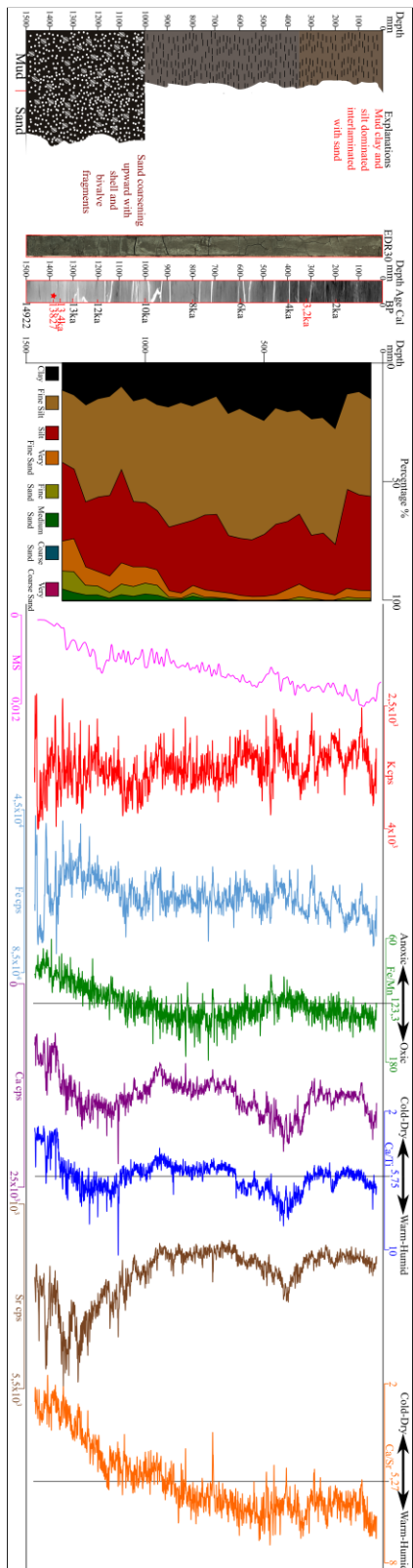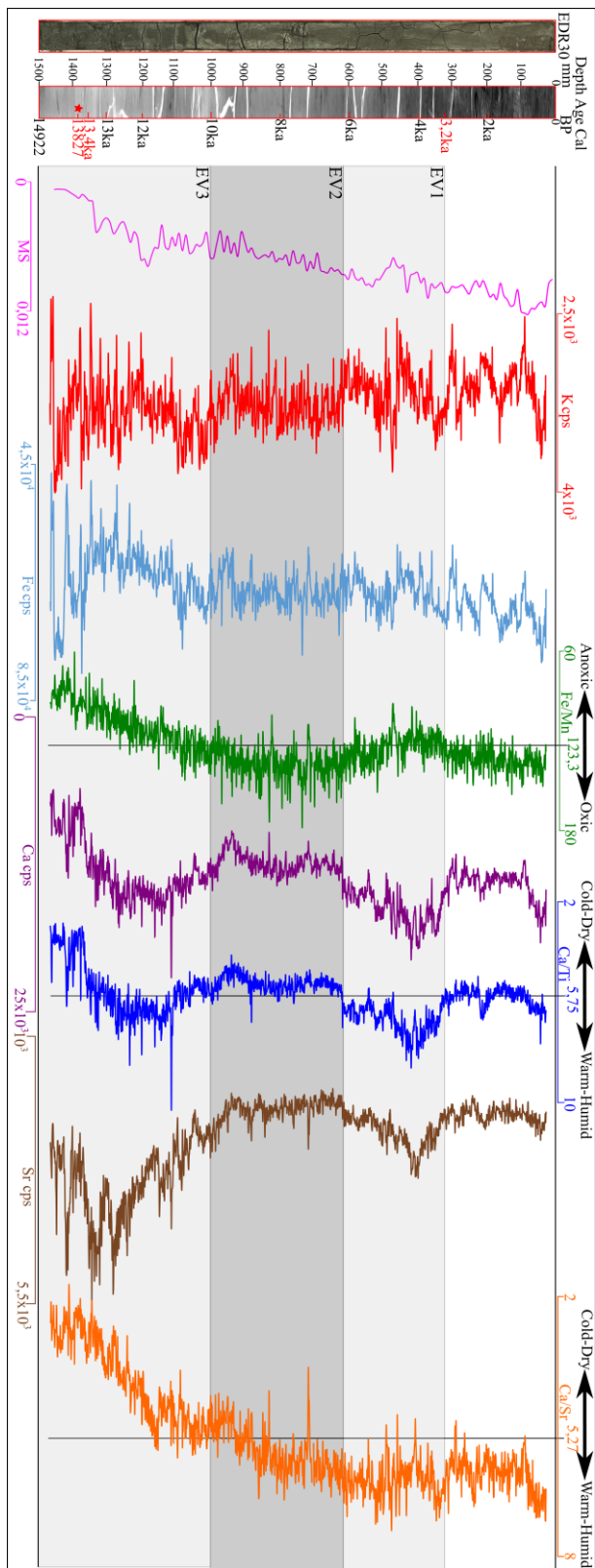
Figure 4.12 EDR30 results without events

Figure 4.13 EDR30 results with events

4.2.5 EDR51 Core Insight: A Proxy-Driven Element Perspective

In Figure 4.14, in the lithostratigraphic column section of EDR51, a homogeneous sediment deposition of mixed clay and silt is observed. Within the first 8 cm, a fossil of Echinoidea (2 cm in diameter) was found. Shell and bivalve fragments are very rarely observed in the core. This core is approximately 1,000 years, making it one of the youngest cores. The sedimentation rate is very high. In the grain size distribution graph, coarse-grained deposition is observed in the first 50 cmbsf. Overall, the grain size remains homogeneous throughout the core. However, starting from 130 cmbsf, there is a noticeable increase in the percentage of clay and fine silt-sized sediment deposition. The age of the core is relatively young, so it was challenging to distinctly separate events, if we consider the period from 0.1 ka to 0.3 ka as event1 (EV1), the interval from 0.7 ka to 0.3 ka determined as event2 (EV2) and period from 1 ka to 0.7 ka specified as event3 (EV3).

EV3: In Figure 4.15, the decrease in Fe and K elements has continued, with a negative trend becoming more pronounced from around 0.7 ka. This suggests a lower terrestrial input. Between bottom of the core 0.9 ka, the Fe/Mn ratio shows a positive trend, but lower than the core average, indicating an increase in bottom water oxygen levels in the environment. Both Ca and Sr elements display a negative trend. The Ca/Sr and Ca/Ti ratios are also trending positively below the core average, suggesting that the environment during this period was likely colder and drier until 0.9ka. The MS values show continuous fluctuations but overall exhibit a positive trend. This could imply that terrestrial input was getting higher.

EV2: In Figure 4.15, above the EV3, Fe and K show continuous fluctuations with a generally positive trend. The Fe/Mn ratio remains around the average, indicating neither a positive nor negative fluctuation. There are local peaks in Ca and Sr elements between 0.6 ka and 0.3 ka. Considering the Ca/Ti and Ca/Sr ratios, the positive trend above the core average from 0.7 ka which is suggesting that the environment was likely warm and humid during this period.

EV1: In Figure 4.15, above the EV2, between 0.3 ka and 0.1 ka K and Fe concentrations are getting higher. The MS values are fluctuated but have an increasing trend. This is suggesting that high detrital input. Ca/Sr and Ca/Ti ratios are getting lower than core average values. So, climatic condition is turning into cold and dry.
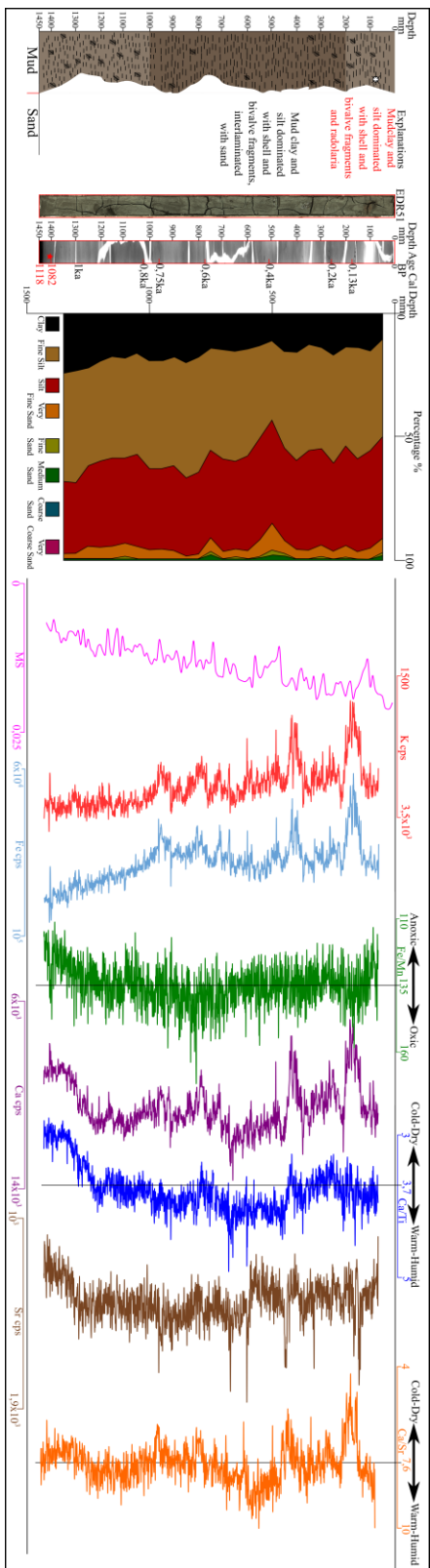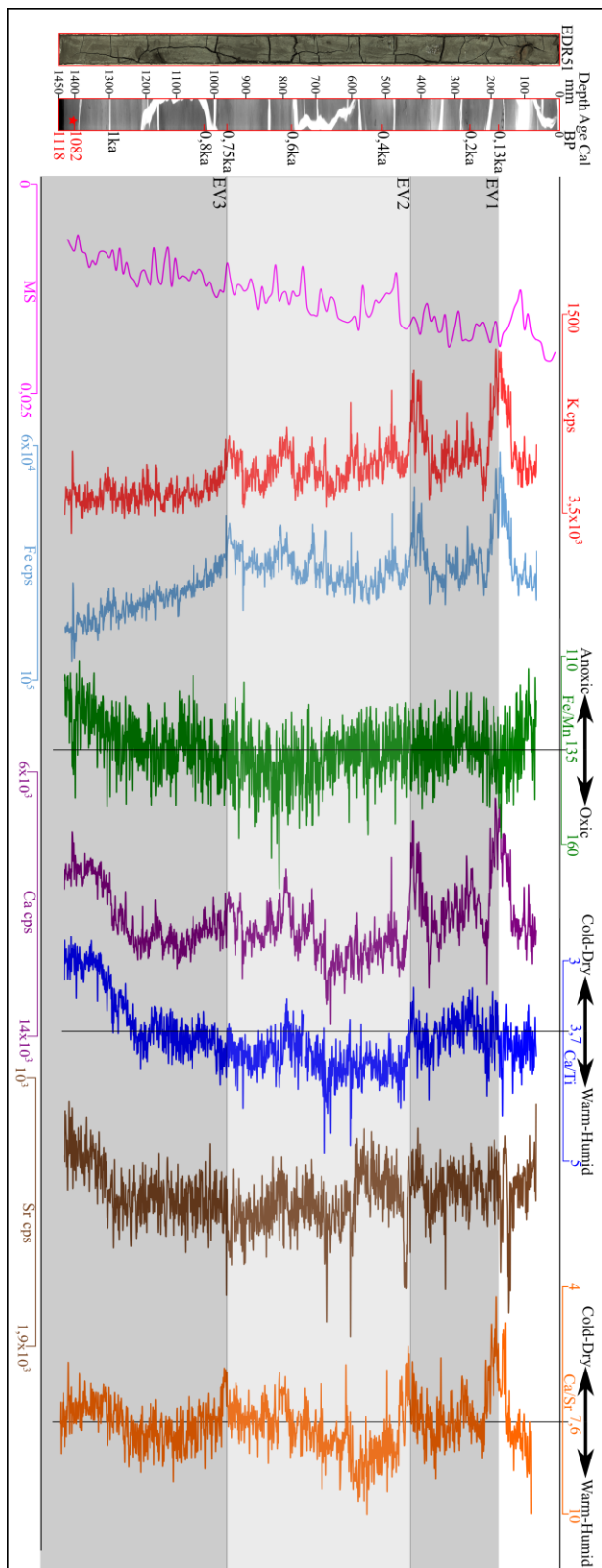
Figure 4.14 EDR51 results without events

Figure 4.15 EDR51 results with events

4.2.6   EDR23 Core Insight: A Proxy-Driven Element Perspective

In Figure 4.16, in the lithostratigraphic column section of EDR23, a homogeneous mixture of clay and silt grain sizes is observed. Starting from 100 cmbsf, a shift towards the deposition of coarser grains, closer to sand-sized particles, has been identified. According to the Munsell Color Chart, two distinct color changes are noted along the core, occurring at 40 cmbsf and 100 cmbsf. Shell and bivalve fragments are very rarely observed in the first 100 cmbsf. However, from 100 cmbsf to the bottom of the core, shell and bivalve fragments are found in much greater abundance. The grain size distribution graph shows that clay and silt-sized materials are predominant. At 100 cmbsf, where a noticeable color change occurs in the lithostratigraphic column section, there is a percentage increase in very fine sand grain size. The graph also indicates that clay and silt-sized grains are predominant, particularly from the 100 cmbsf, where the deposition of silt and fine sand grains increases. Based on these observations, and considering the changes in elemental composition, the core has been divided into events and sub-events. In Figure 4.17 events are seen, the events have been divided as follows:

I.   Event1 (EV1) from 0.67 ka to 1.62 ka
II.   Event2 (EV2) from 1.62 ka to 2.3 ka
III. Event3 (EV3) from 2.3 ka to 2.78 ka
IV.   Event4 (EV4) from 2.78 ka to 4.4 ka

The reason for subdividing these into sub-events is due to the additional analysis, such as Total Organic Carbon (TOC), $\delta 18O$, and $\delta 13C$, which were previously discussed in different sections of this core. This subdivision helps ensure that the changes in elemental composition, particularly those of climate proxy elements, are consistent with the results from these other analyses. Additionally, the results from the total organic carbon analysis provide insights into whether the sapropelic layers originated from terrestrial or marine sources, aiding in environmental interpretation. In Figure 4.17 sub-events are seen, the sub-events are as follows:

I.   Sub-event1 (SE1) spans from 1.3 ka to 1.62 ka
II.   Sub-event2 (SE2) spans from 1.62 ka to 2 ka
III. Sub-event3 (SE3) covers the period from 2.78 ka to 3.2 ka
IV.   Sub-event4 (SE4) is identified between 3.5 ka and 4.4 ka

Before explaining the changes in events and sub-events, a brief review of the graphical interpretations of TOC (Total Organic Carbon), δ18O (Oxygen-18), δ13C (Carbon-13), and the C/N ratios can be given. (Figure 4.16 and 4.17)

TOC (Total Organic Carbon):

High TOC Values: Indicate high biological productivity in the marine environment, leading to significant organic matter accumulation. This is often associated with anoxic (low-oxygen) conditions, where organic matter is better preserved due to reduced decomposition.

Low TOC Values: This may suggest lower biological productivity or indicate that the organic matter has undergone decomposition in a more oxygenated environment.

Example: In a sediment core from the seabed, high TOC values imply that the region experienced high biological productivity and/or anoxic conditions in the past (Meyers, 1994).

δ18O:

Positive δ18O Values: Typically associated with colder climate conditions and/or increased evaporation. These values can also indicate processes related to glaciation, such as ice sheet growth, where heavier oxygen isotopes (18O) are more prevalent in ocean water.

Negative δ18O Values: Suggest warmer climate conditions or the addition of freshwater to the ocean due to glacial melting, which dilutes the heavier isotopes and leads to lighter (more negative) δ18O values.

Example: In a δ18O graph, a positive trend indicates colder climate periods (e.g., Ice Ages), while a negative trend points to warmer periods (e.g., the Holocene thermal maximum) (Shackleton, 1982).

δ13C:

Positive δ13C Values: Indicate high marine biological productivity and/or the presence of organic matter derived more from marine sources rather than terrestrial plants. This is often associated with periods of high marine productivity.

Negative δ13C Values: Suggest a greater contribution of terrestrial organic matter or lower biological productivity in the marine environment.

Example: If a positive trend in δ13C values is observed in a core, it points to periods of high marine biological productivity. In contrast, a negative trend indicates periods where terrestrial organic matter contribution increased or marine productivity decreased (Deines, 1980).

C/N Ratio:

High C/N Ratio: Typically indicates that organic matter in the marine sediment is primarily derived from terrestrial sources. This is because terrestrial plant tissues contain high levels of lignin and cellulose, leading to a higher C/N ratio.

Low C/N Ratio: Suggests a greater contribution of marine organic matter, as marine phytoplankton and other marine organisms generally have lower C/N ratios.

Example: If the C/N ratio in a core is high, it suggests that terrestrial organic matter dominates the sediment. Conversely, a low C/N ratio indicates that marine organic matter is more prevalent (Meyers and Teranes, 2001).

EV4**:** In Figure 4.17, the Fe and K elements concentrations are decreasing between 4.4 ka and 3.5 ka. On the other hand, between 3.5 ka and 2.78 ka these concentrations are increasing. Similarly, the Fe/Mn ratio decrease between 4.4 ka and 3.5 ka and increase between 3.5 ka and 2.78 ka intervals. But the ratio is always lower than the core average value, pointing to that further bottom water oxygen level lower respect to other periods. The Ca and Sr ratios follow a pattern similar to the changes in Fe and K elements. This similarity suggests, as in other events, that the origins of Ca and Sr are terrestrial. When examining the Ca/Ti and Ca/Sr ratios, the Ca/Ti ratio

generally remains above core average. The Ca/Sr ratio shows fluctuation of positive and negative trends, at some levels falling below the average. These observations suggest that this period was relatively warm and rainy. To identify the detailed local variations within this event, the period will be further divided into two sub-events, subevent3 (SE3) and subevent4 (SE4). These sub-events will provide a more detailed explanation of the local changes.

SE4: In Figure 4.17, SE4 is located in the EV4. Between 4.4 ka and 3.5 ka, Fe and K elements show a decreasing trend, but there is an abrupt increase at around 4ka. Following this increase, their concentrations decrease again until the end of the event at approximately 3.5ka. MS (magnetic susceptibility) values have periodic local fluctuations during this time. So, the detrital input is also fluctuated with the change MS values, Fe and K elements concentrations. From 4 ka to 3.5 ka, there is a significant increase in grain size, indicating coarser sediment deposition. The Fe/Mn ratio generally remains below the core average, suggesting a lower bottom water oxygen levels in the environment, although bottom water oxygen levels gradually decrease toward the end of the event around 3.5 ka. The Ca/Ti and Ca/Sr ratios consistently trace above the average, indicating a relatively warm and humid environment during this period. When examining TOC and C/N ratios, there are layers where TOC exceeds 0.7%, indicating significant organic matter accumulation. Around 4.1 ka, however, the amount of organic matter drops below 0.7%, and the C/N ratio shows a negative trend, indicating a reduction in terrestrial contribution to organic matter accumulation during that time. In contrast, during periods when the C/N ratio trends positively, the organic-rich layers suggest that the source of the organic matter was predominantly terrestrial. From 4.4 ka to 4 ka, as organic matter increases in the environment, the proportion of clay and silt-sized grains also rises, indicating finer sediment deposition likely associated with increased organic input. These observations suggest a complex interplay of climatic conditions during this period, with fluctuations in terrestrial input and organic matter accumulation driven by changes in both temperature and precipitation. The coarsening of grain size at the

end of the period, followed by finer sediment deposition, reflects these environmental dynamics.

SE3: In Figure 4.17, SE3 is located in the EV4. The Fe and K elements have a positive trend, there is an abrupt change around 2.8 ka. The MS values are decreasing, suggesting that terrestrial input was likely very limited during this period. The $\delta18O$ ratio is generally negative, but shows a decreasing trend up to around 2.9 ka, indicating relatively warmer climate conditions. The TOC level spikes above 0.7%, which indicates that significant organic matter accumulation. The $\delta13C$ ratio is fluctuated first decreased which means biological productivity is decreased. Then, from 3.1 ka and 2.78 ka $\delta13C$ has an increase trend. So, the effect of the biological productivity is decreased. The Fe/Mn ratio is below the core average, indicating low bottom water oxygen levels in the environment, which is a crucial factor for the preservation of organic matter. Between 3.2 ka and 3 ka, the $\delta18O$ and $\delta13C$ ratios decrease, suggesting a reduction in marine productivity, increased terrestrial origin, and a warmer, wetter climate. This is also reflected in a decrease in TOC levels, as warmer conditions likely increased decomposition rates. During this period, the C/N ratio shows a positive trend, indicating that the deposited organic matter has terrestrial origin. From 3 ka to 2.78 ka, the conditions reverse, with the opposite trends observed in the $\delta18O$ and $\delta13C$ ratios, indicating a period of cooler, possibly drier conditions, with reduced terrestrial influence and increased marine productivity. These alternating local cycles are a characteristic feature of this period.

EV3: In Figure 4.17, above EV4, when examining the concentrations of Fe and K elements, a decreasing trend is observed. The MS values show spikes in layers, which indicates terrestrial input is getting lower. The Fe/Mn ratio suggests a relative increase in the oxidation state of the environment. The TOC value is decreasing. These trends illustrate the relationship between the increase in oxygen levels and the less accumulation of organic matter. The Ca/Ti ratio traces below the core average, the decrease in the Ca/Sr ratio points to colder and drier period. This suggests that terrestrial input is getting lower in both terrestrial elements and organic material.

EV2: In Figure 4.17, above EV3, between 2.3 ka and 1.8 ka, the concentrations of K and Fe elements show an increasing trend, followed by a decreasing trend up to 1.62 ka. The grain size distribution graph also shows an increase in grain size. The MS values fluctuated but general trend is increasing in this interval. The increase in grain size between 1.62 ka and 1.8 ka suggests a period of higher terrestrial input. The Ca and Sr elements exhibit trends similar to those of Fe and K. This similarity suggests that Ca and Sr may have a terrestrial origin. The Ca/Ti and Ca/Sr ratios are above core average and show an increasing trend between 2.3 ka and 1.62 ka, indicating a relatively warm and rainy climate during this period. The Fe/Mn ratio is generally above the average, indicating a period with relatively high bottom water oxygen levels in the environment.

SE2: In Figure 4.17, SE2 is located in EV2. In this section, TOC, C/N, δ18O, and δ13C ratios are examined. Although the organic carbon percentage is around 0.7%, it is not identified as a sapropelic layer since it remains below 0.7%. However, it can still be considered a layer with a relatively high organic matter concentration. The C/N ratio has decreased in this section, indicating that the contribution of marine organic matter is higher compared to other organic rich layers. Both δ18O and δ13C ratios show negative values, which may indicate warmer climate conditions or the addition of freshwater to the seawater due to glacial melting. This also suggests a greater contribution of terrestrial organic matter or lower biological productivity. Despite the negative values, if the δ18O ratio shows an increasing trend, it could indicate a colder period compared to previous intervals. Between 2 ka and 1.62 ka, the δ18O ratio increases, suggesting that the climate condition around 2ka is warmer compared to 1.62 ka. The δ13C ratio shows a more pronounced increase between 2 ka and 1.62 ka. This suggests that biological productivity and the accumulation of marine-derived organic matter were relatively higher around 1.62 ka compared to 2 ka. The decrease in the C/N ratio supports this hypothesis, indicating that the organic matter deposited in this interval is likely of marine origin.

EV1: In Figure 4.17, above the EV2, when examining the K and Fe elements, their concentrations are at their lowest around the 0.67 ka level, from 1.3 ka a decreasing

trend up to 0.67 ka. From 1.62 ka increasing trend is observed. Correspondingly, the MS (magnetic susceptibility) values increase as the concentrations of K and Fe rise, and decrease when K and Fe transition to a declining trend. This pattern suggests that terrestrial input was relatively high up to around 1.3 ka but then decreased. The Fe/Mn ratio tracing generally above the core average, indicating that the bottom water oxygen levels in this environment are relatively high. However, there are intervals where the Fe/Mn ratio falls below the core average, indicating periods with further lower oxygen conditions in the environment. The Ca and Sr elements show a trend similar to that of Fe and K. Their concentrations increase until around 1.3 ka, then decrease between 1.3 ka and 0.67 ka, suggesting that Ca and Sr might also have a terrestrial origin. When looking at the Ca/Ti and Ca/Sr ratios, a distinct negative trend below the core average is evident in the Ca/Ti ratio, while the Ca/Sr ratio does not show such a clear trend. In fact, between 1.62 ka and 1.3 ka, the Ca/Sr ratio exhibits a positive trend above the core average, indicating that, although the period was generally expected to be colder and drier compared to other events, there were fluctuations with intermittent warmer and rainy periods. Due to the highly variable nature of the elemental concentrations and their ratios in this core, sub-event1 (SE1) has been separated from event1 (EV1) to account for these fluctuations.

SE1: In Figure 4.17, SE1 is located within the EV1. At this level, where TOC and C/N ratios are present, the TOC level exceeds 0.7%, indicating the presence of a sapropelic layer. Sapropels, which are rich in organic matter, typically form more easily in anoxic environments with low oxygen levels, particularly in marine settings. In such conditions, the decomposition of organic matter by microorganisms is slower, allowing for better preservation. Between 1.3 ka and 1.4 ka, the Fe/Mn ratio falls below the core average, indicating a decrease in bottom water oxygen levels in the environment. This coincides with the deposition of the sapropelic layer, which is rich in organic matter, further validating the interpretation of reduced bottom water oxygen levels based on the Fe/Mn ratio. The C/N ratio shows a positive spike, suggesting that the organic-rich layer has a terrestrial origin. This spike supports the conclusion that the period was rainy and that the organic matter was

transported from terrestrial sources. Additionally, the Ca/Sr ratio during this period is above core average, which already suggested a relatively warm and rainy environment. This observation confirms the earlier interpretations.
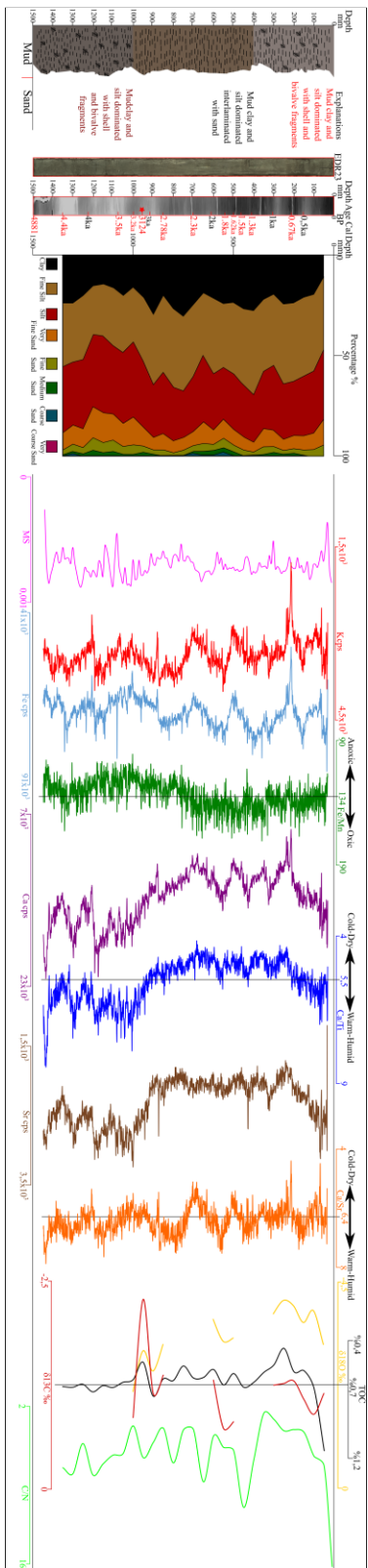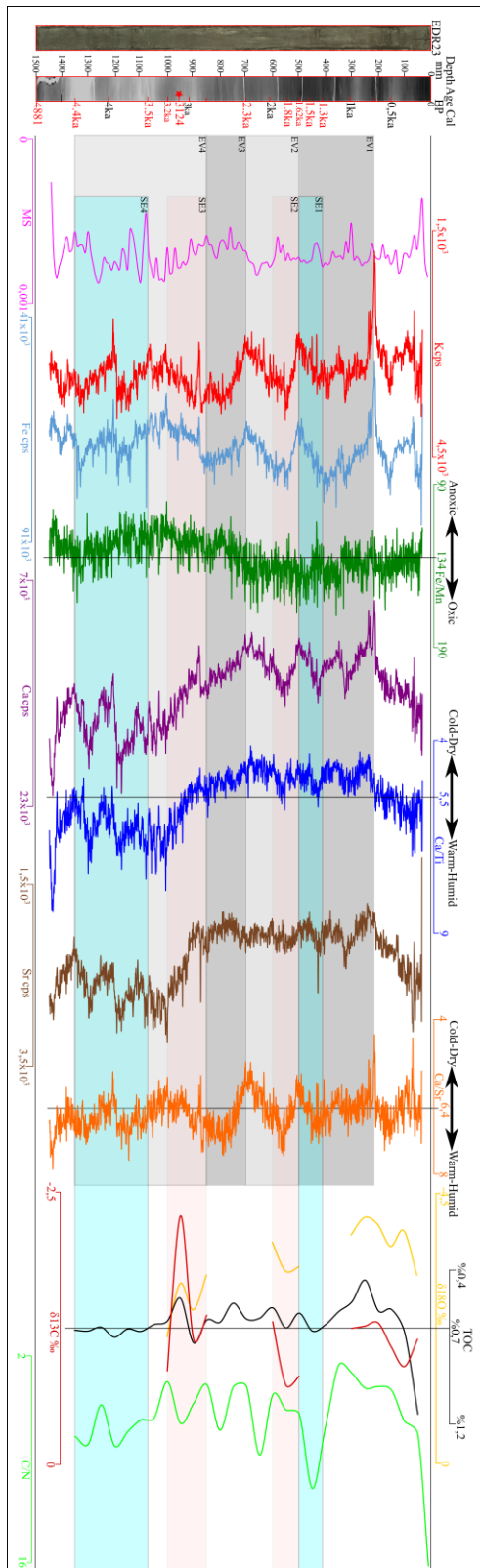
Figure 4.16 EDR51 results without events

103

Figure 4.17 EDR51 results with events

4.2.7   EDR47 Core Insight: A Proxy-Driven Element Perspective

In Figure 4.18, the results of EDR47 lithostratigraphic column section which is drawn according to the Munsell Color Chart, three distinct levels of color change are observed. From the top of the core to a depth of 65 cmbsf, a homogeneous mixture of clay and silt is present. At the 40 cmbsf and 50 cmbsf levels, bands shaped dark material were interpreted, which are organic rich materials. Following this, from 65 cmbsf to 90 cmbsf, the homogeneous clay-silt mixture continues with a color change noticeable up to around 90 cmbsf. From 90 cmbsf, coarser, sand-sized material is deposited. Below 105 cmbsf, down to the bottom of the core, another color change is interpreted a different level. In this section, the grain size consists of a mixture of clay and silt, with sparsely deposited sand-sized grains. Starting from the 90 cmbsf level, bivalve and shell fragments are observed in significant quantities. Additionally, wood fragments are intermittently found throughout the core. EDR-47, which has 15 ka old, is considered one of the cores that best represents the study area. Based on the information provided and considering the elemental changes, the core has been divided into three distinct events which is seen in Figure 4.19. These are;

  I.   Event1 (EV1) spans from the top of the core to approximately 5.3ka.
 II.   Event2 (EV2) covers the period between 5.3ka and 9.8ka.
III.   Event3 (EV3) extends from 9.8ka to the bottom of the core.

Sub-events have also been identified within these events which are seen in Figure 4.19 and these sub-events are following:

  I.   Sub-event1 (SE1) is located within Event1, between 0.5ka and 2.9ka.
 II.   Sub-event2 (SE2) is within Event2, between 5.3 ka and 6.4 ka.
III.   Sub-event3 (SE3) falls within Event3, spanning from 9.8 ka to 12.5 ka.
IV.   Sub-event4 (SE4) is also part of Event3, covering the period from 12.5 ka to 13.2 ka.

These divisions allow for a more detailed analysis of the sedimentary and environmental changes that occurred throughout the deposition of this core.

EV3: In Figure 4.19, EDR47 results are given, when analyzing the concentration graphs for Fe and K elements, there is a noticeable increasing trend until around 11 ka, after which there is a significant decrease. Around 11 ka and thereafter, the MS (magnetic susceptibility) values show a highest peak. However, from 14 ka to 11 ka an increasing trend of MS values is seen. The terrestrial input is very limited at 14ka. But it is getting higher up to 11 ka levels. The grain size distribution graph reveals that between 12.5 ka and 9.8 ka, coarser-grained material was deposited. The Fe/Mn ratio shows an increasing trend, remaining below the core average, with a noticeable drop starting from 9.8ka. This suggests that bottom water oxygen levels are relatively low in the environment during this period. The concentrations of Ca and Sr elements increase around 12ka. When examining the Ca/Ti and Ca/Sr ratios, the Ca/Ti ratio is above core average until around 12 ka, before which it falls below average. This indicates that the climate is relatively cold and dry up to 12 ka, but transitioned to more warm and humid conditions afterward. The Ca/Sr ratio generally traces around core average values, suggesting that while some climate variability occurred, the changes were less extreme compared to the Ca/Ti ratio. In summary, during the period from 12.5 ka to 11 ka, there is high terrestrial input, as indicated by the increase in Fe and K concentrations, coarse-grained sediment deposition, and positive MS peaks. Bottom water oxygen level is low, as shown by the below the core average value Fe/Mn ratio, while Ca and Sr concentrations are increasing up to 9.8 ka. The transition from cold to warm climate conditions around 12 ka is reflected in the changes in the Ca/Ti ratio.

SE4: In Figure 4.19, SE4 is located in the EV3. In this section, the TOC values have increased beyond 0.7%, indicating the presence of a sapropelic layer. Both $\delta18O$ and $\delta13C$ values are seen to be decreasing. However, given that $\delta13C$ values were positive in sub-event3, where an organic-rich deposit was also observed, it suggests that the organic-rich material in this sub-event is likely of marine origin as well. The C/N ratio is quite low, further indicating a significant contribution of marine organic matter. Additionally, MS values during this period have increased, it is nearly zero, which suggests a very limited terrestrial input. The Fe/Mn ratio is also well below

the core average, indicating lower bottom water oxygen levels, possibly pointing to an anoxic condition of environment conducive to the preservation of organic material. When all these evidences are considered together, it can be inferred that the organic-rich sapropelic layer deposited between approximately 13.1 ka and 12.5 ka is most likely a result of marine activity. This result might be ancient organic rich layer finding in Aegean Sea.

SE3: In Figure 4.19, SE3 is located in the EV3. To begin with, the TOC (Total Organic Carbon) values show a decrease between 12.5 ka and 11 ka, followed by an increase from 11 ka to 9.8 ka. The C/N ratio is generally low but show oscillations in layers. At around 11 ka, the C/N ratio shows a positive spike, indicating the transport of terrestrial organic matter; however, the overall amount of organic matter is quite low. As the amount of organic matter begins to increase before 11 ka, a negative spike is observed in the C/N ratio. By 12.5 ka, when organic matter is at its peak during this event, the C/N ratio decreases further, suggesting that the organic matter deposited at this time is likely of marine origin. When examining the δ18O and δ13C values, δ18O continues to show positive trends, indicating colder climate conditions. Interestingly, δ13C values show positive readings for the first time in this section, which suggests a localized period of high marine biological productivity and/or the accumulation of marine-derived organic matter, as opposed to terrestrial sources. Over time, the δ13C values show an increasing trend, but the fact that they are positive for the first time in this section, combined with the low presence of organic matter, strongly suggests that the low organic matter deposited in this layer is marine origin.

EV2: In Figure 4.19, above EV3, between 6.4 ka and 5.3 ka, the concentrations of Fe and K elements show an increasing trend, while between 9.8 ka and 6.4 ka, the trend decreases. When looking at MS values, there is a decreasing trend up to around 9 ka, followed by an increase between 9 ka and 5.3 ka. The MS values also display positive spikes in layers, which can be interpreted as periods of increased terrestrial input. The grain size analysis around 9 ka indicates the deposition of coarse-grained material. The concentration graphs for Ca and Sr elements show an abrupt increase

between 6.4 ka and 5.3 ka. However, from 9.8 ka to 6.4 ka, the concentrations of these elements increase. When examining the Ca/Ti and Ca/Sr ratios, a positive trend above the core average is observed between 9.8 ka and 5.3 ka. It is suggesting a relatively warm and humid climate during this time. The Fe/Mn ratio shows a positive trend between 9.8 ka and 5.3 ka, with values generally above core average, indicating that an increase in the oxidation state of the environment during that period. These observations suggest that from 6.4 ka to 5.3 ka, there was an initial decline in terrestrial input, followed by an increase, as reflected in the elemental and MS data. The relatively warm and humid climate likely contributed to the increased transport of terrestrial materials, particularly during periods where the MS spikes are observed, indicating higher sedimentation rates of coarse material. The sufficient bottom water oxygen levels in the environment indicated by the Fe/Mn ratio would have supported organic matter preservation during this time.

SE2: In Figure 4.19, SE2 is located within the EV2. During the period between 6.4 ka and 5.3 ka, as mentioned previously, the concentrations of Ca and Sr elements are notably high, indicating relatively warm and humid climate conditions. The TOC values show that a sediment package with more than 0.7% organic matter is present. This corresponds closely with the band shaped dark layers observed in the lithostratigraphic column, which are thought to be rich in organic material. When examining the δ18O and δ13C values, δ18O shows negative values, and δ13C is close to zero but still negative. These values suggest that the climate was warm, with the addition of freshwater from melting glaciers mixing with seawater, and that biological productivity is low. Furthermore, since the values increase further between 6.4 ka and 5.3 ka, it indicates a decrease in temperature and a further incline in biological productivity during this time. The C/N ratio show a very high positive spike, which strongly suggests that the organic matter in this sediment package is transported and deposited from terrestrial sources. Consequently, it is reasonable to infer that the Ca and Sr elements were also transported from land. This combination of data supports the conclusion that during this time, warmer and more humid conditions prevailed, leading to increased terrestrial input, including organic matter

and elements such as Ca and Sr, into the marine environment. The presence of freshwater from glacial melting and the low biological productivity further characterizes the environmental conditions during this period.

EV1: In Figure 4.19, above the EV2, when examining the concentrations of Fe and K elements, a decreasing trend is observed. The MS values show an increasing trend from the 5.2 ka. The Fe/Mn ratio graph generally remains above average but traces a positive trend. This suggests that while the bottom water oxygen level is relatively high during sediment deposition at the top of the core, they gradually increased towards around 0.5 ka. The concentrations of Ca and Sr display both positive and negative spikes, indicating fluctuations, but the overall trend is positive. When looking at the Ca/Ti and Ca/Sr ratios, the graph traces around the core average values, but with more frequent occurrences below the core average, suggesting that the climate was relatively cold and dry during this period. These trends suggest a shift from less bottom water oxygen in the environment conditions to more from 5.2 ka to 0.5 ka level.

SE1: In Figure 4.19, SE1 is located within EV1. The TOC ratio is increased from 2.9 ka to 0.5 ka level of the core. The organic matter accumulation in the top section is thought to be directly related to anthropogenic pollution. Between 2.9 ka and 0.5 ka the $\delta 18O$ and $\delta 13C$ ratios are negative, indicating a warm climate or the presence of freshwater input due to glacial melting, along with low biological productivity. Although the general trend is negative, indicating warmer conditions and lower productivity, minor fluctuations allow for some interpretation of relatively colder periods or periods of increased biological productivity. Up to around 2.5 ka, $\delta 18O$ and $\delta 13C$ show a decreasing trend, suggesting that climate conditions were relatively warm and biological productivity was lower. However, between 2.5 ka and 2.9 ka, an increasing trend in these ratios is observed, indicating a decrease in temperature and an increase in biological productivity. Between 2.9 ka and 2.5 ka $\delta 18O$ and $\delta 13C$ show decreasing trend suggesting the climate condition is relatively warm and marine productivity is low. Then from 2.5 ka to 0.5 ka $\delta 18O$ and $\delta 13C$ show increasing trend. So, the climate condition is relatively cold and marine productivity

is getting higher. During this period, the amount of organic matter increases. The combination of rising temperatures and increased biological productivity created favorable conditions for the accumulation of organic matter. Additionally, the decreasing C/N ratio during this time suggests a reduction in terrestrial sediment input, further supporting the idea of reduced terrestrial influence on the sedimentation process
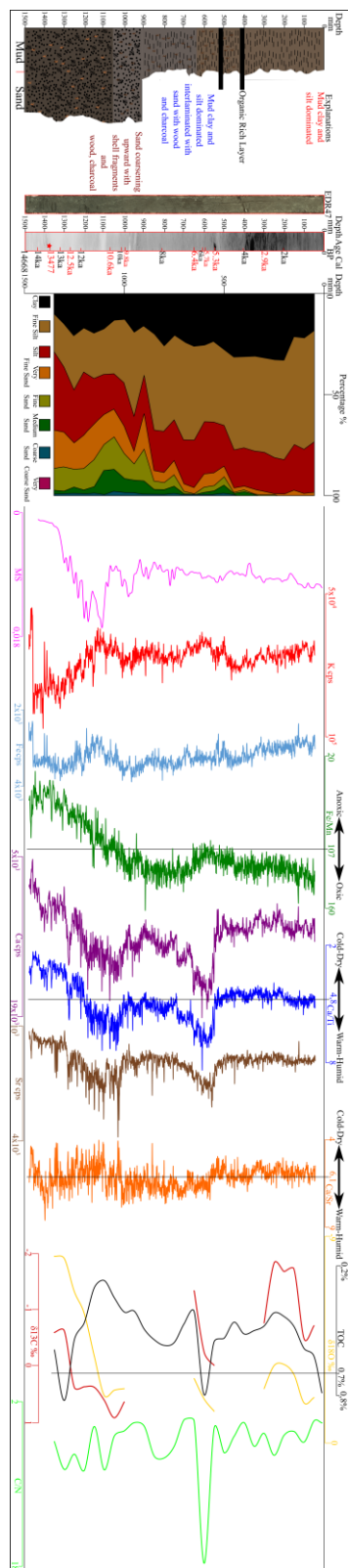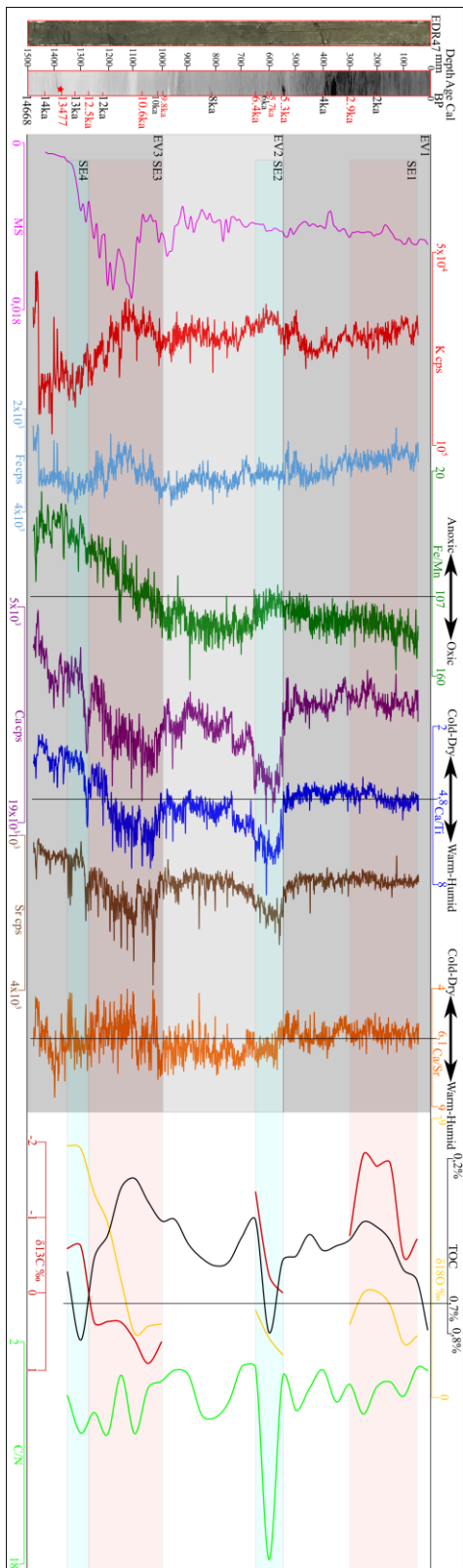
Figure 4.18 EDR47 results without events

111

Figure 4.19 EDR47 results with events

4.3 Granular Insights: Tracking Depositional Shifts Over Time

4.3.1 Core Narratives: Grain Size as a Record of Environmental Shifts

First, in order to observe the grain size variations in some of the cores within the study area, samples were taken every 5 cm, and the grain size variation results were obtained. The locations of these cores are marked in the Figure 4.20. Subsequently, the cores with similar grain size variations were selected and grouped together. Based on the results, depositional patterns were then interpreted in this section.
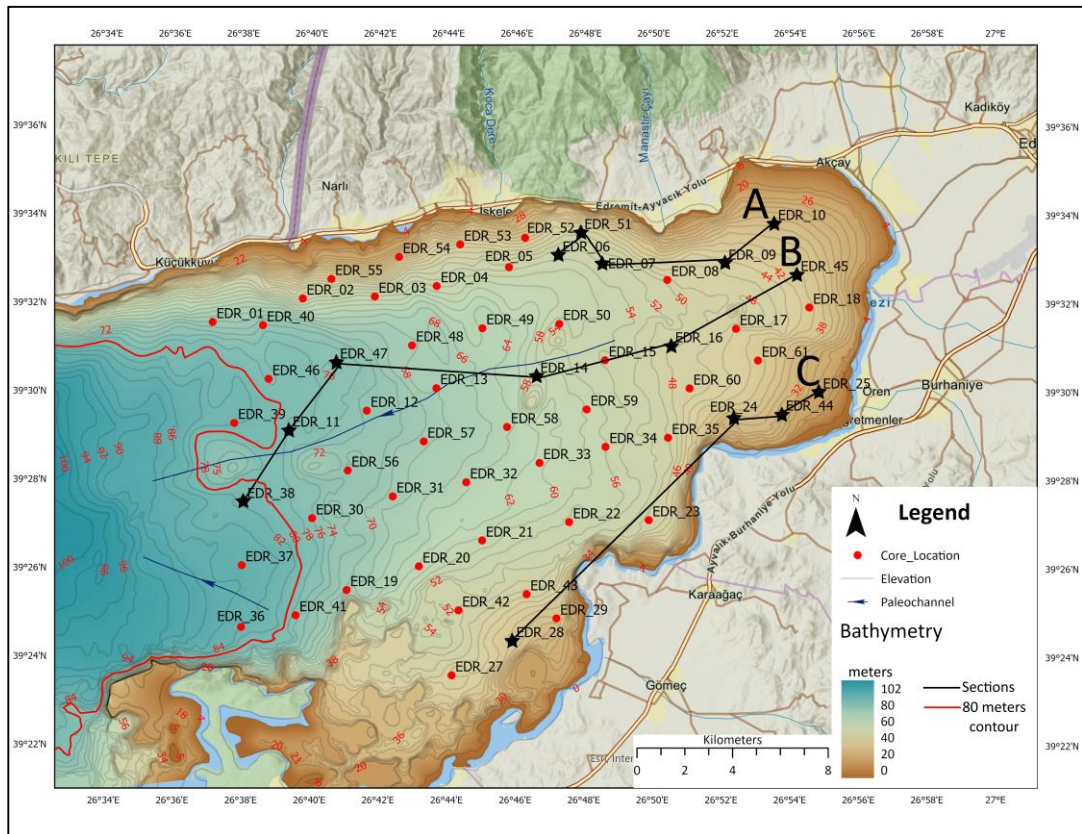

Figure 4.20 Grain size change within core samples section's locations

Table 4.5 Sections and included core samples

Section Name	Section A	Section B	Section C
Core Number	EDR06	EDR11	EDR24
	EDR07	EDR14	EDR25
	EDR09	EDR16	EDR28
	EDR10	EDR45	EDR44
	EDR51	EDR47	
		EDR38	

In the Table 4.5, the cores from the sections are listed, and the core numbers highlighted in red are those with radiocarbon age dating.

Before presenting the results, it is important to note that Yaltırak (2003) and Duman et al. (2018) mentioned that between 10,000 and 16,000 years ago, the sea level was 60 to 90 meters below the current sea level, and that the sea level rise has continued from the Holocene to the present. Accordingly, it is predicted that transgression began with the sea level rise, and transgressive deposits covered the basin from the sea towards the land.

4.3.1.1   The Texture of Section-A: Grain Size Variability Unveiled

In Figure 4.21, when examining the grain size variation graphs for the cores numbered EDR06, EDR51, EDR07, EDR09, and EDR10, it is noticeable that the grain size is predominantly composed of clay, very fine silt, and silt. At certain levels, an increase in the concentration of coarse sand-sized material has been observed.

Moving from west to east in Figure 4.20, especially in the core number EDR10, it is found that very fine sand and fine sand sized materials concentration is increased. The drainage concentration at the northern sight of the study area is higher than southern sight. It is expected that significant amount of material is transported from

north. There is a significant issue related with the seabed morphology. Seabed is very steep respect to other parts of the study area. So, the low accumulation of sand-sized material in the northern part of the study area may be due to the inability of such coarse material to settle in this region because of the steep slope. In marine environment, landslides are frequently observed in such fault-controlled basins, especially due to earthquakes. In Yaltırak (2003) fault interpretations, numerous shallow seated normal faults have been observed in the northern part of the gulf. For this reason, when looking at past earthquakes, the epicenters are mostly concentrated in the northern part. Consequently, due to the steep slope of the northern part of study area morphology, the formation of submarine landslides makes it difficult for coarse sand-sized material to settle. Additionally, when examining EDR10 location the slope of the seabed is getting gentle. As a consequence, the deposition of sand-sized material concentration is increased.

In conclusion, it is believed that the relationship between sediment transport and deposition in the northern part of the study area is primarily influenced by tectonic activity and morphology.
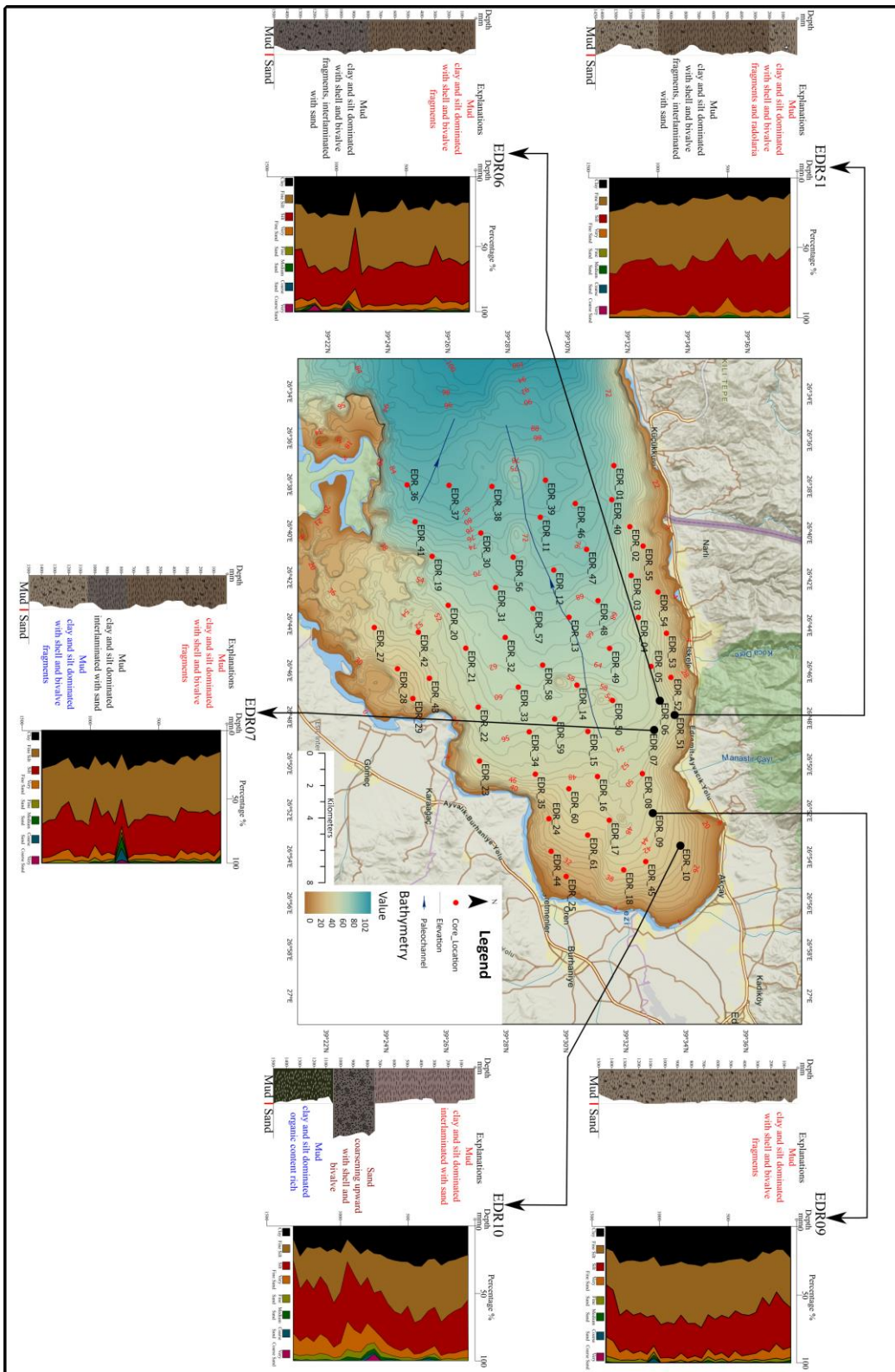
Figure 4.21 Section-A grain size change within core samples

4.3.1.2   The Texture of Section-B: Grain Size Variability Unveiled

Section B consist of another group of cores with similar characteristics of the grain size variation graphs for cores EDR38, EDR11, EDR47, EDR14, EDR16, and EDR45 are seen in Figure 4.22. As mentioned before in Yaltırak (2003) and Duman et.al. (2018), the shoreline was located between 60 and 90 meters below current levels between 16,000 and 10,000 years ago. Therefore, cores EDR11 and EDR47 were either near the shoreline or submerged underwater during that period. Additionally, the location of Section B is very close to the paleochannel that Yaltırak (2003) observed and interpreted in the seismic sections of GoE. As a result, coarse-grained materials are clearly visible in the bottom section of the core. Considering that radiocarbon dating has been performed on core EDR47, and the bottom part dates back to approximately 15,000 years ago, it is likely that the sea level was much lower when the coarse sand material was deposited. The transported material could consist of coarse-grained sediments carried by the high-energy flow of the river basin at that time. When move upward to the EDR47 core sample, 90 cm below the top of the core, where the grain size begins to decrease, corresponds to around 9,000 years ago. This period coincides with the sea level rise and transgression has already started. A similar pattern is observed in core EDR11, where it begins with coarse grains, and then, starting from around 70 cmbsf below the top of the core, there is an increase in clay and silt-sized material. As the sea level rose, it began to flood the river basin, with the help of transgression, sweeping coarse material towards to landside. For this reason, coarse sandy material is observed predominantly at the top of the cores numbered EDR14, EDR16 and EDR45. This group of cores actually follows the path of a paleochannel. In areas where rivers flow into the sea, such as in submarine deltas, it is normal to observe finer-grained material in the distal parts and coarser-grained material in the proximal parts due to the decrease in energy. Through these cores, we can clearly observe the paleochannel and the transgression event mentioned by Yaltırak (2003) as reflected in the grain size variations. EDR38 is located in the region between two paleochannels. The deposition pattern of EDR38

shows different grain size variations compared to other cores within the channel. Sharp increases in grain size can be observed across different layers. In channel structures, levees are formed when the channel's discharge increases, leading to the accumulation of relatively coarse materials along the channel edges. Although EDR38 may not be located directly within the channel, its deposition pattern suggests the accumulation of coarse grains in the levee area.
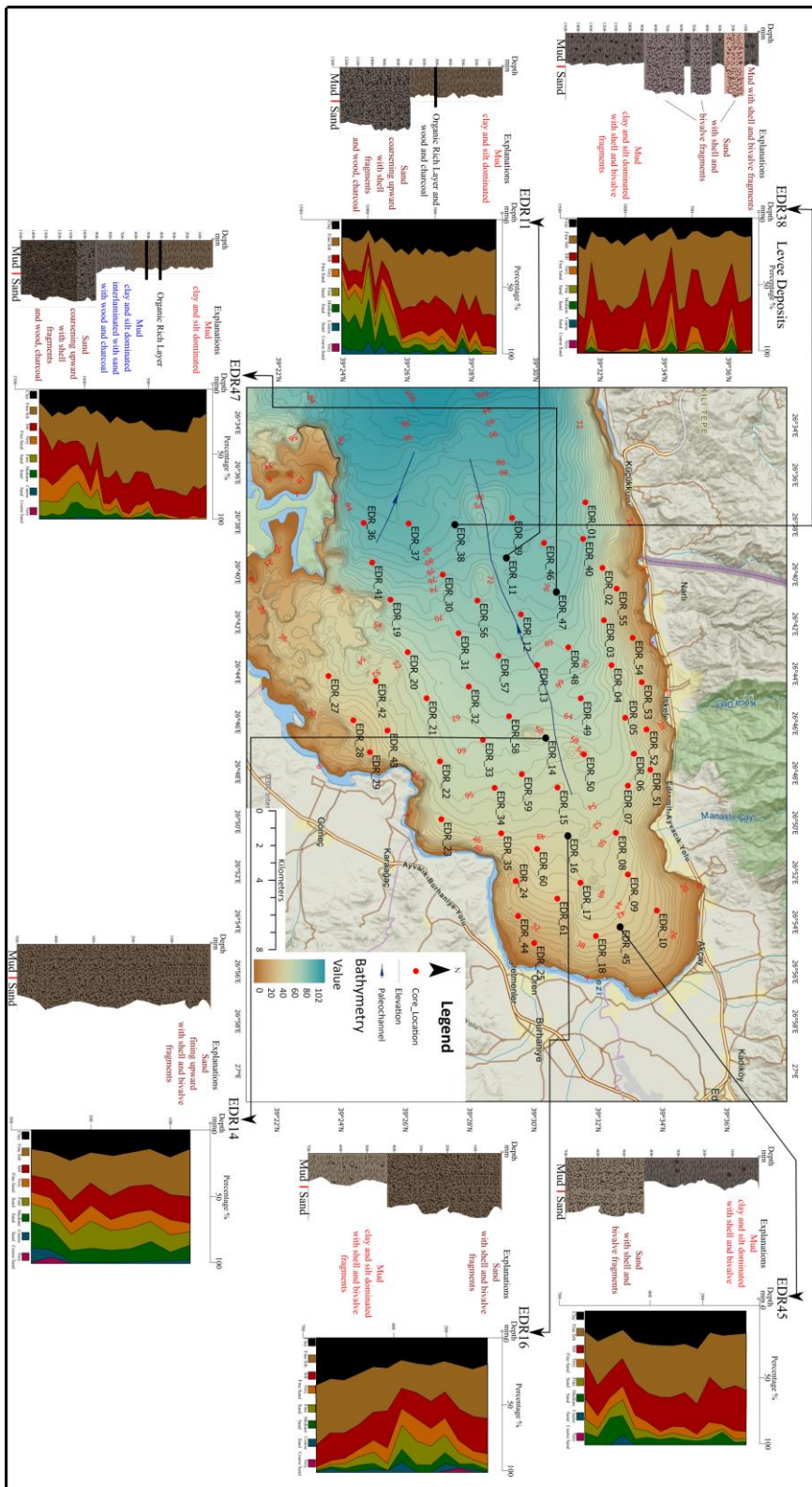
Figure 4.22 Section-B grain size change within core samples

119

4.3.1.3   The Texture of Section-C: Grain Size Variability Unveiled

Section C consist of core numbers EDR25, EDR44, EDR24, and EDR28 which is seen in Figure 4.20. In Figure 4.23 when examining these cores, it is noticeable that they are relatively short. As a result, the grain size variations show coarser sand-sized material being more dominant throughout the cores, which is quite normal. Considering their proximity to the shore and changes in sea level, the short length and coarse grain size are consistent with the patterns observed in previous cores. Especially in section B closer to the land, such as EDR16 and EDR45. The same depositional pattern seen in these cores can be attributed to the same mechanism mentioned in the previous core group, where the transgressive unit, driven by rising sea levels, transported coarse material from the sea toward the land.

In conclusion, the grain size variations in the cores from the northern slope of the study area differ significantly from those in the cores on the southern slope. The results suggest that on the northern part, the depositional pattern is primarily influenced by the slope of the seabed and tectonic control. In contrast, on the southern part, the depositional pattern is more influenced by sea level changes driven by climatic factors. For the cores located in between—those associated with the paleochannel system and its surroundings—a depositional pattern influenced by both tectonic activity and sea level changes is observed.
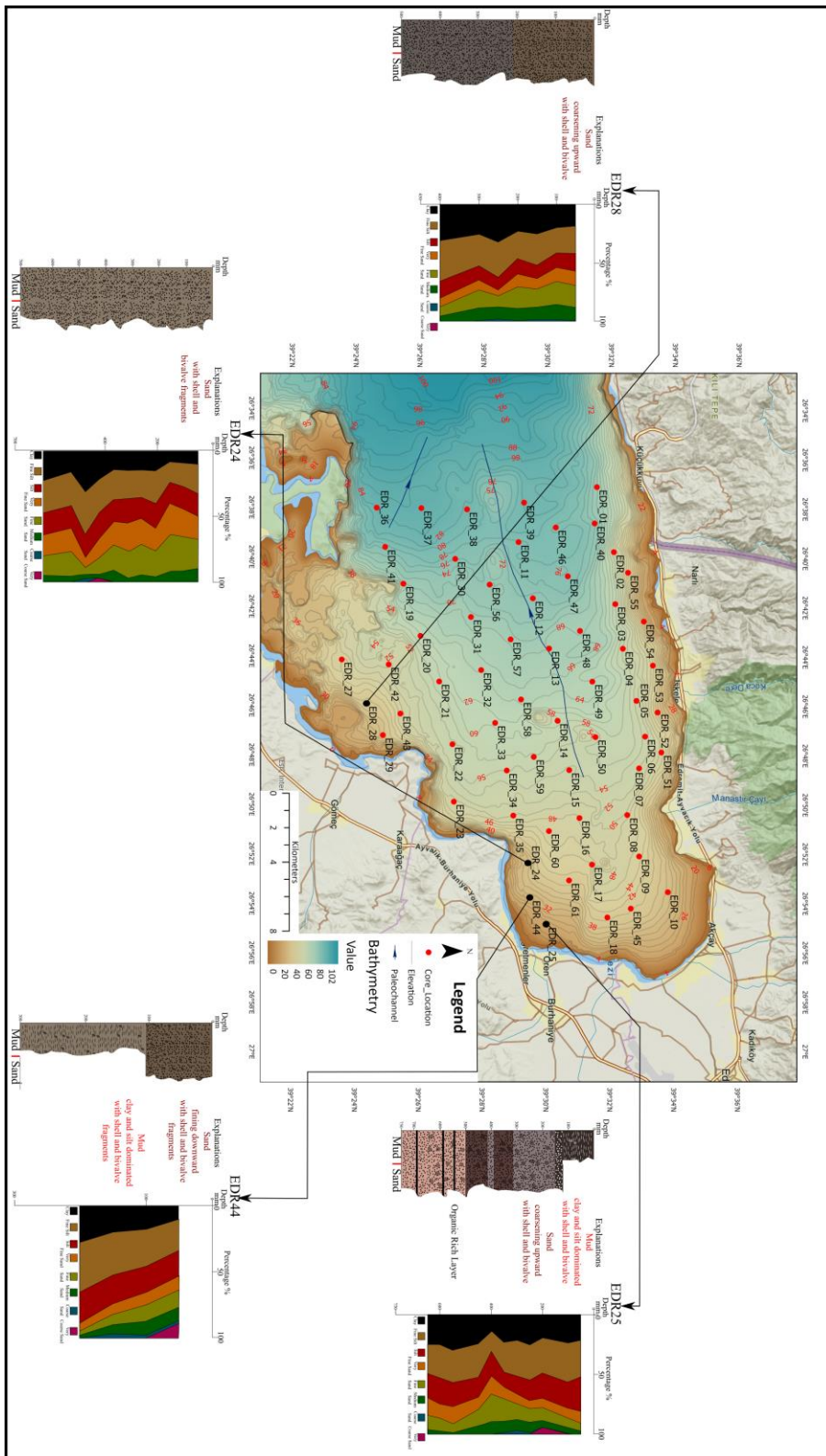
Figure 4.23 Section-C grain size change within core sample

4.3.2   Shifting Surfaces: Grain Size Dynamics Across the Top Layers
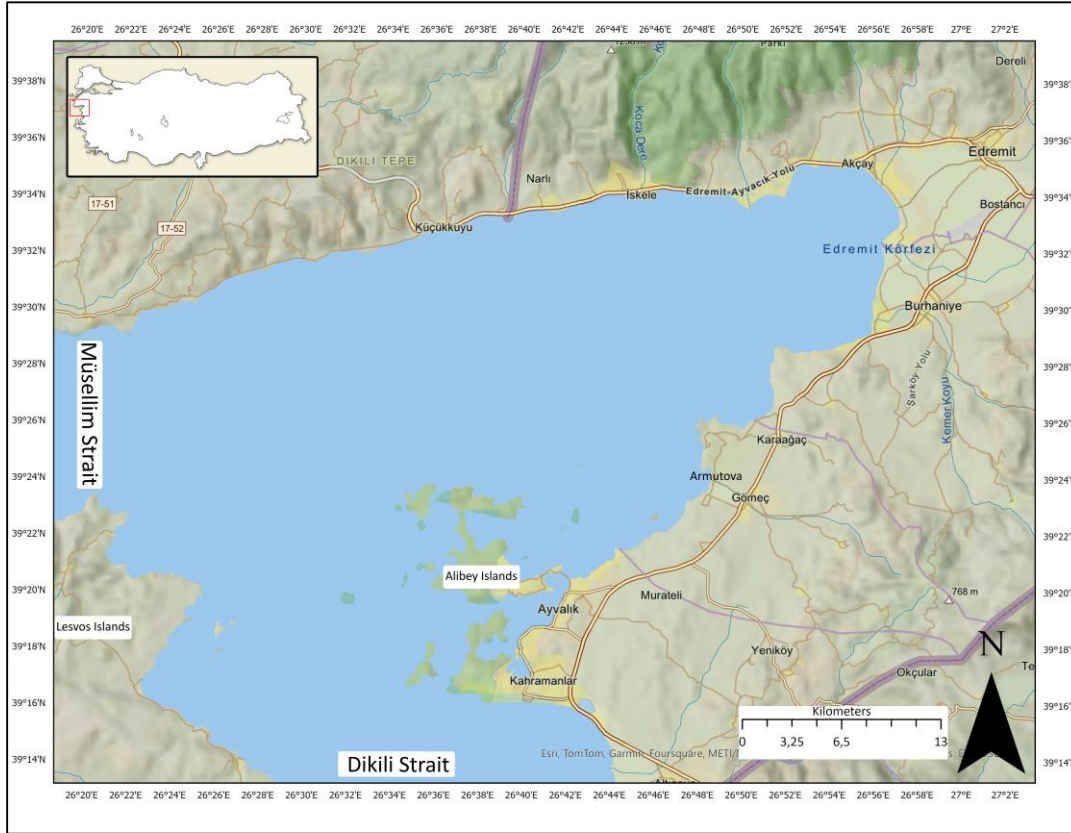

Figure 4.24 Geographic settings around GoE

In Figure 4.26, considering the depositional areas of clay-sized particles, an increased concentration of clay material is observed in the northeastern part through the western part of the study area and to the north of the Alibey Islands (southern islands). Following the current directions, clay-sized particles accumulating in the western part of the study area appear to be transported by currents flowing in southwest. Additionally, materials transported by the northern drainage network seem to accumulate in the western part of the study area from offshore Küçükkuyu, influenced by local currents.

In the northeastern part of the study area, eddy currents appear to contribute to clay particle deposition. Similarly, to the north of the Alibey Islands (southern islands), the concentration of clay-sized particles increases in areas with southwest-directed

currents. Notably, there is a regional increase in clay material around the Yaltırak (2003), determined paleochannel structure, which is a significant observation. The paleochannel structure location is seen in Figure 4.25.
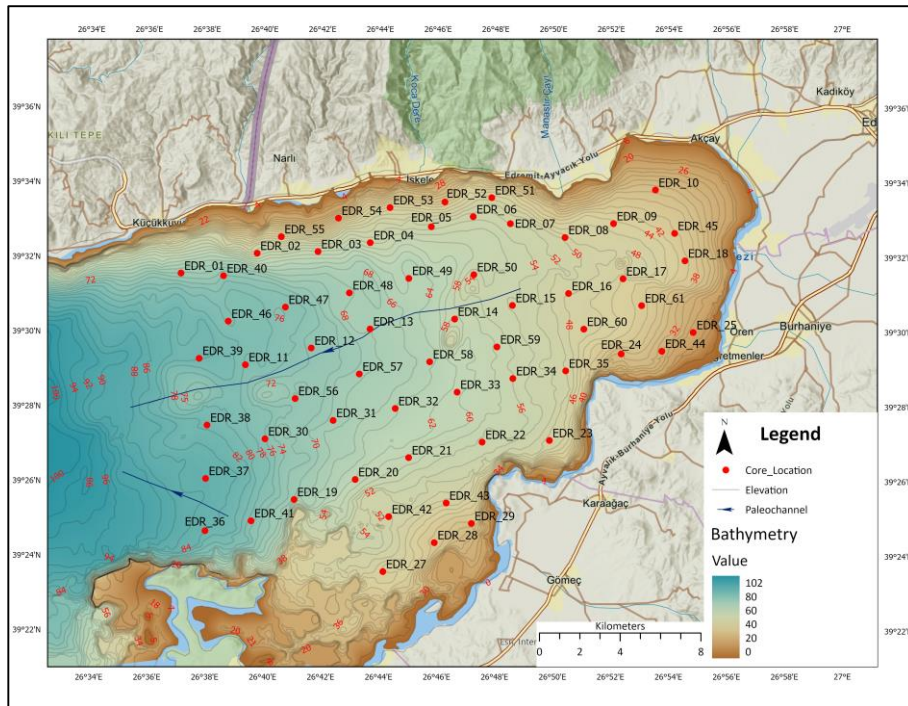

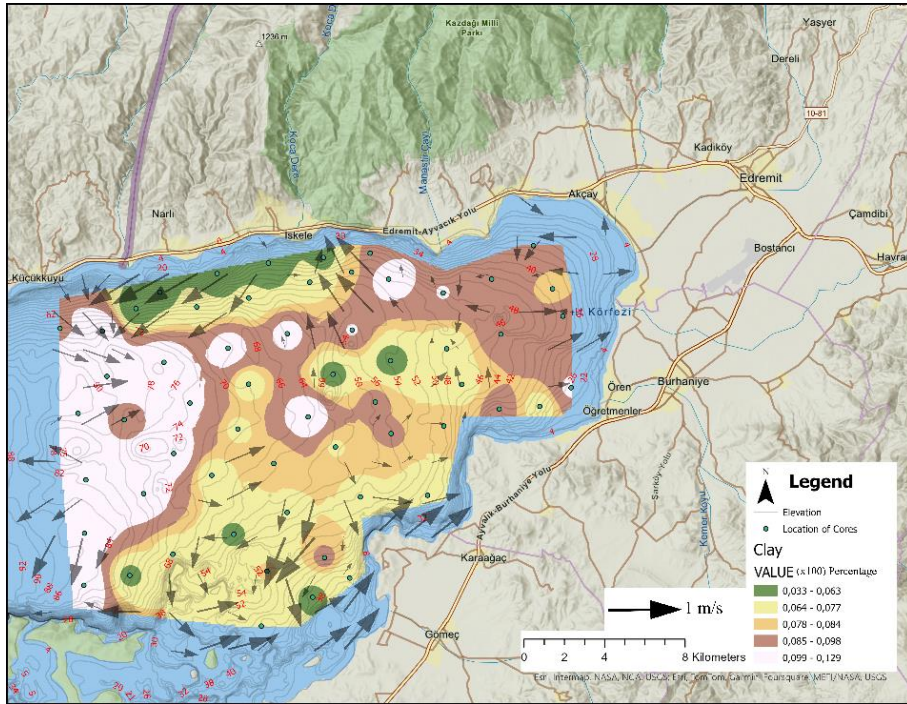Figure 4.25 Paleochannel location

Figure 4.26 Clay sized sediments surface grain size variation (current directions are drawn by Duman et al., 2018)

Considering the depositional areas of very fine (Figure 4.27) and medium silt-sized (Figure 4.28) particles, these materials accumulate primarily in the northeastern part of the study area and to the north of Armutova. The accumulation in the northeast is likely due to sediments transported by the drainage network in the north, which are deposited in this area with the influence of eddy currents. To the north of Armutova, sediments carried by the southern drainage network seem to accumulate and concentrate in front of the headland north of Armutova, aided by northeast-directed currents.

Additionally, a notable finding is the regional increase in very fine and medium silt-sized materials in the paleochannel area discussed in previous sections. The paleochannel location is seen in Figure 4.25.

When considering the depositional areas of very fine and medium silt-sized particles, significant accumulation is observed in the northeastern part of the study area and offshore Karağaç. The northeastern accumulation is likely due to materials

transported from the northern drainage network, which are transported in this area by eddy currents. Offshore Karağaç, sediment carried by the southern drainage network appears to accumulate transported through the offshore Karaağaç by northeast-direction currents.

Additionally, there is a notable regional increase in very fine and medium silt-sized particles in the western part of the study area where paleochannel is located.
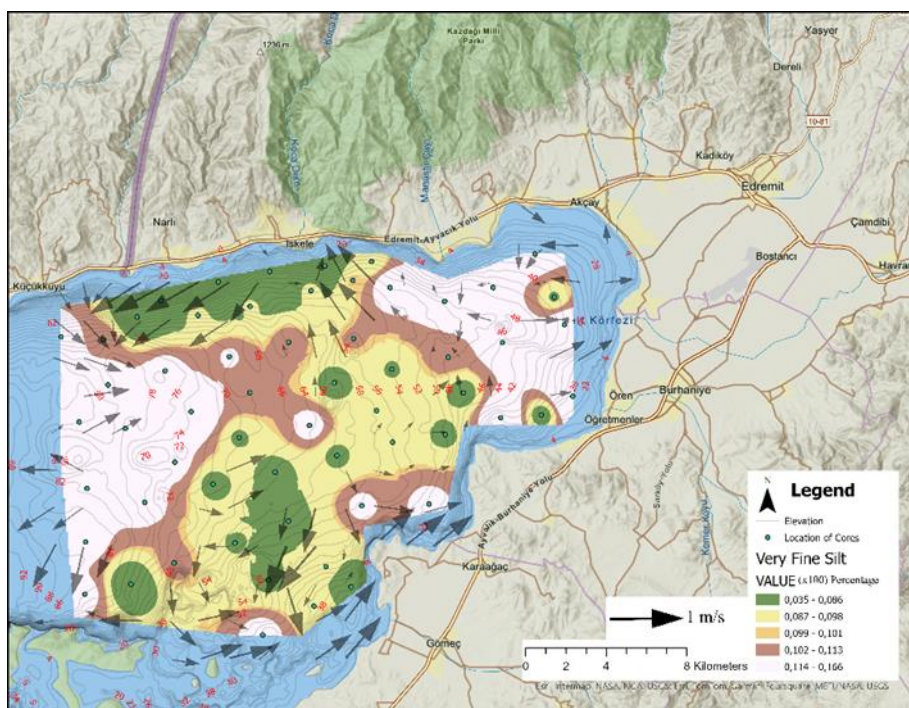

Figure 4.27 Very fine silt sized sediments surface grain size variation (current directions are drawn by Duman et al., 2018)
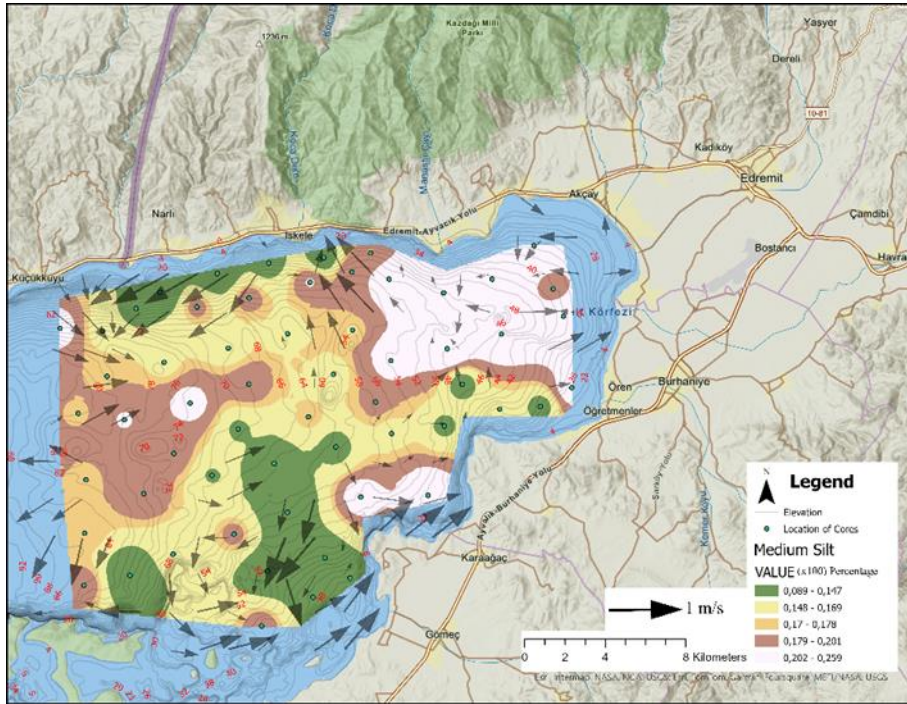
Figure 4.28 Medium silt sized sediments surface grain size variation (current directions are drawn by Duman et al., 2018)

In Figure 4.29, considering the depositional areas of coarse silt-sized particles, there appears to be a distribution spreading from the northern to the southern parts of the study area. Additionally, coarse silt sediment accumulation is observed north of Alibey Island (southern islands), particularly in the deeper sections of the study area. Coarse silt is generally considered a relatively large grain size in the marine environment. The material transported by the drainage network in the northern part of the study area is composed of coarser grains like silt and sand sized sediments. Additionally, it is observed that southwest-directed currents disperse the material from offshore İskele toward Küçükkuyu. The anomalies in the deep part and the southern part of the study area are thought to originate from material transported by currents from the northern drainage network. The deposition of coarse silt-sized material in the north and its widespread distribution into the basin are influenced not only by currents but also by the normal faults in the northern part of the study area, as interpreted by Yaltırak (2003). The steep angle of the seabed morphology in the northern part of the study area, which is thought to directly influence sediment

126

deposition and was discussed in previous sections, can be explained by tectonic factors. The gentler slope of the seabed morphology in the south, combined with the limited drainage network in that area, suggests that most of the sediment entering the basin originates from the north. This factor is thought to predominantly control the depositional patterns within the study area.
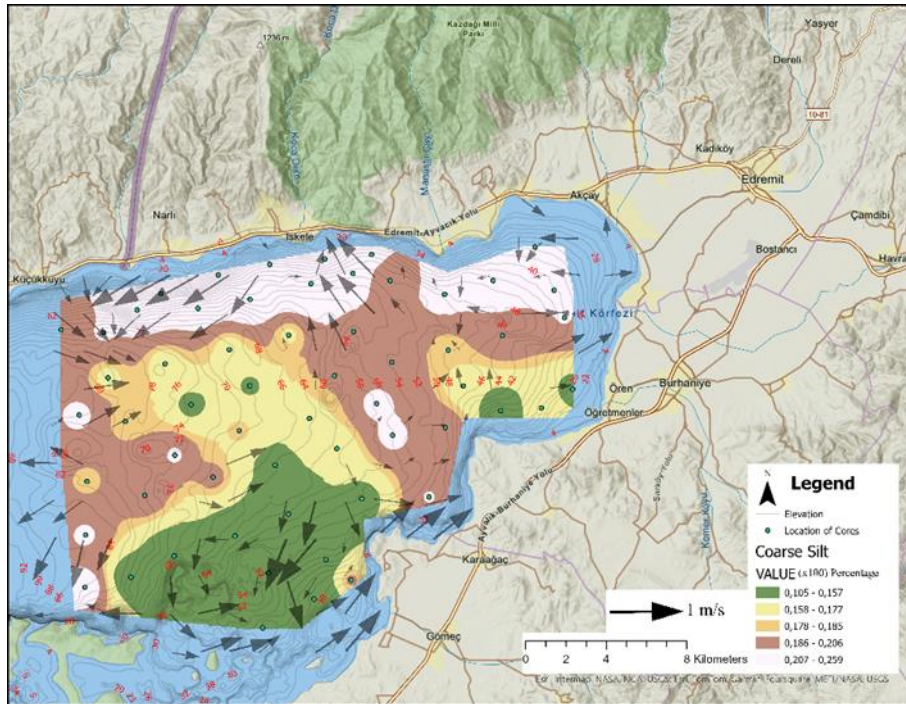

Figure 4.29 Coarse silt sized sediments surface grain size variation (current directions are drawn by Duman et al., 2018)

In Figure 4.30, considering the depositional areas of fine sand-sized particles, a distribution from the northern to the southern parts of the study area is observed. An anomaly is particularly observed in the southern part of the study area. The presence of sand-sized material in the southern area, where silt-sized particles are less concentrated, is a significant observation. It is thought that the anticyclonic eddy currents which are located northeast of the Alibey Islands (southern islands), along with the southward currents from the middle part of the study area, transport fine sand-sized sediment to the southern region. In conclusion, the primary source of sand-sized material is thought to be the northern catchments; however, the southern streams also have an influence.
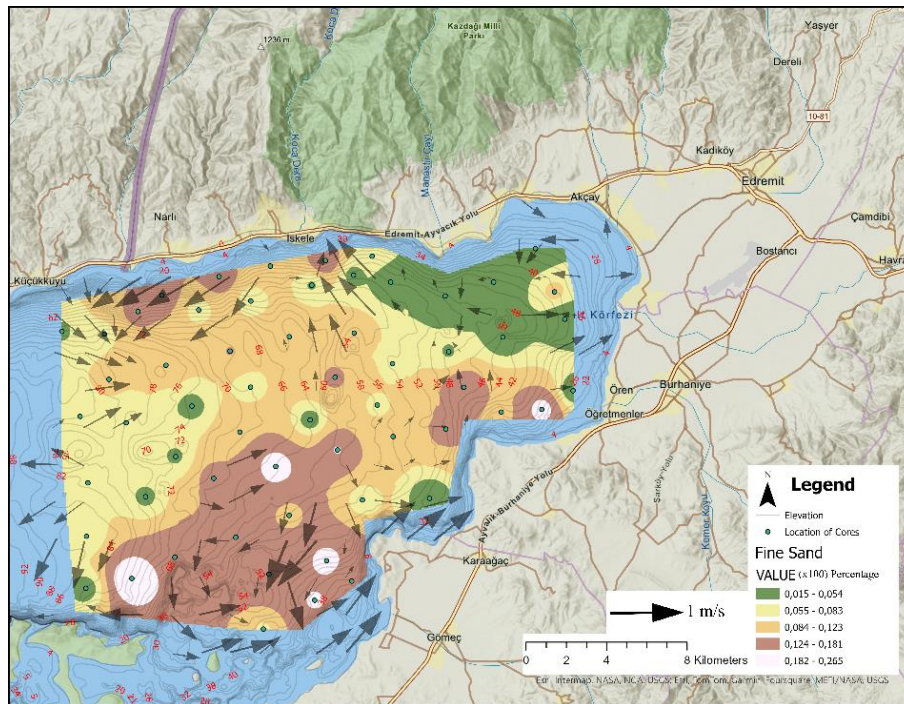
Figure 4.30 Fine sand sized sediments surface grain size variation (current directions are drawn by Duman et al., 2018)

In addition to the surface grain size results, pie charts on the map display the percentage distribution of clay, silt, and sand at each location, based on the Wentworth Grain Size Classification Chart (Figure 4.31). Sand-sized sediments, which are representing the largest grain size, are locally concentrated in the northern part of the study area (offshore Narlı) and are present in higher percentages in the cores located along same line from west to east. Additionally, similar high percentages of sand-sized material is seen in the southern part of the study area as well. They are deposited specifically offshore Gömeç. The surface distribution map for sand also discussed in the previous section. It shows that sand-sized particles are densely concentrated in both the northern and southern areas. The reason is obviously caused by the surface water discharge, which are located drainage networks at northern and southern part of the study area. In certain cores, a regional concentration of sand-sized material has been observed. For example, in cores EDR41 and EDR44, nearly 50% of the deposited material is sand-sized. However, since the surrounding cores do not show similarly high percentages, this

128

concentration is interpreted as a local high concentrations. Clay- and silt-sized material appears to be evenly distributed throughout the basin. In particular, in the offshore area of Akçay, located in the northeastern part of the study area, clay and silt sized material is deposited almost 60-80% of the deposited material.
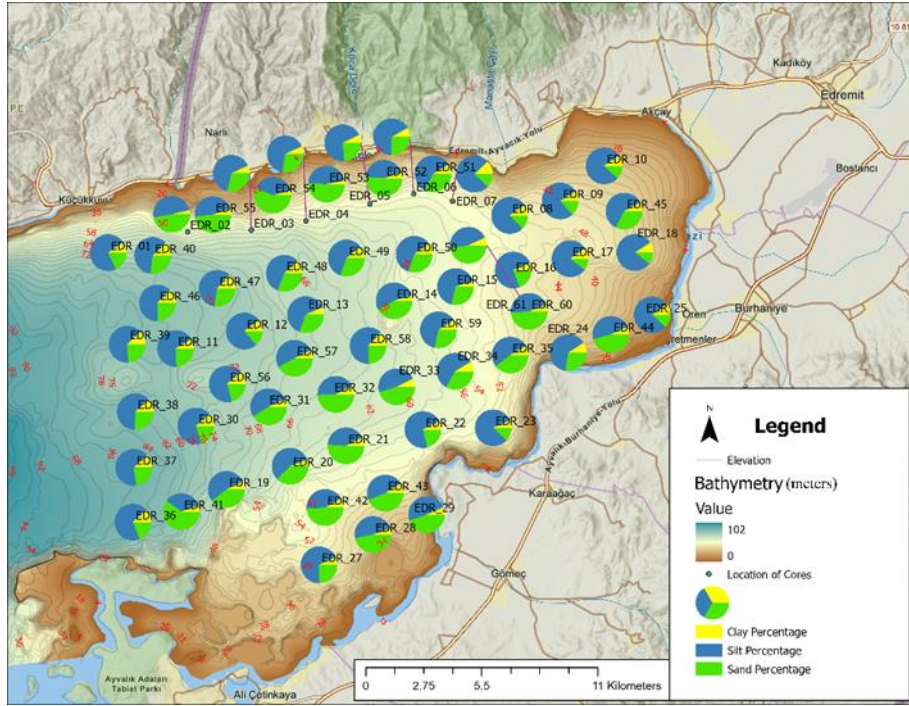

Figure 4.31 Surface clay silt and sand percentage result for each core

In conclusion, the Gulf of Edremit is a bay that prominently reflects the characteristic sedimentological features of the watershed that drains into it. In addition to that, it also has limited marine productivity.

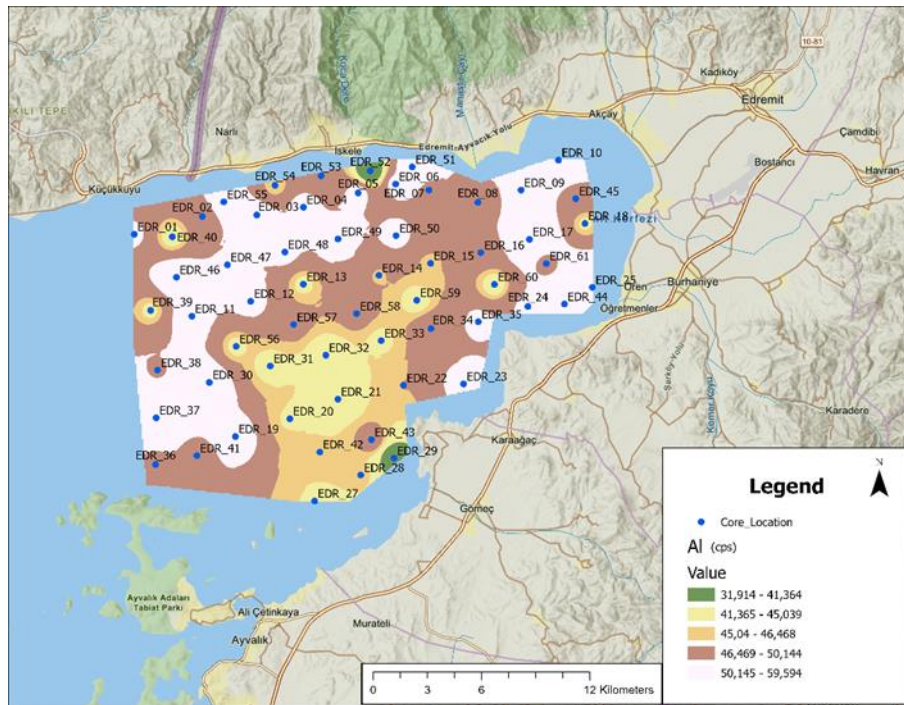## 4.4 Elemental Signatures: Mapping Concentration Variability

Figure 4.32 Al concentration map

Al (Aluminum): Aluminum is typically transported to the sea from terrestrial silicate minerals (e.g., feldspar, clay minerals). Therefore, its concentration increases in areas with high terrestrial sediment input, such as river mouths, delta regions, and continental shelves. In Figure 4.32, Al is observed at high concentrations throughout the entire basin, indicating the dominance of terrestrial transport influence of the basin.
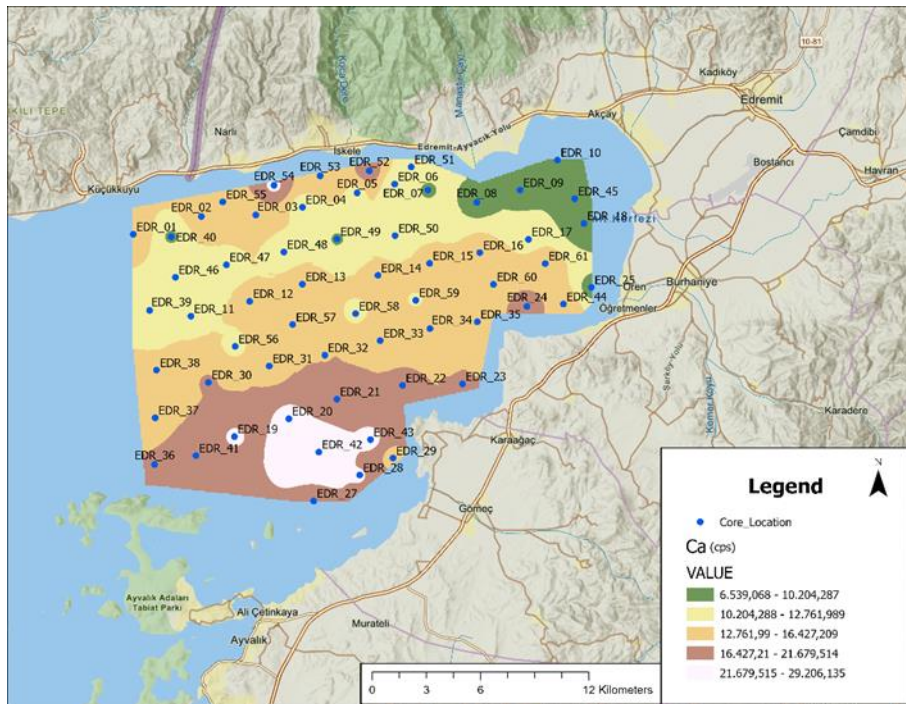
Figure 4.33 Ca concentration map

Ca (Calcium): Calcium is typically associated with carbonate minerals (e.g., calcite, aragonite). Areas with high Ca concentrations are often coral reefs, regions where plankton shells accumulate, or carbonate-rich seafloor. High Ca concentrations on the seafloor can be observed in areas with high marine biological productivity, where carbonate organism remnants accumulate extensively. In areas with freshwater input, Ca concentrations may be lower. As a result, in Figure 4.33, Ca concentration is observed to be higher in the southern part of the study area, which could be attributed to relatively higher marine biological productivity in that region. In contrast, the northern area likely has significant freshwater input, which reduces Ca concentration there.
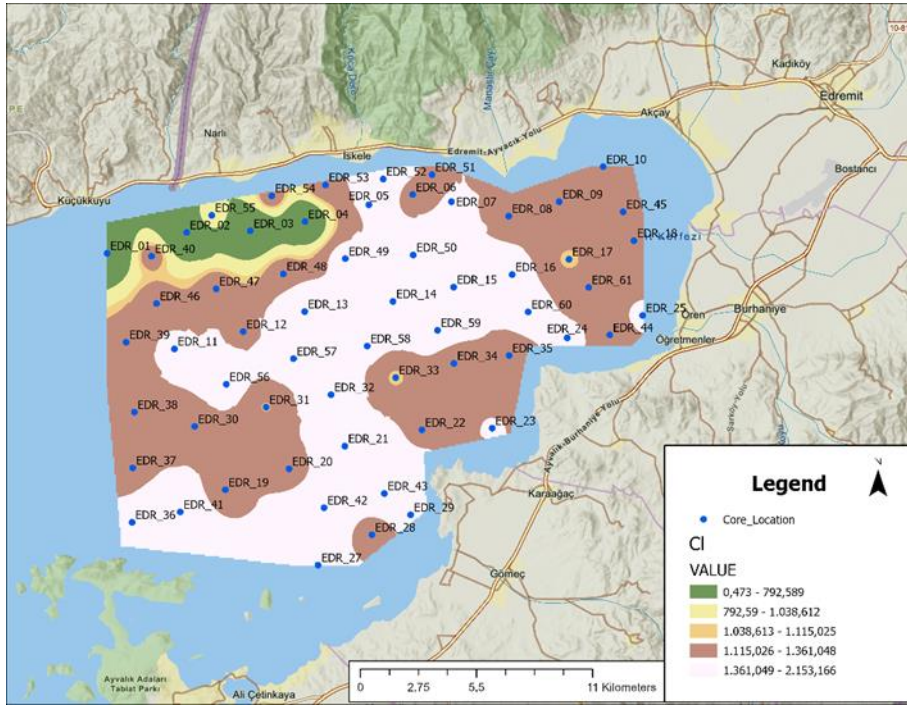
131

Figure 4.34 Cl concentration map

Cl (Chlorine): Areas with high Cl concentrations on the seafloor are often associated with evaporites. In these regions, high salinity leads to increased Cl concentrations. Cl levels may also be high in closed seas or bays where intense evaporation of seawater occurs. In Figure 4.34, the high concentration of chlorine indicates that evaporation is intense in the study area. Additionally, In the northwest of the study area, lower evaporation rates have been observed.
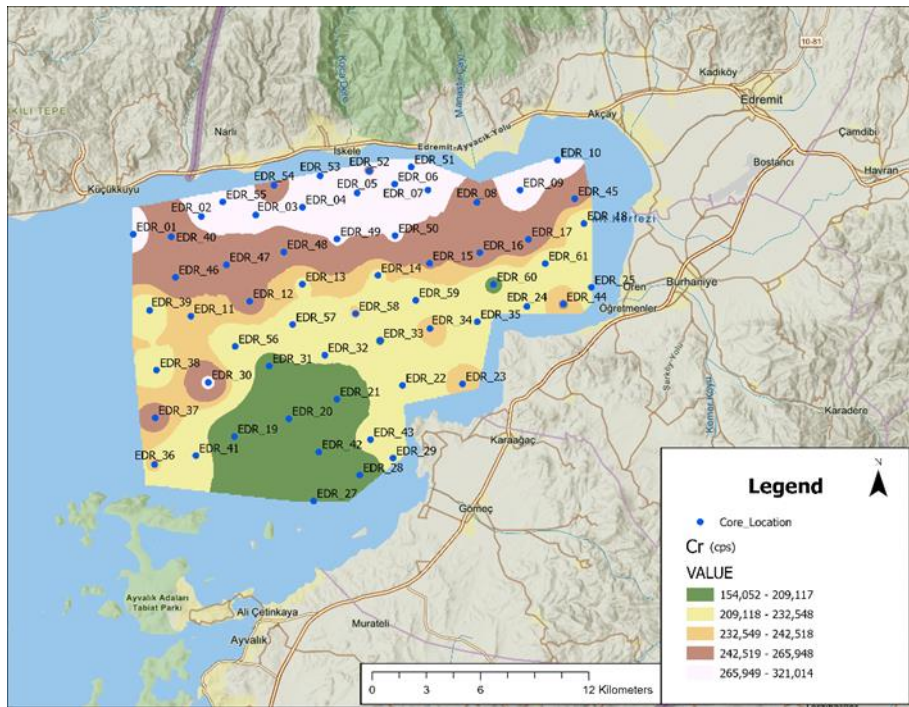
Figure 4.35 Cr concentration map

Cr (Chromium): Chromium is often associated with industrial pollution. Areas of the seafloor with high Cr concentrations may be influenced by metal processing plants or industrial discharges. Additionally, sediments from hydrothermal activities can be rich in Cr. In Figure 4.35, the northern part of the study area, there is a significant accumulation of Cr, suggesting possible industrial pollution influences in that region.
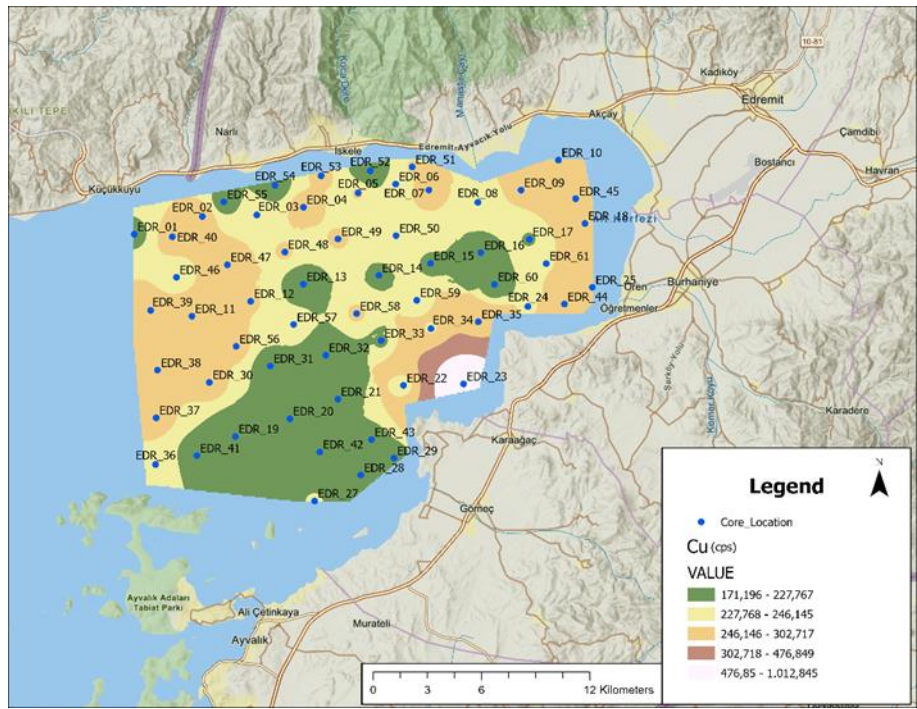
Figure 4.36 Cu concentration map

Cu (Copper): Copper is commonly found in areas of hydrothermal activity or near ore deposits on the seafloor. It can also be concentrated in coastal regions affected by industrial waste. In Figure 4.36, around the offshore Karaağaç there is a significant accumulation of Cu, suggesting possible industrial pollution influence in that region.
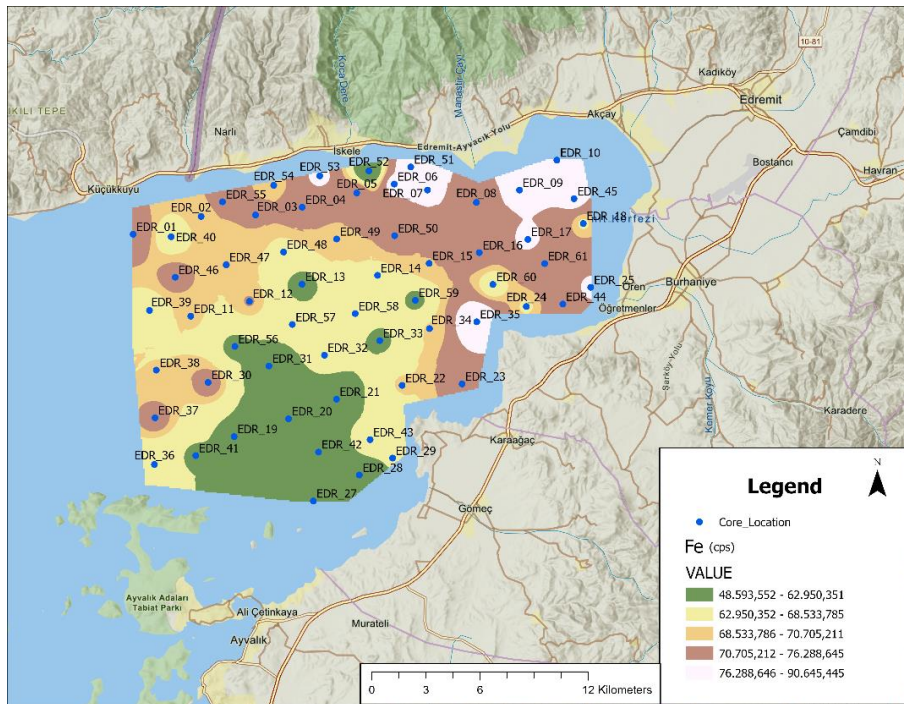
Figure 4.37 Fe concentration map

Fe (Iron): Iron is found in high concentrations around hydrothermal vents, sediments from terrestrial sources, and if delivery rates are high, they can be preserved as pyrite in anoxic environments with low oxygen levels. Under oxygenated conditions, it is often associated with iron oxide and hydroxide minerals. In Figure 4.37, it has produced an anomaly map that is the exact opposite of Ca, indicating consistent results. Since iron is a terrestrial element and sediment input is higher in the north, it is quite normal to observe high concentrations there. The region is not believed to have experienced highly anoxic periods recently.
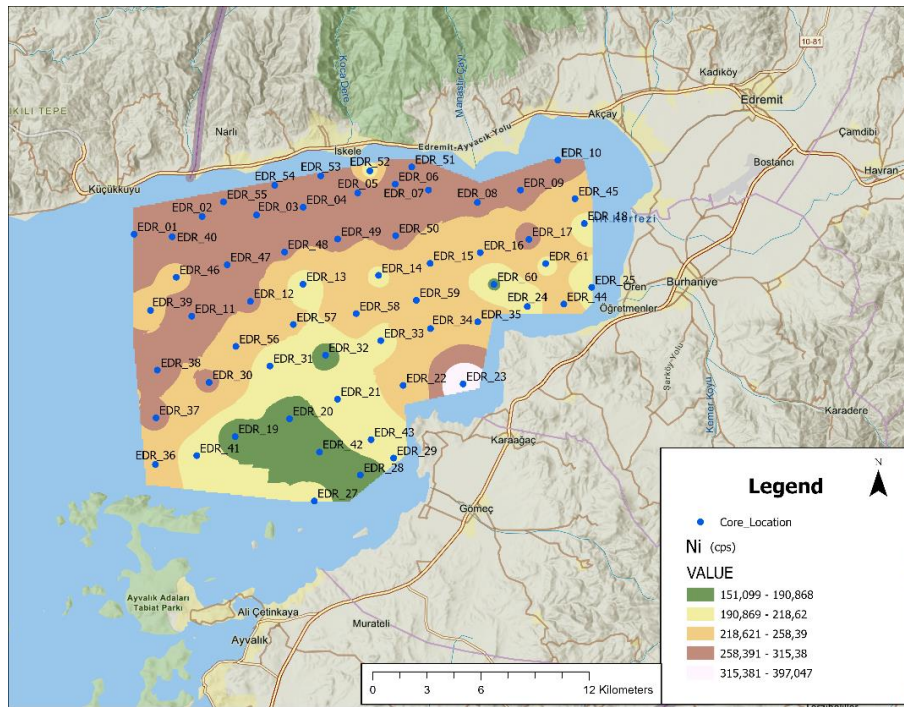
Figure 4.38 Ni concentration map

Ni (Nickel): Nickel typically originates from magmatic sources such as hydrothermal activities or serpentinized rocks. It is also found in metallic nodules on the seafloor. In Figure 4.38, nickel concentration is higher in the northern part of the study area. This is attributed to the presence of magmatic rocks in the north. The presence of magmatically rich formations, such as the Kazdağ Massif and the Karakaya Complex, in the northern part of the study area should be taken into consideration.
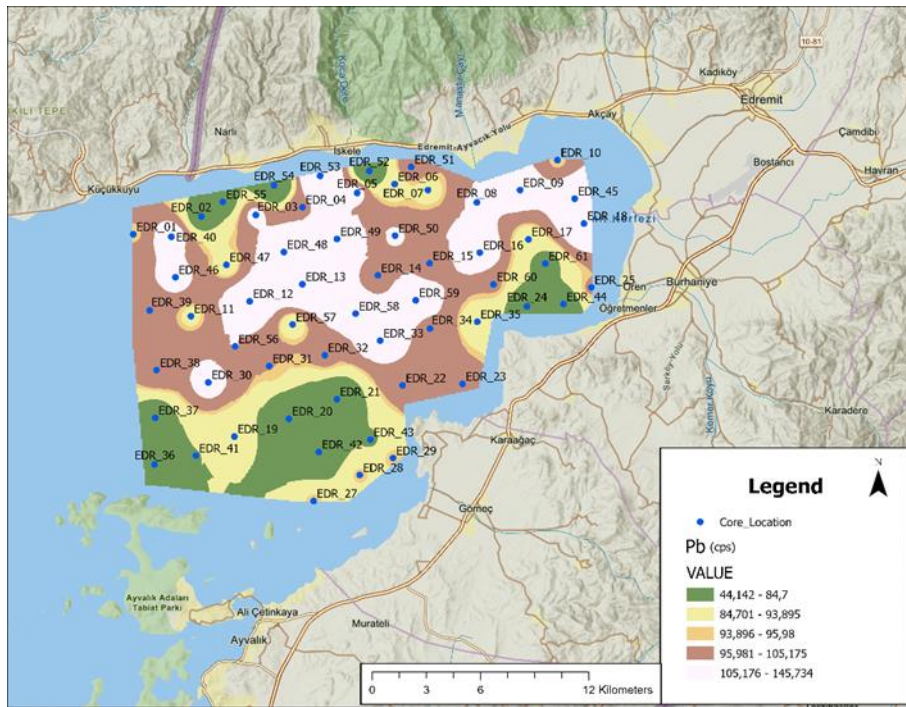
Figure 4.39 Pb concentration map

Pb (Lead): Lead is a metal typically associated with industrial pollution. It can be found in high concentrations in coastal areas affected by contamination, waste from metal processing facilities, or on the seafloor near former mining sites. In Figure 4.39, when considering Pb as an indicator of anthropogenic pollution, the entire basin shows high levels of contamination, except for the offshore the southern islands in the study area.
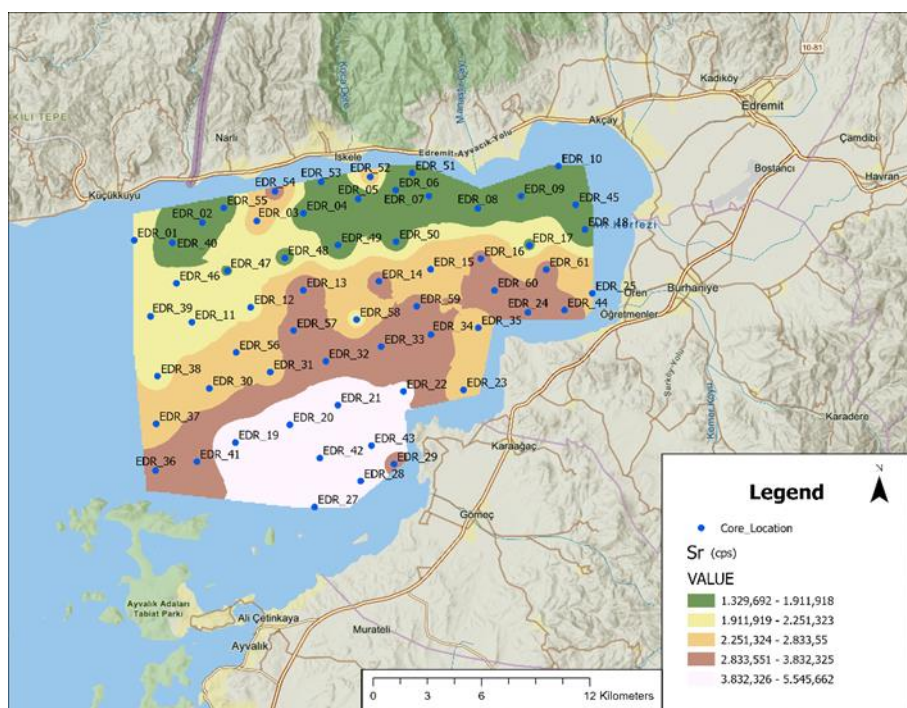
Figure 4.40 Sr concentration map

Sr (Strontium): Strontium is associated with carbonate sediments and marine biogenic structures (e.g., corals). It can also be found in high concentrations in environments with evaporites in seawater. In Figure 4.40, the similarity between the concentration change maps of Sr and Ca are seen. Both maps show anomalies in the southern region, suggesting that this area is likely more active in terms of marine biological productivity.
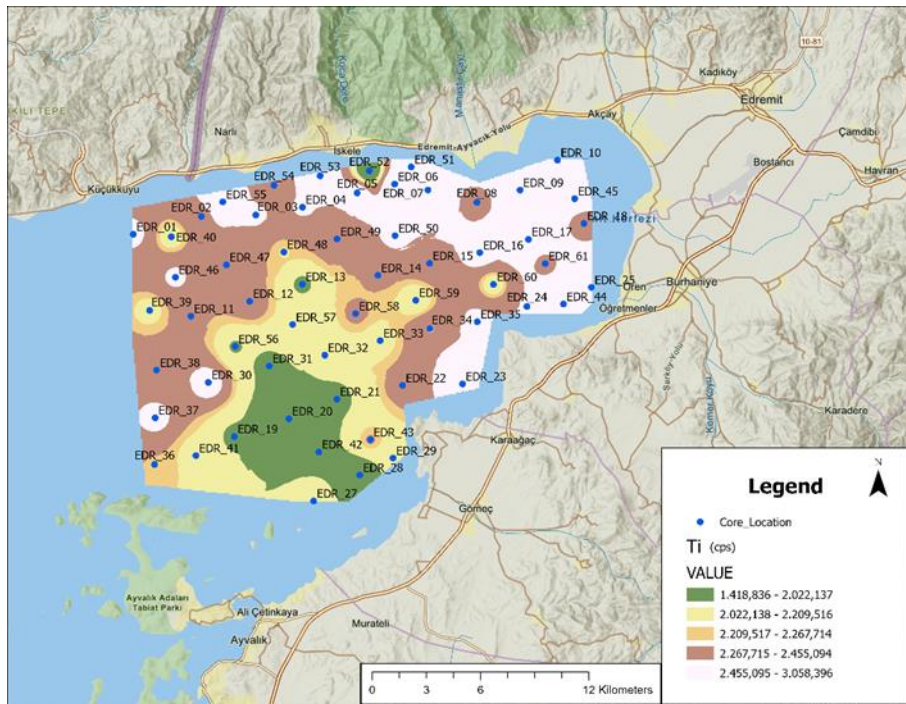
Figure 4.41 Ti concentration map

Ti (Titanium): Titanium is typically associated with sediment transport from terrestrial sources. It can be concentrated in coastal sedimentary environments and river mouths. As a result, observing an anomaly in the northern part of the study area is not surprising. Titanium is more difficult to transport compared to other elements due to its heavier nature. In Figure 4.41, serves as evidence of the marine distribution of Ti concentrations and correlation with the geochemistry results originating from river study which is mentioned in the previous section.
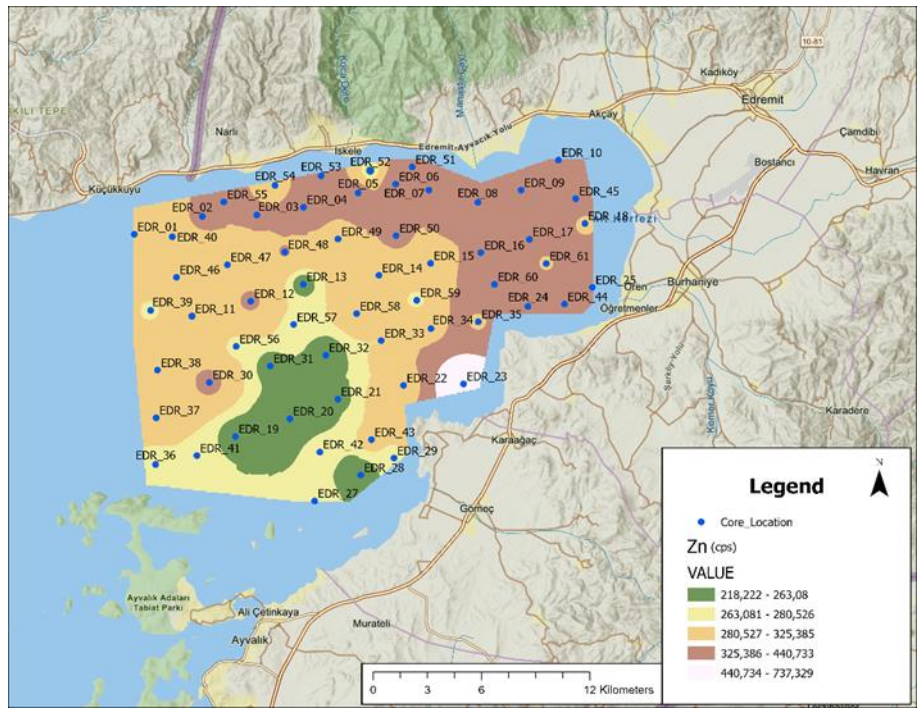
Figure 4.42 Zn concentration map

Zn (Zinc): Zinc is associated with hydrothermal activities, metallic ore deposits, and sources of industrial pollution. It can be concentrated in coastal regions and areas exposed to contamination. In Figure 4.42, the Zn anomaly observed on this map is believed to be directly related to pollution.

CHAPTER 5

DISCUSSION

5.1   Tracing Tectonics: Tectonic Mechanism Driving the GoE

The Gulf of Edremit is primarily situated at the intersection of the strike-slip regime of the NAFZ and AES. As a result, the neotectonic deformation of the area has been shaped by these two factors (Taymaz et al., 1991; Yılmaz et al., 2000; Gürer et al., 2003, 2006). Many researchers have provided interpretations of the tectonic elements of the Gulf of Edremit based on seismic sections. (Table 5.1) However, seismic interpretations differentiate between each other's. This is an expected result, especially in a complex area like the Gulf of Edremit. Other reason for these variations is the difference in datasets used by different researchers. However, this should not be attributed solely to differences in datasets. This chapter will examine the primary factors contributing to the differences in fault interpretations, focusing on the underlying methodological and analytical variations among the studies.

Table 5.1 Researchers' fault interpretations and data properties

Researcher	Data	Properties	Interpretations
Beyhan (1999)	1	Number of Profiles: 8	N-S direction oblique normal faults within the gulf. Strike slip fault expected within the GoE.
		Total Length of Profiles 182 km	
		Data Type: Multi Channel (Airgun 1270psi)	
		Vertical Resolution 4-6 sec.	
		Collected By: TPAO	
Yaltırak (2003)	1	Number of Profiles 17	Three groups of normal faults observed. First group is 60-65 degrees rotated clockwise direction normal faults which are mostly located at the northern boundary. Second group 130-135 degrees clockwise directed normal faults which are located at the eastern boundary. Those two groups are mainly control the deposition at the gulf. Third group is transform faults that located at the middle part of the basin and their direction is E-W.
		Total Length of Profiles: 377 km	
		Data Type: Single Channel	
		Vertical Resolution: 350 msec.	
		Collected By: R/V Piri Reis (NATO Project,1999)	
	2	Number of Profiles: 24	
		Total Length of Profiles: 444 km	
		Data Type: Multi Channel	
		Vertical Resolution: 2.5 sec.	
		Collected By: NV Turkse Shell (1978) and Amocco Turkey Petroleum Company (1985)	

Table 5.1 (continued)

Researcher	Data	Properties	Interpretations
Kurtuluş (2009)	1	Number of Profiles: 20	In Early Miocene NNW-SSE trending low angle normal faults control the synrift. Neogene and during Holocene high angle ENE-WSW trending normal faults developed especially at the northern boundary.
		Total Length of Profiles: 1000 km	
		Data Type: Multi Channel (Airgun 1270psi)	
		Vertical Resolution: 3 sec.	
		Collected By: Amocco Turkey Petroleum Company and Western Geophysical Company (1986)	
Eytemiz (2020)	1	Number of Profiles: 15	NAF southern strand, Yenice Gönen Fault continue within the Gulf towards Lesvos Island.
		Total Length of Profiles: 300 km	
		Data Type: Multi Channel	
		Vertical Resolution: 3 sec.	
		Collected By: R/V Piri Reis	

Beyhan (1999) proposed that the Gulf of Edremit is formed by N-S oriented oblique normal faults. Beyhan reached this conclusion by interpreting eight seismic sections. A map of his interpreted fault lines is provided (Figure 5.1). Beyhan (1999) interpretations are also visible in seismic section EK-6, collected by the Turkish Petroleum Corporation (TPAO), with a planned depth range of 4-6 seconds. The depth information in EK-6 is hidden, which is a common practice due to the high costs of offshore seismic acquisition and processing, governed by confidentiality agreements.
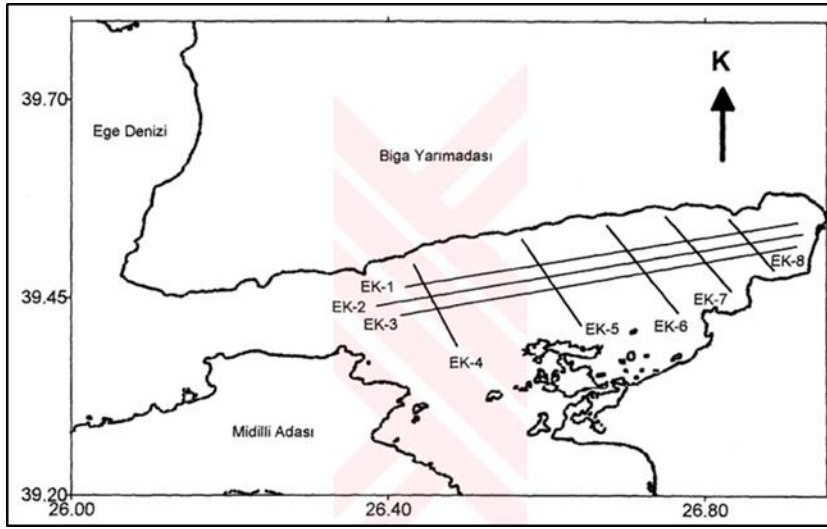
Figure 5.1 Beyhan (1999) seismic sections

Considering that the entire section has a depth range of 4-6 seconds, the resolution significantly decreases beyond the initial 2-second range due to seismic artifacts like noise, multiples or smiles. Data processing is studied to eliminate these artifacts, but incorrect parameter selection during processing can lead to data loss.

Figure 5.2 Beyhan (1999) EK-6 section and interpretations

Within the first 2 seconds, sediment packages are well-defined and easily distinguishable. The section shows a thickening of sediment packages in the northern part of the gulf and a thinning in the south, indicating a fold structure. This sediment thickness increase in the north is attributed to greater fault displacement associated

144

with northern faulting. However, due to the lower resolution of the seismic sections, there are uncertainties regarding the exact locations of faults.
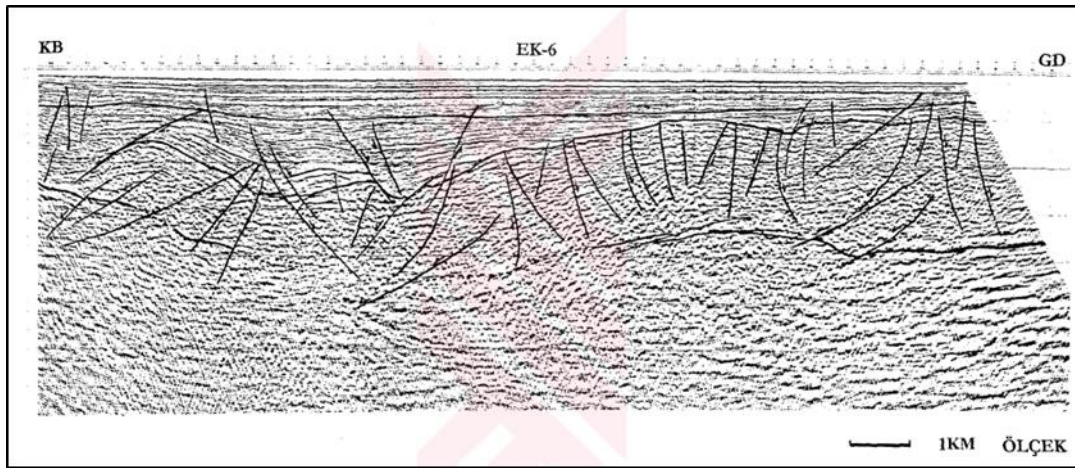
Beyhan (1999) interprets these fault lines as being directly linked to the formation and widening directions of the basin. In this study also speculated that a strike-slip fault controls the mechanism of the bay's formation along the northern boundary of the gulf. Consequently, Beyhan (1999) concludes in his study that oblique normal faults, often resembling flower structures, are present within the study area.

Eytemiz (2020) seismic study which show the presence of strike-slip faults within the GoE. According to Eytemiz (2020), the southern strand of the NAFZ, specifically the Yenice-Gönen Fault, extends into GoE toward Lesbos Island. The locations of Eytemiz (2020) study seismic sections are shown below (Figure 5.3), revealing that the north-south-oriented sections intersect the gulf more steeply.
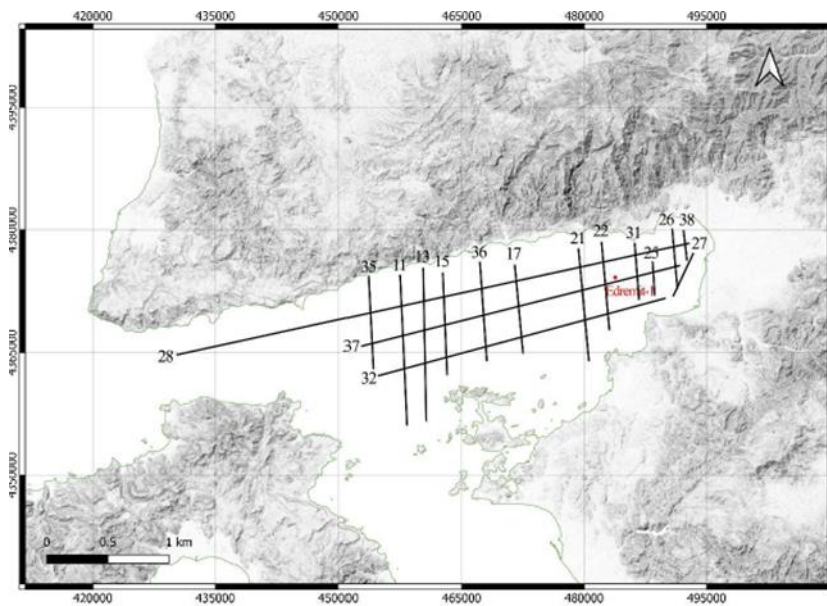
Figure 5.3 Eytemiz (2020) seismic sections

In seismic section 28, Eytemiz (2020) interpreted faults at every point where reflections become discontinuous, which is not considered an accurate approach. Additionally, starting from 0.5 ms, the section is dominated by multiples. It is recommended that sediment package correlations, verified against Edremit-1 well

data, be applied across all sections before making fault interpretations based on sediment thickness variations.
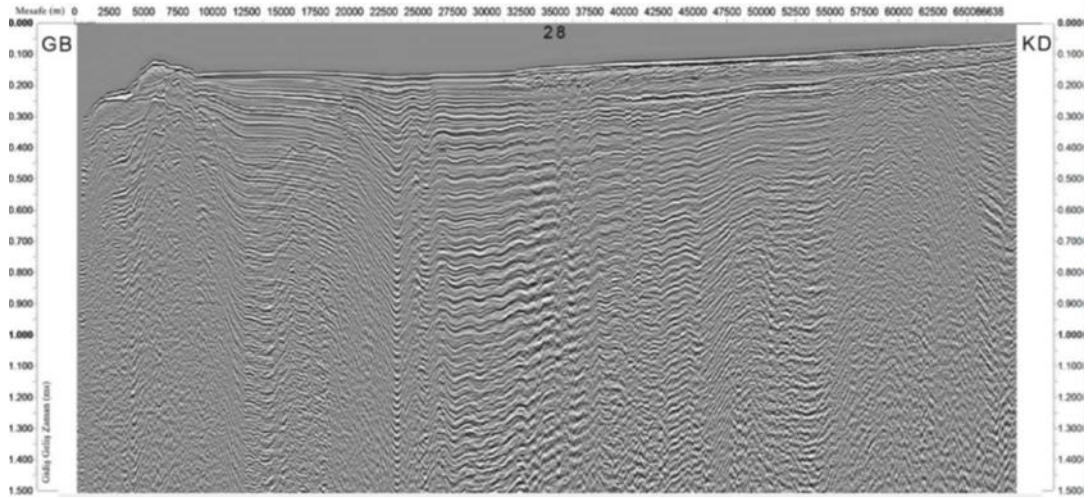
Figure 5.4 Section 28 without interpretations (Eytemiz, 2020)
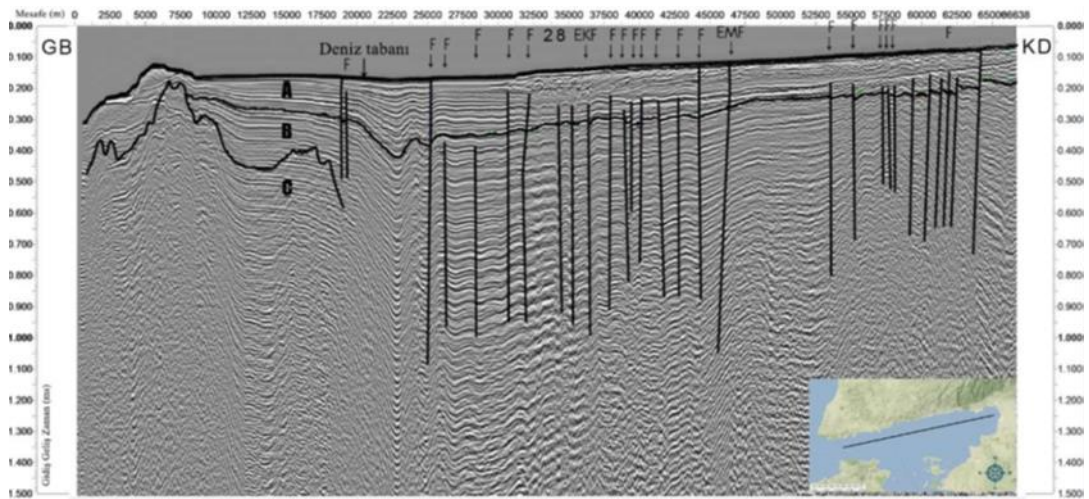
Figure 5.5 Section 28 with interpretations (Eytemiz, 2020)

Sediment packages A, B, and C have been interpreted in Eytemiz (2020) study. Faults labeled EKF (Edremit Körfezi Fayı) and EMF (Edremit Midilli Fayı) are thought to be strike-slip faults, and they are more likely to be visible in seismic sections that cross the strike-slip structures perpendicularly. In section 13b, a structure resembling a flower structure is drawn; however, this feature requires

146

further investigation using additional techniques, such as specific seismic attributes, to ensure more detailed analysis.
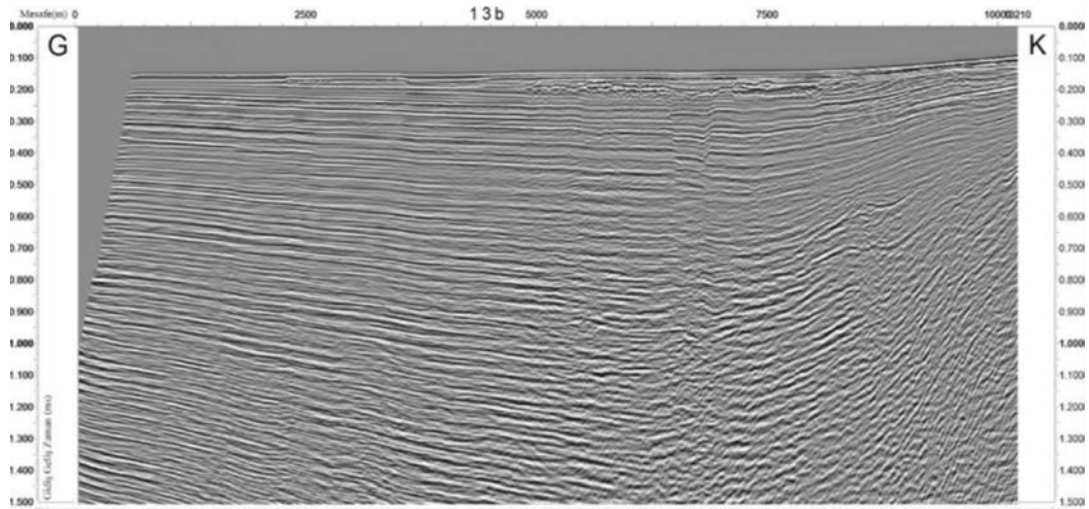
Figure 5.6 Section 13b without interpretations (Eytemiz, 2020)
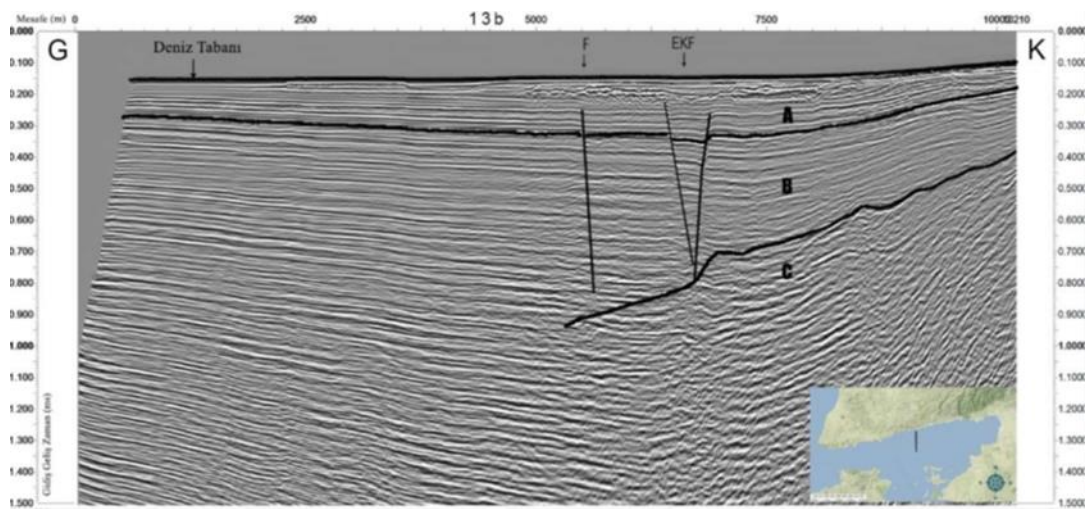
Figure 5.7 Section 13b with interpretations (Eytemiz, 2020)

Contrary to Beyhan (1999) and Eytemiz (2020), Yaltırak (2003) study claim that, gulf is tectonically controlled by normal faults. Yaltırak (2003) used two different datasets in his study to identify the tectonic elements of the GoE. According to Yaltırak (2003), the faults in the GoE can be categorized into three groups of normal faults:

147

I. Northern-bound normal faults
II. Southern-bound normal faults
III. A transform fault located in the middle of the basin
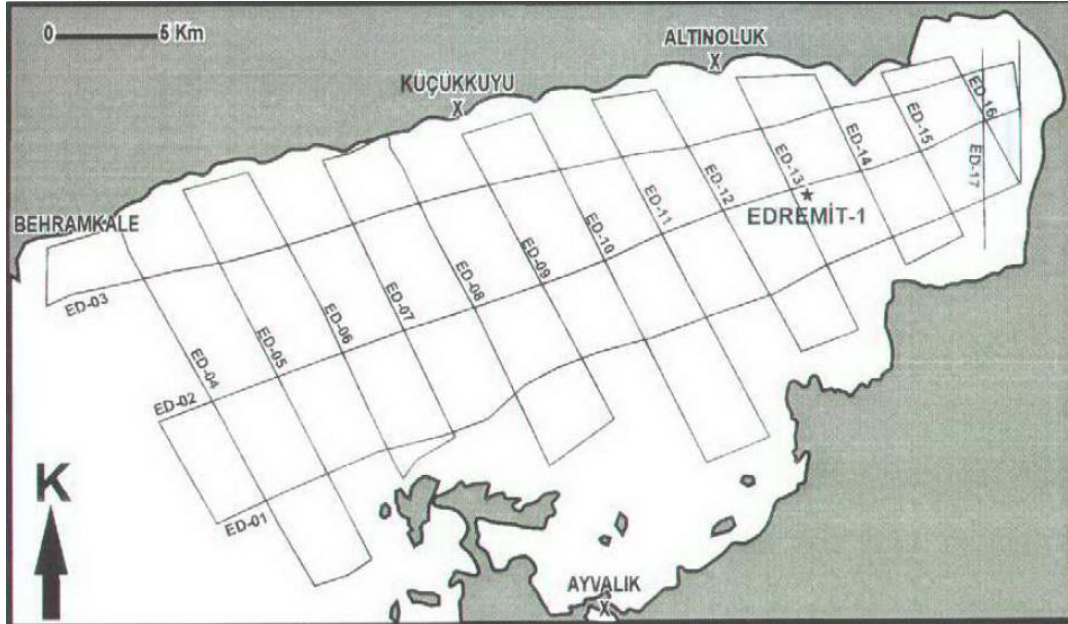
Figure 5.8 Yaltırak (2003) seismic sections

The fault directions differ among these groups. The locations of the seismic sections used by Yaltırak (2003) are provided below (Figure 5.9), along with the interpreted versions of these sections. Due to the age of the seismic sections, it is difficult to comment on their resolution. However, based on the fault locations indicated on the map, Yaltırak (2003) interpretations appear to be accurate.

Figure 5.9 Yaltırak (2003) interpretations

149
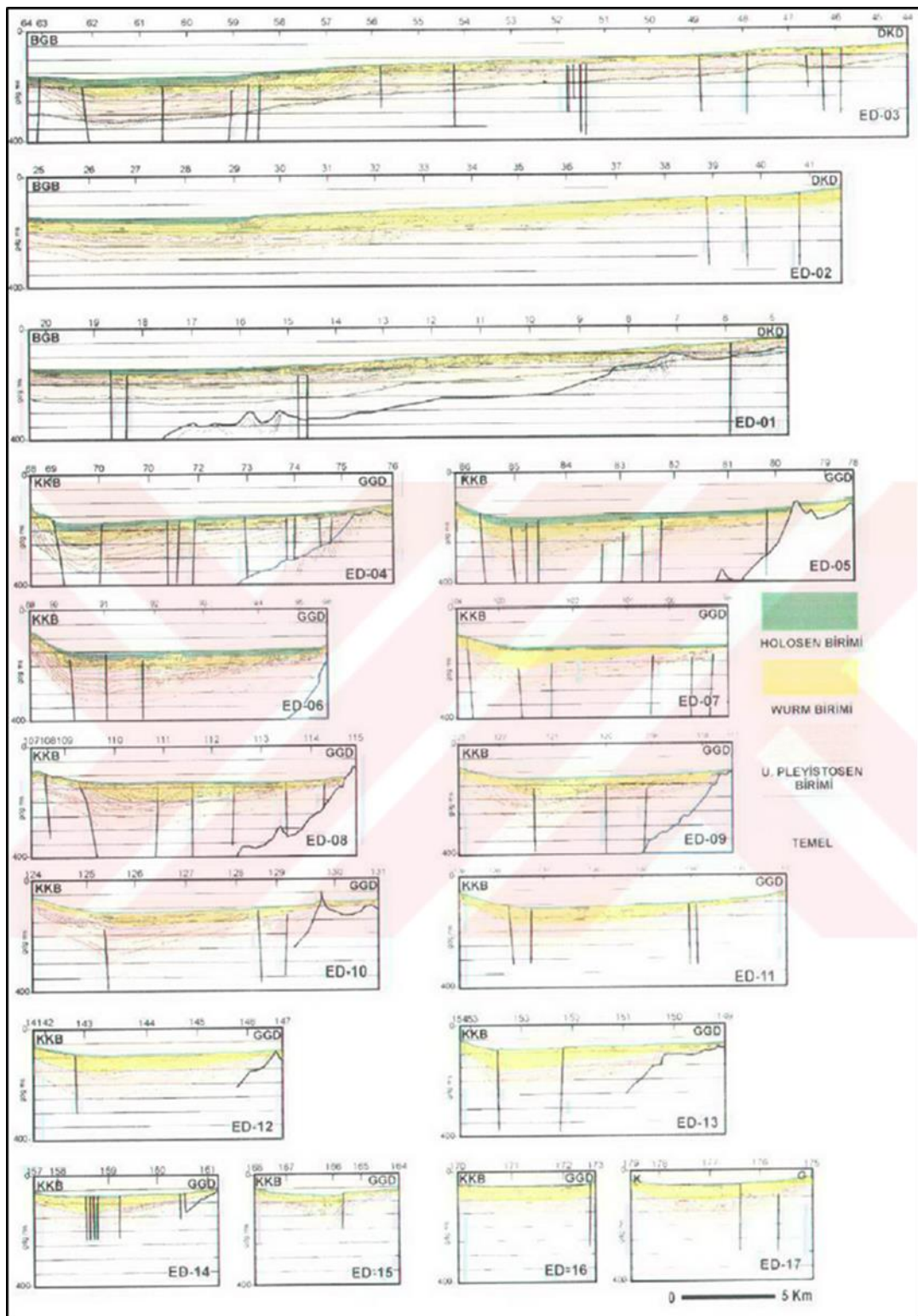
Finally, Kurtuluş (2009) seismic interpretations of the GoE was reviewed. Like Yaltırak (2003), Kurtuluş (2009) also claim that there is no strike-slip fault within the gulf, identifying two different groups of normal faults.

I. In the Early Miocene, low-angle normal faults controlled the synrift deposits.
II. During the Holocene, high-angle ENE-WNW normal faults along the northern boundary controlled the basin.
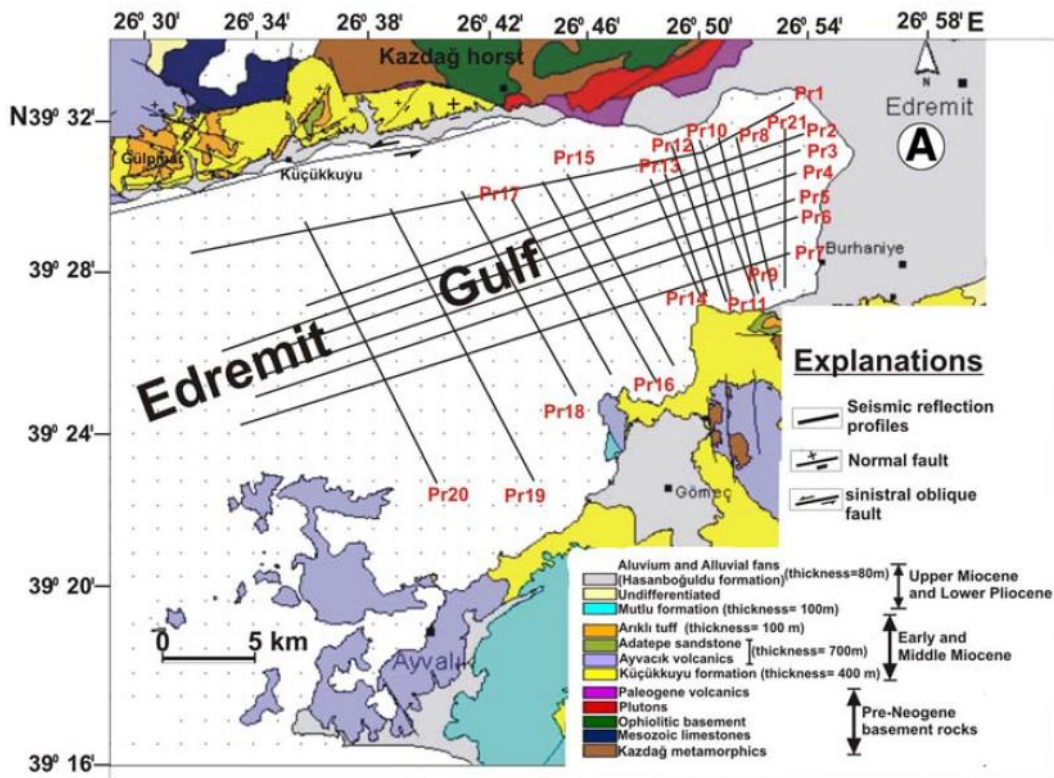
Figure 5.10 Kurtuluş (2009) seismic sections

In seismic section Pr-3, the vertical resolution decreases significantly beyond the 1-second. The section shows a separation by a bedrock with unconformity.

The locations and orientations of the normal faults appear accurate, especially those placed along the northern boundary, However, the interpretation of N-S oriented normal faults at the central part of the GoE raises some question marks.
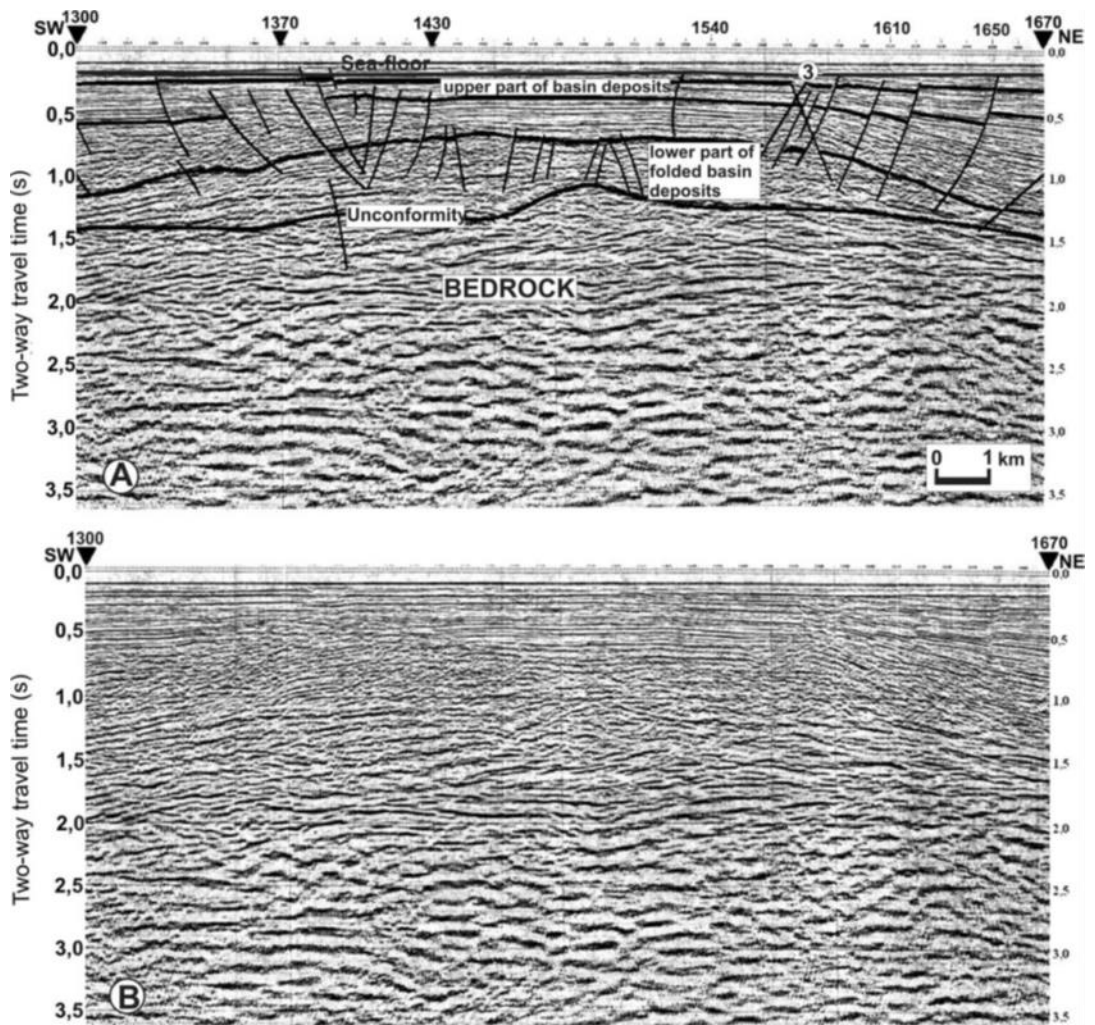
Figure 5.11 Kurtuluş (2009) Pr-3 seismic section

Their final interpretation related to the faults is given in Figure 5.12. According to the map, understanding the most common type of fault within the GoE is normal faults, except for Eytemiz (2020) strike slip fault interpretation.
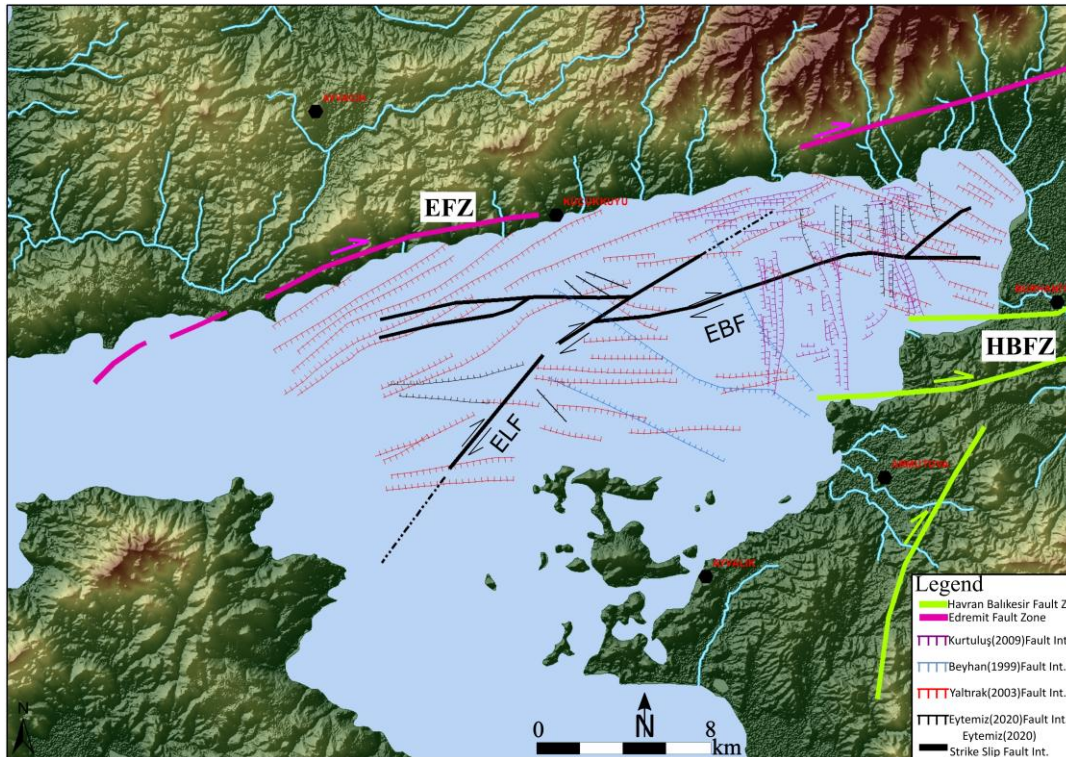
Figure 5.12 Fault interpretations of researchers within GoE (ELF: Edremit-Lesvos Fault and EBF: Edremit Bay Fault)

In conclusion, interpretations are inherently subjective, as researchers analyze data based on their own perspectives of accuracy. However, a major limitation of the dataset is the lack of data beyond the 1-1.5-second range. While technological advances have improved the quality of seismic data over time, the collected data might still have lower resolution due to the older equipment used during acquisition.

Data collection parameters; such as line orientation, source strength, and seafloor variations are critical for correct results. The distinction between shallow and deep marine surveys is significant. For instance, in active fault studies, where source strength and seafloor depth must be adjusted accordingly. High-resolution data acquisition, tailored to specific areas, can greatly enhance fault analysis.

Effective data processing is also vital. For instance, velocity picking is often debated, as different geological layers transmit sound waves at varying speeds. Continuous

collaboration between researchers and data processors ensures more accurate results of final seismic sections.

In the Gulf of Edremit, reprocessing of existing seismic data is necessary to correct artifacts and refine fault interpretations. High-resolution data should be collected in targeted areas to reduce costs while clarifying whether normal or strike-slip faults dominate the region. While the seismic sections currently do not clearly indicate strike-slip faulting, some features suggest potential structures that require further analysis. Advanced interpretation software filters can help verify these potential faults.

Re-evaluating fault interpretations using these techniques is crucial for a better understanding of the gulf's tectonic elements. As previously mentioned, not every discontinuity in seismic reflections should be interpreted as a fault. For this reason, using interpretation software filters, such as attributes (e.g., Ant-tracking, Amplitude Contrast, Consistent Curvature, Consistent Dip, Edge Evidence, Instantaneous Phase, General Spectral Decomposition, and Variance [edge method]), can help verify fault accuracy. A re-evaluation of fault interpretations using these attributes is needed in this area.

In this study, the fault interpretation proposed by Yaltırak (2003) has been adopted, indicating that the tectonic framework of the study area is predominantly controlled by normal faults.

5.2   Core-to-Core Insight: Unlocking Relationships with 'Mn' Concentrations

In core EDR47, Mn concentrations begin to increase from the MWP-1a period. Considering that this increase is directly linked to sea level rise, similar trends were checked in other cores. As a result, same increase in Mn concentration was observed 16 different cores. One of these cores, EDR25, which has radiocarbon age result. In Figure 5.14, comparing the ages at which the Mn concentration began to rise, the

increase in EDR47 is observed around 11 ka BP, while in EDR25, it begins around 10 ka BP. The proximity of these ages is one of the noticeable findings. Therefore, it is likely that similar Mn increases occurred at roughly the same time in other cores as well. The Mn correlation and their locations are seen in the Figure 5.13 and 5.14. The shaded area is showing the location of Mn correlated core samples.
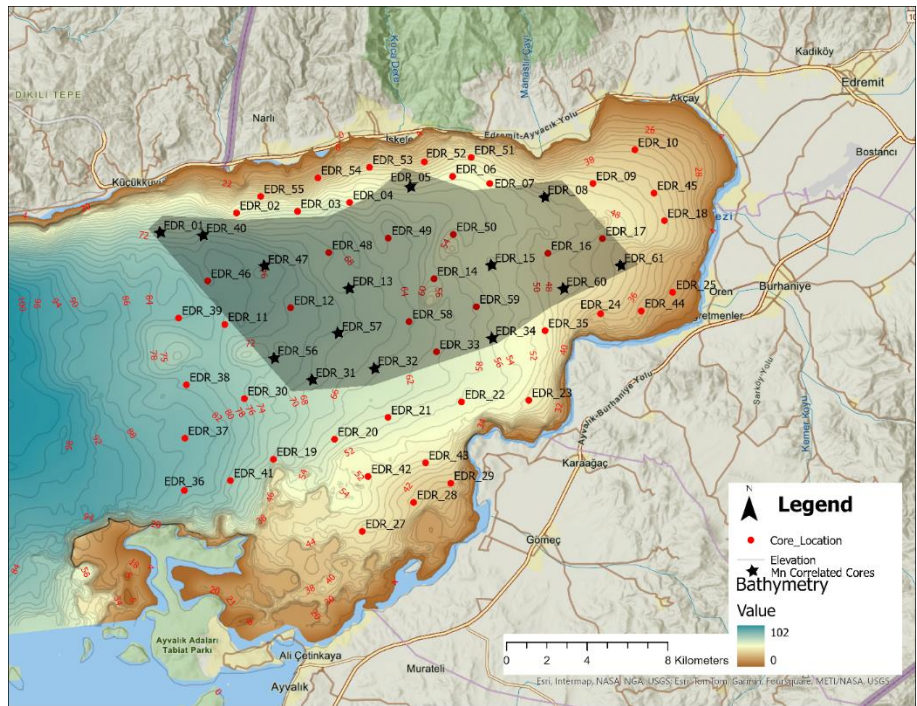
Figure 5.13 Mn correlated core samples location
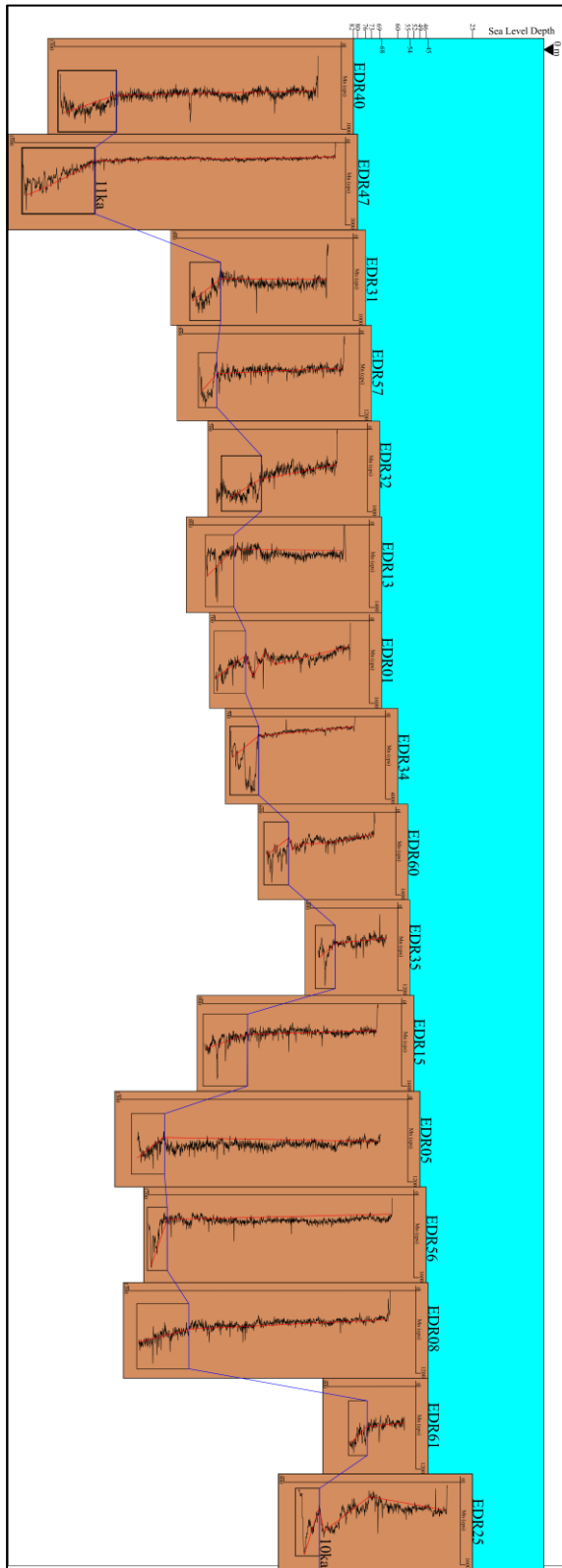
Figure 5.14 Mn correlation within cores

155

If the period in which Mn values increased in the 16 cores mentioned above is considered to be around 10 ka BP. With the help of this information, element concentration maps are regenerated for using values from the 10,000 years ago and present element concentration of each 16 cores. The results are given alongside each other's. Specifically, the Ca, Pb, Ti and Cl elements changings are interpreted in this section.
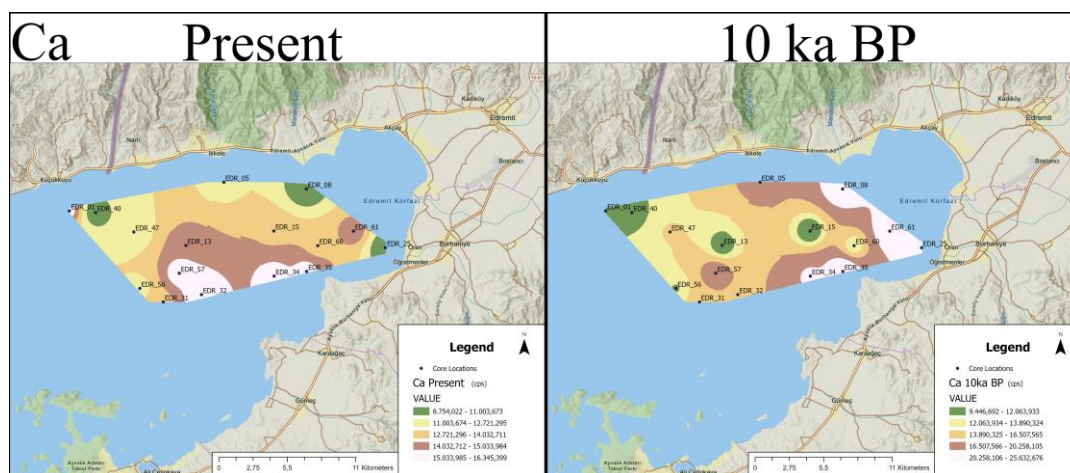
Figure 5.15 Cl concentration 10,000 years ago and present comparison

Areas with high Cl concentrations on the seafloor are often associated with evaporite deposits. Additionally, the area of highest concentration appears to whole study area except the northwestern part of the study area. These are the interpretations related with the present Cl concentration map. Before 10,000 years ago, the anomalies are divided into two as well. There were two different depocenters and both have high level of evaporations. So, the different anomalies interpretation claims the idea of two different depocenters within the study area. Additionally, the anomaly observed near the land 10,000 years ago was formed as a result of sea level rise. Evaporation began in that region, leading to evaporite accumulation. This supports the theory that the sudden sea level rise during the Holocene caused rivers to flood and retreat inland.
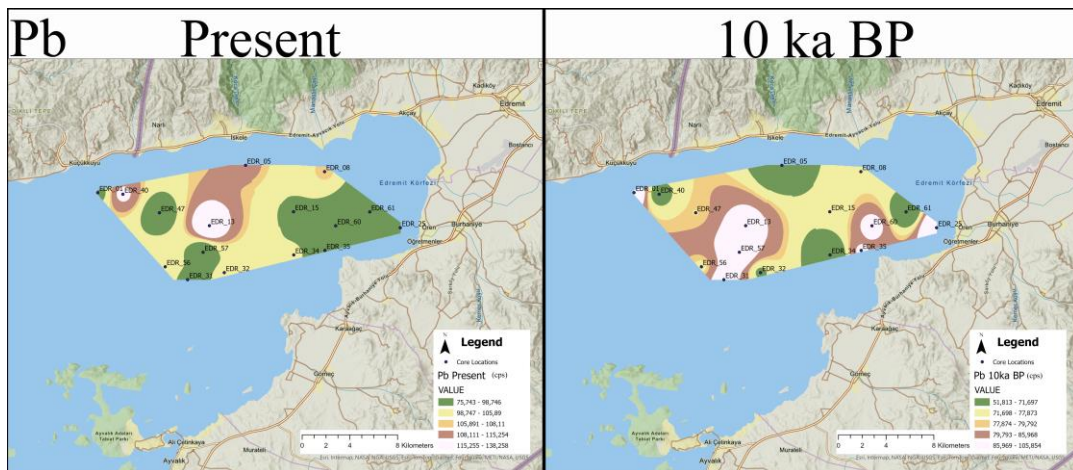
Figure 5.16 Pb concentration 10,000 years ago and present comparison

Lead is a metal typically associated with industrial pollution. When considering Pb as an indicator of anthropogenic pollution, the entire basin shows high levels of contamination, except for the offshore the southern islands in the study area. When observing the map for Pb, low anomaly is seen in the southern region on the present-day map, whereas a high Pb anomaly is evident along the southern coast 10,000 years ago concentration map. This controversial requires further investigation, as it is unlikely that anthropogenic pollution was this significant 10,000 years ago. Therefore, it is recommended to explore the possible sources of this Pb anomaly.
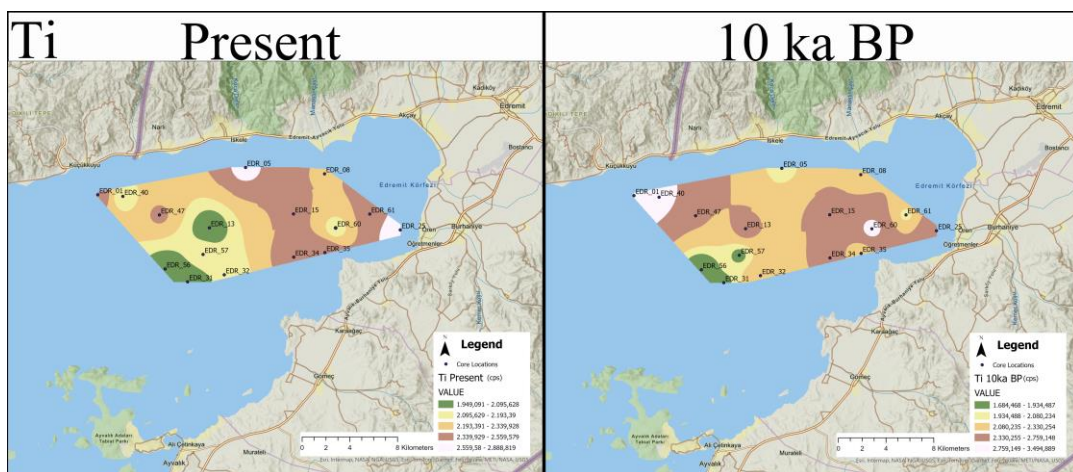
Figure 5.17 Ti concentration 10,000 years ago and present comparison

Titanium is typically associated with sediment transport from terrestrial sources. It can be concentrated in coastal sedimentary environments and river mouths. As a result, present Ti concentration map showing anomalies in the northern and southern part of the study area is not surprising. The study area receives freshwater input from both the north and the south. When examining the 10,000 years before Ti concentration map. The northwestern part anomaly which is located exactly the same place of east west fluvial system. Probably the river mouth was located closer to this Ti anomaly 10,000 years ago.
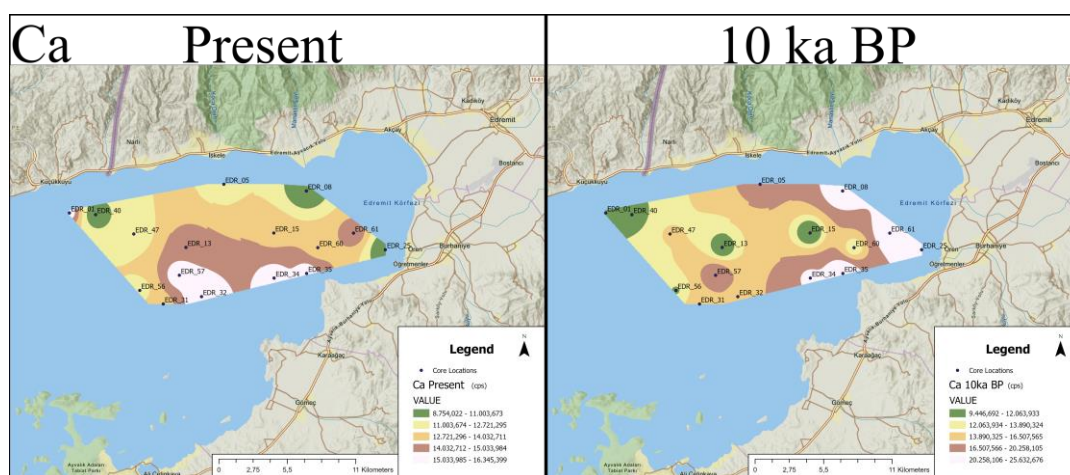
Figure 5.18 Ca concentration 10,000 years ago and present comparison

Calcium is typically associated with carbonate minerals (e.g., calcite, aragonite). High Ca concentrations on the seafloor can be observed in areas with high marine biological productivity, where carbonate organism remnants accumulate extensively. The anomaly of Ca at present concentration map is located at the southern part. The marine productivity relatively higher at those areas. On the other hand, 10,000 years ago Ca concentration map show anomalies towards to landward and southern part of the study area. The source of the Ca concentration landward sight of the study area is probably originated from carbonate minerals. Because the sea level is not enough high 10,000 years ago.

5.3 GoE and Beyond: Aligning Gulf Dynamics with Climatic Milestones

As mentioned in previous sections, over the last 16 ka, the planet has experienced both warm and cold periods. Globally, the period between 16 ka and 10 ka is generally considered a cold period, while the time from 10ka to the present is characterized as the warm period (Holocene Warm Period). During the cold period, there were local warming events, such as the Bølling–Allerød warming (14.7 ka - 12.9 ka), and during the warm period, there were local cooling events, including the 8200, 4200, and Little Ice Age cooling events. Additionally, the Figure 5.19 includes a graph showing global sea level changes and a graph from the North Greenland Ice Core Project (NGRIP) representing global $\delta 18O$ measurements. Duman et al. (2018), also suggests that the Aegean coasts have been affected by global meltwater pulses (MWPs). In this section will examine whether the global temperature changes, sea level fluctuations, NGRIP $\delta 18O$ results, and MWP events align with the geochemical results of EDR47 obtained in this study.
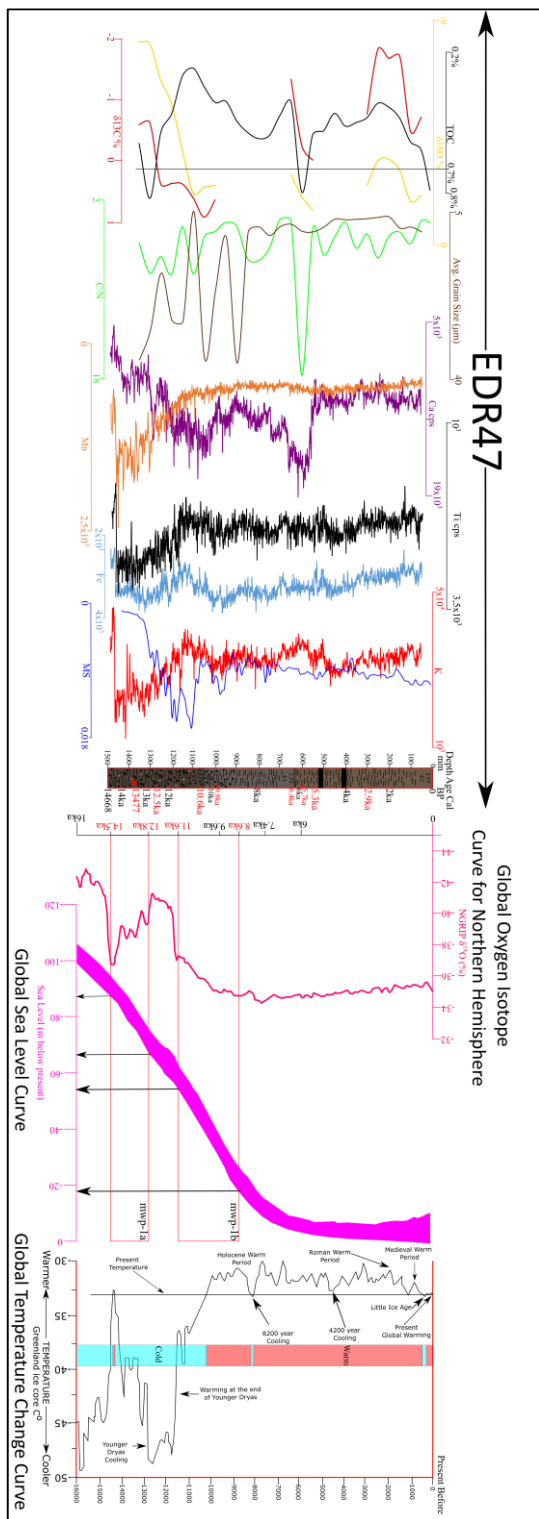
Figure 5.19 EDR47 results comparison with global climatic events (global temperature curve by Thomasson and Gerhard (2019); NGRIP δ18O and Global Sea Level Curve by Stanford et al. (2011))

5.3.1   Rapid Melt, Rising Seas: The MWP-1a (14.5 ka - 12.8 ka) Event in Focus

During the MWP-1a period, a global cooling event is observed. As previously mentioned, sea level changes during this period were driven by the melting of glaciers, resulting in catastrophic sea level rise due to freshwater influx. According to Stanford et al. (2011), in this period sea level rise 20 meters approximately. The graph indicates that around 14.5 ka, sea levels were approximately 80 meters below current levels. Core EDR47, considered one of the most representative cores of the study area, which is selected for interpretation. EDR47 took from 76 meters below sea level, it would have been on land at 14,500 years before present. During the MWP-1a period, with the sea level rise EDR47 have been deposited.

In Figure 5.19, EDR47 Mn concentration shows a significant increase at the bottom of the core, which is also seen in other cores, suggesting that this is flood-related. Additionally, elements indicating terrestrial input such as K, Fe, and Ti show positive peaks during this period. Towards 12.8 ka, their concentrations decrease. MS values exhibit an increasing trend during this interval, indicating high terrestrial input during the MWP-1a period. This increasing trend is expected outcome of increased erosion and terrestrial sediment transport due to rising sea levels.

Moreover, the mean grain size shows a significant positive peak during the MWP-1a period, indicating intense terrestrial input. The δ18O results, which show an increasing trend, suggest a shift toward colder climatic conditions. This compatible with the global temperature change curve, it is also indicating a transition toward a colder period at same interval.

5.3.2   Frozen in Time: Multiproxy Responses to Younger Dryas Period (12.9 ka – 11.7 ka)

During the Younger Dryas period, global temperatures entered a cooling phase. Glacier melting reduction is, the influx of freshwater into the ocean diminished,

leading to a slower rate of sea level rise. The global sea level change graph indicates an approximate 10 meters change during this period. Consequently, a decrease in terrestrial sediment transport to the sea is expected.

In Figure 5.19, EDR47 concentrations of terrestrial elements such as K, Fe, and Ti show a decline, indicating reducing terrestrial input. The MS values exhibit an increasing but oscillating at some levels, suggesting that terrestrial input was relatively lower compared to other periods, which compatible with expectations for this cooling phase. Meanwhile, $\delta18O$ values show a positive trend, confirming continued cooling during this period.

5.3.3   A Second Pulse: GoE Response MWP-1b (11.6 ka – 8.6 ka) Event

During the MWP-1b period, global temperatures entered a warming phase, marking the transition of the Holocene Warm Period. According to Stanford et al. (2011), sea levels rise by approximately 40 meters, causing a second catastrophic rise. This increase was driven by the influx of freshwater into the ocean due to glacial melting.

In Figure 5.19 the impact of MWP-1b on the GoE can be observed in core EDR47, where the concentrations of terrestrial elements such as K, Ti, and Fe show a relative increase compared to the Younger Dryas period. The average grain size also increases, indicating enhanced sediment transport. Additionally, MS values rise, which aligns with the expected result of intensified erosion and terrestrial material transport due to the rapid sea level rise.

The $\delta18O$ values initially show an increasing trend but then begin to decrease, indicating a shift toward warmer climatic conditions. However, the $\delta18O$ isotope record does not fully cover the entire MWP-1b period. Between 11.2 ka and 9.8 ka, a decrease in $\delta18O$ indicates a transition into a warmer climate. The global temperature curve also shows rising temperatures, marking the transition into the Holocene Warm Period.

162

5.3.4 Bridging Land and Sea: Insight from Sofular Cave and GoE Sediments

In the study based on the Sofular Cave record by Göktürk et al. (2011), the climatic changes along the Black Sea coast during the Holocene were investigated. Using stalagmite $\delta 13C$ values, growth rates, and initial (234U/238U) ratios, the study provides insights into hydrological changes above the cave. Changes in $\delta 13C$ values in stalagmites are generally associated with shifts in vegetation and soil microbial activity, which are influenced by temperature and rainfall as long as the system remains open to external factors (McDermott, 2004). Lower (234U/238U) ratios, in particular, indicate increased rainfall, which enhances weathering and dissolution of the surrounding carbonate rock (e.g., Kaufman et al., 1998; Ayalon et al., 1999; Hellstrom and McCulloch, 2000).

In Figure 5.20 based on this interpretation of Göktürk et al. (2011) the period between 9.6 ka and 5.4 ka, corresponding to the early- to mid-Holocene, is identified as a wet period. During this period, core EDR47 shows a significant increase in Ca concentration. Starting from 9.6 ka, Ca concentrations rise, peaking around 5.7 ka, before decreasing between 5.7 ka and 5.3 ka. K, Fe, and Ti elements are also increasing trends periodically. MS values are not as high as in the MWP-1b or Younger Dryas periods, but they still increasing at some levels. So, the surface runoff increasing as well at some levels.

Examining the TOC and C/N ratios reveals that the increase in TOC levels contributes to the accumulation of relatively organic-rich material. As previously mentioned, a high C/N ratio indicates that the organic matter in the marine sediment is primarily derived from terrestrial sources. This observation in core EDR47 aligns with the Sofular Cave Record, which suggests that this period was characterized by increased precipitation. Furthermore, since Ca can have both terrestrial and marine origins, it is likely that the high Ca concentration during this period is primarily of terrestrial origin.
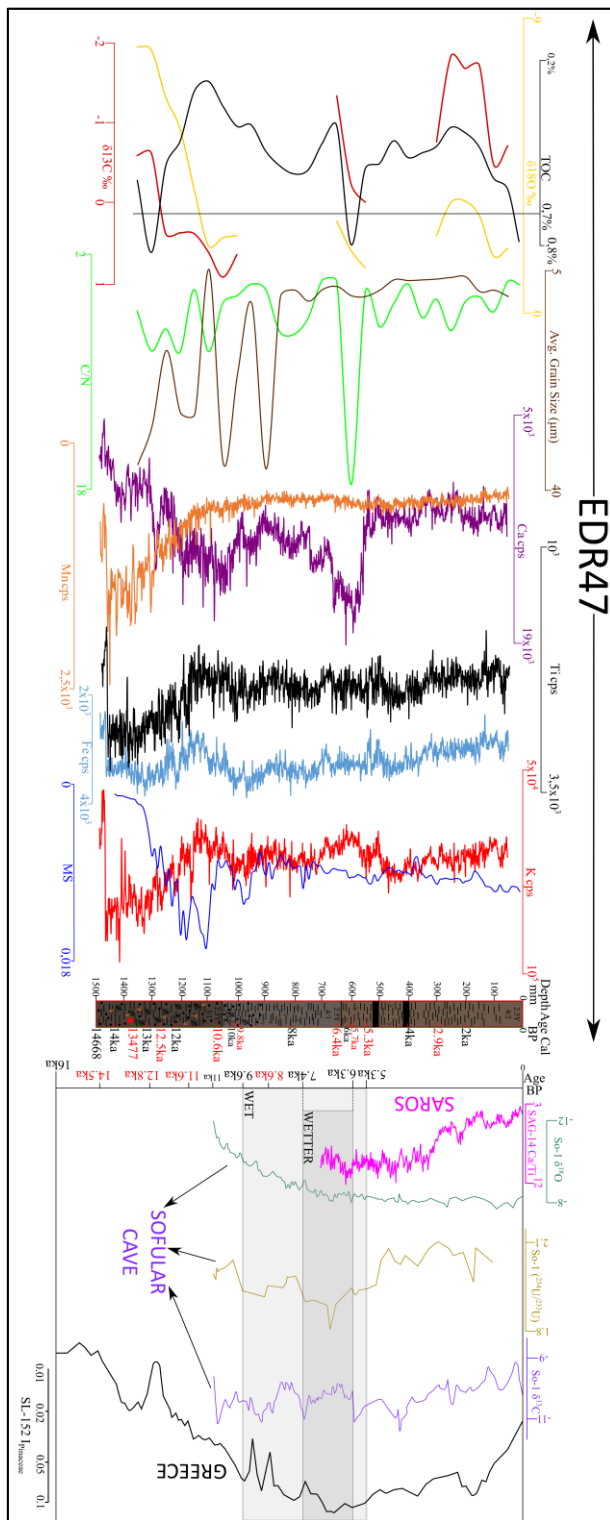
Figure 5.20 EDR47 multi proxy results comparison with, SAG14 Ca/Ti ratio (Bozyiğit et. al., 2022), SL152 Pinaceae Index (Kotthoff et. al., 2008) and Sofular Cave Records δ18O; δ13C; 233U/234U results (Göktürk et. al., 2011)

5.3.5 Aegean Connections: Linking GoE with Mount Athos Basin
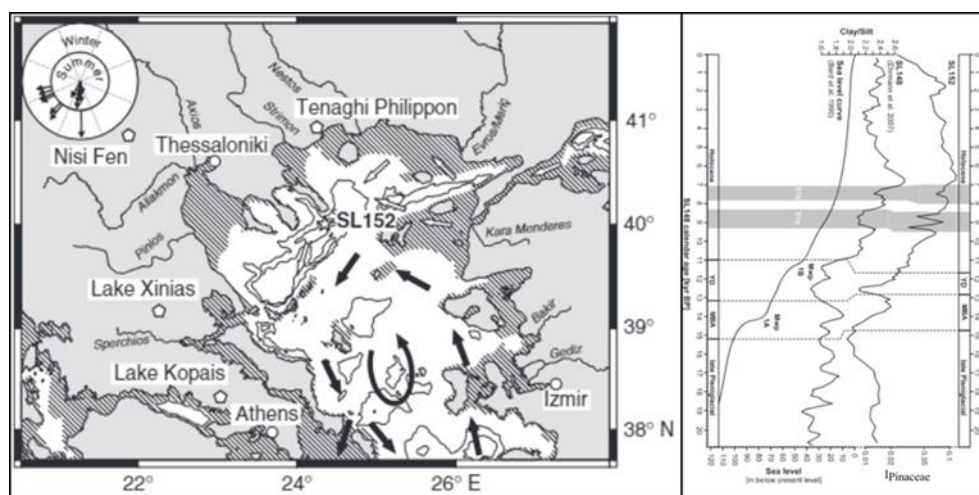
Figure 5.21 Location map and SL152 results from Kotthoff et al. (2008)

Kotthoff et al. (2008) they took a core sample from offshore Greece (Thessaloniki). The name of the core is SL-152. They have research on core sample about the vegetation dynamics in the Aegean region over the past 20,000 years, primarily driven by changes in moisture availability. The location map of SL152 and the late glacial to present variations in Pinaceae index IPinaceae (Abies/Abies+Pinus, 5-point running means) in core SL152, northern Aegean Sea are given in the Figure 5.20 and 5.21. The climatic impacts related periods and their moisture availability is given in last 20,000 years,

Early Dry Period (20 - 14.6 ka BP): Steppe vegetation dominated, indicating dry conditions.

Lateglacial Period (Meiendorf/Bølling/Allerød Interstadial Complex): Moisture increased slightly, leading to some broadleaved tree growth, though steppe vegetation persisted. Pine forests covered shelf areas of the Aegean until they were submerged by sea-level rise, which coincided with a significant drop in pine pollen (15 - 13 ka BP) due to meltwater pulse MWP-1a.

Younger Dryas (12.9 - 11.7 ka BP): Identified as the driest period of the last 20,000 years.

Post-Younger Dryas (11.7 - 10.2 ka BP): Insufficient humidity delayed reforestation, with a notable setback around 10.9 kyr BP.

Holocene (Last 10,000 years): Repeated setbacks in vegetation due to reduced moisture occurred at intervals around 9.3, 8.7, 8.3, 7.6, 6.7, 5.6, and 4.3 ka BP, characterized by reduced tree pollen and increased steppe vegetation.

As Kotthoff et al. (2008) described, the Early Dry Period (20 - 14.6 ka BP) cannot be analyzed in this study since our age data does not extend that far back. However, results from core EDR47 align with the characteristics of the Late Glacial Period and MWP-1a, which Kotthoff et al. (2008) identified as a period of increased moisture. High concentrations of K, Fe, and Ti indicate significant terrestrial input during this time, and MS values also show an increasing trend. The rise in Mn concentration, associated with MWP-1a as well. So, the findings from core SL152 and results from EDR47 is similar to each other.

Kotthoff et al. (2008) identified the Younger Dryas as the driest period of the last 20,000 years. In core EDR47, this period is reflected to some extent by a decrease in concentrations of terrestrial elements such as K, Fe, and Ti. However, pointing this interval as the driest period within core EDR47 is challenging.

Post-Younger Dryas (11.7 - 10.2 ka BP) and Holocene (last 10,000 years) periods show decreasing humidity over time, as seen in the results from core SL-152. The findings from core EDR47 align with this interpretation, except for the interval between 9.6 - 5.2 ka BP. According to the Sofular Cave records, this interval is considered a wet period, which is also reflected in core EDR47 by a significant peak in Ca concentration. Additionally, TOC analysis from EDR47 indicates that the organic matter deposited during this period was transported from terrestrial sources, as suggested by the C/N ratio. The evidence of Ca being transported from land,

coinciding with the wet period identified in the Sofular Cave records, supports this hypothesis.

5.3.6   A Tale of Two Gulfs: Comparing Climate Records of Edremit and Saros
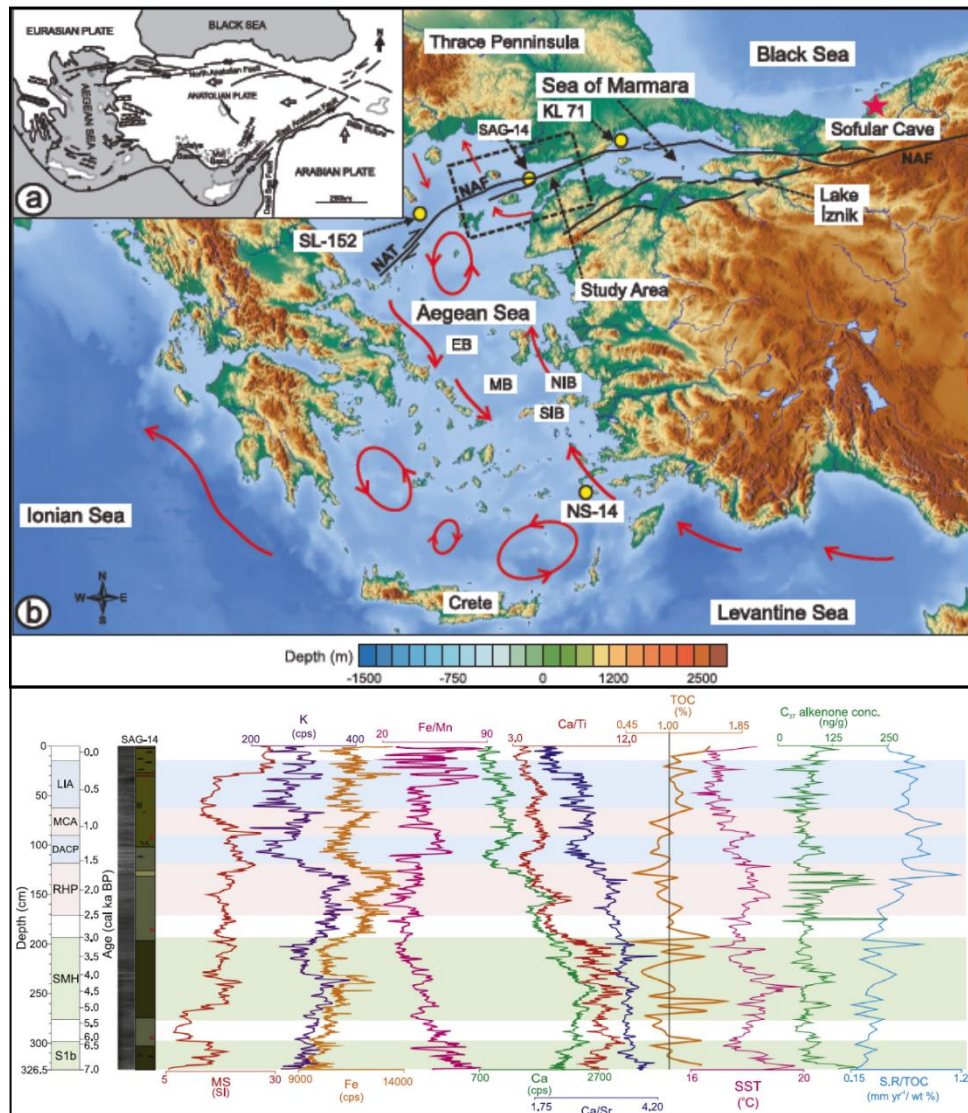
Figure 5.22 SAG-14 core location and multiproxy results (Bozyiğit et al., 2022)

Bozyiğit et al. (2022), researched the sedimentary and climatic history of the Gulf of Saros (GoS) and its relation to regional climate events, primarily during the middle-to-late Holocene. There is a close match between the GoS sedimentary records and broader marine and continental records from the northern Aegean and Black seas, indicating similar timing of past climate events. They compare their results with Sofular Cave Records as well. Two distinct sapropel layers were deposited in the GoS and each climate conditions changes are given as below from 7,000 years ago,

Older Sapropel Layer (S1b): Formed under warm, humid conditions with high river discharge and enhanced productivity, driven by weakly stratified surface waters and high sedimentation rates.

Younger Holocene Sapropel (SMH; 5.4 – 3.0 ka BP): Initially developed under warm, dry conditions until 4.5 ka BP, later transitioning to cold, wet conditions, possibly linked to Black Sea outflow. The μ-XRF Fe/Mn ratio suggests a shift from suboxic to anoxic bottom waters during this time, with highly variable total organic carbon (TOC) levels.

Recent Holocene Phases:

Roman Humid Period (RHP; 2.5 – 1.55 ka BP): Characterized by a shift from dry to wet conditions.

Dark Ages Cold Period (DACP; 1.55 – 1.3 ka BP): Started dry but transitioned to wetter conditions, which continued into the Medieval Climate Anomaly (MCA; 1.1–0.7 ka BP).

Little Ice Age (LIA): Marked by a shift from dry to wet conditions from its early to late phases, accompanied by increased soil erosion and detrital delivery due to deforestation and human activities, leading to delta progradation across southern Europe.

According to Bozyiğit et al. (2022), the results from core SAG-14 indicate warm and humid conditions with high terrestrial input during the S1b period (7 - 5.4 ka BP) which is seen in Figure 5.20 and 5.22. EDR47 shows a similar pattern, with high

terrestrial input between 9.6 - 5.2 ka BP, as suggested by the high Ca concentration and C/N ratio obtained from TOC analysis. Between 6.3 - 5.4 ka BP, δ18O values exhibit a positive trend, indicating a shift towards a cold and dry climate.

In Figure 5.20 and 5.22, Bozyiğit et al. (2022), also identified a transition to colder and drier conditions starting around 4.5 ka BP, within the Younger Holocene Sapropel (SMH, 5.4 - 3 ka BP) period. They further noted that during the Recent Holocene, the climate alternated between dry and wet conditions, a similar pattern also observed in core EDR47. For example, between 2.9 - 1.8 ka BP, δ18O values show a decreasing trend, indicating a relatively warmer and more humid period, while from 1.8 ka BP, δ18O values show an increasing trend, pointing to a relatively colder and drier climate. But at the end, as Kotthoff et al. (2008), suggest that, the general trend throughout the Holocene has been decreasing moisture level, leading to a drier climate over time. The concentration of terrestrial elements also shows a gradual decline in EDR47 and showing the climate is leading to drier over time as well.

5.4 Environmental Stories Written in Sediments: GoE Insights
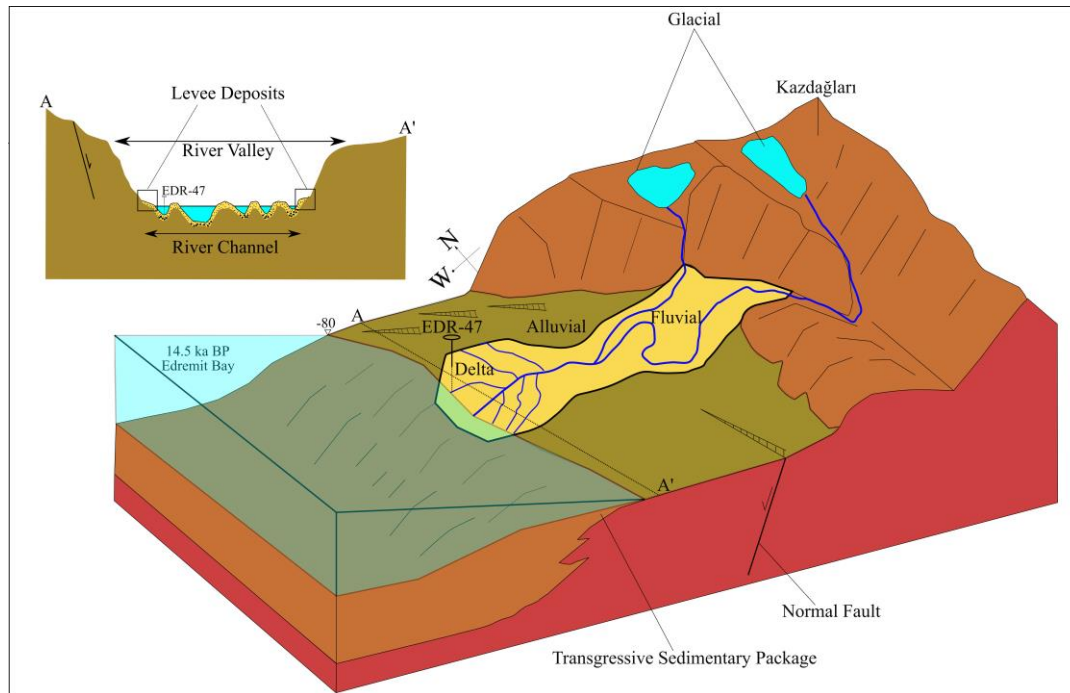
Figure 5.23 GoE schematic diagram of 14.5 ka BP

The previously discussed MWP-1a and MWP-1b floods are two significant events that directly influenced the deposition patterns in the GoE. The schematic diagram above illustrates the position of the sea level at the gulf around 14.5 ka. So, before MWP-1a, sea level was approximately 80 meters below its present level.

Throughout the Edremit Basin, an east-west-oriented fluvial system was present in each period, which Yaltırak (2003) identified as a paleochannel in seismic interpretations. The deltaic deposition brought by this fluvial system is illustrated in yellow. In the A-A' cross-section, a river channel is visible along with the yellow-colored delta deposit accumulated within it. Core EDR47, however, was not yet underwater at this time; it was located in the delta plain and not deposited yet. The schematic diagram shows the location of core EDR47 within the delta system.
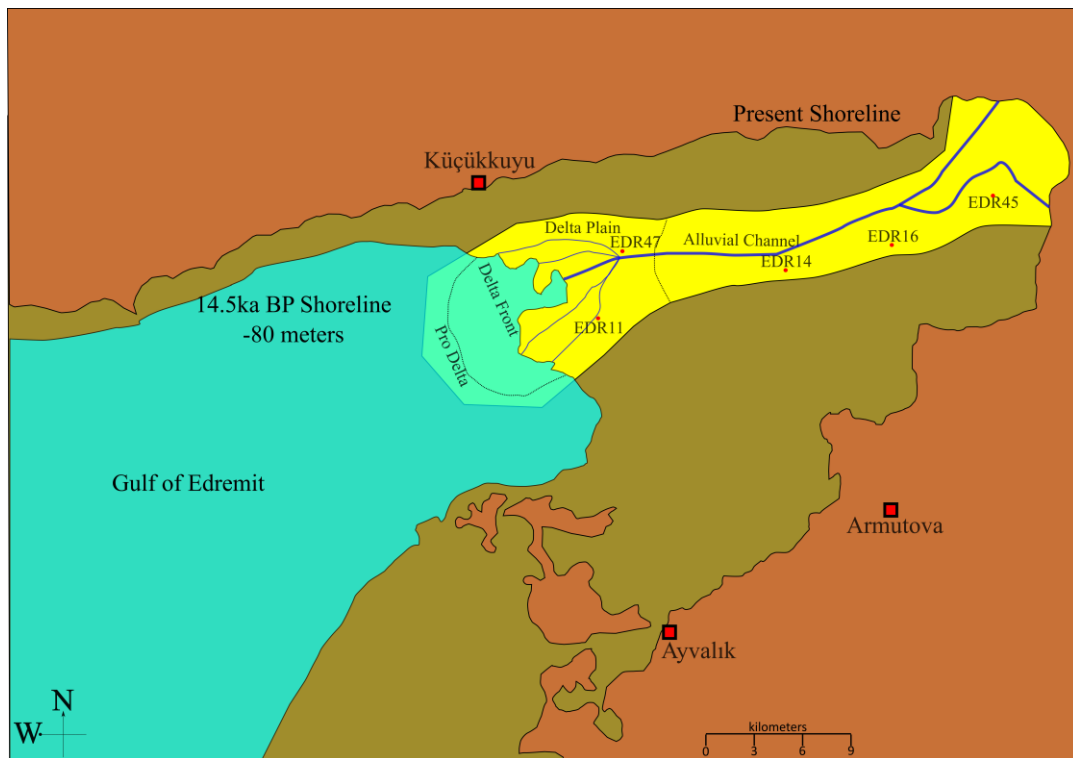
Figure 5.24 GoE top view 14.5 ka BP

The shoreline is drawn at a sea level 80 meters below the present morphology, and additional core locations, where grain size measurements were taken, are also marked on the diagram.
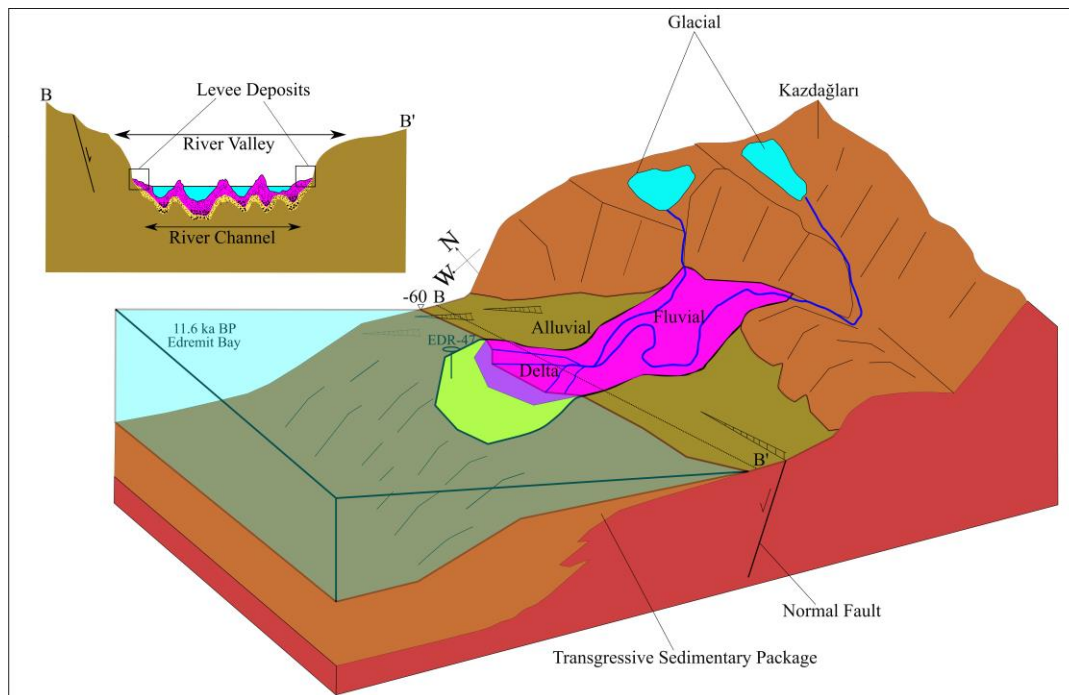
Figure 5.25 GoE schematic diagram of 11.6 ka BP

Later, at 11.6 ka BP, the schematic diagram shows the sea level during this period. Between 14.5 ka and 11.6 ka, MWP-1a and the Younger Dryas periods occurred, causing a rise in sea level of approximately 20 meters. As a result, an incised valley fill system formed.

Similar examples are found in Asia's Changjiang, Song Hong, and Kiso Rivers, where sudden Holocene Sea level rise led to a shift in sedimentary facies from estuarine sand and mud to shelf or prodelta mud, indicating increased marine influence within these valleys during this period. Consequently, estuarine systems and their depocenters migrated inland.

A similar situation is observed in the GoE. Due to a 20 meters sea level rise, cores EDR11 and EDR47 were submerged. With the retreat of the delta, core EDR47, which was located on the delta plain around 14.5 ka, continued to accumulate sediments at the delta front (subaqueous delta plain) as sea levels rose. By 11.6 ka, it likely shifted to the prodelta zone, continuing its deposition. This is an expected outcome.

The grain size variation in core EDR47 supports this interpretation: initially deposited on the delta plain, EDR47 shows a predominance of coarse materials like medium sand and fine sand. The delta plain and delta front are characterized by coarser, sand-sized grains. As the core progresses towards the middle, the abundance of coarse material decreases, indicating a transition to the finer, silt- and clay-rich prodelta zone as sea levels continued to rise.

A similar grain size shift is observed in core EDR11, reinforcing the interpretation of depositional changes due to rising sea levels.
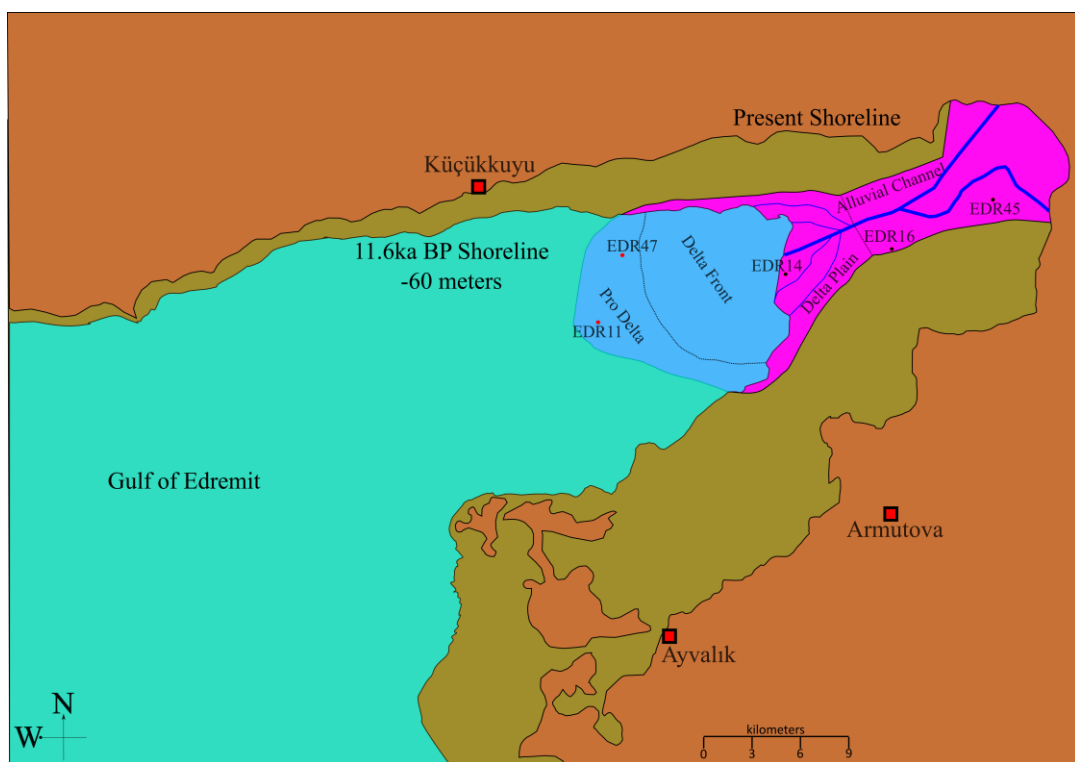
Figure 5.26 GoE top view 11.6 ka BP
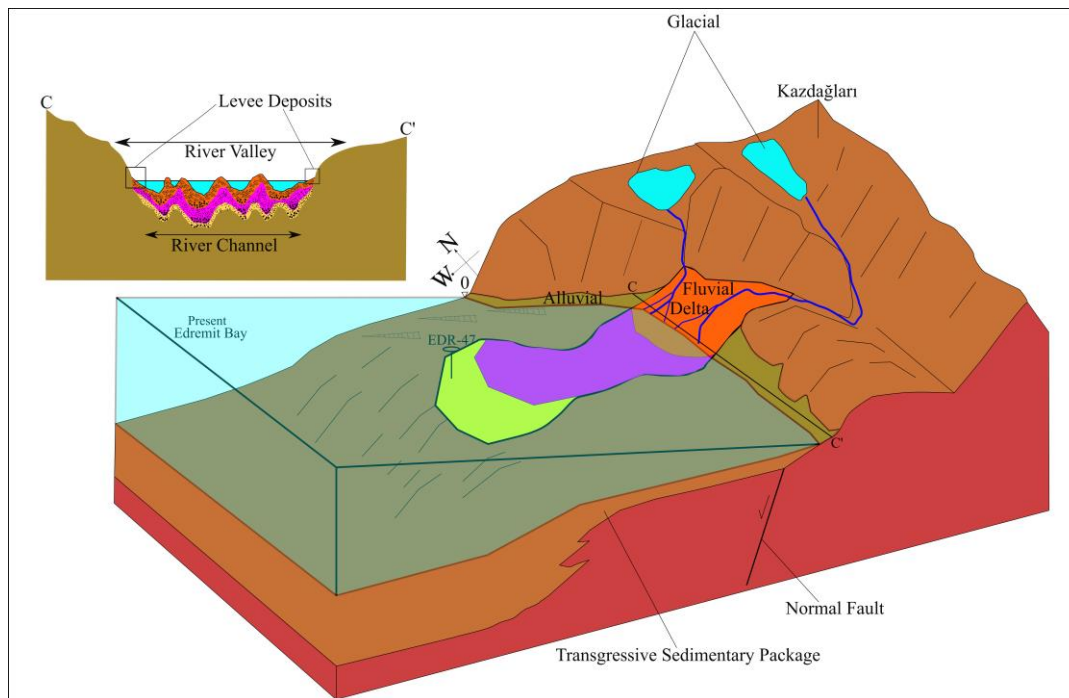
Figure 5.27 GoE schematic diagram of present

The final schematic diagram illustrates the current sea level. Transgression has continued, including a second sea level rise during MWP-1b, resulting in an approximate 40 meters increase that brought the sea level to its present state. According to the Sofular Cave records, the period between 9.4 ka and 5.4 ka experienced rainy and very wet conditions. This period likely intensified terrestrial input, affecting the delta system. However, the incised valley fill system is generally thought to have persisted to the present.

Figure 5.28 GoE top view present

In the schematic view representing 11.6 ka BP, cores EDR14 and EDR16 were located within the delta plain. Over time, as sea levels rose, they transitioned to the delta front and prodelta zones, respectively. This shift is reflected in the grain size change, showing a gradual transition from coarse to finer material.

EDR45, however, still remains within a part of the delta system, specifically in the prodelta zone. This is evident from the grain size distribution, where coarse material is abundant at the base of the core, while finer material dominates closer to the present, indicating the gradual transition from deltaic to marine deposition over time.

In conclusion, as discussed in earlier sections, a fluvial system extends from the east to the west of the gulf. During the Holocene, catastrophic sea level rises, such as MWP-1a and MWP-1b, caused this fluvial system's depocenter to migrate inland. These findings are supported by elemental changes in core EDR47, various additional analysis, and grain size variations in the cores. To illustrate this more

175

clearly, several visual representations have been created, showing the locations of cores within this fluvial system and its delta system.

5.5   From Past to Future: Predicting Environmental Trends in GoE

Building upon detailed reconstructions of climatic variability, depositional evolution, and sediment dynamics in the Gulf of Edremit, this study offers a valuable framework for understanding and predicting future environmental and sedimentary changes in similar coastal and tectonically active regions. The findings emphasize the critical interplay between global climatic events, local environmental variability, and tectonic processes as key drivers shaping sedimentary systems in the context of ongoing climate change and anthropogenic pressures.

A major conclusion of this study is the sensitivity of the Gulf of Edremit to abrupt sea-level rise events, such as those associated with Meltwater Pulses (MWP-1a and MWP-1b). These events caused significant changes in sedimentary dynamics and depositional environments, highlighting the potential for future rapid sea-level rise to trigger similar shifts. The documented inland migration of depocenters and transitions from deltaic to marine environments serve as analogs for coastal evolution under accelerating sea-level rise. Moreover, the influence of redox conditions on sediment preservation and elemental distribution suggests that ongoing marine deoxygenation, driven by climate change, could further alter sedimentary processes and geochemical patterns in the region.

Comparative analyses with other Aegean and Mediterranean sites demonstrate that the Gulf of Edremit is part of a broader system highly responsive to global climatic oscillations. These findings provide a foundation for predictive models of sedimentation and environmental change across the Mediterranean and other similar regions. Such insights are critical for coastal management, hazard assessment, and the development of strategies to mitigate the impacts of climate change. Future research should integrate these findings with advanced modeling approaches to

better anticipate the effects of climate variability and tectonic activity on coastal and marine depositional systems in the Anthropocene.

CHAPTER 6

CONCLUSION

I. This study successfully reconstructed the climate variability in the Gulf of Edremit from the Late Pleistocene to the Holocene by employing a multi-proxy approach. Key climatic and oceanographic oscillations were identified and characterized, providing a detailed understanding of the region's climatic history and its broader environmental context.

II. Depositional evolution of the Gulf of Edremit was documented in detail through an integrated geochemical and sedimentological analysis. The findings demonstrate how shifts in climate, sea level, and redox conditions influenced sedimentary processes, shaping the depositional history of the region over time.

III. Identification of forcing factors, this research identified the primary forcing factors driving sedimentation dynamics in the Gulf of Edremit, including global climatic events, local environmental variability, and tectonic processes. The interplay between these factors was shown to strongly influence depositional patterns and sedimentary characteristics within the gulf.

IV. This study also traced the origins of sediments and mapped their transport pathways. Elemental concentration maps for key elements such as Fe, Pb, Ti, and Ca provided significant insights into sediment sources, transport dynamics, and depositional environments through time.

V. The impact of catastrophic sea level rises, the influence of Meltwater Pulse (MWP) events, specifically MWP-1a and MWP-1b, on sedimentary dynamics was identified. These rapid sea level rises triggered significant changes in sedimentary facies, illustrating how the depositional environment of the Gulf of Edremit responded to abrupt global climatic events.

VI. The findings were compared with global climatic events and local records, including data from the Sofular Cave in Black Sea coast, the SL152 core and the SAG-14 core in the Gulf of Saros in Northern Aegean Sea. These comparisons validated the study's results and revealed connections between local sedimentary changes and broader climatic and oceanographic events.

VII. Schematic representations of the depositional patterns in the Gulf of Edremit during key intervals (e.g., 14.5 ka BP, 11.6 ka BP, and the present) illustrated the progressive impacts of transgression and sediment dynamics. These visualizations revealed the inland migration of depocenters and transitions from deltaic to fully marine environments over time.

VIII. The application of a multi-proxy approach; including ITRAX-XRF, MSCL, TOC, radiocarbon dating, oxygen isotope analysis, and grain size distribution; offered a robust framework for interpreting paleoclimate, paleoceanography, and depositional history. The integration of these datasets allowed for a comprehensive understanding of sedimentary processes and environmental changes in the study area.

IX. By situating the findings within the broader context of the Aegean Sea, this study advanced the understanding of how climate variability influenced depositional evolution across the region during the Late Pleistocene and Holocene. Comparative analyses with other Aegean regions provided valuable insights into the spatial and temporal variability of sedimentary and climatic processes.

X. This research highlights the influence of redox conditions and climate variability on sediment dynamics, offering a valuable dataset for future investigations of marine depositional systems. It underscores the importance of integrating geochemical and sedimentological analyses to study the interactions between climate, tectonics, and sedimentary processes.

Finally, the findings of this study emphasize the complex interplay of climate, tectonics, and sediment dynamics in shaping the depositional history of the Gulf of Edremit. By providing a detailed and high-resolution reconstruction of the region's

paleoenvironment, this research not only enhances our understanding of the Gulf of Edremit but also serves as a reference for comparative studies in other tectonically active and climatically sensitive regions. The conclusions drawn from this thesis contribute to broader efforts in paleoenvironmental research and improve the understanding of sedimentary responses to global and local climatic events.

REFERENCES

A. Barka, & R. Reilinger. (1997). Active tectonics of the Eastern Mediterranean region: deduced from GPS, neotectonic and seismicity data. Annals of Geophysics, 40(3). https://doi.org/10.4401/ag-3892

Agnihotri, R., Altabet, M. A., Herbert, T. D., & Tierney, J. E. (2008). Subdecadally resolved paleoceanography of the Peru margin during the last two millennia. Geochemistry, Geophysics, Geosystems, 9(5). https://doi.org/10.1029/2007GC001744

Ak Sefa. (2019). Alluvial geomorphological research on the Edremit Plain.

Aktug, B., Nocquet, J. M., Cingöz, A., Parsons, B., Erkan, Y., England, P., Lenk, O., Gürdal, M. A., Kilicoglu, A., Akdeniz, H., & Tekgül, A. (2009). Deformation of western Turkey from a combination of permanent and campaign GPS data: Limits to block-like behavior. Journal of Geophysical Research: Solid Earth, 114(B10). https://doi.org/10.1029/2008JB006000

Alley, R. B. (2000). The Younger Dryas cold interval as viewed from central Greenland. Quaternary Science Reviews, 19(1–5), 213–226. https://doi.org/10.1016/S0277-3791(99)00062-1

Alley, R. B., Mayewski, P. A., Sowers, T., Stuiver, M., Taylor, K. C., & Clark, P. U. (1997). Holocene climatic instability: A prominent, widespread event 8200 yr ago. Geology, 25(6), 483. https://doi.org/10.1130/0091-7613(1997)025<0483: HCIAPW>2.3.CO;2

Arz Helge W., Patzold Jurgen, Muammar Mustafa O., & Rohl Ursula. (2001). Late quaternary climate records from the Northern Red Sea: results on gravity cores retrieved during the R V METEOR Cruise M44 3. Journal of King Abdul Aziz University: Marine Science, 12, 101–113.

Ayalon, A., Bar-Matthews, M., & Kaufman, A. (1999). Petrography, strontium, barium and uranium concentrations, and strontium and uranium isotope ratios in speleothems as palaeoclimatic proxies: Soreq Cave, Israel. The Holocene, 9(6), 715–722. https://doi.org/10.1191/095968399673664163

Aysal, N., Ustaömer, T., Öngen, S., Keskin, M., Köksal, S., Peytcheva, I., & Fanning, M. (2012). Origin of the Early-Middle Devonian magmatism in the Sakarya Zone, NW Turkey: Geochronology, geochemistry and isotope systematics. Journal of Asian Earth Sciences, 45, 201–222. https://doi.org/10.1016/j.jseaes.2011.10.011

Bard, E., Hamelin, B., Arnold, M., Montaggioni, L., Cabioch, G., Faure, G., & Rougerie, F. (1996). Deglacial sea-level record from Tahiti corals and the

timing of global meltwater discharge. Nature, 382(6588), 241–244. https://doi.org/10.1038/382241a0

Bard, E., Hamelin, B., & Fairbanks, R. G. (1990). U-Th ages obtained by mass spectrometry in corals from Barbados: sea level during the past 130,000 years. Nature, 346(6283), 456–458. https://doi.org/10.1038/346456a0

Beccaletto, L., Bonev, N., Bosch, D., & Bruguier, O. (2007). Record of a Palaeogene syn-collisional extension in the north Aegean region: evidence from the Kemer micaschists (NW Turkey). Geological Magazine, 144(2), 393–400. https://doi.org/10.1017/S001675680700310X

Beccaletto, L., & Steiner, C. (2005). Evidence of two-stage extensional tectonics from the northern edge of the Edremit Graben, NW Turkey. Geodinamica Acta, 18(3–4), 283–297. https://doi.org/10.3166/ga.18.283-297

Beuselinck, L., Govers, G., Poesen, J., Degraer, G., & Froyen, L. (1998). Grain-size analysis by laser diffractometry: comparison with the sieve-pipette method. CATENA, 32(3–4), 193–208. https://doi.org/10.1016/S0341-8162(98)00051-4

Bingöl, E., Akyürek, B., Korkmazer, B. 1975. Biga Yarımadası'nın jeolojisi ve Karakaya Formasyonu'nun bazı özellikleri. Cumhuriyetin 50. Yılı Yerbilimleri Kongresi Tebliğleri, Maden Tetkik ve Arama Genel Müdürlüğü Enstitüsü, 70–77.

Blaauw, M. (2010). Methods and code for 'classical' age-modelling of radiocarbon sequences. Quaternary Geochronology, 5(5), 512–518. https://doi.org/10.1016/j.quageo.2010.01.002

Blott, S. J., & Pye, K. (2001). GRADISTAT: a grain size distribution and statistics package for the analysis of unconsolidated sediments. Earth Surface Processes and Landforms, 26(11), 1237–1248. https://doi.org/10.1002/esp.261

Bonev, N., Klain, L., & Pimpirev, C. (2009). Lithologic-tectonic aspect of the Circum-Rhodope Belt flysch in the Chalkidiki Peninsula (Sithonia) and Rodopi-Thrace districts, northern Greece. Proceedings of Annual Conference of the Bulgarian Geological Society "Geosciences, 8.

Boztepe-Güney, A., Yılmaz, Y., Demirbağ, E., Ecevitoğlu, B., Arzuman, S., & Kuşçu, İ. (2001). Reflection seismic study across the continental shelf of Baba Burnu promontory of Biga Peninsula, northwest Turkey. Marine Geology, 176(1–4), 75–85. https://doi.org/10.1016/S0025-3227(01)00170-0

Bozyiğit, C., Eriş, K. K., Sicre, M.-A., Çağatay, M. N., Uçarkuş, G., Klein, V., & Gasperini, L. (2022). Middle-late Holocene climate and hydrologic changes in the Gulf of Saros (NE Aegean Sea). Marine Geology, 443, 106688. https://doi.org/10.1016/j.margeo.2021.106688

Bramlette M. N., & Bradley W. H. (1940). Geology and biology of North Atlantic deep-sea cores. Lithology and Geologic Interpretations. U. S. Geol. Survey, Prof. Paper, 34.

Burdige, D. J. (2007). Preservation of Organic Matter in Marine Sediments: Controls, Mechanisms, and an Imbalance in Sediment Organic Carbon Budgets? Chemical Reviews, 107(2), 467–485. https://doi.org/10.1021/cr050347q

Carlson, A. E., Oppo, D. W., Came, R. E., LeGrande, A. N., Keigwin, L. D., & Curry, W. B. (2008). Subtropical Atlantic salinity variability and Atlantic meridional circulation during the last deglaciation. Geology, 36(12), 991. https://doi.org/10.1130/G25080A.1

Casford, J. S. L., Abu-Zied, R., Rohling, E. J., Cooke, S., Fontanier, C., Leng, M., Millard, A., & Thomson, J. (2007). A stratigraphically controlled multiproxy chronostratigraphy for the eastern Mediterranean. Paleoceanography, 22(4). https://doi.org/10.1029/2007PA001422

Cavazza, W., Okay, A. I., & Zattin, M. (2009). Rapid early-middle Miocene exhumation of the Kazdağ Massif (western Anatolia). International Journal of Earth Sciences, 98, 1935–1947.

Cenk Yaltırak. (2003). Geodynamic Evolution of Gulf of Edremit and Northern Area.

Coleman, J.M. and Prior, D.B. (1980) Deltaic Sand Bodies. Short Course Education Course Note Series, AAPG, 5.

Cooper, J. A. G., Green, A. N., & Compton, J. S. (2018). Sea-level change in southern Africa since the Last Glacial Maximum. Quaternary Science Reviews, 201, 303–318. https://doi.org/10.1016/j.quascirev.2018.10.013

Cronan, D. S., Rothwell, G., & Croudace, I. (2010). An ITRAX Geochemical Study of Ferromanganiferous Sediments from the Penrhyn Basin, South Pacific Ocean. Marine Georesources & Geotechnology, 28(3), 207–221. https://doi.org/10.1080/1064119X.2010.483001

Deines, P. (1980). The Isotopic Composition of Reduced Organic Carbon. In The Terrestrial Environment, A (pp. 329–406). Elsevier. https://doi.org/10.1016/B978-0-444-41780-0.50015-8

Druffel, E. R. M., Williams, P. M., Bauer, J. E., & Ertel, J. R. (1992). Cycling of dissolved and particulate organic matter in the open ocean. Journal of Geophysical Research: Oceans, 97(C10), 15639–15659. https://doi.org/10.1029/92JC01511

Du, X., Rate, A. W., & Gee, M. A. M. (2012). Redistribution and mobilization of titanium, zirconium and thorium in an intensely weathered lateritic profile in

Western Australia. Chemical Geology, 330–331, 101–115. https://doi.org/10.1016/j.chemgeo.2012.08.030

Duru, M., Pehlivan, Ş., Okay, A.İ., Şentürk, Y., Kar, H. 2012. Biga Yarımadası'nın Tersiyer Öncesi Jeolojisi. Biga Yarımadası'nın Genel ve Ekonomik Jeolojisi. Maden Tetkik ve Arama Genel Müdürlüğü Özel Yayın Serisi 28, 7-74

Dymond, J., & Collier, R. (1996a). Particulate barium fluxes and their relationships to biological productivity. Deep Sea Research Part II: Topical Studies in Oceanography, 43(4–6), 1283–1308. https://doi.org/10.1016/0967-0645(96)00011-2

Dymond, J., & Collier, R. (1996b). Particulate barium fluxes and their relationships to biological productivity. Deep Sea Research Part II: Topical Studies in Oceanography, 43(4–6), 1283–1308. https://doi.org/10.1016/0967-0645(96)00011-2

Eastwood, W. J., Leng, M. J., Roberts, N., & Davis, B. (2007). Holocene climate change in the eastern Mediterranean region: a comparison of stable isotope and pollen data from Lake Gölhisar, southwest Turkey. Journal of Quaternary Science, 22(4), 327–341. https://doi.org/10.1002/jqs.1062

Emeis, K.-C., Struck, U., Schulz, H.-M., Rosenberg, R., Bernasconi, S., Erlenkeuser, H., Sakamoto, T., & Martinez-Ruiz, F. (2000). Temperature and salinity variations of Mediterranean Sea surface waters over the last 16,000 years from records of planktonic stable oxygen isotopes and alkenone unsaturation ratios. Palaeogeography, Palaeoclimatology, Palaeoecology, 158(3–4), 259–280. https://doi.org/10.1016/S0031-0182(00)00053-5

Emiliani, C. (1955). Pleistocene temperatures. The Journal of Geology, 63(6), 538–578.

EPA (1999) Total Organic Carbon in Water (Combustion or Oxidation), Method 415.1 (UV Promoted, Persulfate Oxidation). U.S. Environmental Protection Agency, Washington DC.

Epstein, S., & Mayeda, T. (1953). Variation of O18 content of waters from natural sources. Geochimica et Cosmochimica Acta, 4(5), 213–224. https://doi.org/10.1016/0016-7037(53)90051-9

Ercan T., Satır M., Steinitz G., Dora A., Sarıfakıoğlu E., Adis C., Walter J., & Yıldırım T. (1995). Biga Yarimadasi İle Gökçeada, Bozcaada Ve Tavşan Adalarindaki (Kb Anadolu) Tersiyer Volkanizmasinin Özellikleri. MTA Dergisi, 55–86.

Erdoğan, B., Akay, E., Hasözbek, A., Satır, M., & Siebel, W. (2013). Stratigraphy and tectonic evolution of the Kazdağı Massif (NW Anatolia) based on field studies and radiometric ages. International Geology Review, 55, 2060–2082. https://api.semanticscholar.org/CorpusID:128630657

Eytemiz, C., & Özel, F. E. (2020). Investigation of Active Tectonics of Edremit Gulf, Western Anatolia (Turkey), Using High-Resolution Multi-Channel Marine Seismic Data. Marine Science and Technology Bulletin, 9(1), 51–57. https://doi.org/10.33714/masteb.635468

Fairbanks, R. G. (1989). A 17,000-year glacio-eustatic sea level record: influence of glacial melting rates on the Younger Dryas event and deep-ocean circulation. Nature, 342(6250), 637–642. https://doi.org/10.1038/342637a0

Finney, B. P., Lyle, M. W., & Heath, G. R. (1988). Sedimentation at MANOP Site H (eastern equatorial Pacific) over the past 400,000 years: Climatically induced redox variations and their effects on transition metal cycling. Paleoceanography, 3(2), 169–189. https://doi.org/10.1029/PA003i002p00169

Folk, R. L., & Ward, W. C. (1957). Brazos River bar [Texas]; a study in the significance of grain size parameters. Journal of Sedimentary Research, 27(1), 3–26. https://doi.org/10.1306/74D70646-2B21-11D7-8648000102C1865D

Gebhardt, H., Sarnthein, M., Grootes, P. M., Kiefer, T., Kuehn, H., Schmieder, F., & Röhl, U. (2008). Paleonutrient and productivity records from the subarctic North Pacific for Pleistocene glacial terminations I to V. Paleoceanography, 23(4). https://doi.org/10.1029/2007PA001513

Genç, Ş. C., Dönmez, M., Akçay, A. E., Altunkaynak, Ş., Eyüpoğlu, Ilgar, M. Y. 2012. Biga Yarımadası Tersiyer Volkanizmasının Stratigrafik, Petrografik ve Kimyasal Özellikleri. Yarımadası'nın Tersiyer Öncesi Jeolojisi. Biga Yarımadası'nın Genel ve Ekonomik Jeolojisi. Maden Tetkik ve Arama Genel Müdürlüğü Özel Yayın Serisi 28, 122-162

Gessner, K., Gallardo, L. A., Markwitz, V., Ring, U., & Thomson, S. N. (2013). What caused the denudation of the Menderes Massif: Review of crustal evolution, lithosphere structure, and dynamic topography in southwest Turkey. Gondwana Research, 24(1), 243–274. https://doi.org/10.1016/j.gr.2013.01.005

Göktürk, O. M., Fleitmann, D., Badertscher, S., Cheng, H., Edwards, R. L., Leuenberger, M., Fankhauser, A., Tüysüz, O., & Kramers, J. (2011). Climate on the southern Black Sea coast during the Holocene: implications from the Sofular Cave record. Quaternary Science Reviews, 30(19–20), 2433–2445. https://doi.org/10.1016/j.quascirev.2011.05.007

Goldberg, E. D., & G.O.S., A. (1958). Chemistry of Pacific pelagic sediments. Geochimica et Cosmochimica Acta, 13(2–3), 153–212. https://doi.org/10.1016/0016-7037(58)90046-2

Grove, J. M. 2004. Little Ice Ages. Ancient and Modern. Volumes 1 and 2, 2nd ed. London, New York: Routledge.

Grützner, J., Hillenbrand, C.-D., & Rebesco, M. (2005). Terrigenous flux and biogenic silica deposition at the Antarctic continental rise during the late Miocene to early Pliocene: implications for ice sheet stability and sea ice coverage. Global and Planetary Change, 45(1–3), 131–149. https://doi.org/10.1016/j.gloplacha.2004.09.004

Grützner, J., Rebesco, M. A., Cooper, A. K., Forsberg, C. F., Kryc, K. A., & Wefer, G. (2003). Evidence for orbitally controlled size variations of the East Antarctic Ice Sheet during the late Miocene. Geology, 31(9), 777. https://doi.org/10.1130/G19574.1

Günay Beyhan. (1999). Investigation of tectonic characteristics of Saroz, Edremit and Gökova gulves by means of seismic reflection data interpretation.

Gürer, Ö. F., Kaymakçı, N., Çakır, Ş., & Özburan, M. (2003). Neotectonics of the southeast Marmara region, NW Anatolia, Turkey. Journal of Asian Earth Sciences, 21(9), 1041–1051. https://doi.org/10.1016/S1367-9120(02)00140-2

Gürer, Ö. F., Sangu, E., & Özburan, M. (2006). Neotectonics of the SW Marmara region, NW Anatolia, Turkey. Geological Magazine, 143(2), 229–241. https://doi.org/10.1017/S0016756805001469

Gürer, Ö. F., Sangu, E., Özburan, M., Gürbüz, A., Gürer, A., & Sinir, H. (2016). Plio-Quaternary kinematic development and paleostress pattern of the Edremit Basin, western Turkey. Tectonophysics, 679, 199–210. https://doi.org/10.1016/j.tecto.2016.05.007

Hedges, J. I., & Oades, J. M. (1997). Comparative organic geochemistries of soils and marine sediments. Organic Geochemistry, 27(7–8), 319–361. https://doi.org/10.1016/S0146-6380(97)00056-9

Hellstrom, J. C., & McCulloch, M. T. (2000). Multi-proxy constraints on the climatic significance of trace element records from a New Zealand speleothem. Earth and Planetary Science Letters, 179(2), 287–297. https://doi.org/10.1016/S0012-821X(00)00115-1

Hodell, D. A., Channell, J. E. T., Curtis, J. H., Romero, O. E., & Röhl, U. (2008). Onset of "Hudson Strait" Heinrich events in the eastern North Atlantic at the end of the middle Pleistocene transition (∼640 ka)? Paleoceanography, 23(4). https://doi.org/10.1029/2008PA001591

Holzwarth, U., Esper, O., & Zonneveld, K. A. F. (2010). Organic-walled dinoflagellate cysts as indicators of oceanographic conditions and terrigenous input in the NW African upwelling region. Review of Palaeobotany and Palynology,159(1–2), 35–55. https://doi.org/10.1016/j.revpalbo.2009.10.005

Hori, K., & Saito, Y. (2007). An early Holocene sea-level jump and delta initiation. Geophysical Research Letters, 34(18). https://doi.org/10.1029/2007GL031029

Intergovernmental Panel on Climate Change. (2021). Climate change 2021: The physical science basis. Contribution of Working Group I to the Sixth Assessment Report of the Intergovernmental Panel on Climate Change (V. Masson-Delmotte, P. Zhai, A. Pirani, et al., Eds.). Cambridge University Press. https://doi.org/10.1017/9781009157896

İşseven T., Tapırdamaz M. C., Özçep F., Hisarlı M., Orbay N., & Sanver M. (1995). Kuzeybatı Anadolu'nun tektoniği ve paleomanyetik sonuçlar. Jeofizik Dergisi, 9(1).

Jackson, J., & McKenzie, D. (1988). The relationship between plate motions and seismic moment tensors, and the rates of active deformation in the Mediterranean and Middle East. Geophysical Journal International, 93(1), 45–73. https://doi.org/10.1111/j.1365-246X.1988.tb01387.x

Jenkins, R., & de Vries, J. L. (1970). Determination of dead time. In R. Jenkins & J. L. de Vries (Eds.), Worked Examples in X-Ray Analysis (pp. 105–107). Springer New York. https://doi.org/10.1007/978-1-4899-2647-0_39

Jolivet, L., Faccenna, C., Huet, B., Labrousse, L., le Pourhiet, L., Lacombe, O., Lecomte, E., Burov, E., Denèle, Y., Brun, J.-P., Philippon, M., Paul, A., Salaün, G., Karabulut, H., Piromallo, C., Monié, P., Gueydan, F., Okay, A. I., Oberhänsli, R., … Driussi, O. (2013). Aegean tectonics: Strain localisation, slab tearing and trench retreat. Tectonophysics, 597–598, 1–33. https://doi.org/10.1016/j.tecto.2012.06.011

Jorry, S. J., & Biévre, G. (2011). Integration of sedimentology and ground-penetrating radar for high-resolution imaging of a carbonate platform. Sedimentology, 58(6), 1370–1390. https://doi.org/10.1111/j.1365-3091.2010.01213.x

Kaufman, K. D., Olsen, E. A., Whiting, D., Savin, R., DeVillez, R., Bergfeld, W., Price, V. H., van Neste, D., Roberts, J. L., Hordinsky, M., Shapiro, J., Binkowitz, B., & Gormley, G. J. (1998). Finasteride in the treatment of men with androgenetic alopecia. Journal of the American Academy of Dermatology, 39(4), 578–589. https://doi.org/10.1016/S0190-9622(98)70007-6

Kaya, O. (1979). Ortadoğu Ege çöküntüsünün (Neojen) stratigrafisi ve tektoniği. Türkiye Jeoloji Kurumu Bülteni, 22(1), 35-58.

Kaymakci, N., Aldanmaz, E., Langereis, C., Spell, T. L., Gurer, O. F., & Zanetti, K. A. (2007). Late Miocene transcurrent tectonics in NW Turkey: evidence from palaeomagnetism and ^{40}Ar–^{39}Ar dating of alkaline volcanic rocks.

Geological Magazine, 144(2), 379–392. https://doi.org/10.1017/S0016756806003074

Klump, J., Hebbeln, D., & Wefer, G. (2000). The impact of sediment provenance on barium-based productivity estimates. Marine Geology, 169(3–4), 259–271. https://doi.org/10.1016/S0025-3227(00)00092-X

Kotthoff, U., Müller, U. C., Pross, J., Schmiedl, G., Lawson, I. T., van de Schootbrugge, B., & Schulz, H. (2008). Lateglacial and Holocene vegetation dynamics in the Aegean region: an integrated view based on pollen data from marine and terrestrial archives. The Holocene, 18(7), 1019–1032. https://doi.org/10.1177/0959683608095573

Kuhlmann, H., Freudenthal, T., Helmke, P., & Meggers, H. (2004). Reconstruction of paleoceanography off NW Africa during the last 40,000 years: influence of local and regional factors on sediment accumulation. Marine Geology, 207(1–4), 209–224. https://doi.org/10.1016/j.margeo.2004.03.017

Kujau, A., Nürnberg, D., Zielhofer, C., Bahr, A., & Röhl, U. (2010). Mississippi River discharge over the last ~560,000 years — Indications from X-ray fluorescence core-scanning. Palaeogeography, Palaeoclimatology, Palaeoecology, 298(3–4), 311–318. https://doi.org/10.1016/j.palaeo.2010.10.005

Kurtuluş, C., Doğan, B., Sertçelik, F., Canbay, M., & Küçük, H. M. (2009). Determination of the tectonic evolution of the Edremit Gulf based on seismic reflection studies. Marine Geophysical Researches, 30(2), 121–134. https://doi.org/10.1007/s11001-009-9072-2

Kwiecien, O., Arz, H. W., Lamy, F., Wulf, S., Bahr, A., Röhl, U., & Haug, G. H. (2008). Estimated Reservoir Ages of the Black Sea Since the Last Glacial. Radiocarbon, 50(1), 99–118. https://doi.org/10.1017/S0033822200043393

Lamb, H. H. (1965). Frequency of Weather Types. Weather, 20(1), 9–12. https://doi.org/10.1002/j.1477-8696.1965.tb02130.x

Lamb, H. H. (1995). Climate, History and the Modern World. Routledge. https://books.google.com.tr/books?id=0Nucx3udvnoC

Lambeck, K., Yokoyama, Y., & Purcell, T. (2002). Into and out of the Last Glacial Maximum: sea-level change during Oxygen Isotope Stages 3 and 2. Quaternary Science Reviews, 21(1–3), 343–360. https://doi.org/10.1016/S0277-3791(01)00071-3

Marsh, R., Mills, R. A., Green, D. R. H., Salter, I., & Taylor, S. (2007). Controls on sediment geochemistry in the Crozet region. Deep Sea Research Part II: Topical Studies in Oceanography, 54(18–20), 2260–2274. https://doi.org/10.1016/j.dsr2.2007.06.004

Mayewski, P. A., Rohling, E. E., Curt Stager, J., Karlén, W., Maasch, K. A., Meeker, L. D., Meyerson, E. A., Gasse, F., van Kreveld, S., Holmgren, K., Lee-Thorp, J., Rosqvist, G., Rack, F., Staubwasser, M., Schneider, R. R., & Steig, E. J. (2004). Holocene climate variability. Quaternary Research, 62(3), 243–255. https://doi.org/10.1016/j.yqres.2004.07.001

McDermott, F. (2004). Palaeo-climate reconstruction from stable isotope variations in speleothems: a review. Quaternary Science Reviews, 23(7–8), 901–918. https://doi.org/10.1016/j.quascirev.2003.06.021

McKenzie, D. (1972). Active Tectonics of the Mediterranean Region. Geophysical Journal International, 30(2), 109–185. https://doi.org/10.1111/j.1365-246X.1972.tb02351.x

Meijers, M. J. M., Kaymakci, N., van Hinsbergen, D. J. J., Langereis, C. G., Stephenson, R. A., & Hippolyte, J.-C. (2010). Late Cretaceous to Paleocene oroclinal bending in the central Pontides (Turkey). Tectonics, 29(4), n/a-n/a. https://doi.org/10.1029/2009TC002620

Meyers, P. A. (1994). Preservation of elemental and isotopic source identification of sedimentary organic matter. Chemical Geology, 114(3–4), 289–302. https://doi.org/10.1016/0009-2541(94)90059-0

Meyers, P. A., & Teranes, J. L. (2001). Sediment Organic Matter. In W. M. Last & J. P. Smol (Eds.), Tracking Environmental Change Using Lake Sediments: Physical and Geochemical Methods (pp. 239–269). Springer Netherlands. https://doi.org/10.1007/0-306-47670-3_9

Mohtadi, M., Romero, O. E., Kaiser, J., & Hebbeln, D. (2007). Cooling of the southern high latitudes during the Medieval Period and its effect on ENSO. Quaternary Science Reviews, 26(7–8), 1055–1066. https://doi.org/10.1016/j.quascirev.2006.12.008

Moreno, E., Thouveny, N., Delanghe, D., McCave, I. N., & Shackleton, N. J. (2002). Climatic and oceanographic changes in the Northeast Atlantic reflected by magnetic properties of sediments deposited on the Portuguese Margin during the last 340 ka. Earth and Planetary Science Letters, 202(2), 465–480. https://doi.org/10.1016/S0012-821X(02)00787-2

Muhammet Duman, Barış Akçalı, Filiz Küçüksezgin, & Gökhan Kaboğlu. (2018). Ege Kıyı Sularında Deniz Taban Yapılarının Sınıflandırılması ve Haritalanması. https://search.trdizin.gov.tr/en/yayin/detay/620709/ege-kiyi-sularinda-deniz-taban-yapilarinin-siniflandirilmasi-ve-haritalanmasi

Munsell Color (Firm). (2010). Munsell soil color charts: with genuine Munsell color chips. Grand Rapids, MI: Munsell Color

Okay, A. I., & Tüysüz, O. (1999). Tethyan sutures of northern Turkey. Geological Society, London, Special Publications, 156(1), 475–515. https://doi.org/10.1144/GSL.SP.1999.156.01.22

Okay A., & Göncüoğlu M. C. (2004). The Karakaya Complex: A Review of Data and Concepts. Turkish Journal of Earth Sciences, 75–95.

Okay A., & Satır M. (2000). Coeval plutonism and metamorphism in a latest Oligocene metamorphic core complex in northwest Turkey. Geol. Mag, 495–516.

Okay A., Satır M., Maluski H., Siyako M., Monie P., Metzger R., & Akyuz H. S. (1996). Paleo- and Neo-Tethyan events in northwest Turkey: geological and geochronological constraints. The Tectonic Evolution of Asia, 420–441.

Okay A., Siyako M., & Bürkan K. A. (1991). Geology and tectonic evolution of the Biga Peninsula. Bulletin of the Technical University of Istanbul, 191–255.

Özhan, N., Keleş, N., Atalay, E., Atuk, N., Kuran, H., Dumlu, O., Tuzcu, G., Günay, G., Korkmaz, N., Bilginer, Ö. ve Çuhadar, G., 1977. Edremit ve Armutova (Gömeç) Ovaları, DSİ Hidrojeolojik Etüt Raporu, Ankara

Özkaymak, Ç., Sözbilir, H., & Uzel, B. (2013). Neogene–Quaternary evolution of the Manisa Basin: Evidence for variation in the stress pattern of the İzmir-Balıkesir Transfer Zone, western Anatolia. Journal of Geodynamics, 65, 117–135. https://doi.org/10.1016/j.jog.2012.06.004

Peltier, W. R., & Fairbanks, R. G. (2006). Global glacial ice volume and Last Glacial Maximum duration from an extended Barbados sea level record. Quaternary Science Reviews, 25(23–24), 3322–3337. https://doi.org/10.1016/j.quascirev.2006.04.010

Pickett, E. A., & Robertson, A. H. F. (1996). Formation of the Late Palaeozoic–Early Mesozoic Karakaya Complex and related ophiolites in NW Turkey by Palaeotethyan subduction–accretion. Journal of the Geological Society, 153(6), 995–1009. https://doi.org/10.1144/gsjgs.153.6.0995

Piva, A., Asioli, A., Trincardi, F., Schneider, R. R., & Vigliotti, L. (2008). Late-Holocene climate variability in the Adriatic Sea (Central Mediterranean). The Holocene, 18(1), 153–167. https://doi.org/10.1177/0959683607085606

Potts, P. J., & Webb, P. C. (1992). X-ray fluorescence spectrometry. Journal of Geochemical Exploration, 44(1–3), 251–296. https://doi.org/10.1016/0375-6742(92)90052-A

Radczewski, O. E. (1939). Eolian Deposits in Marine Sediments, In Recent Marine Sediments. American Association of Petroleum Geologists. https://doi.org/10.1306/SV10340C26

Rebolledo, L., Sepúlveda, J., Lange, C. B., Pantoja, S., Bertrand, S., Hughen, K., & Figueroa, D. (2008). Late Holocene marine productivity changes in Northern Patagonia-Chile inferred from a multi-proxy analysis of Jacaf channel sediments. Estuarine, Coastal and Shelf Science, 80(3), 314–322. https://doi.org/10.1016/j.ecss.2008.08.016

Reimer, P. J., Austin, W. E. N., Bard, E., Bayliss, A., Blackwell, P. G., Bronk Ramsey, C., Butzin, M., Cheng, H., Edwards, R. L., Friedrich, M., Grootes, P. M., Guilderson, T. P., Hajdas, I., Heaton, T. J., Hogg, A. G., Hughen, K. A., Kromer, B., Manning, S. W., Muscheler, R., … Talamo, S. (2020). The IntCal20 Northern Hemisphere Radiocarbon Age Calibration Curve (0–55 cal kBP). Radiocarbon, 62(4), 725–757. https://doi.org/10.1017/RDC.2020.41

Revel, M., Ducassou, E., Grousset, F. E., Bernasconi, S. M., Migeon, S., Revillon, S., Mascle, J., Murat, A., Zaragosi, S., & Bosch, D. (2010). 100,000 Years of African monsoon variability recorded in sediments of the Nile margin. Quaternary Science Reviews, 29(11–12), 1342–1362. https://doi.org/10.1016/j.quascirev.2010.02.006

Rex, R. W., & Goldberg, E. D. (1958). Quartz Contents of Pelagic Sediments of the Pacific Ocean. Tellus, 10(1), 153–159. https://doi.org/10.1111/j.2153-3490.1958.tb01995.x

Richter, T. O., van der Gaast, S., Koster, B., Vaars, A., Gieles, R., de Stigter, H. C., de Haas, H., & van Weering, T. C. E. (2006). The Avaatech XRF Core Scanner: technical description and applications to NE Atlantic sediments. Geological Society, London, Special Publications, 267(1), 39–50. https://doi.org/10.1144/GSL.SP.2006.267.01.03

Röhl, U., Brinkhuis, H., Sluijs, A., & Fuller, M. (2004). On the search for the Paleocene/Eocene boundary in the Southern Ocean: Exploring ODP Leg 189 holes 1171D and 1172D, Tasman Sea (pp. 113–125). https://doi.org/10.1029/151GM08

Rohling, E. J. (1994). Glacial conditions in the Red Sea. Paleoceanography, 9(5), 653–660. https://doi.org/10.1029/94PA01648

Romero, O. E., Kim, J., & Donner, B. (2008). Submillennial-to-millennial variability of diatom production off Mauritania, NW Africa, during the last glacial cycle. Paleoceanography, 23(3). https://doi.org/10.1029/2008PA001601

Rossignol-Strick, M., Nesteroff, W., Olive, P., & Vergnaud-Grazzini, C. (1982). After the deluge: Mediterranean stagnation and sapropel formation. Nature, 295(5845), 105–110. https://doi.org/10.1038/295105a0

Rothwell, R. G., & Croudace, I. w. (2015). Micro-XRF Studies of Sediment Cores: A Perspective on Capability and Application in the Environmental Sciences (pp. 1–21). https://doi.org/10.1007/978-94-017-9849-5_1

Rothwell, R. G., & Rack, F. R. (2006). New techniques in sediment core analysis: an introduction. Geological Society, London, Special Publications, 267(1), 1–29. https://doi.org/10.1144/GSL.SP.2006.267.01.01

Sabine, C. L., Feely, R. A., Gruber, N., Key, R. M., Lee, K., Bullister, J. L., Wanninkhof, R., Wong, C. S., Wallace, D. W. R., Tilbrook, B., Millero, F. J., Peng, T.-H., Kozyr, A., Ono, T., & Rios, A. F. (2004). The Oceanic Sink for Anthropogenic CO_2. Science, 305(5682), 367–371. https://doi.org/10.1126/science.1097403

Sayın, E., Eronat, C., Uçkaç, Ş., & Beşiktepe, Ş. T. (2011). Hydrography of the eastern part of the Aegean Sea during the Eastern Mediterranean Transient (EMT). Journal of Marine Systems, 88(4), 502–515. https://doi.org/10.1016/j.jmarsys.2011.06.005

Schindler, C., Pfister, M., & Aksoy, A. (1997). Active tectonics of northwestern Anatolia: The Marmara Poly-Project: a multidisciplinary approach by space-geodesy, geology, hydrogeology, geothermics and seismology (M. Poly-Project., Ed.). vdf, Hochschulverlag AG an der ETH.

Seeberg-Elverfeldt, J., Schlüter, M., Feseker, T., & Kölling, M. (2005). Rhizon sampling of porewaters near the sediment-water interface of aquatic systems. Limnology and Oceanography: Methods, 3(8), 361–371. https://doi.org/10.4319/lom.2005.3.361

Sengör, A. M. C. (1979). The North Anatolian transform fault: its age, offset and tectonic significance. Journal of the Geological Society, 136(3), 269–282. https://doi.org/10.1144/gsjgs.136.3.0269

Şengör, A. M. C., Yılmaz, Y., & Sungurlu, O. (1984). Tectonics of the Mediterranean Cimmerides: nature and evolution of the western termination of Palaeo-Tethys. Geological Society, London, Special Publications, 17(1), 77–112. https://doi.org/10.1144/GSL.SP.1984.017.01.04

Şengün, F., Yiğitbaş, E., & Tunç, İ. O. (2011). Geology and Tectonic Emplacement of Eclogite and Blueschists, Biga Peninsula, Northwest Turkey. Turkish Journal of Earth Sciences. https://doi.org/10.3906/yer-0912-75

Shackleton, N. J. (1982). The deep-sea sediment record of climate variability. Progress in Oceanography, 11(2), 199–218. https://doi.org/10.1016/0079-6611(82)90008-8

Sharp, Zachary. "Principles of Stable Isotope Geochemistry, 2nd Edition." (2017). doi:https://doi.org/10.25844/h9q1-0p82

Shaw, T. J., Gieskes, J. M., & Jahnke, R. A. (1990). Early diagenesis in differing depositional environments: The response of transition metals in pore water. Geochimica et Cosmochimica Acta, 54(5), 1233–1246. https://doi.org/10.1016/0016-7037(90)90149-F

Siani, G., Paterne, M., Arnold, M., Bard, E., Métivier, B., Tisnerat, N., & Bassinot, F. (2000a). Radiocarbon Reservoir Ages in the Mediterranean Sea and Black Sea. Radiocarbon, 42(2), 271–280. https://doi.org/DOI: 10.1017/S0033822200059075

Siani, G., Paterne, M., Arnold, M., Bard, E., Métivier, B., Tisnerat, N., & Bassinot, F. (2000b). Radiocarbon Reservoir Ages in the Mediterranean Sea and Black Sea. Radiocarbon, 42(2), 271–280. https://doi.org/10.1017/S0033822200059075

Siddall, M., Rohling, E. J., Almogi-Labin, A., Hemleben, Ch., Meischner, D., Schmelzer, I., & Smeed, D. A. (2003). Sea-level fluctuations during the last glacial cycle. Nature, 423(6942), 853–858. https://doi.org/10.1038/nature01690

Sluijs, A., & Brinkhuis, H. (2009). A dynamic climate and ecosystem state during the Paleocene-Eocene Thermal Maximum: inferences from dinoflagellate cyst assemblages on the New Jersey Shelf. Biogeosciences, 6(8), 1755–1781. https://doi.org/10.5194/bg-6-1755-2009

Sluijs, A., Brinkhuis, H., Crouch, E. M., John, C. M., Handley, L., Munsterman, D., Bohaty, S. M., Zachos, J. C., Reichart, G., Schouten, S., Pancost, R. D., Damsté, J. S. S., Welters, N. L. D., Lotter, A. F., & Dickens, G. R. (2008). Eustatic variations during the Paleocene-Eocene greenhouse world. Paleoceanography, 23(4). https://doi.org/10.1029/2008PA001615

Stanford, J. D., Hemingway, R., Rohling, E. J., Challenor, P. G., Medina-Elizalde, M., & Lester, A. J. (2011). Sea-level probability for the last deglaciation: A statistical analysis of far-field records. Global and Planetary Change, 79(3–4), 193–203. https://doi.org/10.1016/j.gloplacha.2010.11.002

Straub, C. (1997). Recent crustal deformation and strain accumulation in the Marmara Sea region, NW Anatolia, inferred from repeated GPS measurements. Active Tectonics of Northwestern Anatolia, The Marmara Poly Project.

Straub, C., Kahle, H.G., 1997. Recent crustal deformation and strain accumulation in the Marmara Sea region, NW Anatolia, inferred from repeated GPS measurements. In: Schindler, C., Pfister, M. (Eds.), Active Tectonics of Northwestern Anatolia-The Marmara Poly-Project. VdF Hochschulverlag AG der ETH, Zürich, pp. 417–447.

Stuiver, M., & Reimer, P. J. (1993). Extended ^{14}C Data Base and Revised CALIB 3.0 ^{14}C Age Calibration Program. Radiocarbon, 35(1), 215–230. https://doi.org/10.1017/S0033822200013904

Stuut, J.-B. W., Kasten, S., Lamy, F., & Hebbeln, D. (2007). Sources and modes of terrigenous sediment input to the Chilean continental slope. Quaternary International, 161(1), 67–76. https://doi.org/10.1016/j.quaint.2006.10.041

Tarbuck, E. J., Lutgens, F. K., & Tasa, D. G. (2017). Earth Science. Pearson Education. https://books.google.com.tr/books?id=z45ODwAAQBAJ

Taymaz, T., Jackson, J., & McKenzie, D. (1991). Active tectonics of the north and central Aegean Sea. Geophysical Journal International, 106(2), 433–490. https://doi.org/10.1111/j.1365-246X.1991.tb03906.x

TDI-Brook. (2022). TDI-Brooks Piston Corer.

Thomson, J., Croudace, I. W., & Rothwell, R. G. (2006). A geochemical application of the ITRAX scanner to a sediment core containing eastern Mediterranean sapropel units. Geological Society, London, Special Publications, 267(1), 65–77. https://doi.org/10.1144/GSL.SP.2006.267.01.05

Thomson, J., Higgs, N. C., Croudace, I. W., Colley, S., & Hydes, D. J. (1993). Redox zonation of elements at an oxic/post-oxic boundary in deep-sea sediments. Geochimica et Cosmochimica Acta, 57(3), 579–595. https://doi.org/10.1016/0016-7037(93)90369-8

Tunç, İ. O., Yiğitbaş, E., Şengün, F., Wazeck, J., Hofmann, M., & Linnemann, U. (2012). U-Pb zircon geochronology of northern metamorphic massifs in the Biga Peninsula (NW Anatolia-Turkey): new data and a new approach to understand the tectonostratigraphy of the region. Geodinamica Acta, 25(3–4), 202–225. https://doi.org/10.1080/09853111.2013.877242

Uzel, B., Sözbilir, H., Özkaymak, Ç., Kaymakcı, N., & Langereis, C. G. (2013). Structural evidence for strike-slip deformation in the İzmir–Balıkesir transfer zone and consequences for late Cenozoic evolution of western Anatolia (Turkey). Journal of Geodynamics, 65, 94–116. https://doi.org/10.1016/j.jog.2012.06.009

van Rooij, D., Blamart, D., Kozachenko, M., & Henriet, J.-P. (2007). Small mounded contourite drifts associated with deep-water coral banks, Porcupine Seabight, NE Atlantic Ocean. Geological Society, London, Special Publications, 276(1), 225–244. https://doi.org/10.1144/GSL.SP.2007.276.01.11

van Rooij, E., Sutherland, L. B., Qi, X., Richardson, J. A., Hill, J., & Olson, E. N. (2007). Control of Stress-Dependent Cardiac Growth and Gene Expression by a MicroRNA. Science, 316(5824), 575–579. https://doi.org/10.1126/science.1139089

Vidal, L., Bickert, T., Wefer, G., & Röhl, U. (2002). Late Miocene stable isotope stratigraphy of SE Atlantic ODP Site 1085: Relation to Messinian events. Marine Geology, 180(1–4), 71–85. https://doi.org/10.1016/S0025-3227(01)00206-7

Weaver, P. P. E., & Schultheiss, P. J. (1990a). Current methods for obtaining, logging and splitting marine sediment cores. Marine Geophysical Researches, 12(1–2), 85–100. https://doi.org/10.1007/BF00310565

Weaver, P. P. E., & Schultheiss, P. J. (1990b). Current methods for obtaining, logging and splitting marine sediment cores. Marine Geophysical Researches, 12(1–2), 85–100. https://doi.org/10.1007/BF00310565

Wentworth, C. K. (1922). A Scale of Grade and Class Terms for Clastic Sediments. The Journal of Geology, 30(5), 377–392. https://doi.org/10.1086/622910

Westerhold, T., Röhl, U., Laskar, J., Raffi, I., Bowles, J., Lourens, L. J., & Zachos, J. C. (2007). On the duration of magnetochrons C24r and C25n and the timing of early Eocene global warming events: Implications from the Ocean Drilling Program Leg 208 Walvis Ridge depth transect. Paleoceanography, 22(2). https://doi.org/10.1029/2006PA001322

Yaltırak, C., Alpar, B., Sakınç, M., & Yüce, H. (2000). Origin of the Strait of Çanakkale (Dardanelles): regional tectonics and the Mediterranean–Marmara incursion. Marine Geology, 164(3–4), 139–156. https://doi.org/10.1016/S0025-3227(99)00134-6

Yaltırak, C., İşler, E. B., Aksu, A. E., & Hiscott, R. N. (2012). Evolution of the Bababurnu Basin and shelf of the Biga Peninsula: Western extension of the middle strand of the North Anatolian Fault Zone, Northeast Aegean Sea, Turkey. Journal of Asian Earth Sciences, 57, 103–119. https://doi.org/10.1016/j.jseaes.2012.06.016

Yaltırak C., & Okay A. (2004). Geology of the Paleotethys units at the northern part of Edremit Bay. Itüdergisi, 3(1), 67–79.

Yilmaz, Y., Genç, Ş. C., Gürer, F., Bozcu, M., Yilmaz, K., Karacik, Z., Altunkaynak, Ş., & Elmas, A. (2000). When Did the Western Anatolian Grabens Begin to Develop? Geological Society, London, Special Publications, 173(1), 353–384. https://doi.org/10.1144/GSL.SP.2000.173.01.17

Yılmaz, Y., Genç, Ş. C., Karacık, Z., & Altunkaynak, Ş. (2001). Two contrasting magmatic associations of NW Anatolia and their tectonic significance. Journal of Geodynamics, 31(3), 243–271. https://doi.org/10.1016/S0264-3707(01)00002-3

Yılmaz, Y., & Karacık, Z. (2001). Geology of the northern side of the Gulf of Edremit and its tectonic significance for the development of the Aegean grabens. Geodinamica Acta, 14(1–3), 31–43. https://doi.org/10.1080/09853111.2001.11432433

Zachos, J., Pagani, M., Sloan, L., Thomas, E., & Billups, K. (2001). Trends, Rhythms, and Aberrations in Global Climate 65 Ma to Present. Science, 292(5517), 686–693. https://doi.org/10.1126/science.1059412

CURRICULUM VITAE

Surname, Name: Kartal, Pir Çağatay

EDUCATION

Degree	Institution	Year of Graduation
MS	RHUL Petroleum Geoscience	2018
BS	METU Geological Engineering	2015
High School	Kılıçarslan Lisesi, Ankara	2011

FOREIGN LANGUAGES

English

PUBLICATIONS

1. Kartal Pir Çağatay, Gürboğa Şule, Ertekin Mustafa Batuhan, Türkmen Özgür, Yavuzoğlu Ayhan, Kırat Uğur Zeki, Kayadibi Önder, Aylan Eşref, & Deveci Aral Zehra. (2022). Edremit Körfezi (KB Anadolu) karot sedimanlarının jeokimyasal özellikleri: Kaynak vedağılım koşullarının araştırılması. MTA Yerbilimleri ve Madencilik Dergisi, 47–66.

2. Gürboğa, Ş., Yavuzoğlu, A. Z., Güney, R., Karci, F. B., Yavuzoğlu, A., Türkmen, Ö., Kartal, P. Ç., Aydemir, B. S., Evren, M., Cenk, M., Şimşek, B., Özbek, E., Yurtsever, T. Ş., Yiğit Fethi, F., Aylan, E., & Kirat, U. Z. (2020). Gaziköy-Mürefte (Marmara Denizi) arasında yer alan sığ denizel bölgenin sismik yansıma verileri ışığında tektonik anlamı, KB Anadolu. Bulletin of The Mineral Research and Exploration, 1–24. https://doi.org/10.19111/bulletinofmre.784476

Skiing, Windsurf, Computer Technologies, Movies